Dumbbell-shaped colloids: Equilibrium and nonequilibrium phase behaviour

D i s s e r t a t i o n

zur Erlangung des akademischen Grades

d o c t o r r e r u m n a t u r a l i u m

(Dr. rer. nat.)

im Fach Chemie

eingereicht an der

Mathematisch-Naturwissenschaftlichen Fakultät

der Humboldt-Universität zu Berlin

von

M. Sc. Fangfang Chu

Präsident der Humboldt-Universität zu Berlin

Prof. Dr. Jan-Hendrik Olbertz

Dekan: der Mathematisch-Naturwissenschftlichen Fakultät

Prof. Dr. Elmar Kulke

Gutachter: 1. Prof. Dr. Matthias Ballauff

2. Prof. Dr. Jürgen P. Rabe

Tag der mündlichen Prüfung: 22.10.2014

Better to light one candle than to curse the darkness.

Anna Louise Strong

To my family

Abstract

In the present work the phase behaviour of hard dumbbells has been explored as a function of aspect ratio (L*, the center to center distance to the diameter of one composed sphere) and volume fractions using thermosensitive dumbbell-shaped microgels as the hard dumbbell model system. A fluid-to-plastic crystal phase transition indicated by Bragg reflections has been observed for $L^* < 0.4$. The experimental phase diagrams at $L^* \sim 0.24$ and $L^* \sim 0.30$ are comparable to the theoretical prediction of the Monte Carlo simulations.

Rheological measurements reveal that the hard dumbbells in the biphasic gap show the yielding behaviour with a single yielding event, while two yielding events have been observed for the plastic crystalline phase. The two yielding events, referred to as the double yielding behaviour, are proved to be related to the crystallization of hard dumbbells. The underlying structural evolution has been investigated by rheo-SANS experiments and the scattering data has been interpreted by BD simulations. It is demonstrated that the plastic crystal structure of the hard dumbbells is polycrystalline at rest, which has been induced into the twinned fcc structure at low strain, the partially oriented sliding layers at high strain and the intermediate state at the strain in-between. The shear-induced structural evolution corresponds to the double yielding events of the fully crystallized hard dumbbells. Additionally, we prove that the increase of L* ($L^* < 0.4$) does not change the structural evolution of the sheared hard dumbbells. Only more extensive or longer oscillations are required to form the shear-induced crystal structures due to the slowdown of the dynamics in the vicinity of the glass transition.

In a second part, the work of this thesis is extended to hollow systems composed of hollow spheres and hollow Janus dumbbells that can be used as model systems to probe phase behaviour of hollow capsules.

Key words: hard dumbbell, phase behaviour, crystallization, partially oriented sliding layers, thermosensitive microgels, shear-induced, plastic crystal, hollow capsules, Janus dumbbells

Zusammenfassung

In der vorliegenden Arbeit wurde das Phasenverhalten von harten Hantelteilchen (Dumbbells) als Funktion des Aspektverhältnisses (L*, der Quotient aus dem Abstand der Massenzentren zum Durchmesser der Kugel) und der Volumendichte untersucht. Bragg-Reflexe weisen darauf hin, das harte Dumbbells mit L* < 0.4 einen Phasenübergang von einer Fluid-artigen Phase zu einem plastischen Kristall zeigen. Die experimentellen Phasendiagramme bei L* ~ 0.24 und L*~ 0.30 sind vergleichbar mit Vorhersagen aus Monte Carlo-Simulationen.

Rheologie Messungen zeigen, dass harte Dumbbells verschiedene Gleichgewichts- und Nichtgleichgewichtsphasen annehmen. Suspensionen von harten Dumbbells im Zweiphasenbereich zeigen ein einziges Fließgrenzen-Ereignis, wohingegen in der plastischen Kristallphase zwei Fließgrenzen-Ereignisse beobachtet werden. Diese, im Folgenden als „double yielding“ bezeichneten Ereignisse, hängen mit der Kristallisation der Suspensionen von harten Dumbbells zusammen. Die entsprechende Strukturentwicklung wurde mit rheo-SANS-Experimenten untersucht und mithilfe von BD Simulationen interpretiert. Es konnte gezeigt werden, dass die plastische Kristallphase polykristallin im Ruhezustand ist. Unter schwacher Scherung wird eine fcc-Schwerzwilling Struktur ausgebildet. Bei hoher Scherung formt sich eine teilweise orientierte Struktur aus gleitenden Schichten. Zwischen diesen beiden Strukturen existiert eine ungeordnete Übergangsphase. Die Scher-induzierte Strukturausbildung eintspricht dem „double yielding“ Ereignis der kristallinen harten Dumbells. Es wurde gezeigt, dass ein größeres L* (L* < 0.4) die Strukturentwicklung unter Scherung qualitativ nicht beeinflusst. Aufgrund verlangsamter Dynamik in der Nähe des Glasübergangs sind lediglich stärkere oder längere Oszillationen von Nöten, um Scher-induzierte Kristallisation zu erzeugen.

Im zweiten Teil dieser Arbeit werden Systeme aus hohlen Kugeln und „Janus“-Dumbbells vorgestellt, die als kolloidale Modellsysteme dienen können.

Schlagwörter: harte Dumbbell, Phasenverhalten, Kristallisation, teilweise orientierte Schichtstruktur, thermosensitive Mikrogele, scherinduziert, plastischer Kristall, hohle Kapseln, Janus-Dumbbell

Table of Contents

Abstract ..... **V**

Zusammenfassung ..... **VI**

1. Introduction **1**

1.1 Hard spheres 1

1.2 Hard dumbbells 3

1.3 Strategy of synthesis 7

2. Objective of this thesis **10**

3. Theory **12**

3.1 Hard dumbbell model system 12

3.1.1 Thermosensitive microgels 12

3.1.2 Brownian motion of hard dumbbells 14

3.2 Dynamic light scattering 16

3.2.1 Dynamic light scattering 16

3.2.2 Depolarized dynamic light scattering 17

3.2.3 Hydrodynamic modeling (shell model) 18

3.3 Rheology and small angle neutron scattering (SANS) 20

3.3.1 Rheology 20

3.3.2 Small angle neutron scattering 23

3.3.3 Rheo-SANS 25

3.4 Crystallization of colloids under shear 26

3.4.1 Geometric packing model 27

3.4.2 Model calculation 29

3.4.3 Dynamics of sheared hard dumbbells 31

4. Hard Dumbbells **34**

4.1 Synthesis and characterization of dumbbell-shaped microgels 34

4.1.1 Synthesis 34

4.1.2 Characterization 35

4.2 Phase diagram and crystallization of hard dumbbells 43

4.2.1 Phase diagram 43

4.2.2 Crystallization process 46

4.3 Yielding behaviour of hard dumbbells 51

4.3.1 Hard dumbbells with $L^* \sim 0.24$ 52

4.3.2 Hard dumbbells with L*~0.30 55

4.4 The plastic crystalline phase and its structural evolution 57

4.4.1 Plastic crystalline phase 58

4.4.2 Partially oriented sliding layers at high strain 67
4.4.3 Biphasic region of hard dumbbells with $L^* \sim 0.24$ 75
4.4.4 Effect of L^* 77

5. Thermosensitive hollow capsules 82

5.1 Hollow spherical capsules 83
5.1.1 Thermosensitive hollow spheres 83
5.1.2 Monolayer hollow spheres 84
5.1.3 Bilayer hollow spheres 87
5.2 Hollow Janus dumbbells 90
5.2.1 Thermosensitive hollow Janus dumbbells 90
5.2.2 Dissolution of Janus dumbbell-shaped core 91
5.2.3 Hollow Janus dumbbells 94

6. Summary and outlook 100

7. Experimental 103

7.1 Materials 103
7.2 Synthesis procedures 103
7.2.1 Synthesis of the core-shell spherical microgels 103
7.2.2 Synthesis of the dumbbell-shaped microgels 105
7.2.3 Preparation of thermosensitive hollow capsules 107
7.3 Characterization 109
7.3.1 Light scattering 109
7.3.2 Electron microscopy 111
7.3.3 Scanning force microscopy (SFM) 112
7.3.4 Rheology and Rheo-SANS 112

Bibliography 120

List of Figures 140

List of Tables 151

List of Abbreviations 152

List of Publications 155

Presentations at Conferences and Meetings 156

Acknowledgement 157

Selbstständigkeitserklärung 159

1. Introduction

Colloidal particles dispersed in a liquid exhibit a variety of phase behaviour, which can mimic that of simple atomic or molecular liquids and solids.[1-3] In general, the phase transition of colloidal systems can be divided into two classes: disorder-order transitions driven by entropic effects in systems dominated by repulsive interparticle potentials and fluid-fluid or fluid-solid transitions caused by weak attractions. This thesis studies the first one that corresponds to the disorder-order or freezing transition in the molecular system. Synthetic colloids have been prepared and used as model systems.[4-7] The phase behaviour of both spherical[8-10] and nonspherical systems[11-12] have been intensively investigated. In the following the main results of these studies will be presented and discussed.

1.1 Hard spheres

Up to now, spherical colloids have been synthesized and used as model systems.[4, 13-15] Sterically stabilized suspensions have been regarded as hard spheres to study crystallizations and the vitrification at a fundamental level.[16-19] Pusey and van Megen first reported on the crystallization[1] and the glass transition[20-21] of hard spheres. Sterically stabilized poly(methyl methacryalate) (PMMA) covered by a thin surface layer of poly-(12 hydroxystearic acid) (PHSA)[4, 22] are used as the hard sphere model system. The phase diagram of hard spheres is only a function of volume fraction, ϕ as shown in Figure 1.1.1.

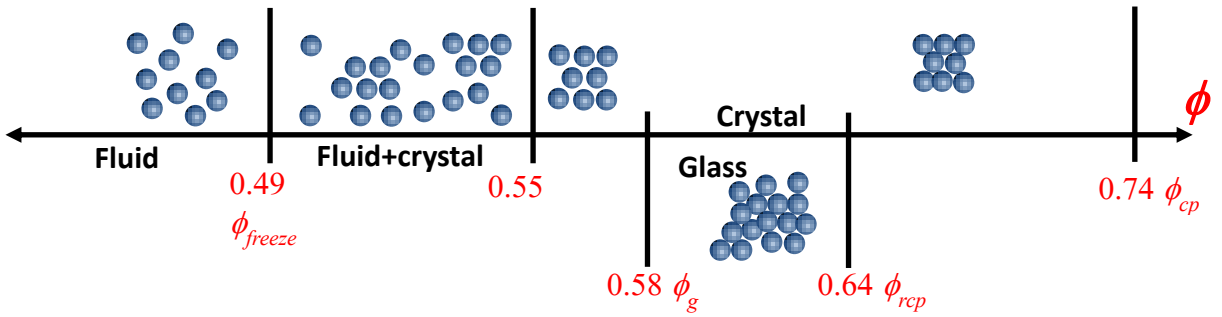

Figure 1.1.1 Phase diagram of hard spheres .[9] As shown in the top part, monodisperse hard spheres with $\phi > \phi_{freeze}$ crystallize,[23] and the glass transition (in the bottom part) is at ϕ_g~0.58.[2, 24–25] Random-close packing of the spheres is reached at ϕ_{rcp} = 0.64 and a dense packing of spheres is at ϕ_{cp} = 0.74.

In case of monodisperse hard spheres, the suspension with the volume fraction below the freezing point ϕ_{freeze}= 0.49 is in a disordered fluid phase where particle positions are not correlated over a long distance. For 0.49 < ϕ < 0.55, an ordered crystal phase coexists with the fluid phase in equilibrium. When the volume fraction is above 0.55, the suspensions are in the fully crystalline phase. In addition to this, a glassy phase exists for 0.58 < ϕ < 0.64 as shown in the bottom part of Figure 1.1.1. Polydispersity of the hard spheres can prevent crystallization and such a suspension is the ideal system for the study of colloidal glasses. ϕ_{rcp} is the random close packing volume fraction, that is, the maximum density of a completely random sphere packing.[26-27]

Recently, thermosensitive core-shell microgels that can serve as the model system of hard spheres[19] have been developed. [28-29] As shown in Figure 1.1.2, the core-shell microgels are composed of polystyrene (PS) spheres as core and thermosensitive poly (N-isopropylacrylamide) (PNIPA) network as shell.[30-31] Due to the themosensitivity of the PNIPA shell, the shell thickness and volume fractions can be adjusted via controlling temperature.[31-32] Thus, the fluid-to-crystal transition[33] as well as the fluid-to-glass transition[34-35] can be easily realized by changing the temperature.

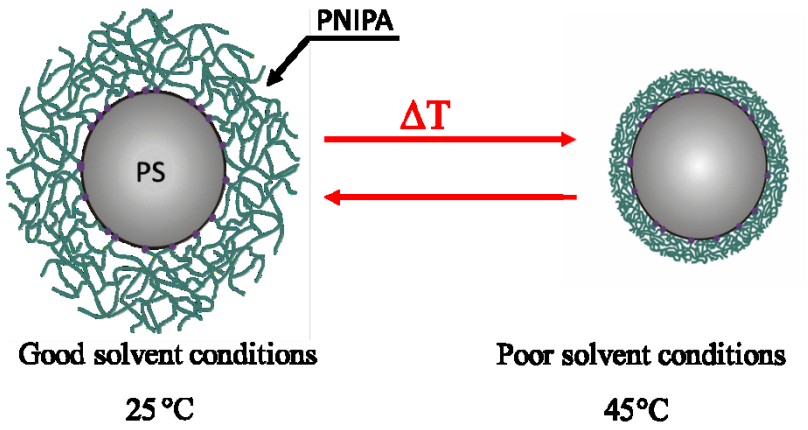

Figure 1.1.2 Scheme of the thermosensitive core-shell microgels. The PNIPA shell is attached onto the surface to the PS cores. At room temperature of ca. 25 °C, the PNIPA network takes up the dispersion medium water, which will be mostly expelled when the temperature is raised above 32 °C.[36]

Using the core-shell microgels as model systems, the crystallization of hard spheres has been investigated.[14] The phase diagram obtained from this model system is identical to the theoretical prediction.[37] It is also comparable to that achieved by using the sterically stabilized PMMA latex as a model system.[38] Moreover, suspensions of the core-shell

microgels have become one of the most important model systems to study the glass transition and to test statistical-mechanical theories.[19, 29] For example, the flow behaviour of hard spheres in the glassy state has been investigated by rheological measurements[19, 39-40] and the results are in accordance with the theoretical predictions of mode-coupling theory (MCT).[34-35, 41-42] Thus, the phase behaviour and dynamics of concentrated spherical colloidal suspensions have been extensively investigated using synthetic colloids as model systems.[19, 43-44]

1.2 Hard dumbbells

The phase behaviour of spherical colloidal suspensions is well understood by now and recent research focuses more and more on nonspherical objects. Frenkel and co-workers[45] are one of the first groups to investigate the shape and size effect on the phase behaviour of hard ellipsoids by Monte Carlo simulations. It is found that hard ellipsoids with large anisotropies freeze into the fully ordered phase with both translation and orientation order. In case of small anisotropies, hard ellipsoids freeze into a plastic crystal phase, exhibiting long range translational order without long range orientational order.[45-47]

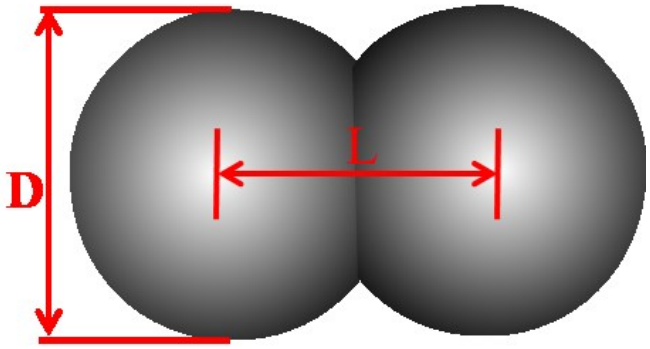

Figure 1.2.1 Schematic figure of a hard dumbbell that consists of two interpenetrating identical spheres. *L* denotes the center to center distance and *D* represents the diameter of one composed sphere. The particle's anisotropy is defined by aspect ratio, $L^* = L/D$.

Based on the hard dumbbell model system as schematically shown in Figure 1.2.1, Singer *et al.*[48] calculated the coexistence curve between the fully ordered phase and the plastic crystal phase as a function of the particle's anisotropy. Vega and his co-workers[49] used Monte Carlo (MC) simulations to study the solid-fluid phase equilibria of hard dumbbells, indicating that the phase diagram of hard dumbbells is a function of ϕ and aspect ratio, L^*.[50] MC simulations predict that the plastic crystal phase is stable for $L^* < 0.38$ within a certain range

of volume fractions[49-50] and a fully ordered phase forms at higher volume fractions. For $L^* > 0.38$, hard dumbbells undergo the transition from fluid to a fully ordered state.[51]

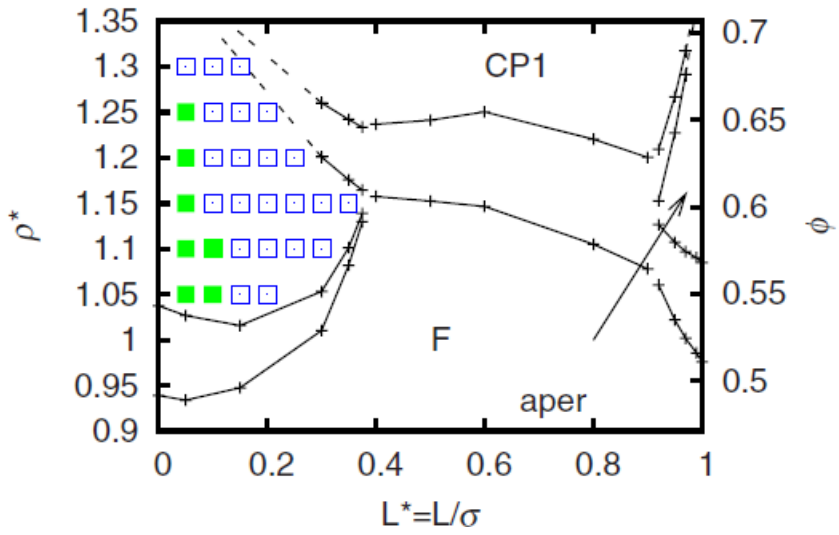

Figure 1.2.2 The phase diagram of hard dumbbells in the number density ρ^* (and the packing fraction ϕ) versus $L^* = L/D$ representation.[52] *F* denotes the fluid phase and CP1 means the periodic crystal. The aperiodic phase (aper) is stable only in a narrow region of the phase diagram. The stable fcc type plastic crystal is denoted by filled squares, the hcp plastic crystal phase is denoted by empty squares. The coexistence densities for $L^* < 0.9$ are taken from Refs. [49-50].

To further investigate the phase behaviour of hard dumbbells, Marechal *et al.* calculated the stability of crystal structures of hard dumbbells using MC simulations.[52] The calculated structure diagram is shown in Figure 1.2.2, the boundary of which is comparable to that of the phase diagram calculated by Vega *et al.*[49-50],[53] As shown in Figure 1.2.2, the calculation based on the MC method indicates that the hexagonal-close-packed (hcp) structure is more stable than the face-centered-cubic (fcc) structure for the plastic crystal formed from the hard dumbbells with $L^* < 0.38$. Both fcc and hcp structures consist of hexagonally close-packed layers, but they are different in the stacked way of hcp planes. Hexagonal layers of fcc structure stack in the ABC sequence, while the layers of hcp structure stack in the ABAB sequence. In the case of hard dumbbells with $L^* > 0.88$, the data of Figure 1.2.2 indicates that the aperiodic crystal structure is more stable, where the spheres of the dumbbells are on a random-hexagonal-close-packed lattice.

The theoretic work discussed above indicates that the hard dumbbells can order into manifold structures, which are determined by L^* and ϕ. With the availability of colloidal dumbbells,[5, 54-55] new crystal structures have been recently created based on the self-assembly of

dumbbells.[56] In the absence of external fields, most of the work focused on 2D structures produced by the convective drying.[57-58] Using slightly charged dumbbells with $L^* \sim 0.26$ as a model system, Zukoski's group first observed the plastic crystal and a body-centered tetragonal (bct) structure with aligned particles by ultra-small-angle X-ray scattering (USAXS).[59] Additionally, they analyzed the structure of the plastic crystal by the combination of rheology and small angle neutron scattering (rheo-SANS).[60] The plastic crystal in equilibrium was observed to be in the polycrystalline phase, and the sliding hexagonally packed layers developed under steady shear. However, the long-range order was lost at larger shear rates.

In external fields (e.g. magnetic field[61] or electric field[62]), field-induced crystals can be formed from dumbbell-shaped colloids,[63] which are mainly explored using the real-space confocal microscopy.[64-66] Here the group of van Blaaderen observed several different crystal structures by varying the particle's aspect ratio, range of interactions and electric field strength as shown in Figure 1.2.3. It was demonstrated that a tetragonal crystal (Figure 1.2.3a) and a bct structure (Figure 1.2.3d) were formed for high electric fields, while based-centered-monoclinic (bcm) structures were observed for low electric fields. In addition, they directed the orientation of asymmetric composite dumbbells with an electric field, increasing the potential for finding new crystal structures.[67-68]

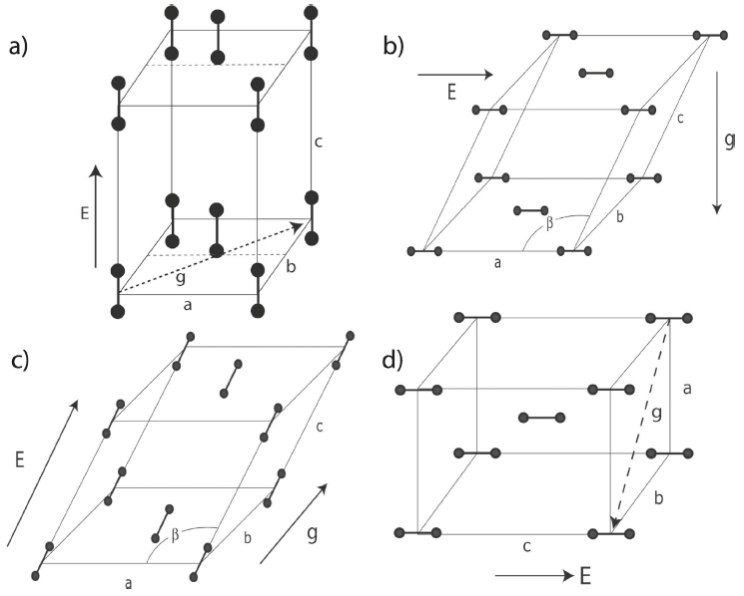

Figure 1.2.3 Unit cells for various structures of dumbbells crystals. They were obtained by sedimentation of charged dumbbells in a refractive index matching solvent within the presence of an electric field. (a) Tetragonal unit cell of dumbbell crystals formed from dumbbells with $L^* = 0.9$ in an electric field of 28 V_{rms}/mm. The crystal has a *P4/nmm* symmetry with space group number 129. (b) Based-centered monoclinic phase observed for dumbbells with $L^* = 0.7$ in a field of 23 V_{rms}/mm and for dumbbells with $L^* = 0.44$ in a field of 78 V_{rms}/mm. (c) Based-centered monoclinic phase observed less frequently for charged dumbbells of $L^* = 0.44$. (d) Body-centered-tetragonal (bct) phase observed for dumbbells with $L^* = 0.7$ and $L^* = 0.44$ at higher electric fields. 'E' stands for the electric field and 'g' for the direction of gravity.[69]

The theoretical and experimental studies discussed so far show that colloidal dumbbells are of great interest. A comprehensive investigation on the phase behaviour of hard-dumbbell-like colloids would provide the experimental comparison and verification for the theoretical studies on the phase behaviour of anisotropic particles.[52] As analogues of diatomic molecules,[70] hard-dumbbell-like colloids can provide access to understand the physical phenomenon like the freezing of nitrogen molecules into the plastic crystal.[53] Moreover, the phase behaviour of hard-dumbbell-like colloids can guide the self-assembly of anisotropic particles to create new types of colloidal crystals[71-72] or photonic gap materials[73]. However, there is no experimental report on the phase behaviour of hard dumbbells without an external field yet.

Here, we first present the preparation and comprehensive study of a hard dumbbell model system, which is composed of a dumbbell-shaped PS core and a shell of thermosensitive crosslinked PNIPA. The PNIPA shows a collapse at a lower critical solution temperature (LCST) of ca. 32°C,[31, 36, 74] which can be used to adjust the shell thickness and volume

fractions via temperature. Thus, the transition from fluid-to-solid (crystalline or glassy) state can be easily realized through controlling the temperature as shown in Figure 1.2.4. Based on this model system, the phase behaviour of hard dumbbells is investigated in this thesis.

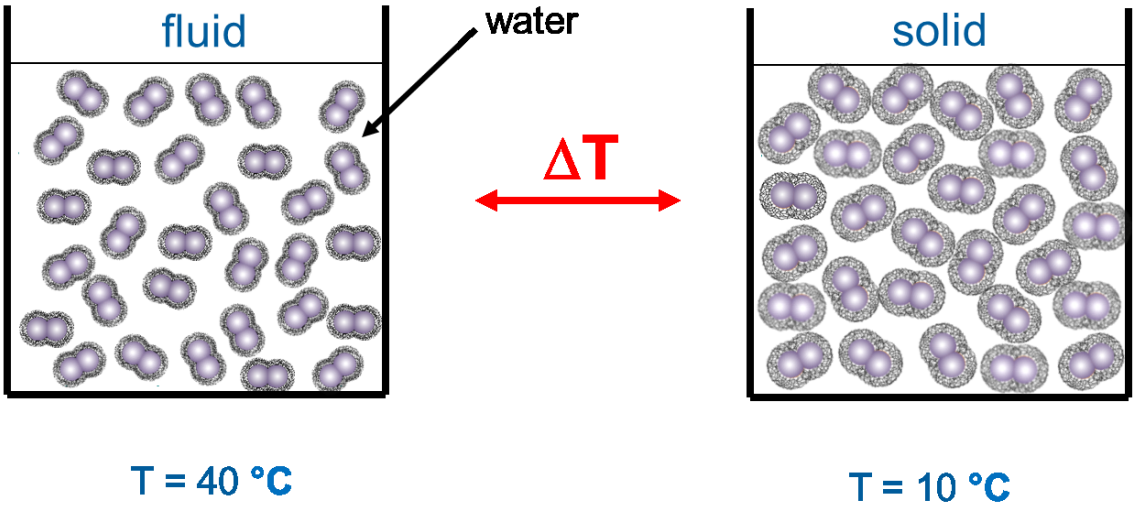

Figure 1.2.4 Schematic representation for the reversible transition of thermosensitive dumbbell-shaped microgels from fluid-to-solid via adjusting temperature from 40°C to 10°C. The dumbbell-shaped microgels have a thermosensitive PNIPA shell attached onto the surface of dumbbell-shaped cores, which is swollen by water at low temperature e.g. 10 °C. However, water will be expelled when the temperature is increased to 40°C.[36, 75-76] In this way, the volume fraction of the particles can be adjusted by temperature.

1.3 Strategy of synthesis

Various methods have been reported to synthesize dumbbell-shaped particles, including inorganic,[77-80] organic-inorganic,[81] and organic (polymeric) dumbbells[82-83]. In general, two routes are mainly used to produce a large scale of homogeneous dumbbells. Colloidal silica dumbbells formed by spherical silica seeds are grown in a microemulsion and aggregated by the depletion effects.[5] One additional silica layer is fabricated to adjust the aspect ratio of these silica dumbbells. A second synthetic strategy for the preparation of non-spherical particles is the seeded emulsion polymerization.[84] Based on this approach, cross-linked spherical seeds particles are firstly swollen with monomers and then give rise to dumbbell-shaped particles by the phase separation of the second monomer during polymerization.[68, 77, 85-86] Moreover, Janus dumbbells with chemical anisotropy are produced through the seeded polymerization by using different monomers in the swelling stage.[68, 83, 86] However, nearly all

dumbbells are charge stabilized colloidal particles, which cannot serve as model systems of hard dumbbells.

Recently, Crassous *et al*.[87] reported the preparation of thermosensitive ellipsoids by stretching spherical polymeric particles. The aspect ratio is varied by controlling the stretching process. Hoffmann *et al*. [82],[88] presented a synthetic strategy based on the seeded emulsion polymerization to fabricate the core-shell dumbbell-shaped microgels with polymeric dumbbell-shaped cores and thermosensitive crosslinked PNIPA shell. The core particles are prepared via the emulsifier-free seeded emulsion polymerization of polystyrene cores onto the surface of poly(methyl methacrylate) (PMMA) seeds.[88] Both ellipsoid-shaped and dumbbell-shaped microgels have a core-shell structure with the thermosensitive PNIPA shell attached onto the surface of anisotropic cores. Moreover, it is proved that the swelling behaviour of the PNIPA shell is not affected by the geometry of their core particles.[82, 87] Similar to the spherical core-shell microgels, the residual charges of the dumbbell-shaped microgels from synthesis can be screened by the addition of salt and thus they can serve as the model system of hard dumbbells.[14] However, one drawback of the methods discussed above is that it is nearly impossible to produce a large scale of homogeneous dumbbell-shaped particles, which is necessary for the application of colloidal dumbbells as a model system.[88] Moreover, the system prepared by Hoffmann *et al*. is too polydisperse and does not exhibit crystalline phases.

To our best knowledge, sufficiently monodisperse dumbbell-shaped colloids that can be used as model systems have not been reported yet. Here we present the synthetic strategy for thermosensitive dumbbell-shaped microgels for the first time that can be used for this purpose. The thermosensitive dumbbell-shaped microgels are prepared in two main steps. First, uniform dumbbell-shaped cores are prepared in a large scale through the seeded polymerization and the phase separation.[55] Second, a crosslinked PNIPA shell is attached onto to the surface of dumbbell-shaped core particles via the seeded emulsion polymerization.[10] A scheme of the core-shell dumbbell-shaped microgels is displayed in Figure 1.3.1a. The residual charges left from the synthesis is screened by the addition of KCl salt. The thermosensitive PNIPA shell provides an excellent steric stabilization.[29] As shown schematically in Figure 1.2.4, the transition of hard dumbbells from fluid-to-solid (crystalline or glassy) state can be easily realized through adjusting temperature. Thus, dumbbell-shaped microgels turn out to be an excellent model system that allows us to study the phase behaviour and dynamics of hard dumbbells in concentrated suspensions.

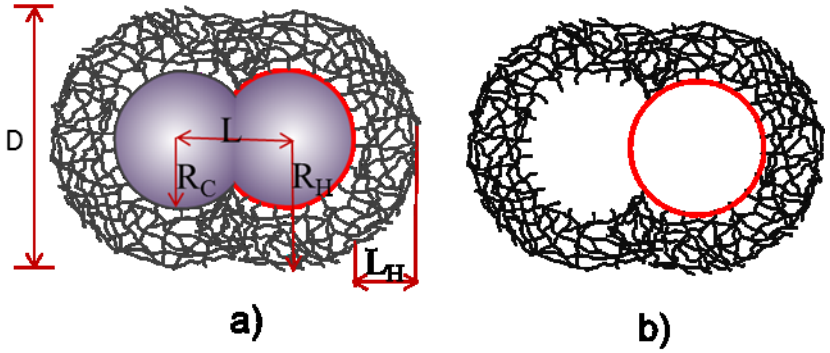

Figure 1.3.1 (a) Scheme of dumbbell-shaped microgels that can serve as the hard dumbbell model system. The residual charges from the synthesis is screened by the addition of salt (potassium chloride, KCl), resulting in sterically stabilized hard dumbbells. The diameter of one sphere is marked as D, center to center distance is L, the thickness of PNIPA shell is L_H. For the dumbbell-shaped core, the radius of one composed sphere is denoted as R_C. (b) Schematic illustration of thermosensitive Janus dumbbells that are prepared via the selective removal of THF using the dumbbell-shaped microgels as templates. The thermosensitive Janus dumbbells with well-defined morphology can also be used as the model system of hard dumbbells, which may have different phase behaviour from hard dumbbells with solid cores.

Moreover, the dumbbell-shaped microgels can be used as templates for the fabrication of thermosensitive hollow Janus dumbbells by the selective removal of PS cores with tetrahydrofuran (THF).[89] Such hollow particles shown schematically in Fig. 1.3.1b can also serve as a model system, which may have different phase behaviour from that of hard dumbbell with solid cores. As non-spherical capsules, hollow Janus dumbbells have potential applications in the fields of catalysts,[90] delivery of encapsulated materials[91-93] and as model systems for the study of soft objects like red blood cells in motion.[94]

2. Objective of this thesis

The main objective of this thesis is to study the phase behaviour of hard dumbbells. Dumbbell-shaped microgels are applied as hard dumbbell model systems, which consist of a dumbbell-shaped PS core and onto which a thermosensitive PNIPA shell is attached. The dumbbell-shaped microgels can be further used as templates to prepare thermosensitive hollow Janus dumbbells by the selective removal of PS cores. The main interest of this study is to investigate the phase diagram and crystallizations of hard dumbbells in concentrated suspensions. The investigation on hard dumbbells in concentrated suspensions is carried out as following:

- The first part of this work focuses on the synthesis of hard dumbbell model systems. The morphology of the hard dumbbells is characterized by methods of TEM and cryo-/TEM.
- To characterize the thermo-sensitivity of the hard dumbbells, DLS and DDLS experiments are performed at various temperatures. The translational and rotational diffusion coefficients are obtained through the CONTIN analysis. Combined with the shell model, the dimensional information including L and D is calculated.
- The next part of this thesis aims at exploring the phase behaviour of hard dumbbells. Phase diagrams of hard dumbbells are determined by crystallization experiments, which are performed on dumbbell-shaped microgels with $L^* \sim 0.24$ and $L^* \sim 0.30$, respectively. This study presents the first time the experimental phase diagrams of hard dumbbells with small anisotropy ($L^* < 0.4$). Rheological measurements are carried out to investigate the crystallization and viscoelastic properties of hard dumbbell suspensions.
- Small angle neutron scattering (SANS) combined with shear is applied to measure the equilibrium structure of the plastic crystal at rest and its structural evaluation under oscillatory shear. The experimental results are compared with theoretical calculations of the sheared dumbbells based on Brownian dynamic simulations to interpret the underlying dynamics.
- Additionally, the effect of L^* on the phase behaviour of hard dumbbells are investigated. A comparison is made between the experimental findings of hard dumbbells with $L^* \sim 0.24$ and $L^* \sim 0.30$.

- Finally, the study is extended to the preparation of theromosensitive hollow Janus dumbbells in order to get another hard dumbbell model system with the hollow structure. The synthetic strategy begins with the preparation of monolayer and bilayer thermosensitive hollow spherical capsules. A comprehensive characterization is performed to characterize the morphology and dimensional information of these thermosensitive capsules.

3. Theory

3.1 Hard dumbbell model system

3.1.1 Thermosensitive microgels

Recently, thermosensitive colloidal microgels[7, 95-96] have been intensively studied as a sphere model system to study crystallization[95, 97-98] or glass transition[19, 34] in the colloidal systems. Most of these systems have been prepared based on cross-linked poly (N-isopropylacrylamide) (PNIPA) or its related copolymers.[19, 95, 99-100] The interaction potential plays an important role in the formation of crystallization or glassy state in the colloidal system, which can be controlled by varying the crosslinking degree from soft-polymer-like to hard sphere-like.[7, 98] The work reported on the spherical microgels demonstrates that the thermosensitive microgels that consist of solid polystyrene (PS) spheres as core and crosslinked PNIPA as shell can serves as an ideal model system of hard spheres.[19, 35, 99] Using this model system, the dynamics of concentrated suspensions have been investigated and the experimental data are fully compatible with the prediction of mode coupling theory (MCT).[34, 44]

In this thesis, the thermosensitive dumbbell-shaped microgels with dumbbell-shaped PS particles as cores and crosslinked thermosensitive PNIPA as shell are applied as the model system of hard dumbbells. The dumbbell-shaped microgels have several advantages that make them well-suited to be used as the hard dumbbell model systems. First, the thermosensitive PNIPA shells enhance the stability of these dumbbell-shaped microgels, especially in the concentrated state. The possible residual charges that are attached onto the surface of PS cores from the synthesis can be screened by the addition of salt. The work reported on the respective hard spheres indicates that 0.05 M KCl is enough to screen the electrostatic interactions.[14] Thus, the dumbbell-shaped microgels are stabilized by a purely steric interaction.

Next, the PNIPA shell shows a volume transition as a function of temperature.[28, 31, 101] In case of the non-spherical microgels, the thermosensitivity of the attached PNIPA shell is proved not to be affected by the geometry of their core particles.[82, 87] Figure 3.1.1 illustrates the thermoresponsive property of the dumbbell-shaped microgels used in this work in a schematic manner. At room temperature (ca. 25 °C), the water solution that disperses dumbbell-shaped

microgels can swell the PNIPA shell due to the formation of relatively strong hydrogen bonds between the already arranged water molecules and the PNIPA polymers.[36, 74] The water molecules must reorient around the nonpolar regions of PNIPA, which results in a decreased entropy. However, these hydrogen bonds become weaker when the temperature is increased above ca. 32 °C (LCST for PNIPA[36]). Instead, the intermolecular hydrogen bonds and nonpolar bonds are formed, resulting in the association of polymer molecules.[102-103] Therefore, PNIPA undergoes a phase separation due to the entropy effect and expels most of the dispersed medium (water).[76] With an increase in temperature, the solvent quality is thus changed from good to poor and the PNIPA shell of the dumbbell-shaped microgels must shrinks. Since the shrinking of PNIPA is fully reversible,[36] the shrunk PNIPA network can be re-swollen again by decreasing the temperature from 32 °C to 25 °C.[102, 104] Consequently, the effective volume fraction of the dumbbell suspensions can be easily adjusted from a moderate value located in the fluid phase to a higher value corresponding to a solid state by varying temperature.[105-106]

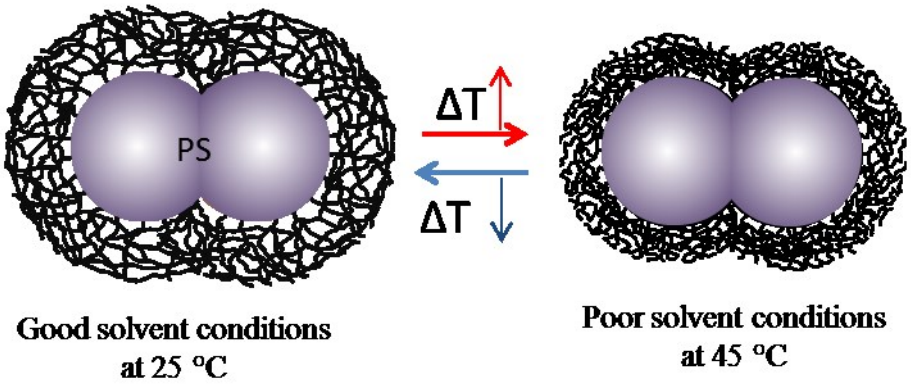

Figure 3.1.1 Illustration of the thermosensitivity of the dumbbell-shaped core-shell microgel, which consists of a dumbbell-shaped PS core and a thermosensitive PNIPA shell. The morphology of the core is proved not to change the temperature dependence of the PNIPA shell.[82]

Third, the aspect ratio, L^*, that is, the ratio of center to center distance to the diameter of one sphere can be also adjusted via the thermosensitive PNIPA shell. Thus, the dumbbell-shaped microgels can be applied as the model system to study the phase behaviour of hard dumbbells as a function of ϕ and L^*.

As discussed above, the thermosensitive dumbbell-shaped microgels are suitable to be applied as a model system. Nevertheless, it is necessary to point out that the crosslinking density of the PNIPA shell plays an important role in the rheological properties. The variation of crosslinking density can change the interaction potential of the particles and lead to different swelling ratios.[43, 107] However, owing to the hard PS core and a high degree crosslinking of the PNIPA shell, the dumbbell-shaped microgels with solid PS cores can be regarded as the hard dumbbell model system.

In order to characterize the core-shell microgels, several techniques are commonly used, including cryo-transmission electron microscopy (cryo-TEM),[28, 32, 108] small angle neutron scattering (SANS)[101, 109-110], small angle X-ray scattering (SAXS)[111] and light scattering.[112-113] Cryo-TEM can provide the direct proof on the core-shell morphology of microgels *in situ* via shock freezing of the diluted microgels suspension.[108] SAXS and SANS experiments can provide the analysis of the fine structure of the microgels.[111] Dynamic light scattering techniques are suitable to study the size of the colloidal microgels based on their Brownian motions.[109, 114] Due to the anisotropic morphology, depolarized dynamic light scattering (DDLS) measurements are necessary to characterize the dimensional information of the dumbbell-shaped microgels.[88] The theory about the Brownian motion and DDLS measurements of hard dumbbells will be discussed in detail in the following sections.

3.1.2 Brownian motion of hard dumbbells

The discovery of Brownian motion is attributed to Robert Brown who observed the random motion of small particles dispersed in water.[115] Based on Einstein's approach,[116] much work has been done to develop mathematical pathways for the description of Brownian motion.[115, 117] The diffusivity of an isolated sphere can be described with the Stokes-Einstein equation[116]

$$D_0 = \frac{kT}{6\pi\eta a} \quad , \tag{3.1.1}$$

with D_0 is the diffusion coefficient, a is the radius of the spherical particle, η is the viscosity of the fluid, k is Boltzmann constant, and T is temperature**.**

For the anisotropic system, F. Perrin[118-119] firstly showed that the anisotropy of particles can lead to a dissipative coupling of translational and rotational motion. The orientation of one

dumbbell can be described by two polar (or three Eulerian) angles θ and ϕ as shown in Figure 3.1.2.

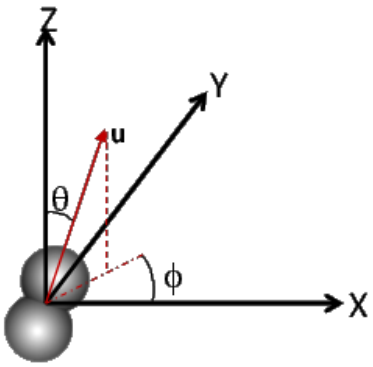

Figure 3.1.2 Orientation of one single dumbbell particle with respect to Cartesian coordinate system with its origin at the center of the particle. The solid red line is along the major axis of the particle and ***u*** is defined as the unit vector along the major axis. The dashed line represents the projection of the hard dumbbells on the x-y plane. ϕ tracks the position of the projected end point on the x-y plane.

In a liquid, hard dumbbells are expected to suffer many reorienting collisions per second. Collisions are assumed to be so frequent in a liquid that a molecule can only rotate through a very small angle before suffering a reorienting collision. Based on this assumption, Debye has developed a model (Debye model) for the reorientation processes.[120],[121] Combined with the diffusion equation, the rotational diffusion equation[122] (Debye equation) follows as

$$\frac{\partial c(\boldsymbol{u},t)}{\partial t} = \Theta \frac{1}{sin^2\theta}\left[sin\theta \frac{\partial}{\partial \theta}\left(sin\theta \frac{\partial}{\partial \theta}\right) + \frac{\partial^2}{\partial \phi^2}\right] c(\boldsymbol{u},t), \tag{3.1.2}$$

where the unit vector $\boldsymbol{u}$ directed along the major axis specifies the orientation of a dumbbell. $c(\boldsymbol{u},t)$ is the concentration of dumbbells with orientation $\boldsymbol{u}$ at time t. Θ is called as the rotational diffusion coefficient. For a symmetric diffusor $\Theta_{XX} = \Theta_{YY} = \Theta_{\perp}$ and $\Theta_{ZZ} = \Theta_{\parallel}$; and for a spherical diffusor $\Theta_{XX} = \Theta_{YY} = \Theta_{ZZ} = \Theta$.[122]

Light scattering is an important tool to characterize the Brownian motion of colloidal particles in a fluid.[13] The basic principles and theories of light scattering will be discussed in detail in Chapter 3.2.

3.2 Dynamic light scattering

In a light-scattering experiment as schematically shown in Figure 3.2.1, the light from a laser firstly passes through a polarizer, defining the polarization of the incident beam. The polarized beam then impinges on the scattering medium and gets scattered in all directions. Only the scattered light of wave vectors $\boldsymbol{q_s}$ will pass through an analyzer with a given polarization and be recorded by the detector. The analyzer is set to filter the scattered light according to the given polarization. The scattering angle θ is defined according to the position of the detector. The intersection of the incident beam and the beam intercepted by the detector defines the scattering volume V.

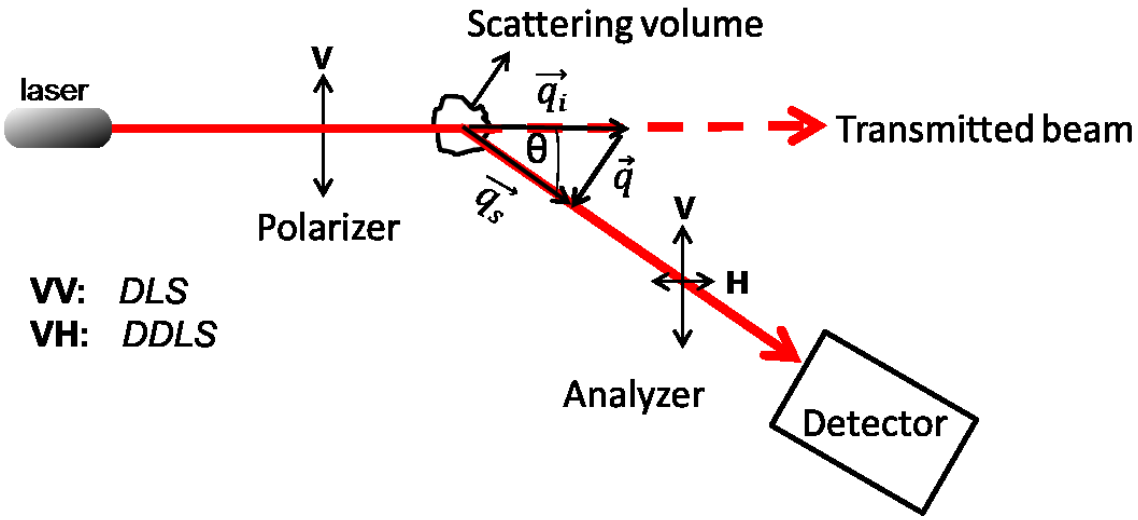

Figure 3.2.1 The light scattering setup with two pairs of commonly used polarization directions. Scattering geometry I: *VV* configuration with a polarizer of the vertical direction and an analyzer of the vertical direction. Scattering geometry II: *VH* configuration with a polarizer of the vertical direction and an analyzer of the horizontal direction. *V* and *H* refer to directions that are vertical and horizontal with respect to the scattering plane, respectively.

3.2.1 Dynamic light scattering

In Figure 3.2.1 a monochromatic laser beam impinges on a sample and the scattered light is recorded by a detector placed at a scattering angle of θ with respect to the transmitted beam. Because of thermal motions, the total scattered electric field at the detector fluctuates in time.[122] In case of the colloidal dispersions,[13] it is the Brownian motions of the colloidal particles that cause the fluctuations of scattered light from the dispersions. The autocorrelation

function of these fluctuating intensities furnishes the information about the diffusion coefficient in suspensions and solutions. The scattering vector $\boldsymbol{q}$ in terms of the scattering geometry is defined as

$$\boldsymbol{q} = \boldsymbol{q_s} - \boldsymbol{q_i},\ q = |\boldsymbol{q}| = \frac{4\pi n sin(\frac{\theta}{2})}{\lambda}, \tag{3.2.1}$$

with n as the refractive index and λ as the incident laser wavelength. q is dependent on the relative positions of particles. $\boldsymbol{q_i}$ and $\boldsymbol{q_s}$ denote the incoming beam and scattered beam, respectively.

For a dilute suspension of monodisperse spherical particles, the autocorrelation function can be written as

$$F_s(\boldsymbol{q}, \tau) = \exp(-\Gamma\tau), \text{with } \Gamma = q^2 D_0, \tag{3.2.2}$$

where τ is a time interval, which is very small compared to the time that refers to fluctuations in the scattering volume V. Thus, the diffusion coefficient of particles can be obtained from the autocorrelation function. The hydrodynamic radius of an isolated sphere can be calculated based on the Stokes-Einstein equation as described in Eq. (3.1.1).

3.2.2 Depolarized dynamic light scattering

In the depolarized dynamic light scattering (DDLS) measurement, geometry II described in Figure 3.2.1 has been applied. The polarized component, I_{VV} or depolarized component, I_{VH} can be resulted from geometry II, where polarizers and analyzers select out the corresponding components of the scattered electric field. I^{α}_{VV} and I^{α}_{VH} are noted[122]

$$I^{a}_{VV}(\boldsymbol{q}, t) =< N >< a_{zz}(0)a_{zz}(t) > F_s(\boldsymbol{q}, t)\ ,$$

and (3.2.3)

$$I^{a}_{VH}(\boldsymbol{q}, t) =< N >< a_{yz}(0)a_{yz}(t) > F_s(\boldsymbol{q}, t),$$

where a is a polarizability tensor. The correlation function $< a_{yz}(0)a_{yz}(t) >$ involves the polarizability sensor in the laboratory fixed coordinate system, and $a_{yz}(t)$ changes with time due to the reorientation. $F_s(\boldsymbol{q}, t)$ is the 'translational' factor that depends on q. The

components are normally determined by the optical anisotropy of scattering centers (for example, particles or molecules or parts of molecules) in the scattering medium.

The time correlation function measured by DDLS experiments with Geometry II (see Figure 3.2.1) consists of two main parts. One part refers to the correlations in both orientation and position between all pairs of molecules. The other one includes information on the dynamic coupling between translation and rotation of a single scattering element. In a dilute solution, the correlations in both orientation and position between all pairs of molecules, however, can be neglected. For the system contains a rotation axis of fourfold symmetry or higher (for example, symmetric molecules, rod-shaped molecule, ellipsoids of revolution), the correlation function is [122]

$$I_{VH}^{a}(q,t) = \frac{1}{15} < N > \beta^2 \exp[-(q^2 D + 6\Theta_{\perp})|t|], \tag{3.2.4}$$

where N is the number of molecules or particles in the scattering volume, β refers to the optical anisotropy of a molecule ($\beta = 0$ in case of spheres).

3.2.3 Hydrodynamic modeling (shell model)

As discussed above, DLS and DDLS can be applied to characterize both translational and rotational motion of anisotropic particles, which are described by translational diffusion (D^T) and rotational diffusion (D^R) respectively. Given both D^T and D^R, the dimensional information of anisotropic particles with various geometries (e.g. rods[123] and double spheres[124]) can be calculated.[88] But the calculation of the rotational diffusion requires proper models to simulate the hydrodynamics of a single anisotropic particle. Within the framework of the Kirkwood-Riseman theory,[125-126] a bead model has been firstly proposed for simple model systems that are composed of identical elements.[127] Concerning the hydrodynamic interactions, Bloomfield *et al*. proposed a shell model[128] as an alternative for bead modeling based on the assumption that the hydrodynamic resistance only takes place on the surface of particles. In the shell model, a particle can be modeled as a shell of small, identical beads .[129-130] To calculate the dimensional information of hard dumbbells in this thesis, the shell model is introduced [124, 131] and the corresponding two dimensional schematic figure is shown in Figure 3.2.2. The corresponding theoretical calculation has been done by Nils Heptner.[132]

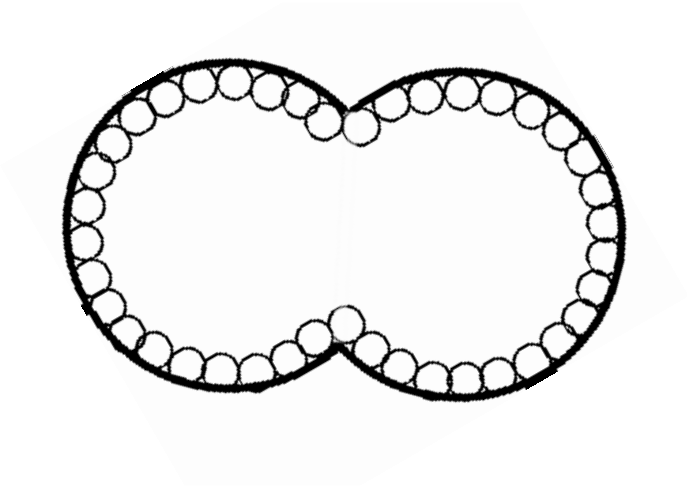

Figure 3.2.2 Two-dimensional analogy of the shell model for a hard dumbbell, which is seen as a shell of small identical beads (denoted by the small empty cycles). There are three possibilities to arrange the small beads: tangent to the inner face of the surface, centered on the surface or tangent to the outer surface (our choice). Owing to the limit of very small bead size, the small difference between these possibilities can vanish.

A large number of discrete minibeads are used to represent the surface of the colloidal dumbbell where the friction is assumed to take place. By extrapolating to zero minibead size to an infinite number of beads, the hydrodynamic properties can be calculated accurately. Based on the generalized Einstein tensorial equation $\mathcal{D} = kT\Xi^{-1}$,[133] the basic relation governing the frictional and Brownian behaviour of a rigid dumbbell can be written as

$$\mathcal{D} = \begin{pmatrix} \mathbf{D}^{\mathbf{tt}} & \mathbf{D}^{\mathbf{tr,T}} \\ \mathbf{D}^{\mathbf{tr}} & \mathbf{D}^{\mathbf{rr}} \end{pmatrix} = kT \begin{pmatrix} \Xi^{\mathrm{tt}} & \Xi^{\mathrm{tr,T}} \\ \Xi^{\mathrm{tr}} & \Xi^{\mathrm{rr}} \end{pmatrix}^{-1}, \tag{3.2.5}$$

In Eq. (3.2.5), the superscript T refers to transposition. The left side of the equation is the Brownian diffusivity expressed by a generalized, 6*6 diffusion matrix, $\mathcal{D}$. The hydrodynamic resistance is on the right side, which is displayed by a 6*6 generalized friction tensor, Ξ. $\mathcal{D}$ on the left side and Ξ on the right side are related through the general Einstein equation. Both matrixes are composed of 3*3 blocks, which correspond to the translation (*tt*), rotation (*rr*) and translation rotation coupling (*tr*) tensors, respectively. In the dilute suspensions, the translation and rotation coupling can be ignored. In other words, $\mathbf{D}^{\mathbf{tr}} = 0$ and $\Xi^{\mathrm{tr}} = 0$.

The hydrodynamic interactions of hard dumbbells are described by means of the Oseen diffusion tensor,[134]

$$\mathrm{T}_{ij} = \frac{1}{8\pi\eta_0 r_{ij}}\left(I + \frac{\boldsymbol{r_{ij}}\boldsymbol{r_{ij}}}{r_{ij}^2}\right), \tag{3.2.6}$$

where I is the unit tensor, $\boldsymbol{r_{ij}}$ is the distance vector between elements i and j and $\boldsymbol{r_{ij}r_{ij}}$ is the dyadic product of vector $\boldsymbol{r_{ij}}$.

In the shell model for a single rigid dumbbell, three axes are defined: one is parallel to the major axis and the other two are perpendicular to each other in the center plane. The entries of diffusion tensors related to the translational motion along each axis are numerically calculated from the *tt* block and averaged, leading to the mean translational diffusion constant D^T. Similarly, the relaxation times are calculated from $\boldsymbol{D^{rr}}$ tensors, resulting in D^R. The relaxation time resulted from the DDLS measurement characterizes rotational dynamics of a dumbbell particle. D^T that refers to the translational motion of dumbbells can be obtained by the DLS measurement. Based on the method described above, dimensions of the dumbbells are calculated by the public-domain HYDROSUB 7c program[135] from the DLS and DDLS measurements.[132]

3.3 Rheology and small angle neutron scattering (SANS)

3.3.1 Rheology

Rheology is defined as the science of the deformation and the flow of matter.[136] The basic concepts are introduced in this section.

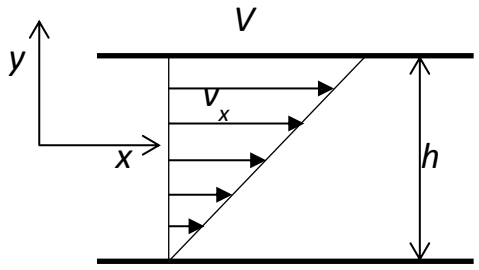

Figure 3.3.1 Shear flow between sliding (upper) and fixed (bottom) plates with a distance of h in between, and the upper plate moves with a velocity in V direction. A liquid is contained between the two parallel plates.

We begin with the simple flow conditions as shown in Figure 3.3.1. The upper plate slides with velocity V in the x direction, while the bottom plate is stationary. Given that velocities are sufficiently low to avoid turbulence, the fluid will flow everywhere parallel to the plates.

The local velocities v_x vary linearly along the gradient direction (y direction shown in Figure 3.3.1). The velocity of liquid layers near each plane is assumed to be the same as that in the plane. The gradient $\frac{dv_x}{dy}$ of v_x in the y direction is thus constant through the liquid:

$$\frac{dv_x}{dy} = \frac{V}{h} = \dot{\gamma} = \text{constant}, \tag{3.3.1}$$

A force $\boldsymbol{F}_{xy}$ is applied onto the upper plate to generate the flow. The index *x* in this case indicates the direction of the applied force, and y specifies the plane to which the force is applied in terms of the normal to the plane. The force required to move the top plate at a velocity *V* is proportional to the surface area of the plate, stress or the force per unit area, $\boldsymbol{\sigma_{xy}}$. The shear stress is transmitted from one plate to the other and acts on each fluid element. The velocity gradient $\boldsymbol{\frac{dv_x}{dy}}$ or shear rate is the parameter in this case to determine the level of the internal stresses. For Newtonian fluids, the Newton's constitutive equation for the viscosity can be used to describe the proportional relation between σ_{xy} and $\boldsymbol{\frac{dv_x}{dy}}$ [137]

$$\sigma_{xy} = \eta \frac{dv_x}{dy}, \tag{3.3.2}$$

The proportionality constant η is the viscosity coefficient, and represents the resistance to flow in Newtonian fluids. Newton's law is the simplest example of a rheological constitutive equation. To solve various flow problems, it must be combined with the conservation laws for mass, momentum and energy.[138]

Oscillatory shear flow can be studied in the same flow geometry as that for the steady shear flow shown in Figure 3.3.2. The upper plate executes a sinusoidal motion expressed by $x_p(t) = x_{p,0} sin\omega t$, in which $x_{p,0}$ is the peak displacement. As a result, a time-dependent, sinusoidal deformation or strain $\gamma(t)$ is generated as shown by the solid line in Figure 3.3.2.

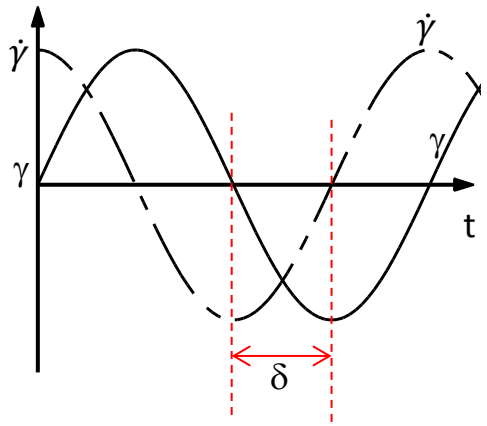

Figure 3.3.2 Oscillatory shear flow: a time dependent, sinusoidal deformation, $\boldsymbol{\gamma(t) = \gamma_0 sin\omega t}$ (the solid line) and the corresponding strain rate $\boldsymbol{\dot{\gamma}(t) = \dot{\gamma}_0 \omega cos\omega t}$ (denoted by the dashed line). δ is the phase angle that defined by the phase shift between stress and strain.

In an oscillatory flow, $\sigma = G * \gamma$ is used to describe an elastic sample. The energy of an elastic sample is stored during the deformation and then can be totally recovered when the deformation is reduced to zero. As for a viscous fluid, $\sigma = \eta\dot{\gamma}$, strain and stress are out of phase and all the energy used for the viscous fluid will be totally 'lost' and converted to heat. As for the viscoelastic material, it can be expressed as [137]

$$\sigma(t) = \gamma_0 [G'(\omega)\sin(\omega t) + G''\cos(\omega t)], \eta = \frac{G''}{\omega} \text{ and } tan(\delta) = \frac{G''}{G'}, \quad (3.3.3)$$

where the storage modulus *G'* describes the elastic component of the stress, and the loss modulus *G"* represents the viscous part. δ is named loss angle, that is, the phase angle between stress and strain (tan δ= *G"*/*G'*), which determines how much of applied mechanical energy is dissipated into heat.

In the rheology of colloidal suspension, the Péclet number (*Pe*) is an important parameter to describe the strength of the convective motion relative to the diffusive motion of a colloid in the sheared dispersion. In the study of transport phenomena in fluid flows, *Pe* is defined as the ratio of the rate of advection of a physical quantity by the flow to the rate of diffusion of the same quantity driven by an appropriate gradient. For Brownian hard spheres in the shear flow, *Pe* is defined as the ratio of the rate of advection by the flow to the diffusion rate by Brownian motion in a dilute dispersion,

$$Pe = \frac{\dot{\gamma}}{D_0/a^2} = \frac{\dot{\gamma}a^2}{D_0} = \frac{6\pi\eta_m\dot{\gamma}a^3}{k_BT}, \quad (3.3.4)$$

where a^2/D_0 is the time that is needed for a colloidal particle to diffuse a distance a (the scale of its own size) by Brownian motion. D_0 is the diffusivity defined in Eq.(3.1.1).

The rotational Péclet number, Pe_r is defined for nonspherical particles,[137] which is the ratio of shear rate to the rotary diffusivity D_r. For hard dumbbells used in this work, D_r can be measured by DDLS experiments,

$$Pe_r = \frac{\dot{\gamma}}{D_r}, \tag{3.3.5}$$

In an oscillatory shear field, the time dependent strain amplitude and shear rate is given by $\gamma(t) = \gamma_{max}\sin(2\pi ft)$, and $\dot{\gamma}(t) = \gamma_{max}2\pi f cos(2\pi ft)$, respectively. Pe_r of hard dumbbells is defined as

$$Pe_r = \frac{2\pi f\gamma_{max}}{D_r}, \tag{3.3.6}$$

3.3.2 Small angle neutron scattering

Small-angle neutrons scattering (SANS) is a diffraction method that is widely used to analyze the structure of matter.[139] In SANS experiments, the collimated neutron beam with the wavelength λ is directed at a sample, illuminating the scattering volume V. Some of the neutrons are transmitted by the sample, some are absorbed and some are scattered. The schematic figure for SANS experiment is similar to that of light scattering as shown in Figure 3.2.1. A detector is positioned at a certain distance from the sample, and at a scattering angle of θ. The detector records the flux of neutrons scattered into a solid angle element, ΔΩ. The scattering intensity scattered by N atoms, $I(q)$ can be calculated in general terms[139]

$$I(\boldsymbol{q}) = |A\,(\boldsymbol{q})|^2,\ A(\boldsymbol{q}) = \int \rho(\boldsymbol{q})\exp(2\pi i\boldsymbol{qr})\boldsymbol{dr}\ \ , \tag{3.3.7}$$

where $A\,(\boldsymbol{q})$ is the amplitude of elastic scattering by any assemble containing N atoms, which is defined through Fourier-transformation of the potential field, $\rho(\boldsymbol{q})$ and $\boldsymbol{r_i}$ are the scattering lengths distribution and coordinates of the atoms, respectively.

The value of ρ for a molecule of i atoms can be calculated

$$\rho = \sum_i b_i \frac{\delta N_A}{m} = N \cdot \sum_i b_i, \tag{3.3.8}$$

where δ is the bulk density of the molecule, m is the relative molar mass, N is the number density of scattering centers, and b_i is the coherent neutron scattering length of nucleus i.

In practice, neutron scattering can be used to investigate a wide range of substances, including poly- and single crystals, metals and alloys, amorphous solids and liquids, synthetic polymers, and biological macromolecules. Here we discuss the scattering by objects with different order. As for the single crystals with the atomic positions in an unit cell, the scattering amplitude is represented by the discrete set

$$A(\boldsymbol{q}) = \sum_{hkl} F_{hkl}\, \delta(\boldsymbol{q} - \boldsymbol{H}_{hkl}), \tag{3.3.9}$$

where $F_{hkl} = \Omega^{-1} \int \rho(\boldsymbol{r}) \exp(2\pi \boldsymbol{H}_{hkl}\boldsymbol{r})\, dr$, $\boldsymbol{H}_{hkl} = h\boldsymbol{a}^* + k\boldsymbol{b}^* + l\boldsymbol{c}^*$, a, b, and c deterring corresponding periodicities along the x, y, z axes, $\Omega = \left(\mathbf{a}[\mathbf{bc}]\right]$ is the volume of the unit cell, h, k and l are integers.

In case of isotropic systems, there is no long-range order. Due to the anisotropy of the samples, the scattering intensity is also isotropic and the intensity depends on only on the magnitude of the scattering vector. Based on the spherical coordinates, the radial Patterson function is expressed with the aid of the Fourier transform of the scattering intensity

$$P(r) = \frac{1}{2\pi^2} \int_0^\infty I(s) \frac{\sin(sr)}{sr} s^2 ds, \tag{3.3.10}$$

This equation leads to certain conclusions as to typical distances between the atoms in liquids or gases, the dimensions of clusters or pores in amorphous solids, or the particles dimensions in solutions.

In terms of anisotropic particles, the scattering intensity also includes the orientation information.[140-141] In this work, the orientation of hard dumbbell i is denoted by the unit vector $\boldsymbol{u}_i$. The scattered intensity of oriented hard dumbbells is calculated[142] including the scattering amplitude $A(\boldsymbol{q}; \boldsymbol{u}_i)$ of a uniaxial particle with orientation $\boldsymbol{u}_i$

$$I(q) \propto \left\langle \sum_{j,i} A(\boldsymbol{q}; \boldsymbol{u}_i) A(\boldsymbol{q}; \boldsymbol{u}_j)\, e^{-iq(\boldsymbol{r}_i - \boldsymbol{r}_j)} \right\rangle, \tag{3.3.11}$$

3.3.3 Rheo-SANS

As discussed above, there is considerable scientific interest to understand the fluid structural reorganization as a result of flow or shear[143] The combination of the shear flow and small angle neutron scattering (rheo-SANS) is suitable to investigate the shear phenomenon of different systems,[143] such as shear hardening of hydrogels,[144-145] shear thinning of polymer/nanoclay systems, [146] and shear-induced order of colloids.[147]

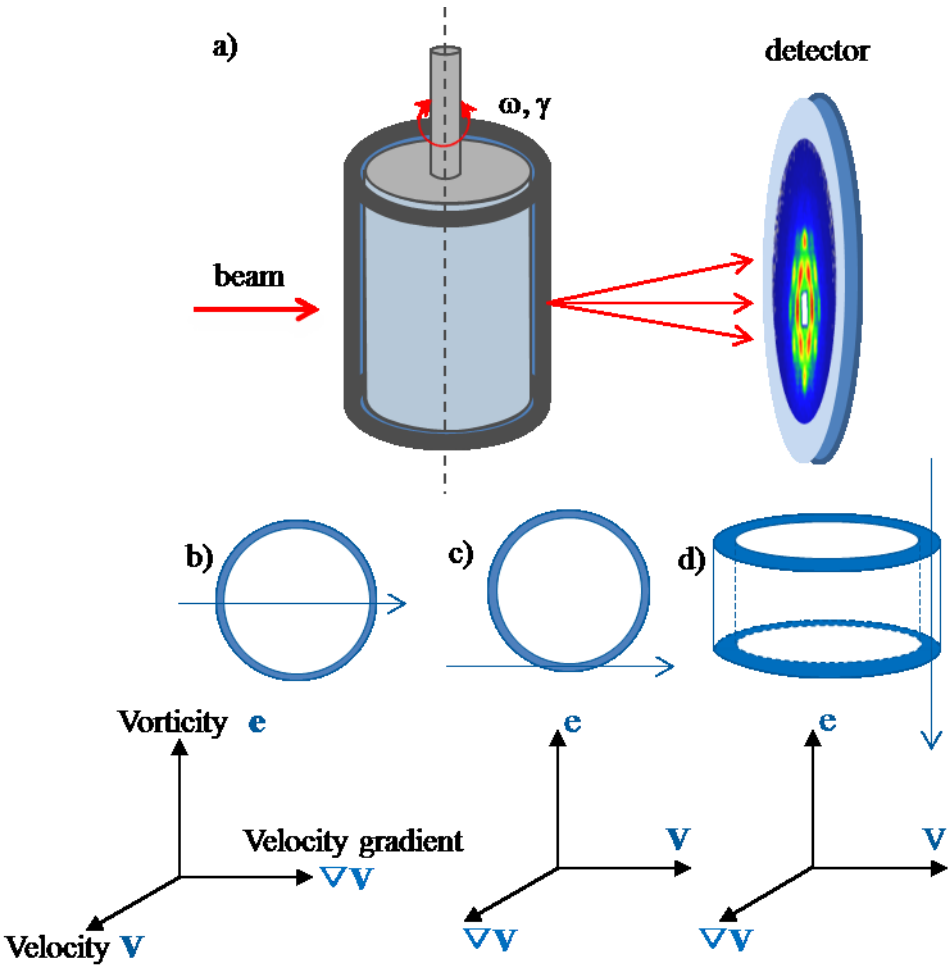

Figure 3.3.3 (a) Schematic illustration of the rheo-SANS setup with the commonly used Couette flow cell. ω and γ denote the angular frequency and the strain of the oscillatory shear applied by the rheometer, respectively. The coordinate frame with velocity(v), velocity gradient (∇v)and vorticity (e) directions is defined to describe the scattering planes for available geometries.[143] They are: (b) radial, (c) tangential and (d) e- ∇v plane flow cell geometries that allow for scattering in e-v, e-∇v, ∇v -v planes, respectively.

In the rheo-SANS experiments, the Couette cell is one commonly used geometry. As schematically shown in Figure 3.3.3a, the Couette cell is made up of a cup–bob geometry in which either the cup or the bob is fixed while the other rotates. The coordinate system is used to describe the scattering geometry and the shear flow for the particular case of rotational Couette flow with definitions of flow or velocity (v), velocity gradient (∇v) and vorticity (e) directions. There are three accessible configurations for the Couette cell with the incident beam normal to the velocity–vorticity (e-v) plane, the vorticity–velocity gradient (e-∇v) plane or the velocity gradient-velocity (∇v–v) plane, respectively.[148] In this work, the Couette cell is applied with a fixed cup and a bob that can rotate to impose shear. The velocity-vorticity plane is the measured scattering plane with the incident beam along the velocity gradient direction as shown in Figure 3.3.3b.

3.4 Crystallization of colloids under shear

Recently, colloidal crystals formed from organized colloids have attracted substantial interest.[97, 149-150] The scattering techniques can be used to explore the microstructures of the concentrated colloids in equilibrium.[151] As discussed in section 3.3, the application of rheology to scattering techniques can provide access to the investigation on the non-equilibrium microstructures of colloidal crystals under shear.[151-154] Two dimensional hexagonal close-packed (2D hcp) layers are found to form from sheared colloidal crystals and get arranged to minimize the resistance against the flow.[153, 155-156]

Ackerson *et al.*[152] performed a comprehensive study of shear induced orders of hard sphere suspensions by light scattering. It is observed that four basic structures are formed from the sheared hard spheres. The corresponding scattering patterns are shown in Figure 3.4.1. First, the shear-induced fcc twin structure is shown in Figure 3.4.1a and b, indicating by an underlying threefold symmetry in the ordering of particles. Second, Figure 3.4.1c and d display the scattering patterns for the sliding layers, the scattering spots of which are rotated by 30° with respect to that of the fcc structure. Third, Figure 3.4.1e demonstrates the string structures, which is correlated with shear thinning behaviour.[157-159] The scattering pattern in Figure 3.4.1f shows a diffuse Debye-Scherrer ring for an equilibrium sample without the preferred orientation but a preferred separation between particles.

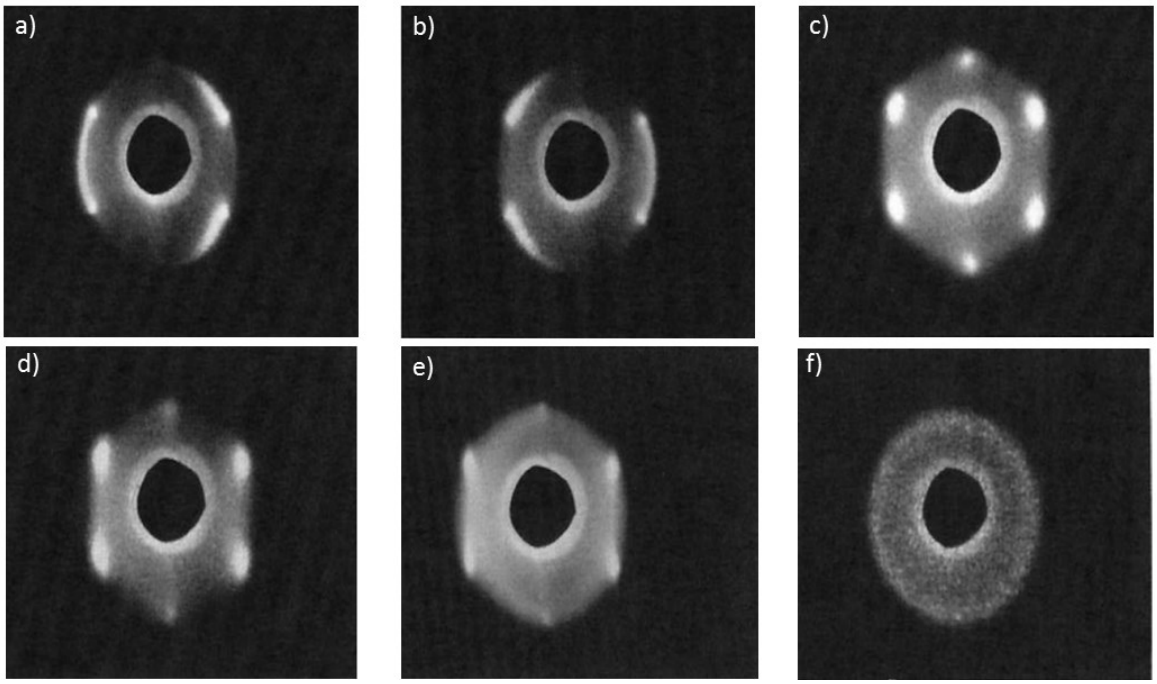

Figure 3.4.1 Observed scattered intensity distributions of hard spheres undergoing oscillatory shear flow. The incident laser beam is parallel to the velocity gradient direction. (a) Threefold pattern produced by a fcc structure, (b) and its fcc twin structure, (c) sixfold pattern produced by a registered random stacking of layers, (d) fourfold pattern produced by a centering of slipping layers over the other, (e) scattering pattern by the string-like ordering, (f)scattering pattern with a diffuse Debye-Scherrer ring by the amorphous or liquid-like ordering.[152]

The transition between these four different ordered structures depends on both volume fractions of samples and shear conditions. The geometric packing model [153, 160] in section 3.4.1 is used to elucidate the shear-induced structural evaluation of hard spheres. Section 3.4.2 presents the model calculation proposed by Ackerson *et al.* [155, 161] for the interpretation of scattering patterns of the sheared structures. In section 3.4.3, Brownian dynamics simulations are discussed, which have been performed on sheared hard spheres recently by the group of van Blaaderen.[156] The results of Brownian dynamics simulations are in a good agreement with the experiment results.

3.4.1 Geometric packing model

At low strain ($\gamma_{max} < 1$), hard spheres under shear order into two oscillating fcc twins shown in Figure 3.4.1a and b and the corresponding geometric packing is shown in Figure 3.4.2a and b, respectively.[152] It is indicated that the (111) lattice plane lies in the velocity-vorticity plane, and is mostly close packed along the vorticity direction. To form an fcc structure, the (111) planes must be stacked upon one another in a particular sequence. When one plane is placed

on another, there are two choices for registrations as shown by the triangle voids in Figure 3.4.2a and b. Having chosen one of the sites for the registration, to form an fcc structure, the particles in the next added layer must lie over the interstices of the two layers below (ABC or ACB ordering). At low strain, a particle in one layer oscillates between the two adjacent triangle voids in neighbouring layers.[152] This motion is assumed to minimize the stress caused by collisions with other particles during the shear.[156] The corresponding scattering pattern are shown in Figure 3.4.1a and b, which were obtained by light scattering.[152] With an increase in shear strains ($\gamma_{max} > 1$), the ordered structure is reorganized to allow a more extensive motion of a particle in the flow direction. The shear-induced hexagonal planes are aligned with a close packed direction parallel to the velocity axis shown in Figure 3.4.2c and d. The corresponding scattering patterns are shown in Figure 3.4.1c and d, respectively. The geometric packing shown in Figure 3.4.2c indicates that the particles in layers are registered in triangular voids for $0.58 < \phi < 0.64$, which are similar to the case of the twinned fcc structure. The layers in the applied shear flows can still slip over each other but along a zig-zag path. This microstructure is referred to as registered random stacked layers.[152] However, the oriented layers under high strain are found to slip freely over one another along straight lines up to $\phi = 0.58$ as shown in Figure 3.4.2d.[160] The microstructure for this case is referred to as freely slipping layers.[152]

Hence, the transition from twinned fcc structure to the sliding layers can be induced by the increasing shear strain. The geometric packing model indicates that the most densely packed axis of the twinned fcc structure at low strain is along the vorticity direction. However, the shear-induced hexagonal plane is most densely packed along the velocity direction at high strain. The transition can be evidenced by a 30° shift of their corresponding scattering patterns.

The further increase of shear strain induces a string-like structure, and the scattering pattern is shown in Figure 3.4.1e, which is similar to that for the sliding layers in Figure 3.4.1d. However, the intensity maxima with decreased intensity along the velocity direction reveals a smearing out along the vorticity direction. It indicates a one-dimensional structure as shown in Figure 3.4.2e. The string-like structure is aligned to the velocity direction, which is resulted from the broken up of the sliding layers as shown in Figure 3.4.2d.

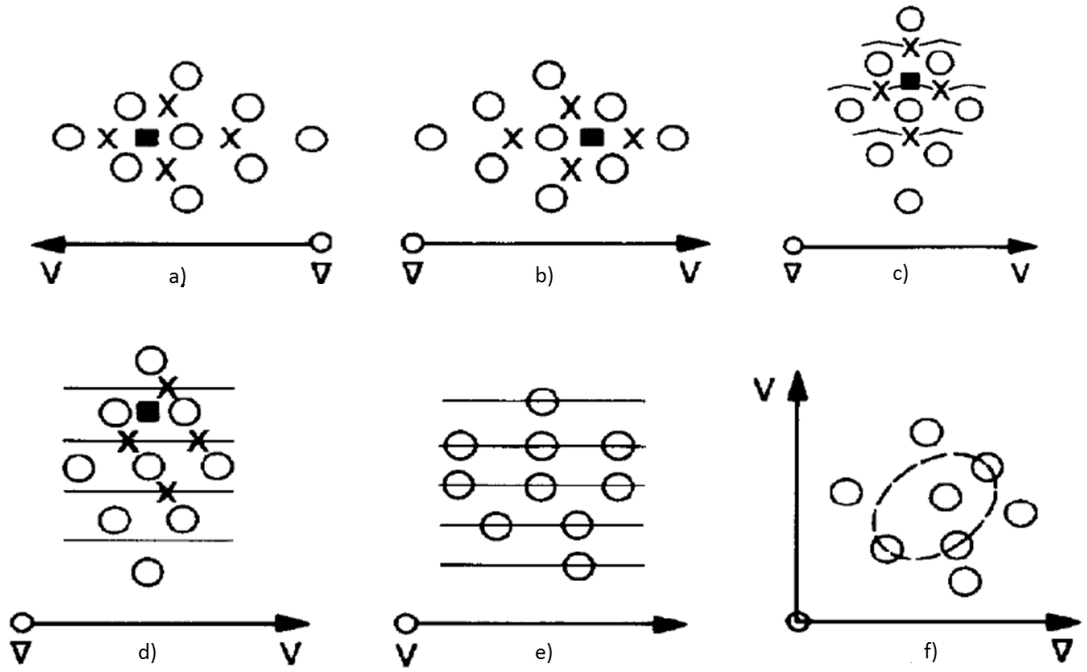

Figure 3.4.2 Geometric packing of hard spheres at low and high strains, corresponding to the shear-induced twinned fcc structure and the sliding layer phase. (a) and (b) refer to the twin structures having the characteristic …ABCA…stacking sequence. Registered randomly stacked layers having no characteristic…ACAB…stacking order. The layers may slip over one another along the zig-zag path as indicated in (c) or along the straight lines as marked in (d). (e) String-like ordering where the layers become disordered but regular spacing of particles along the velocity direction persists. (f) Amorphous or liquid-like equilibrium ordering indicating the distortion of the isotropic equilibrium order when a shear flow is not present.[152]

In Figure 3.4.1f, the scattering pattern from an equilibrium sample is shown with the liquid-like or amorphous glassy ordering. The diffuse Debye-Scherrer ring indicates that there is no preferred orientation in an equilibrium sample but a preferred separation between particles. The applied shear tends to distort the structure as shown in Figure 3.4.2f since the average distance among particles decreases along the dense packing axis.[162]

3.4.2 Model calculation

The scattering technique is a helpful tool to clarify the structural information of shear-induced structures. Ackerson *et al.*[161] carried out the model calculation for the interpretation of scattering patterns that correspond to different shear-induced structures as described in Figure 3.4.1. The coordinate system is firstly defined (see Figure 3.3.3b) to analyze hexagonal patterns observed in the velocity-vorticity plane. Two axis are fixed based on the flow direction (v) and the gradient direction (∇v), and the third axis is defined along the vorticity direction (e). The unit vectors along the flow direction and the vorticity directions are defined

as $\hat{\mathbf{v}}$ and $\hat{\boldsymbol{e}}$, respectively. A two dimensional basis for the hcp layers in the velocity-vorticity plane is given by[161]

$$\boldsymbol{a} = \mathrm{d}\hat{\mathbf{v}};\ \boldsymbol{b} = \frac{d}{2}\sqrt{3}\hat{\boldsymbol{e}}, \tag{3.4.1}$$

where d denotes the nearest-neighbour distance (the lattice constant). The reciprocal basis is determined by the conditions: $\boldsymbol{k_a}\cdot\boldsymbol{a} = \boldsymbol{k_b}\cdot\boldsymbol{b} = 2\pi$ and $\boldsymbol{k_a}\cdot\boldsymbol{b} = \boldsymbol{k_b}\cdot\boldsymbol{a} = 0$. If the k space unit vectors in flow, gradient, and vorticity direction are denoted by $\widehat{\boldsymbol{k_v}}$, $\widehat{\boldsymbol{k_\nabla}}$ and $\widehat{\boldsymbol{k_e}}$, respectively, the basic vectors follows[161]

$$\boldsymbol{k_a} = \frac{2\pi}{d}\left(\widehat{\boldsymbol{k_v}}, -\sqrt{\frac{1}{3}}\widehat{\boldsymbol{k_e}}\right), \boldsymbol{k_b} = \frac{2\pi}{d}\sqrt{\frac{4}{3}}\widehat{\boldsymbol{k_e}}, \tag{3.4.2}$$

The locations of the peaks (denoted by q_i) are expressed by the linear combination of these two basic vectors,

$$q_i = m\boldsymbol{k_a} + n\boldsymbol{k_b},\ m, n = \ldots, -2, -1, 0, 1, 2 \tag{3.4.3}$$

Thus, the peak positions should be located at q_i/q_0 ratio $1:\sqrt{3}:2:\sqrt{7}:3:\sqrt{12}$. Based on the model calculation brought up by Ackerson *et al.*,[161] the scattering corresponding to the hexagonal layers stacked as shown in Figure 3.4.2a-d has been calculated by Nils Heptner.[132] Figure 3.4.3 displays the calculation results for the twinned fcc structures (a), the sliding layers performing motions along zig-zag paths (b) or straight lines(c).

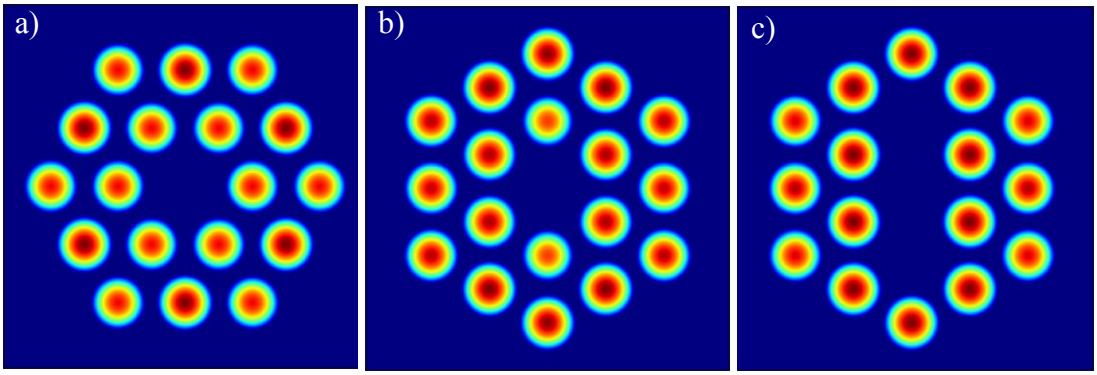

Figure 3.4.3 Juxtaposition of the main predictions of the stacking model calculations. The relative intensity of the spots of the three innermost rings in the $\boldsymbol{k_v}$-$\boldsymbol{k_e}$ plane is indicated analogously to contour plots of real scattering data: (a) corresponds to random registered scattering (highly twinned fcc crystal); The sliding layers performing motion along zig-zag paths (b) for $0.58 < \phi < 0.64$ or straight lines(c) at $\phi < 0.58$.[132]

As discussed in section 3.4.1, the hexagonal layers in the twinned fcc structure either are stacked in ABCABCA… sequence or its twin sequence. Based on these two stacking sequences, the scattering patterns are calculated as shown in Figure 3.4.3a for the highly twinned fcc structure. The six-fold scattering in Figure 3.4.3b corresponds to the registered random stacked layers as discussed above, where the hexagonal layers move along zig-zag paths due to the registration of neighbouring layers for $0.58 < \phi < 0.64$ (see Figure 3.4.2c). However, freely slipping layers for ϕ up to 0.58 are predicted to form, producing a four-fold scattering (Figure 3.4.3c). For this case, the layers slip over each other freely without collisions of particles as shown in Figure 3.4.2d. The centering of freely slipping layers results in the four-fold scattering with reduced magnitude of the intensity maxima in the vorticity direction (Figure 3.4.3c). Even though the form factor is not included in these simulation scatterings, a comparison of scattering intensities between the members of the same ring can still give insight into the preferred stacking sequence.

3.4.3 Dynamics of sheared hard dumbbells

The group of van Blaaderen[156] recently investigated the non-equilibrium phase behaviour of colloidal spheres in real-space with experiments by the combination of shear and confocal microscopy. Brownian dynamics (BD) computer simulations were performed to explore the underlying dynamics.[156] Four oscillatory shear induced phases have been experimentally observed in the velocity-vorticity plane, which are in a good agreement with the simulation results. Three of them correspond to the results of existing light scattering experiments.[152] The three phases are an oscillating twinned fcc phase, a sliding layer phase and a string phase.

In this work, we compare our experiment results with that of the BD simulations that have been performed by Nils Heptner[132] to explore the dynamics of sheared hard dumbbells. For non-spherical Brownian particles, orientations of the particles must be included since translational motion and rotational motion are coupled. The motions of hard dumbbells are described by the Smoluchowski equation,[163]

$$\frac{\partial}{\partial t} P(\boldsymbol{r_1}, \dots, \boldsymbol{r_N}, \widehat{\boldsymbol{u}}_1, \dots, \widehat{\boldsymbol{u}}_N, t) = \widehat{\boldsymbol{\mathcal{L}}}_S P(\boldsymbol{r_1}, \dots, \boldsymbol{r_N}, \widehat{\boldsymbol{u}}_1, \dots, \widehat{\boldsymbol{u}}_N, t), \tag{3.4.4}$$

where $(\boldsymbol{r_1}, \dots, \boldsymbol{r_N}, \widehat{\boldsymbol{u}}_1, \dots, \widehat{\boldsymbol{u}}_N)$ is a stochastic variable $\mathbf{X}$, $\widehat{\boldsymbol{\mathcal{L}}}_S$ is the Smoluchowski operator. The position and orientation of hard dumbbells are characterized by single unit vector $\boldsymbol{r}$ and $\widehat{\boldsymbol{u}}$ (the

direction of which is along the major axis, see Figure 3.1.2**),** respectively**.** The probability density function of **X** is denoted as *P*(**X**, t), which is a function of time in general.

More details related with the BD simulations on the sheared hard dumbbells are descried in the work of Heptner *et al*.[132] For the structural analysis, the orientation of hard dumbbells is described by the nematic order parameter as given by Allen *et al*.[164] The nematic order parameter is given through the largest eigenvalue λ_+ of the **Q** tensor[142]

$$\boldsymbol{Q} = \frac{1}{N}\sum_{i=1}^{N}\left(\frac{3}{2}\boldsymbol{u_i u_i} - \frac{1}{2}\mathbf{1}\right), \tag{3.4.5}$$

$\boldsymbol{u_i u_i}$ denotes the hyadic product of the orientation vectors of particle *i*. In this work, the sheared dumbbells are investigated in the vorticity-velocity plane as shown in Figure 3.3.3. The calculated orientations are only limited to the direction along $\boldsymbol{k_e}$ and $\boldsymbol{k_v}$.

To describe the crystalline structure of our sheared dumbbells, the method of bond-orientational order parameters is applied.[165] The idea of the bond order parameters is to capture the symmetry of bond orientations regardless of the bond lengths. A bond is defined as the vector joining a pair of neighbouring particles. Based on the spherical harmonics Y_{lm}, the local order parameters of each particle associated with a bond **r** are the set of numbers[156, 165]

$$q_{lm}(i) = \frac{1}{n_c(i)}\sum_{j=1}^{n_c(i)} Y_{lm}\left(\hat{\boldsymbol{r}}_{ij}\right), \tag{3.4.6}$$

with *l* as an integer parameter and *m* as an integer running from –*l* to *l*. The unit vector $\hat{\boldsymbol{r}}_{ij}$ connects particle *i* and one of its nearest neighbours *j*. $n_c(i)$ is the number of nearest neighbours of particle *i*.

To make the order parameters invariant with respect to the rotations of the reference frame, the second-order invariants are defined as

$$Q_l = \sqrt{\frac{4\pi}{2l+1}\sum_{m=-l}^{l}|q_{lm}(i)|^2}, \tag{3.4.7}$$

And the third-order invariants are defined as

$$W_l = \sum_{\substack{m_1,m_2,m_3 \\ m_1+m_2+m_3=0}} \begin{pmatrix} l & l & l \\ m_1 & m_2 & m_3 \end{pmatrix} q_{lm_1} q_{lm_2} q_{lm_3}, \tag{3.4.8}$$

where the coefficients (…) are the Wigner 3j symbols. It is standard to define a normalized quantity

$$\widehat{W}_l = \frac{W_l}{(\sum_m |q_{lm}|^2)^{3/2}}, \tag{3.4.9}$$

The four bond order parameters $Q_4, Q_6, \widehat{W}_4$ and $\widehat{W}_6$ are generally applied to identify different crystal structures. For fcc structure, Q_4 is 0.19 and $\widehat{W}_4$ is -0.16, respectively.[166] In this work, we use the bond order parameters Q_4 and $\widehat{W}_4$ to described the crystal structure of the sheared hard dumbbells.

4. Hard Dumbbells

4.1 Synthesis and characterization of dumbbell-shaped microgels

4.1.1 Synthesis

The dumbbell-shaped microgels used in this work have been prepared in four steps. Figure 4.1.1 displays the synthesis routine in a schematic fashion.[55] In the first step, polystyrene (PS) seeds are synthesized through the conventional emulsion polymerization at 70°C in which potassium peroxodisulfate (KPS) is used as the anionic and water soluble initiator and sodium dodecyl sulfate (SDS) is used as the emulsifier. Second, a layer of copolymer of styrene and 3-(trimethoxysilyl) propyl methacrylate (MPS) is coated onto the surface of spherical PS seeds.[167] During this copolymerization, MPS monomer is either copolymerized with styrene or the organoalkoxysilane is hydrolyzed into silanetriol molecules and condensed into inorganic polysilsesquiloxane networks.[167] Thus, a hybrid copolymer network is attached onto the surface of PS spheres which is designed to facilitate the growth of the second PS sphere in the next step. Third, the homogeneous dumbbell-shaped core particles are prepared using the method of Park *et al.*,[55] which leads to high yields of monodisperse dumbbell-shaped nanoparticles. The dumbbell-shaped PS cores are purified via dialysis for 3 days against Millipore water. In the final step, a shell of poly (N-isopropylacrylamide) (PNIPA) cross-linked by N, N'-methylenebis (acrylamide) (BIS) is coated onto the dumbbell-shaped PS core particles via a seeded emulsion polymerization.[29] The core-shell microgels are purified by ultrafiltration to remove all the possible traces of free polymers and redispersed in 50 mM KCl for further experiments.

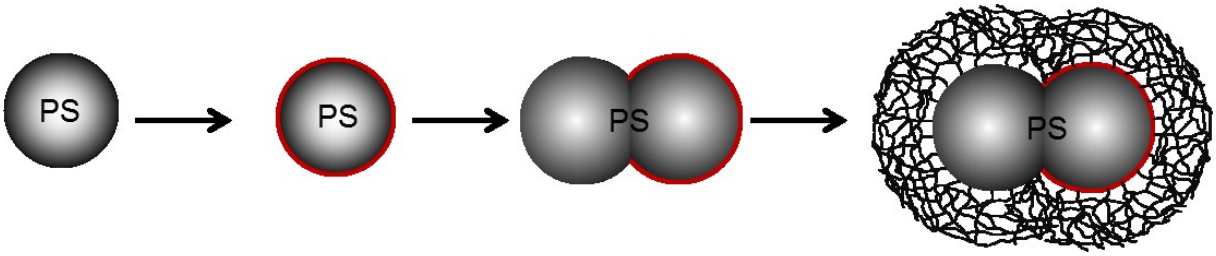

Figure 4.1.1 Illustration of the preparation routine for the thermosensitive dumbbell-shaped microgels that can serve as the hard dumbbell model system in this study.

Since the PNIPA shell fabricated in the last step provides an excellent steric stabilization, no electrostatic stabilization is necessary and all the possible residue charges can be screened by the addition of KCl salt.[19] The dumbbell-shaped microgels dispersed in 50 mM KCl solution are entirely sterically stabilized and can be used as the model system of hard dumbbells.

In this work, the dumbbell-shaped microgels with two different aspect ratios (L^*, the ratio of center to center distance to the diameter of one composed sphere) have been used as model systems. They are the dumbbell-shaped microgels with $L^* \sim 0.24$ (DPM_a) and $L^* \sim 0.30$ (DPM_b), respectively. An overview is given in Table 4.1.1.

Table 4.1.1 Dimensional information of the dumbbell-shaped particles used in this study: the DPM_a microgels with $L^* \sim 0.24$ and the DPM_b microgels with $L^* \sim 0.30$, and their corresponding dumbbell-shaped cores (DPC). The dimensional information displayed here is achieved via DLS and DDLS measurements.

Sample	L [nm]	R_C [nm]	L_H(T) (T: 10 to 20° C)	Lc^*	L^* (T: 10 to 20° C)
DPM_a	105.12	98.80	-1.57*T + 137.39	0.53	0.24 ± 0.01
DPM_b	93.30	74.90	-1.22 * T + 91.36	0.62	0.30 ± 0.02

Note: As defined in Figure 1.3.1, L refers to the centre to centre distance between the two composed spheres, R_C is the radius of one sphere in the dumbbell-shaped core, L_H is the thickness of PNIPA shell and L_C^* indicates the aspect ratio of the corresponding DPC particles.

4.1.2 Characterization

TEM and cryo-TEM measurements are performed to investigate the morphology and size distribution of the dumbbell-shaped cores. The TEM images in Figure 4.1.2 show that both DPC_a and DPC_b particles are homogeneous in both morphology and size. These particles are the core particles for the DPM_a microgels and the DPM_b microgels, respectively. The dumbbell-shaped PS cores consist of two fused spheres, which are nearly identical in size. Based on more than 500 dumbbell-shaped core particles in TEM images, the major axis length, l, of the DPC_a core is determined to be 261.0 ±7.9 nm and the radius of one sphere, R_C is 90.5 ± 6.0 nm. As for the DPC_b cores, l is 229.3 ± 8.9 nm and R_C is 74.5 ± 4.9 nm.

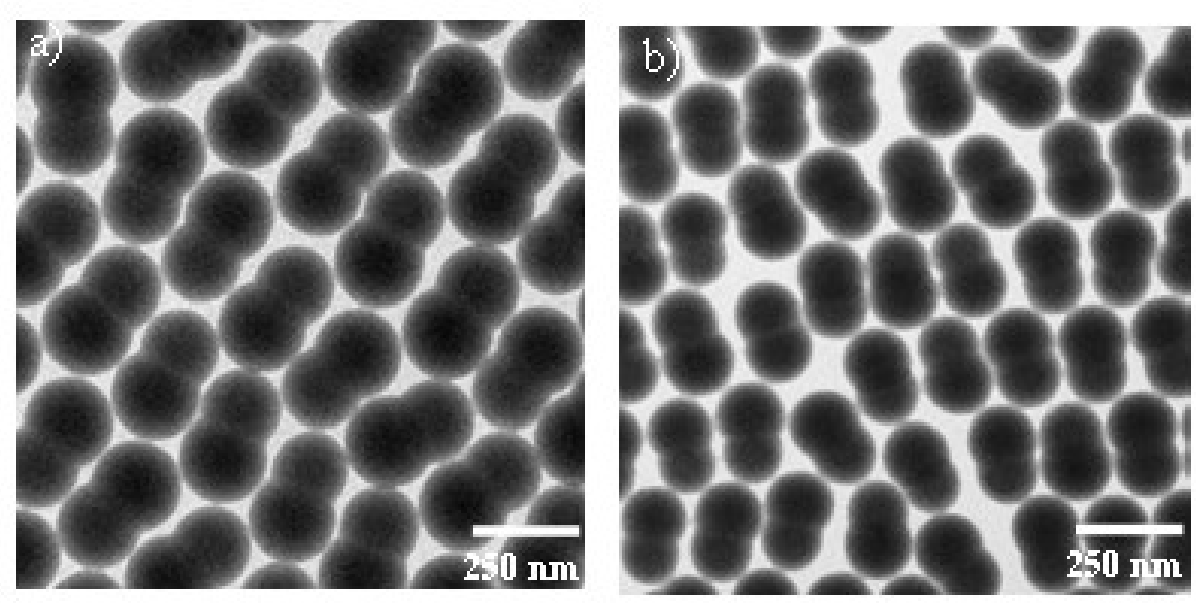

Figure 4.1.2 TEM micrograph of the dumbbell-shaped PS cores (a) DPC_a (b) DPC_b. They are used as seeds for the preparation of the DPM_a microgels and the DPM_b microgels, respectively.

The cryo-TEM image in Figure 4.1.3a demonstrates that the two fused spheres in one dumbbell-shaped core particle have different structures: one side is homogeneously spherical while the other side is a core-shell sphere. Figure 4.1.3b shows the gray scale profile normalized to the background arising from the vitrified water.[108] First, the minimum corresponding to the sphere with a core-shell structure (right hand side Figure 4.1.3b) is less pronounced than the other side. This difference in the grey scale profile points clearly to a difference in compositions. Second, the gray scale profile shows a shoulder at the edge of the right hand sphere of the dumbbell-shaped core (marked by the black arrow) indicating a core-shell structure. The synthesis shown schematically in Figure 4.1.1 leads to a shell of a copolymer from styrene and MPS. The cryo-TEM image in Figure 4.1.3a proves that the copolymer layer is well-maintained as the shell for its spherical PS seed after the growth of the second sphere. Therefore Figure 4.1.3 provides the first direct proof for the Janus-type nature of the dumbbell-shaped core particles through cryo-TEM measurements.

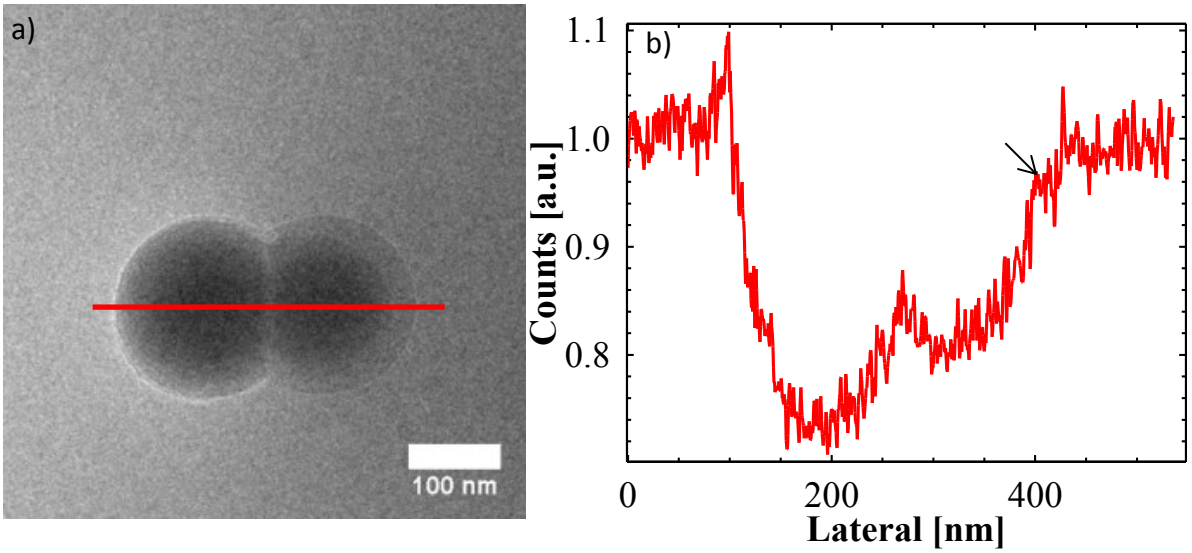

Figure 4.1.3 Cryo-TEM micrograph of a dumbbell-shaped PS core particle, a red line is drawn to indicate the major axis direction (a), and the corresponding normalized gray scale profile along the major axis (b), a black arrow is used to guide eyes to one shoulder on the right side of the gray profile. A homogeneous shell is observed on the core-shell structured part on the right side, which corresponds to the random copolymer of styrene and MPS.

Cryo-TEM measurements are carried out by vitrifying the samples in water to investigate the structure of the dumbbell-shaped microgels *in situ*. The micrographs of the DPM_a microgels (Figure 4.1.4a) and the DPM_b microgels (Figure 4.1.4b) reveal that the cross-linked PNIPA shell is homogeneously attached to the surface of their corresponding dumbbell-shaped core particles. The thickness of PNIPA shell, L_H of the DPM_a microgels is determined to 93.1±8.4 nm at room temperature (T: ca. 25 °C), while L_H of the DPM_b microgels is 81.4 ± 9.5 nm. It is worth noting that in the TEM images of the dumbbell-shaped core particles (see Figure 4.1.2) all particles get aligned with the major axis parallel to the surface. However, the cryo-TEM images exhibit the dumbbell-shaped microgels dispersed in water, where they may show all orientations. As marked by dash line circles in Figure 4.1.4, the particles can align with the major axis nearly perpendicular to or with a certain angle, θ with regard to the direction of the electron beam. Moreover, the particles probably also tend to align parallel to the thin water layer when the suspensions are distributed on the substrate during the sample preparation. The probability of the major axis lying with an angle θ is proportional to $\sin\theta$. Therefore the particles that appear nearly as spheres ($\theta \cong 0$) are observed less frequently than particles lying with the major axis perpendicular to the optical axis.

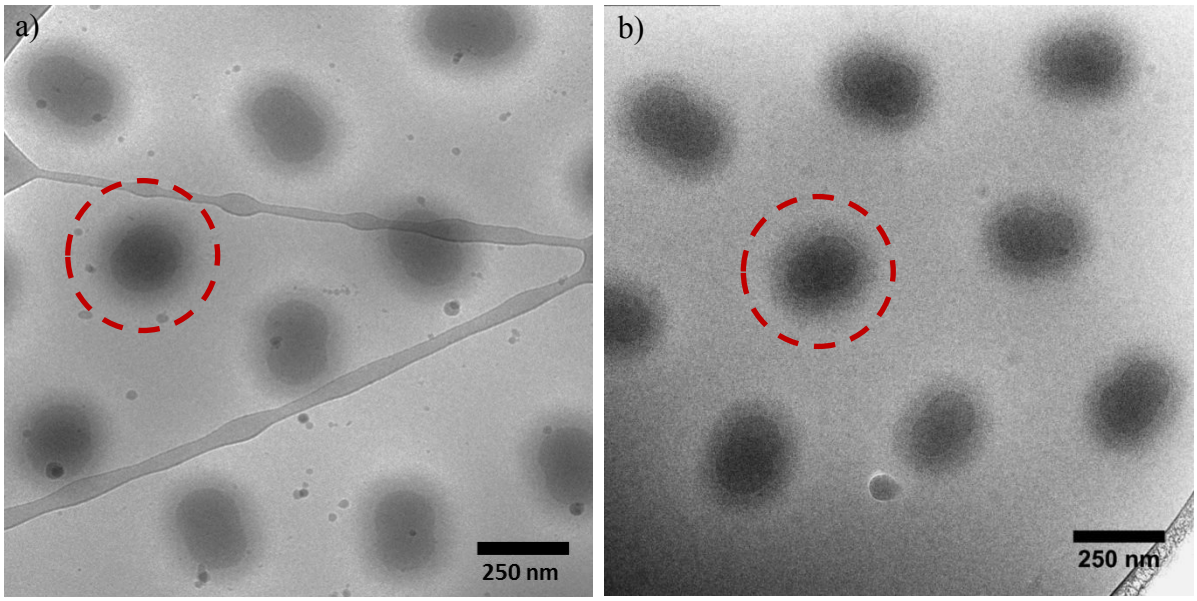

Figure 4.1.4 Cryo-TEM images of the dumbbell-shaped microgels: (a) the DPM_a microgels and (b) the DPM_b microgels. The circles of dash line mark the particles with different orientations. The measurements are done at room temperature with T ~ 25 °C.

In the following, DLS and DDLS measurements are performed to characterize dimensional information of the well-defined dumbbell-shaped particles. We use the CONTIN-2DP software to calculate the relaxation frequencies of different modes from the intensity correlation functions. Figure 4.1.5a and c display the relaxation time distribution for the DPC_a core and the DPM_a microgels, respectively. The autocorrelation function for both suspensions consists of two discrete exponential decays. The peak at smaller relaxation time (fast mode) contains information about the rotational relaxation. The peak at larger relaxation time (slow mode) is attributed to translation motions. In principle, the slow translational mode should be invisible in DDLS experiments.[88, 114] As discussed in Chapter 3, geometry II with a polarizer of the vertical direction and an analyzer of the vertical direction (see Figure 3.2.1) is used for DDLS measurements. According to Eq. (3.2.3) the correlation function, I_{VH} measured by geometry II only contains information related with the rotational relaxation and q-dependent part of the translational diffusion (fast mode).[114] However, the limitation of the Glan-Thomson polarizer (10^{-5}) and the strong scattering of the particles make the slow translational mode visible in DDLS experiments.[168] ,[169]

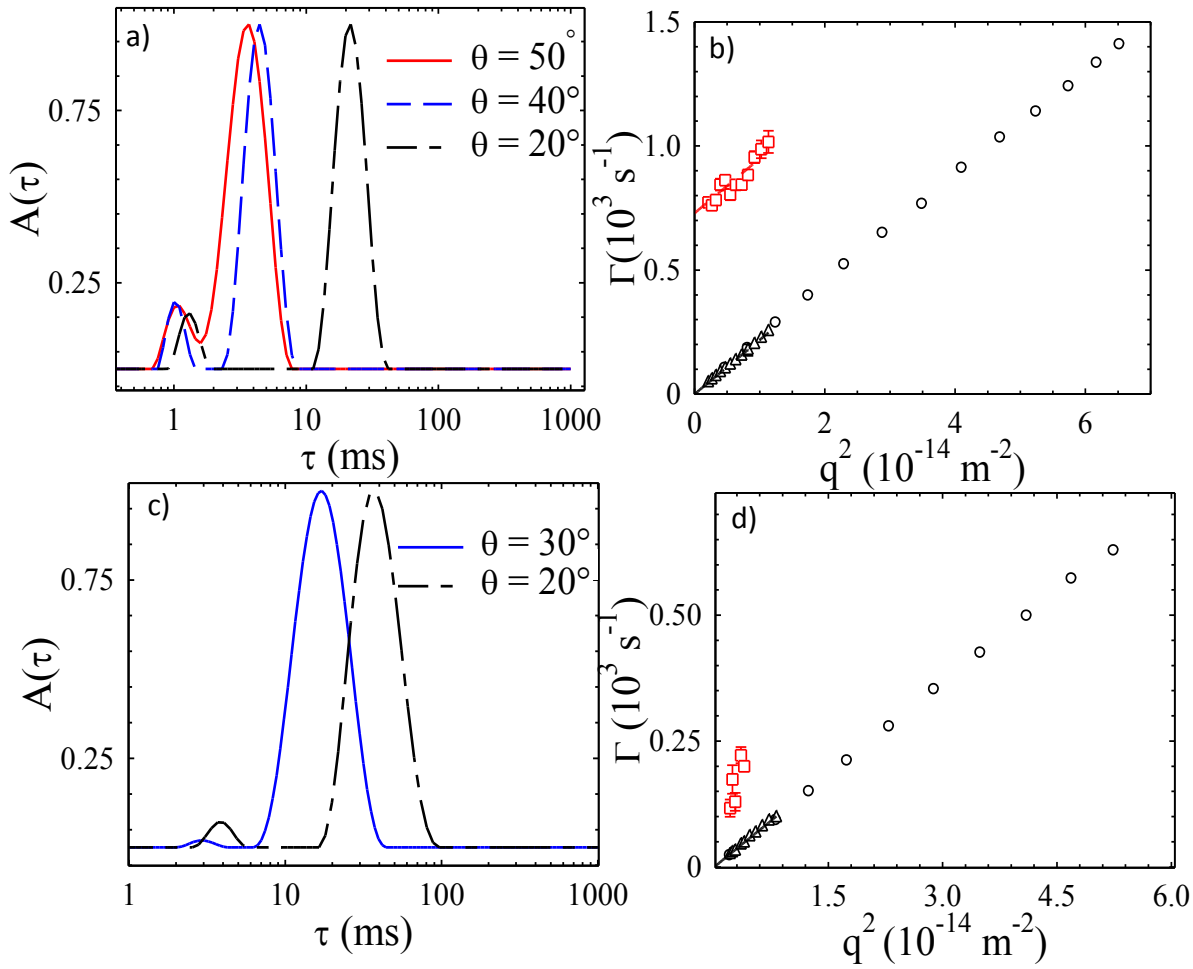

Figure 4.1.5 DDLS-relaxation time distributions (CONTIN-plots) of the DPC_a core (a) dispersed in water at 20 °C and the DPM_a microgel (c) dispersed in 50mM KCl solution at 25 °C calculated from the intensity autocorrelation functions. The corresponding relaxation processes are plotted as a function of the square of the scattering vector ($q2$) for the DPC_a core (b) and the DPM_a microgels (d). The symbols indicate that: DLS slow mode (open circle), DDLS slow mode (open triangle) and DDLS fast mode (open square) and the solid lines in (b) and (d) are the fitted data according to corresponding modes.

The calculated relaxation rates Γ of the DPC_a core and the DPM_a microgel suspensions are shown in Figure 4.1.5b and d, respectively, as a function of q^2, where the slow relaxation mode characterizes the translational motion and the fast relaxation mode is related to the rotational motion. As discussed above, the slow DDLS mode (open triangles) can be explained by the leakage of the polarizer. As shown in Figure 4.1.5b and d, it is evident that this mode is comparable to the slow DLS mode (open circles) within experimental error. Based on the principle of dynamic light scattering described in Chapter 3.2, the translation diffusion D^T and rotational diffusion D^R can be calculated as $D^{\mathrm{T}} = \Gamma_{\mathrm{slow}} / q^2$ and $D^{\mathrm{R}} = (\Gamma_{\mathrm{fast}}$ -

Γ_{slow}) / 6. Γ_{slow} and Γ_{fast} are identified as slow and fast relaxation rates that are displayed in Figure 4.1.5b and d.

Combined with the shell model[132] (see section 3.2.3), the dimensional information including L and R_C of the measured DPC cores can be calculated from the resulting D^T and D^R. However, in case of the DPM microgels, there are only a few data points (open squares) for the fast mode as shown in Figure 4.1.5d, which are not sufficient to calculate D^R with high accuracy. Fortunately, reliable D^T of the DPM microgels can be measured from DLS and DDLS as listed in Table 4.1.2, and they are comparable to each other with experimental error. Based on the shell mode, R_H (the hydrodynamic radius as defined in Figure 1.3.1) of the DPM microgels can be calculated from D^T achieved from DLS and DDLS measurements and L from the corresponding DPC particles.

Table 4.1.2 Characterization of experimental diffusion coefficients D^T, measured from both DLS and DDLS experiments. D^R for the DPC_a and DPC_b cores is measured from DDLS measurements at 20 °C. D^R of the DPM_a and DPM_b microgles is calculated by the shell model based on D^T and L. The calculated dimensional information R_H and L for DPC cores at 20 °C and DPM microgels at 10 °C, 15 °C and 20 °C are included as well.

Sample		D^T_{DLS} [$10^{-12}m^2s^{-1}$]	D^T_{DDLS} [$10^{-12}m^2s^{-1}$]	D^R[s^{-1}]	R_C/R_H[nm]	L[nm]
DPC_a		1.74 ± 0.02	1.67 ± 0.04	77.72 ± 3.09	98.8	105.5
DPC_b		2.31± 0.01	2.25± 0.02	186.03± 7.07	74.9	93.3
DPM_a	10 °C	0.62± 0.03	-	6.05	208.8	105.5
	15 °C	0.75± 0.04	-	7.05	204.5	105.5
	20 °C	0.91± 0.01	-	9.65	197.2	105.5
DPM_b	10 °C	0.84± 0.05	-	14.43	168.53	93.3
	15 °C	0.98± 0.06	-	17.69	158.83	93.3
	20 °C	1.21± 0.03	-	24.12	155.07	93.3

DLS and DDLS measurements are carried out at 20 °C only for dumbbell-shaped core particles. The dumbbell-shaped microgels dispersed in water and 50 mM KCl solutions are measured at temperatures varying from 10 °C to 40 °C in order to investigate their

thermosensitive properties. This in turn leads to the thickness L_H ($L_H = R_H - R_C$) of the thermosensitive microgels at various temperatures depicted in Figure 4.1.6. The thicknesses L_H of microgels in salt-free and 50 mM KCl solutions are comparable within experimental error and exhibit the same linear dependence on T below the lower critical solution temperature (LCST, 32 °C for PNIPA[102]). This finding is in accord with the one found for spherical microgel systems. When temperature is increased above LCST, the dumbbell-shaped microgels dispersed in the salt-free solution remain stable while the microgels dispersed in 50 mM KCl solution aggregate immediately. The PNIPA shells become attractive at temperatures above LCST and the lack of electrostatic interactions due to the screening effect of 50 mM KCl causes the rapid coagulation as has been shown for spherical microgels.[28, 32] Thus, 50 mM KCl is enough to screen the electrostatic interactions from possible residual surface charges and the dumbbell-shaped microgels dispersed in 50 mM KCl solution are sterically stabilized.

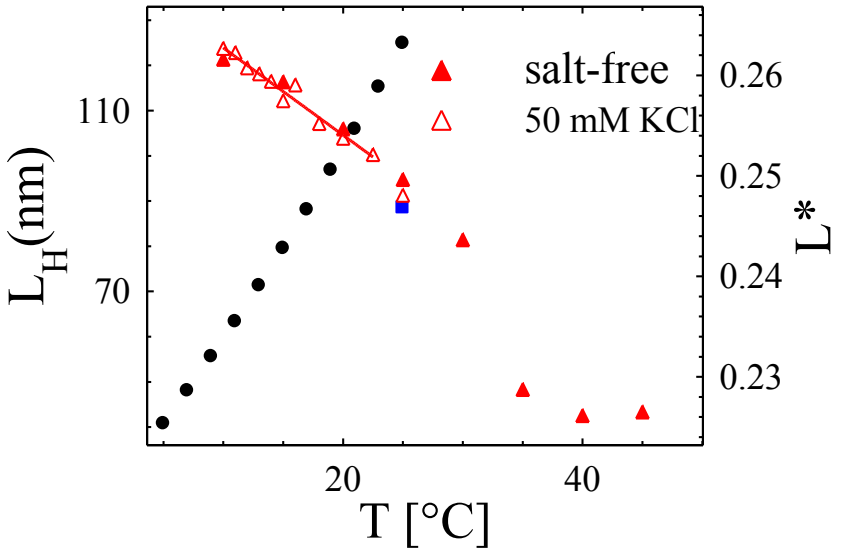

Figure 4.1.6 Temperature dependence of L_H for the dumbbell-shaped microgels dispersed in salt-free solutions (filled triangle) and 50 mM KCl solution (empty triangle) by DLS. The filled square marks L_H measured by cryo-TEM at room temperature (T ~ 25 °C). In the temperature regime from 10 to 22.5 °C, L_H was found to decrease linearly with temperature (L_H = -1.57*T (°C) + 137.39; r^2 = 0.99). The corresponding L^* are denoted by filled circles.

Moreover, Figure 4.1.6 displays a comparison of L_H obtained by cryo-TEM measurements (marked by the blue filled square) and that from DLS and DDLS measurements at room temperature (T ~ 25 °C). It is demonstrated that L_H from cryo-TEM measurements is 93.1 ± 8.4 nm at T ~ 25 °C, which is comparable to 95.3 ± 3.5 nm measured from DLS and DDLS.

DLS and DDLS measurements and the foregoing analysis of dumbbell-shaped particles therefore can provide reliable characterization of L, R_C and R_H at different temperatures. Based on these parameters, the effective volume fraction are calculated according to

$$\phi_{eff} = \frac{N}{V}\alpha\frac{4}{3}\pi R_H^3, \tag{4.1.1}$$

where $\alpha = 1+\frac{3}{2}L^*-\frac{1}{2}L^{*3}$ and $\frac{N}{V}$ is the number density.[49] The latter quality which is same as number density of the corresponding DPC particles, is determined through the element analysis and thermo-gravimetric analysis.

The aspect ratio L^* of the DPM_a microgels is tunable within range from 0.22 to 0.27 by adjusting temperatures from 10 °C to 40 °C. In this thesis, all experiments are done below LCST (temperature ranging from 10 °C to 20 °C). The corresponding L^* of the DPM_a microgels in this range is in good approximation set constant at 0.24 ± 0.01. The thermosensitivity of the DPM_b microgels is measured as well and the measurement data is analyzed following the procedure as described above. The obtained dimensional information for the DPM_b microgels is summarized in Table 4.1.1 and Table 4.1.2, and L^* of the DPM_b microgels is calculated to be 0.30 ± 0.02 within the temperature range from 10 °C to 20 °C.

In conclusion, nearly monodisperse dumbbell-shaped core-shell microgels have been successfully prepared and characterized in this work. The dumbbell-shaped microgels are composed of dumbbell-shaped PS core and cross-linked PNIPA shell. The characterization including TEM and cryo-TEM demonstrates that the resulting dumbbell-shaped cores and microgels are well-defined by morphology and size distribution. Additionally, the dumbbell-shaped core particles are proved to be of Janus-type with two partially fused spheres, which are identical in size but different in structures. One sphere has a core-shell structure, while the other one is homogeneously spherical. DLS and DDLS measurements demonstrate that the size (L_H) and thus the effective volume fraction of the particles can be adjusted by temperature. 50 mM KCl solution is proved to be sufficient to screen all possible residual ions from the synthesis, and the resulting dumbbell-shaped microgels are steric stabilized. Moreover, the anisotropy of dumbbell-shaped mcirogels can be controlled via adjusting the PNIPA shell. The DPM_a microgels with $L^* \sim 0.24$ and the DPM_b microgels with $L^* \sim 0.30$ are prepared to serves as the model system of hard dumbbells. Based on the model system, the phase behaviour of hard dumbbells has been investigated in the ensuing sections.

4.2 Phase diagram and crystallization of hard dumbbells

4.2.1 Phase diagram

The discussion in Chapter 1 indicates that mildly anisotropic systems have a rich phase behaviour as a function of L^* and ϕ.[170] Monte Carlo (MC) studies predict that hard dumbbells with a small aspect ratio ($L^* < 0.40$) undergo the fluid to plastic crystal transition with a concomitant biphasic gap (see Figure 1.2.2).[52] Therefore the homogeneous dumbbell-shaped DPM_a microgels with $L^* \sim 0.24$ and the DPM_b microgels with $L^* \sim 0.30$ are expected to form a plastic crystal in certain volume fraction range. In order to prove this point, the crystallization of hard dumbbell suspensions over a volume fraction region is studied to obtain the phase diagram.

One series of the DPM_a suspensions with weight concentrations ranging from 8.87 wt.-% to 14.46 wt.-% is prepared and quickly cooled down to 7 °C after an extensive tumbling at 30 °C. The extensive tumbling at 30 °C is assumed to destroy all possible crystal formed at the room temperature and randomize positions of all particles. The corresponding volume fraction region of the DPM_a suspensions ranges from 0.41 to 0.67. Following the same procedure, a series of the DPM_b suspensions ($L^* \sim 0.30$) of concentrations from 8.58wt.-% to 12.19 wt.-% is quickly cooled down to 12 °C to achieve a volume fraction region ranging from 0.45 to 0.64. Suspensions of dumbbell-shaped microgels are kept at a fixed temperature without any disturbance for more than one month so that crystallizations can occur. The main experimental results are summarized in Figure 4.2.1.

The photographs of the crystallized hard dumbbell suspensions in Figure 4.2.1a and c reveal that both DPM_a and DPM_b suspensions crystallize after one month as indicated by their Bragg reflections. The fraction of the crystallites is found to be dependent on the corresponding overall volume fraction of the dumbbell suspensions. As shown in Figure 4.2.1a, the percentage of crystals is 18% for the DPM_a suspension with $\phi_{eff} = 0.50$ and 77% for $\phi_{eff} = 0.54$. The fully crystallized region is reached at $\phi_{eff} \cong 0.59$. Hence, the biphasic gap, where the fluid phase coexists with the plastic crystal, is in the approximate range of volume fractions from 0.50 to ca. 0.56. As for the DPM_b microgels, suspensions with $\phi_{eff} = 0.50$ can hardly form crystals, the crystal percentage is 70% for the DPM_b suspension with $\phi_{eff} = 0.55$ and 96% for $\phi_{eff} = 0.57$.

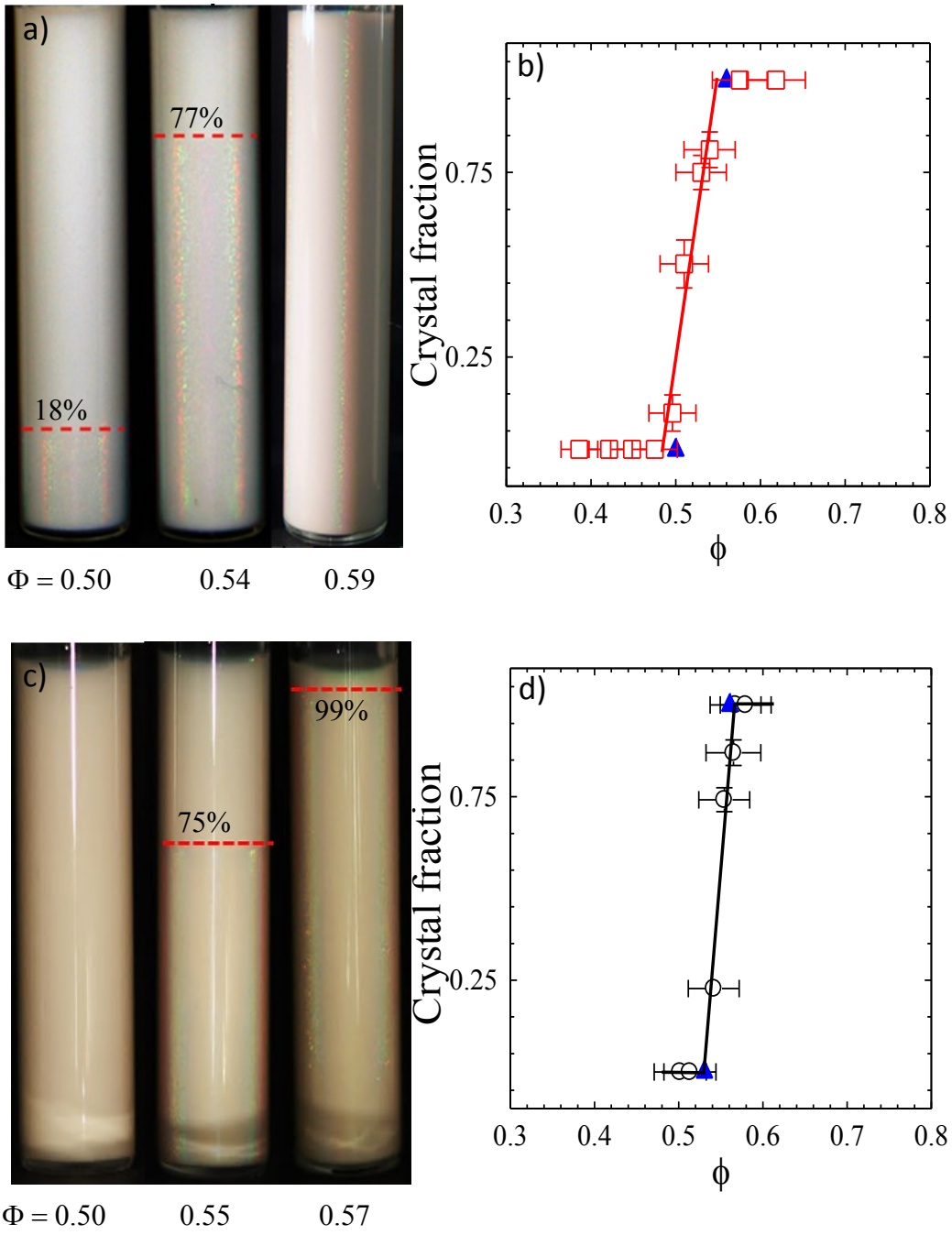

Figure 4.2.1 a) Crystallization of the DPM_a suspensions with various effective volume fractions (ϕ_{eff} = 0.50, 0.54, 0.59 from left to right) at 7 ± 1 °C and formed crystals are indicated by Bragg reflections (b) the corresponding phase diagram based on the visual observation. (c) Direct observation on crystallization of the DPM_b suspensions with ϕ_{eff} = 0.50, 0.55, 0.57 from left to right, and (d) its corresponding phase diagram. Dashed lines in (a) and (c) are used to mark the phase boundaries. The phase diagram achieved based on the linear extrapolation is denoted by solid line for the DPM_a suspension with $L^* \sim 0.24$ (b) and the DPM_b suspension with $L^* \sim 0.30$ (d).The filled triangles in (b) and (d) indicate the freezing and melting volume fractions predicted by the MC simulations[52] for hard dumbbells with $L^* = 0.24$ and 0.30, respectively.

Moreover, the crystal fractions formed from hard dumbbells (both the DPM_a suspensions and the DPM_b suspensions) in the biphasic gap (where the plastic crystalline phase is in equilibrium with the fluid phase) display a linear dependence on the corresponding volume fractions. A linear regression is used to estimate the volume fraction for the onset of crystallization (freezing point) in the DPM suspensions and the point that the one-phase region is reached (melting point). Figure 4.2.1b and d present the phase diagram based on the linear regression for the DPM_a and DPM_b suspensions, respectively. It is demonstrated that the freezing volume fraction for the DPM_a suspension with $L^* \sim 0.24$ is 0.48 ± 0.03 and the melting volume fraction is 0.56 ± 0.02 and that for the DPM_b suspension is 0.52 ± 0.02 and 0.57 ± 0.03, respectively. The experimental phase diagrams, especially the boundary of the biphasic gap, for hard dumbbells with $L^* = 0.24 \pm 0.01$ and $L^* = 0.30 \pm 0.02$ are comparable to the phase boundary predicted by the MC simulations as shown in Figure 4.2.1b and d.[52-53]

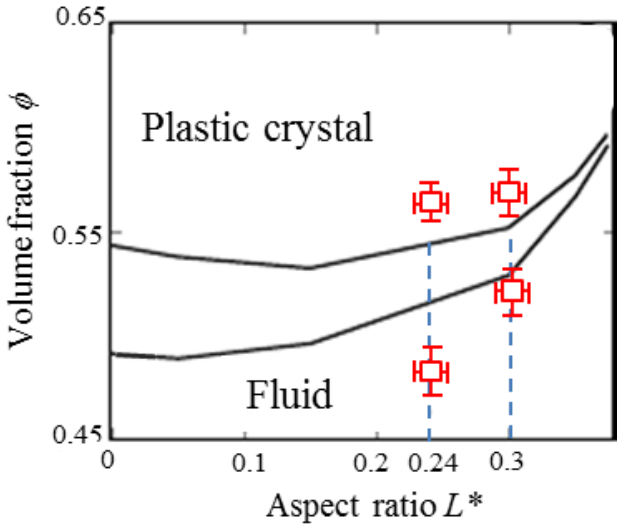

Figure 4.2.2 The experimental phase diagram (denoted by the red squares) is compared with the prediction of MC simulations (solid black line[52]) for $L^* = 0.24$ and $L^* = 0.30$. The blue line is used to mark the corresponding L^*.

Figure 4.2.2 present the experimental phase diagram, which is compared with that of the MC simulations for $L^* < 0.4$.[52-53] It indicates that the experimental phase diagram shows a larger biphasic gap for the hard dumbbells for $L^* = 0.24$, while they nearly coincide for $L^* = 0.30$. Moreover, the comparison shows that the width of the biphasic gap of hard dumbbells (the difference between the melting volume fraction and the freezing volume fraction) is decreased with an increase in L^* from 0.24 to 0.30.

Thus, the dumbbell-shaped microgels synthesized in this work are so monodisperse that they can form plastic crystal indicated by Bragg reflections. Both the DPM_a suspension with $L^* \sim$ 0.24 and the DPM_b suspension with $L^* \sim 0.30$ exhibits the fluid-to-plastic crystal transition. The experimental phase diagrams are obtained by visual observations, which virtually coincide with the prediction of the MC simulations on the phase diagram of hard dumbbells at $L^* \sim 0.24$ and $L^* \sim 0.30$. Moreover, both experiment and theory studies indicate that the increased L^* ($L^* < 0.4$) leads to a decrease in the width of the biphasic gap of hard dumbbells.

4.2.2 Crystallization process

To further investigate the crystallization and phase behaviour of hard dumbbells, rheological measurements, including time dependent measurements in the oscillatory shear field and flow curve measurements have been performed for the suspensions of DPM_a microgels and DPM_b microgels in different phases, respectively. The rheological measurements have been shown to be useful to investigate the dynamics of crystallization for spherical systems.[14, 171],[172] In this study, the volume fractions of the measured hard dumbbell suspensions in different phases are chosen according to the phase diagrams shown in Figure 4.2.1. The time dependent measurements are carried out as a function of time in the oscillatory shear field with fixed frequency f = 1 Hz and fixed strain amplitude γ_{max} = 1%. The flow curve that is the shear stress σas a function of shear rate $\dot{\gamma}$ is measured by increasing and decreasing $\dot{\gamma}$. More experimental details are described in Chapter 7.

4.2.2.1 Dumbbell-shaped microgels with L*~ 0.24

Figure 4.2.3 displays the measurement results for the DPM_a suspensions in different phases. The suspension is firstly investigated at ϕ_{eff} = 0.40 (8.56 wt.-% at 10 °C), which is below the fluid-to-plastic crystal transition. In the second set of experiment, the suspension with ϕ_{eff} = 0.51(12.05 wt.-% at 15 °C) is chosen, which is located in the biphasic gap. Next, the suspension in one phase region is measured with a volume fraction of 0.63 (12.05 wt.-% at 5 °C).

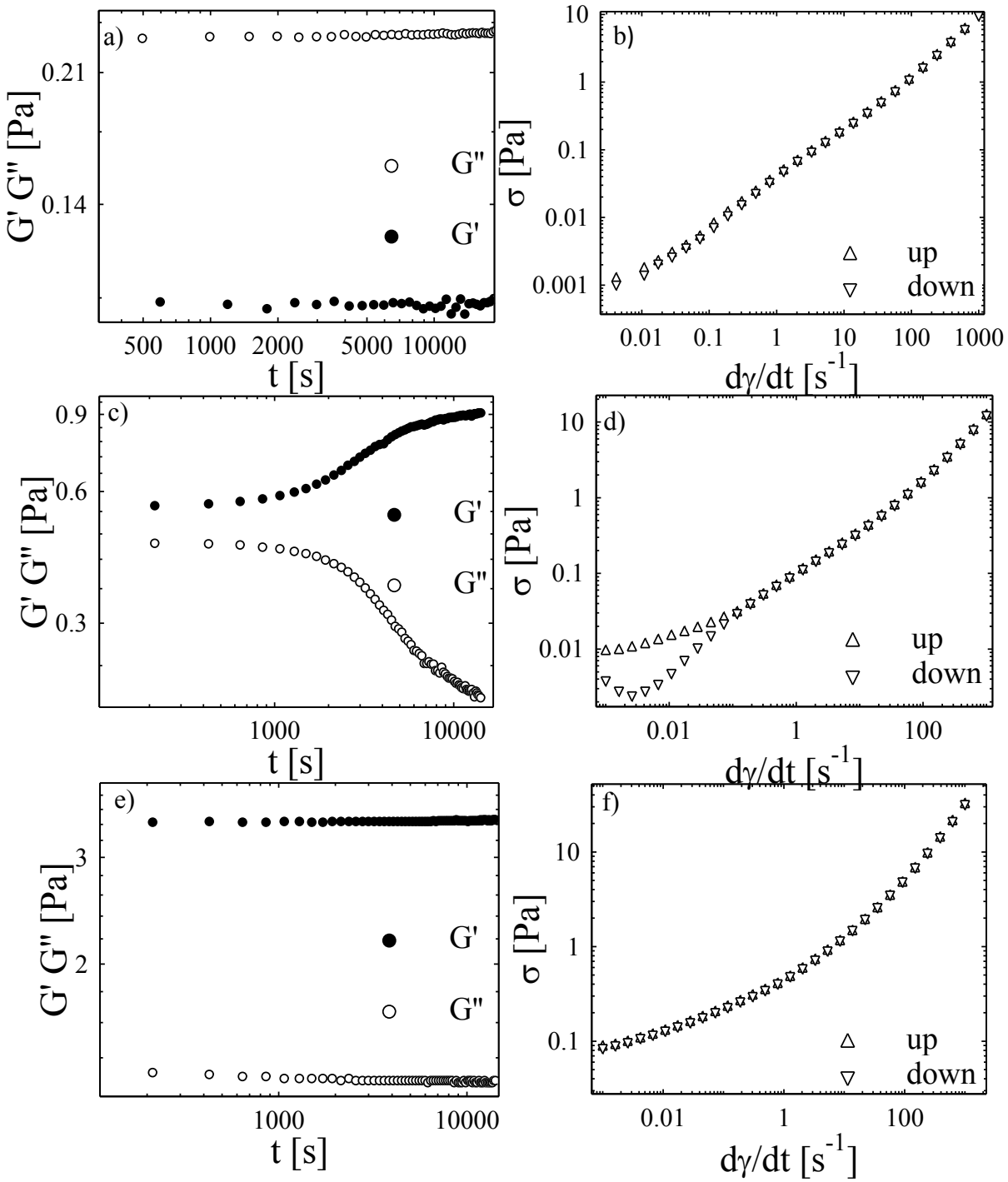

Figure 4.2.3 Rheological behaviour of the DPM_a suspensions in different phases with various volume fractions: the time dependence of storage modulus *G'* (filled circles) and loss modulus *G"* (empty circles) were measured under oscillatory shear strain with γ_{max} = 1% and f = 1 Hz. Panels a), c), e) display the dependence of *G'* and *G"* on time for the DPM_a suspensions with ϕ of 0.40, 0.51, 0.63, respectively. The shear stress versus both increasing (upwards triangles) and decreasing (down wards triangles) shear rate of the DPM_a suspensions with ϕ_{eff} of 0.40, 0.51, 0.63 are shown in b), d), f), respectively.

The dependence of *G'* and *G"* on time of the hard dumbbells with $L^* \sim 0.24$ in the fluid phase, the biphasic gap and the plastic crystalline phase are displayed in Figure 4.2.3a, c and e, individually. Figure 4.2.3b, d, f exhibit the corresponding flow curves measured by increasing $\dot{\gamma}$ from 0.001 to 1000 s^{-1} (upwards empty triangles) slowly with a logarithmic time ramp of 1000 to 10 s and then decreasing shear rate from 1000 to 0.001 s^{-1} with a logarithmic time ramp of 10 to 1000 s (downwards empty triangles).

For the DPM_a suspensions at $\phi_{eff} = 0.40$ (see Figure 4.2.3a), *G"* is observed to be larger than *G'* in the oscillatory shear field. Both *G'* and *G"* are found to be constant for the whole entire time of observation, indicating a stable fluid phase as expected. The flow curve shown in Figure 4.2.3b is fully reversible without hysteresis. In case of the DPM_a suspension in the biphasic gap ($\phi_{eff} = 0.51$), Figure 4.2.3c displays that the time dependence of *G'* and *G"* starts with *G' > G"*, and both *G'* and *G"* are not time dependent at the beginning. After ca.1000s, *G'* increases gradually and *G"* decreases correspondingly, indicating the onset of crystallization. It demonstrates that crystallization begins to set in at about 1000 s, and that the plastic crystallites can be in equilibrium with fluid in the biphasic gap. Figure 4.2.3d shows that there is a strong hysteresis in flow curves of the DPM_a suspension at $\phi_{eff} = 0.51$ with indicative of the shear melting of crystals upon increasing $\dot{\gamma}$. The suspension behaves like a Newtonian fluid in the high shear rate region after shear melting, where the shear stress σ can be simply reversed by decreasing $\dot{\gamma}$. However, σ begins to increase when the decreasing $\dot{\gamma}$ reaches a low sufficient region ($\dot{\gamma} < 10^{-2}$ s^{-1}), where ca. 1000s is needed to measure one point. The increase in σ with decreasing $\dot{\gamma}$ indicates that hard dumbbells in the shear-melted suspension can recrystallize given long enough time and sufficiently low $\dot{\gamma}$.

The decrease in temperature from 15 °C to 5 °C leads to an increase of volume fractions of this suspension up to 0.63. Based on the phase diagram of the DPM_a suspension as shown in Figure 4.2.2, the suspension at 5 °C is located above the plastic crystalline phase, which is probably in the glassy state. The rheological results are indicative of a glassy behaviour of the hard dumbbell suspensions at $\phi_{eff} = 0.63$. Figure 4.2.3e and f demonstrate that the DPM_a suspension in the glassy state has no time dependence of *G'* and *G"* in oscillatory shear filed and there is no hysteresis in flow curves.

4.2.2.2 Dumbbell-shaped microgels with $L^* \sim 0.30$

In this section, the time dependent experiment in the oscillatory shear field and flow curves measurements are carried out on the DPM_b suspensions with $L^* \sim 0.30$ as shown in Figure 4.2.4. According to the phase diagram of the DPM_b suspensions in Figure 4.2.1d, the volume fractions of measured DPM_b suspensions are chosen at 0.36 in the fluid phase, 0.52 in the biphasic gap and 0.64 in the solid phase, respectively. The flow curve of the DPM_b suspensions as a function of increasing and decreasing $\dot{\gamma}$ in the fluid phase, the biphasic gap and the plastic crystalline phase are shown in Figure 4.2.4a, c and e, respectively. The time dependent measurements under oscillatory shear are displayed in Figure 4.2.4b, d and f.

As shown in Figure 4.2.4, there is neither time dependence of *G'* and *G"* nor hysteresis along the flow curve for the DPM_b suspension in the fluid ($\phi_{eff} = 0.36$) and the glassy phase ($\phi_{eff} = 0.64$). The slight deviation along the flow cure in Figure 4.2.4a can be explained by the shear-induced crystallization as reported in spherical systems.[173] As for of the DPM_b suspension in the biphasic gap ($\phi_{eff} \sim 0.52$), there is a weak hysteresis in the flow curve and a slight time dependence of *G'* and *G"* in oscillatory shear field, which is indicative of crystallization. The time window for the DPM_b suspension in the biphasic gap (see Figure 4.2.4d) displays that crystallization begins to set in at ca. 20000 s in the oscillatory shear field with $f = 1$ Hz and $\gamma_{max} = 1\%$. The time that is needed for the onset of crystallization in the suspension of DPM_b is much longer than that in the suspension of DPM_a microgels under the same oscillatory shear. It is indicated that the hard dumbbells with a larger aspect ratio show slower diffusion in the concentrated suspensions. This finding agrees with the theoretical prediction by the group of Schweizer that the glass transitions curve is a monotonically decreasing function of aspect ratio.[174] The glass state mentioned here is a phase where both translation and rotation motion dumbbells are arrested. At a fixed volume fraction, the hard dumbbells with $L^* \sim 0.30$ is closer to the glass state than that with $L^* \sim 0.24$. Thus, more time is required for crystallization due to the slowdown of the dynamics in the vicinity of the glass transition.

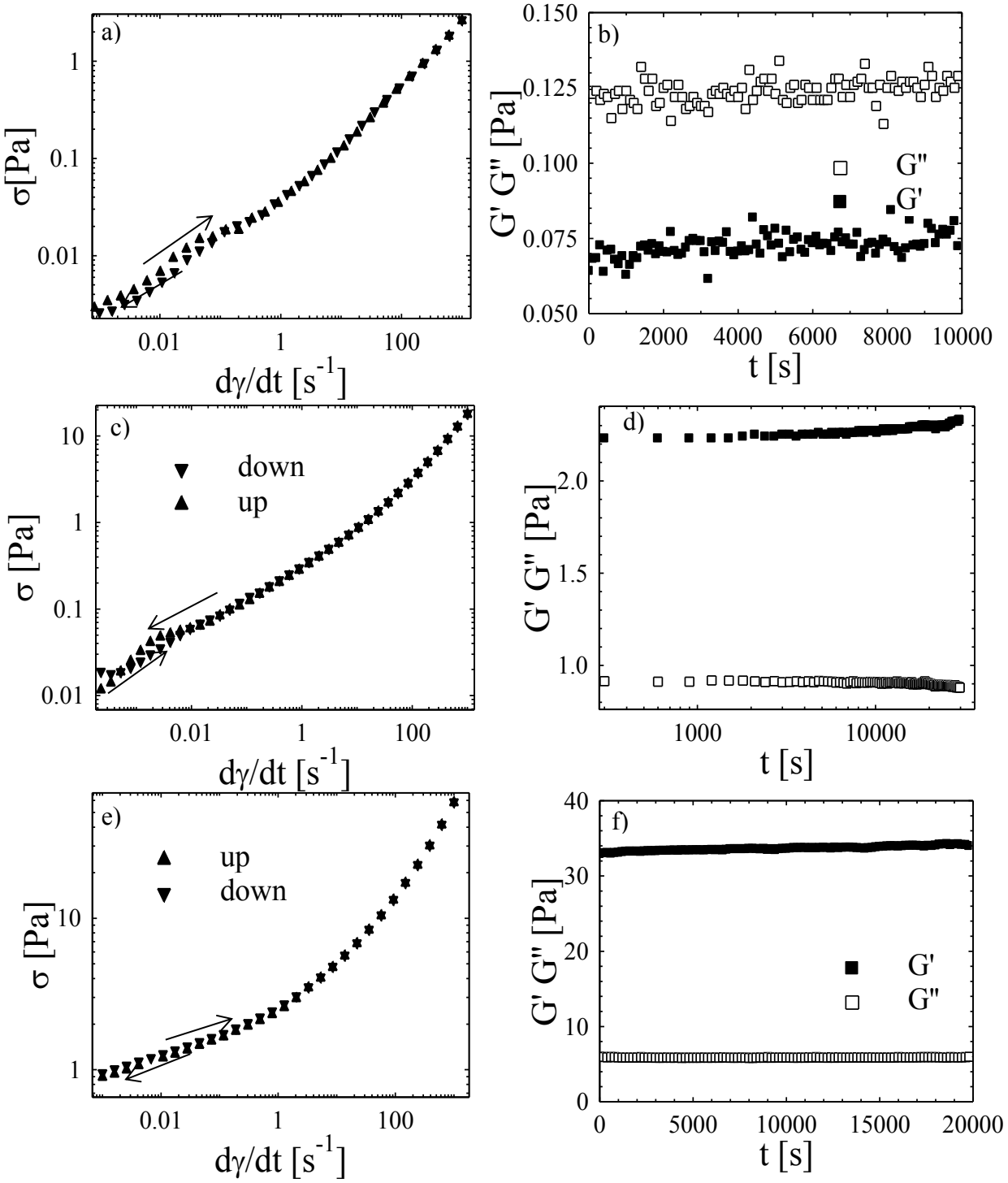

Figure 4.2.4 Rheological behaviour of the DPM_b suspensions in different phases with various volume fractions: Shear stress versus both increasing (upwards triangles) and decreasing (down wards triangles) shear rate at ϕ of 0.36, 0.52, 0.64 are shown in a), c), e) respectively. The dependence of *G'* (filled sqaures) and G" (empty squares) on time are measured in oscillatory shear field with γ_{max} = 1% and f = 1 Hz. b), d), f) on the right side display the time dependent *G'* and *G"* of the DPM_b suspensions with ϕ of 0.36, 0.52, 0.64, respectively.

In conclusion, the dumbbell-shaped microgels have been used as model systems to investigate the crystallization of hard dumbbells. The experimental phase diagrams of hard dumbbells with $L^* \sim 0.24$ and 0.30 are comparable to the boundary of the phase diagram predicted by the MC simulations.[52-53] Rheological measurements have been carried out on the dumbbell-shaped microgels (both $L^* \sim 0.24$ and 0.30) to investigate the crystallization process of hard dumbbells. The crystallization process of hard dumbbells with $L^* \sim 0.30$ in the biphasic gap turn out to be much slower than that of $L^* \sim 0.24$. In the next section, the viscoelastic measurements are performed on the crystallized hard dumbbells to investigate their yielding behaviour.

4.3 Yielding behaviour of hard dumbbells

With the increasing applied stress, many materials exhibit a transition from solid-like to fluid-like response, which is generally known as yielding.[136] The fundamental principles for this phenomenon of glassy solids[175] and various complex fluids[176],[177] have been extensively investigated. Using spherical colloids, a number of investigations mainly by rheological measurements have been done to investigate the yielding behaviour of concentrated colloidal suspensions.[178-180] In case of the hard-spheres in glassy state, a simple yielding process emerges at a strain corresponding to the maximum distortion of the cage of nearest neighbours.[34, 41] However, the attraction-dominated spheres in the glassy state show a two-step yielding process at different ranges of strains.[181] One step is assumed to be related with the breaking of attractive bonds between particles, while the other one is referred to the cage breaking process. The rheological study turns out to be effective to characterize the yielding behaviour and the dynamic relaxation of spherical colloids in a concentrated state.

In case of nonspherical colloidal systems, the theoretical study of Schweizer's group[174, 182-183] reveals that the anisotropy in particles' shape opens up new mechanisms for stress relaxation and thus alters the nature of the glassy and gelled state. Using the dumbbell-shaped colloids with different interactions as model systems, the experimental studies done by Zukoski's group[182, 184-185] indicate that there are nonbonded plastic repulsive glasses, nonbonded double repulsive glasses, bonded repulsive glasses and dense gels in their phase diagram. The nonbonded double repulsive glasses have multiple yielding events, which can be interpreted in light of naïve mode coupling theory (NMCT).[186-187] One yielding process is associated with exceeding the entropic barrier constraining rotational motion and the other is correlated with exceeding the barrier for exchanging nearest neighbours.[174] However, there is

no work done on the stress relaxation and the yielding behaviour of the crystallized hard dumbbells yet. In this section, we perform viscoelastic measurements to investigate the yielding behaviour of the crystallized hard dumbbells in different crystalline phases.

4.3.1 Hard dumbbells with $L^* \sim 0.24$

Using the DPM_a suspensions with $L^* \sim 0.24$ as the model system, the viscoelastic properties of the hard dumbbells have been investigated in both biphasic gap and fully crystalline phase. The corresponding volume fractions are chosen at ϕ_{eff} = 0.55 and ϕ_{eff} = 0.60, respectively according to the phase diagram in Figure 4.2.2. The yielding behaviour is measured under oscillatory shear with increasing strains, $\gamma_{\max}$ from 0.1% to 1000% at a fixed frequency, f = 1 Hz. The dynamic frequency sweep is performed at $\gamma_{\max}$ = 1% to measure G' and G'' as a function of decreasing f from 10 Hz to 0.01 Hz with a logarithmic time ramp from 600 s to 20 s. In all cases, the pre-shear with $\dot{\gamma}$ = 100 s^{-1} for 200 s is set before the measurements to initialize the samples at the same non-equilibrium state. A waiting time, t_w of 60 s is set in between if it is not specially stated. To investigate the effect of crystallization on the yielding behaviour of the hard dumbbell suspensions in the biphasic gap, various t_w is set before the measurements on the DPM_a suspensions with ϕ_{eff} = 0.55 as shown in Figure 4.3.1. t_w is chosen according to the time window (see Figure 4.3.1a) at 60 s, 3000 s and 10000 s, respectively.

Figure 4.3.1a shows the dependence of G' and G'' on time. Here G' begins to increase from t ~ 1000 s and reaches its maximum plateau at t = ca. 7000 s. Meanwhile, G'' decreases correspondingly and remains constant after its minimum at ca. 7000 s. It is indicated that the crystallization process begins to set in at t = ca. 1000 s and the fully crystallization state is reached at ca. 7000 s. The effect of the crystallization process (marked by different waiting time after pre-shear for crystallizations to set in) on the rheological behaviour of the hard dumbbell suspensions are displayed in Figure 4.3.1b and c. For t_w = 60 s and t_w = 3000 s, the dependences of G' and G'' on γ or f are almost identical. The γ or f dependence of G' and G'' after t_w = 10000 s, however, shows a big difference. Compared with the measurements after t_w = 60 s, the values of G' and G'' after t_w = 10000 s is almost ten times larger in the small frequency region (f < 0.01 Hz). Moreover, G' and G'' are nearly independent on f in this region, suggesting a stable structure formed by the crystallized hard dumbbells.

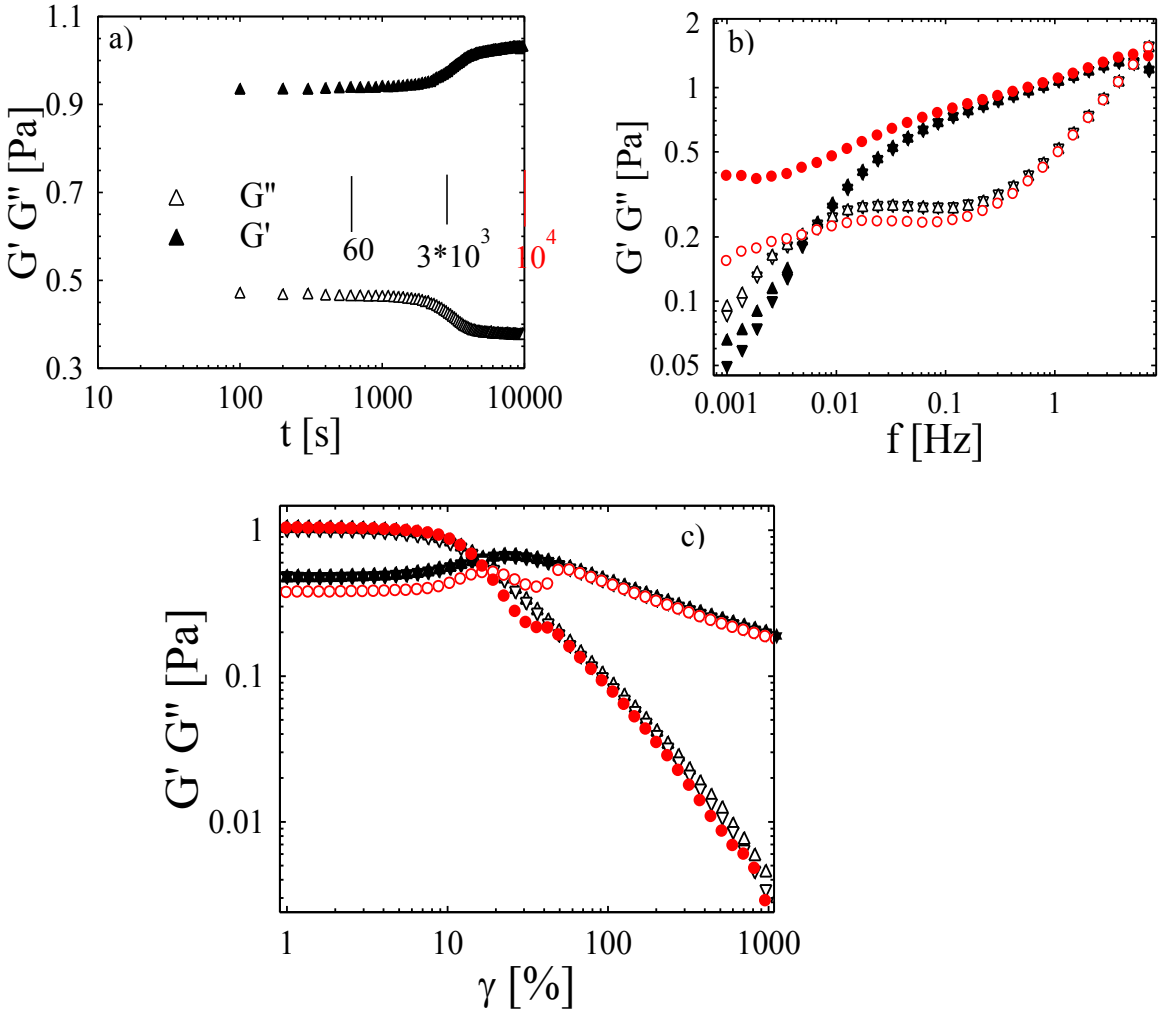

Figure 4.3.1 Time dependence of G' and G'' in the oscillatory shear field of f = 1 Hz and γ_{max} = 1% (a). The dependence of G' and G'' on frequency under oscillatory shear with γ = 1% after various t_w (b) and strain sweep with f = 1Hz after various t_w (c) of the hard dumbbell suspensions at ϕ_{eff} = 0.55. As for the frequency and strain sweep, the different waiting times are set according to time window (a). The upwards triangles mean G curve after t_w = 60 s, downwards triangles represent G curve after t_w = 3000 s and circles stand for G curve after t_w =10000 s. For all three sets of symbols, the filled ones refer to G' and the empty ones are for G''.

The yielding behaviour displayed in Figure 4.3.1c indicates that the linear viscoelastic region is preserved until the strain amplitude is increased up to ca. 10%, where G' and G'' are independent on increasing γ. In this region, the various waiting time nearly makes no difference on the dependence of G' and G'' of the hard dumbbell suspensions on γ except a slight decrease in the value of G'' of the fully crystallized hard dumbbell suspensions after t_w = 10000 s. The main difference before and after the fully crystallization emerges at the transition from the linear to the nonlinear viscoelastic region.

Beyond the strain of ca. 10%, the hard dumbbells in the biphasic gap after t_w = 60 s and t_w = 3000 s only show one yielding event (triangles in Figure 4.3.1c). At the end of the linear region, G' decreases with the increased γ. Correspondingly, G'' increases up to its maximum firstly and then decreases in the nonlinear viscoelastic region. The simple yielding process is similar to that of the hard-sphere glass.[19, 41] Probably, it can be explained by the deformation and yielding of the cage-like microstructure. However, the hard dumbbell suspensions after t_w = 10000 s show a more complex yielding behaviour. Two obvious yielding events (circles in Figure 4.3.1c) appear along the dependence of G' and G'' on γ. In the range from 10% to 20%, G'' increases to its first maximum, while G' decreases correspondingly, and crosses over G'' at $\gamma \sim 20$ %. After the intersection, G'' decreases to its minimum and G' simultaneously reaches its plateau at $\gamma \sim 50$ %. Instead of decreasing along the increased γ, G'' increases again to its second maximum at $\gamma \sim 60$ %, yielding the second yielding event. Afterwards, G' and G'' decrease sharply with further increase in γ. Since the dumbbell-shaped microgels used here are sterically stabilized (see the discussion in Chapter 4.1), these two yielding events should not be related to possible attractions between the particles as discussed by Schweitzer *et al*.[182, 185, 188]. Based on the discussion above, these two yielding events appear as long as the hard dumbbell suspensions are fully crystallized. These two yielding events at the transition from linear to nonlinear regions are therefore considered to be related with the crystallization of the hard dumbbells. This yielding behaviour with the two yielding events as discussed above is referred to as the double yielding behaviour in this work.

To further address this point, the viscoelastic measurements are carried out for the DPM_a suspensions in the fully crystalline phase. Based on the phase diagram as shown in Figure 4.2.2, the volume fraction is chosen at 0.60. The yielding behaviour is measured firstly with increasing strains from 0.01% to 1000% as described above. In the following, the dependence of G' and G'' on decreasing γ is measured as well to check whether the yielding behaviour is reversible or not. Figure 4.3.2 summarizes the yielding behaviour of hard dumbbells in the plastic crystalline phase (ϕ_{eff} = 0.60).

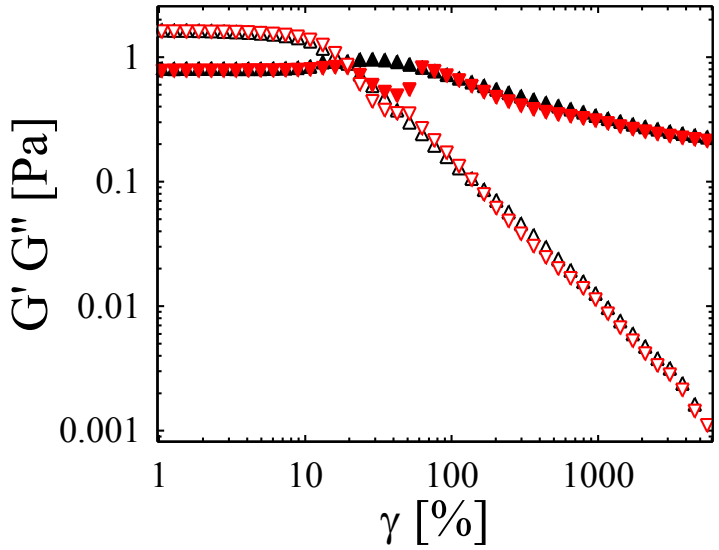

Figure 4.3.2 The yielding behaviour of the DPM_a suspension with $L^* \sim 0.24$ in the fully crystalline phase $\phi_{eff} = 0.60$. It is measured in the oscillatory shear field with $f = 1$ *Hz* as a function of increasing γ (upwards triangles) and decreasing γ (downwards triangles). Filled triangles indicate storage modules, *G'* and empty triangles indicate loss modules, *G''*.

Figure 4.3.2 displays that the hard dumbbells in the plastic crystalline phase exhibit the double yielding behaviour with increasing shear strains, which is similar to that measured for the fully crystallized hard dumbbells in the biphasic gap after $t_w = 10000$ s (see Figure 4.3.1c). However, this double yielding behaviour is not reversible, the two yieding events are observed to emerge to one yielding event with the decreasing strains. The double yielding will be the subject of a further study by rheo-SANS in section 4.4.

4.3.2 Hard dumbbells with L*~0.30

In this section, the viscoelastic measurements are performed to investigate the yielding behaviour of the DPM_b suspensions with $L^* \sim 0.30$ in the plastic crystalline phase. Based on the phase diagram shown in Figure 4.2.2, the volume fraction of the DPM_b suspensions is chosen at 0.60 (12.85 wt.-% at 15°C). Viscoelastic measurements are performed under oscillatory shear with increasing strains from 0.1% to 1000% and at a fixed frequency of $f = 1$ Hz or $f = 5$ Hz. As described in the experimental part (see Chapter **7**), the default measurement time is set as 100s / point. One more set of experiment is performed with 500 s / point in the oscillatory shear field with $f = 1$ Hz. It is designed to apply the equal amount of oscillatory shear cycles on the DPM_b suspension to that under oscillatory shear with $f = 5$Hz

(100s / point). Figure 4.3.3 summarizes the yielding behaviour of the hard dumbbell suspensions with $L^* \sim 0.30$ in an oscillatory shear field of $f = 1$ Hz or 5 Hz, respectively.

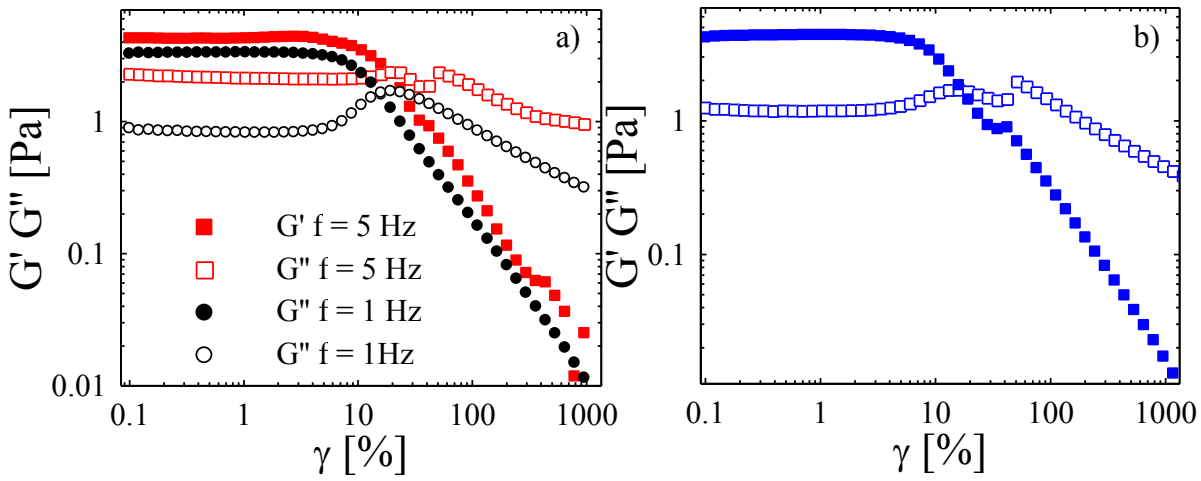

Figure 4.3.3 (a) Dependence of *G'* and *G"* on increasing γ for the hard dumbbells with $L^* \sim 0.30$ in the plastic crystalline phase under oscillatory shear of f = 1Hz (circles) and f = 5Hz (squares). This measurement is performed with default setting (100 s/point). (b) The dependence of *G'* and *G"* on γ of the hard dumbbells with $L^* \sim 0.30$ in the plastic crystalline phase that is measured under oscillatory shear of f = 1Hz with 500 s/point. The filled symbols denote G', while open symbols represent G''.

The yielding behaviour displayed in Figure 4.3.3a show that hard dumbbells with $L^* \sim 0.30$ in the plastic crystalline phase behave only one yielding event under oscillatory shear with $f = 1$ Hz but two yielding events under oscillatory shear with f = 5 Hz. Compared with the oscillatory shear with $f = 1$ Hz, the number of applied oscillatory shear cycles is increased by 5 times within the same measurement time for the oscillatory shear with f = 5 Hz. It is interesting to mention that the double yielding events are observed as well in the oscillatory shear field with $f = 1$ Hz when the measurement time is prolonged by five times as shown in Figure 4.3.3b. Based on these three sets of experiments, it is concluded that the hard dumbbells with $L^* \sim 0.30$ in the plastic crystalline phase can show the same double yielding behaviour as the hard dumbbells with $L^* \sim 0.24$, but the former needs longer and stronger oscillations. As discussed in section 4.2.2, the hard dumbbells with $L^* \sim 0.30$ is closer to the glassy state than that with $L^* \sim 0.24$ at the same volume fraction of 0.6. Due to the slowdown of the dynamics in the vicinity of the glass transition, stronger and longer oscillations are required to induce the same structural evolution as that with $L^* \sim 0.30$.

In conclusion, the viscoelastic measurements have been performed in this section to investigate the yielding behaviour of hard dumbbells in different phases. The hard dumbbells in the biphasic gap shows one yielding process under oscillatory shear, while there are two yielding for the hard dumbbells in the plastic crystalline phase. Moreover, the hard dumbbell suspensions with $L^*\sim$ 0.30 require longer or stronger oscillations to exhibit the double yielding behaviour than that with $L^*\sim$ 0.24. The rheological study reveals that the crystallization of the hard dumbbells is the main reason for their yielding behaviour. However, the underlying structural evolution at oscillatory shear cannot be elucidated by rheological measurements alone. Hence the double yielding will be investigated in detail by the combination of SANS and rheology (rheo-SANS) in Chapter 4.4.

4.4 The plastic crystalline phase and its structural evolution

Section 4.2 has shown that hard dumbbells form plastic crystal as indicated by Bragg reflections. The viscoelastic measurements in section 4.3 indicate that the hard dumbbell suspensions in the plastic crystalline phase exhibit two yielding events in an oscillatory shear field. To clarify the structure of the plastic crystal in equilibrium and their structural evolution under oscillatory shear, rheo-SANS experiments have been performed for the hard dumbbell suspensions in different crystalline phases at rest and under oscillatory shear. Mock and Zukoski were the first to use the rheo-SANS to investigate the microstructure of the plastic crystal formed from slightly charged dumbbells.[60] These authors observed that the plastic crystal is polycrystalline in equilibrium, which evolves into hexagonally packed layers by the application of steady shear. It should be noted, however, that the interaction of the dumbbells used by Mock and Zukoski was quite complicated and had an attractive component as well.[60] Up to now, there is no study of shear induced crystal structures formed by hard dumbbells.

Here we present the first study on the structural evolution of plastic crystal under oscillatory shear by rheo-SANS. The work of this part is organized as follows: using the DPM_a suspensions ($L^* \sim 0.24$) (see Table 4.1.1) as the model system, the hard dumbbells in the plastic crystalline phase have been investigated by rheo-SANS measurements and BD simulations at rest and under oscillatory shear. The BD simulations in this work have been done by Nils Heptner within his PhD-thesis.[132] Moreover, the DPM_a suspension in the biphasic gap is studied as well. In addition to this, the DPM_b suspension with $L^* \sim 0.30$ in the plastic crystalline phase is studied as well by rheo-SANS measurements in order to explore the effect of L^*.

4.4.1 Plastic crystalline phase

SANS measurements have been carried out on the DPM_a suspension in the plastic crystalline phase (ϕ_{eff} = 0.60) at various strains as shown in Figure 4.4.1. The measured strain amplitudes (γ_{max}) as listed in Table 7.3.1 have been chosen to elucidate the dependence of *G'* and *G"* on increasing shear strains. The corresponding Pe_r has been calculated according to Eq. (3.2.5) in section 3.3.1. In Figure 4.4.1, the scattering patterns are shown for the hard dumbbell suspensions at rest and under oscillatory shear with five representative strain amplitudes. They are

a. at rest
b. γ_{max} = 23.6% and Pe_r = 0.24 at the end of linear regime,
c. γ_{max} = 50% and Pe_r = 0.52 at the first minimum of *G''*
d. γ_{max} = 60% and Pe_r = 0.62 at the second maximum of *G''*
e. γ_{max} = 116% and Pe_r = 1.20
f. γ_{max} = 500% and Pe_r = 5.20

For each shear strain, 600 oscillations (10 min) are firstly applied to induce the corresponding structure and the following 900 oscillations (15 min) are averaged to yield the scattering patterns as shown in this part. More details related with the experiments are described in Chapter 7.

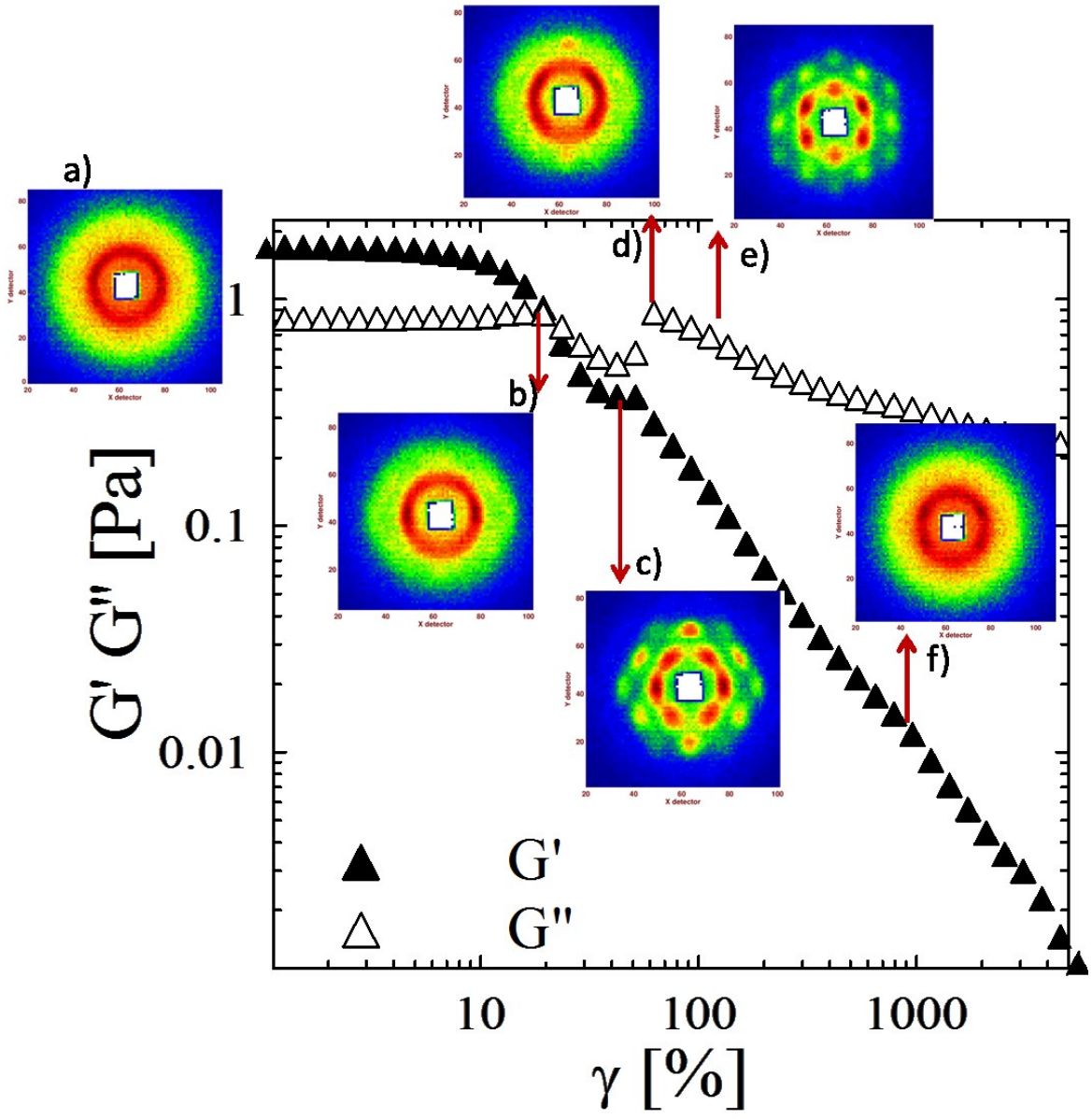

Figure 4.4.1 Evolution of the plastic crystal (a) formed from the hard dumbbells with $L^* \sim 0.24$ and $\phi_{eff} = 0.60$ under oscillatory shears at fixed frequency ($f = 1$ Hz) increasing strain amplitudes. The applied strain amplitudes are chosen based on the dependence of G' and G'' on γ at: $\gamma_{max} = 23.6\%$ and $Pe_r = 0.24$ (b), $\gamma_{max} = 50\%$ and $Pe_r = 0.52$ (c), $\gamma_{max} = 60\%$ and $Pe_r = 0.62$ (d), $\gamma_{max} = 116\%$ and $Pe_r = 1.20$ (e) and $\gamma_{max} = 500\%$ and $Pe_r = 5.2$ (f), respectively.

Figure 4.4.1 displays that there are six main structures corresponding to the plastic crystal at rest and under shear. With the increase in strain amplitudes of the applied oscillatory shear, two pronounced hexagonal patterns with sharp Bragg peaks are seen at $\gamma_{max} = 50\%$ (Figure 4.4.1c) and $\gamma_{max} = 116\%$ (Figure 4.4.1e), respectively. There is a 30° shift between these two patterns, which has been also observed by light scattering[152] or optical microscopy measurements[189],[156] for hard sphere suspensions under oscillatory shear when γ_{max} is

increased from low (< 100%) to high shear strain. Theoretical[152] and experimental[189] studies on hard spheres demonstrate that the 30° shift is indicative of the structure reorganization from a twinned fcc structure to sliding layers. The geometric packing model[152, 160] (see Figure 3.4.2) demonstrates that the most densely packed direction for the twinned fcc structure is perpendicular to the velocity direction in the velocity-vorticity plane at low strain. As shown in Figure 3.4.2, the microstructure is reorganized to the sliding layers at high strain with the most densely packed direction parallel to the velocity direction to facilitate the motion of the hexagonal plane.[152, 189] The 30° shift of hexagonal scattering pattern of the hard dumbbell suspensions is comparable to that reported on hard spheres.[152] It indicates that the sheared hard dumbbells form a twinned fcc structure in the velocity-vorticity plane with the mostly densely packed direction along the vorticity direction at γ_{max} = 50%. The structure is reorganized with the increase of shear strain until γ_{max} = 100% to form sliding layers, in which the sheared hard dumbbells are most densely packed along the velocity direction. Moreover, the scattering pattern at γ_{max} = 500% and Pe_r = 5.2 (Figure 4.4.1f) resembles that for the string structure of the sheared hard spheres (see section 3.4).[152] The hexagonally ordering as shown in Figure 4.4.1d is shear melted by a large shear strain, yielding a one-dimensional structure similar to the string-like order observed in the shear hard spheres.[152]

Apart from the similarities discussed above, there are three major differences between the scattering results of sheared hard spheres and sheared hard dumbbells. First, the hard dumbbell suspensions at γ_{max} = 23.6% show one isotropic pattern with two scattering spots prior to the formation of the first six-fold periodic pattern. This type of pattern has not been reported in the sheared hard sphere suspensions.[152] Second, the first six-fold periodic pattern of hard dumbbells under small strain (Figure 4.4.1c) shows that the intensity of the scattering spots on the same ring are not equal but exhibit an angular variation. Third, an anisotropic pattern without indications of periodic structures is observed at γ_{max} = 60%, where the second yielding event is located. In the following, these scattering data will be evaluated and interpreted step by step.

4.4.1.1 The equilibrium structure of the plastic crystal

As shown in Figure 4.4.1a, the 2D scattering pattern of the hard dumbbell suspensions at a volume fraction of 0.60 at rest reveals uniform primary and secondary rings without evidence for spots of higher intensity. The experimental phase diagram in Figure 4.2.1 displays that the hard dumbbells suspensions (ϕ_{eff} = 0.60) are in the plastic crystalline phase, where hard

dumbbells are predicted to form long-range translational order but with the freedom of orientational motion by MC simulations.[53] Due to the orientational averaging, the scattering is not sensitive to the symmetry of the hard dumbbells in the plastic crystalline phase. Combined with the iridescence of the suspensions in equilibrium (see Figure 4.2.1a), we conclude that the plastic crystal at rest has a polycrystalline structure. This finding agrees with the experimental results found for plastic crystals formed from the slightly charged dumbbells.[60]

4.4.1.2 Shear induced vorticity-alignment

Next we discuss the structural evolution of hard dumbbells after the application of oscillation shears. The dependence of G' and G'' on γ in Figure 4.4.1 reveals that the linear viscoelastic region is kept until γ_{max} = 10%. Figure 4.4.2 displays an overview of scattering patterns for the structural evolution of the sheared hard dumbbells before the formation of the first periodic six-fold patter at γ_{max} = 42.3%. In the linear viscoelastic region, the structure of sheared hard dumbbells (Figure 4.4.2b) turns out to be same as that in the equilibrium state (Figure 4.4.2a). At the end of the linear region, an anisotropic 2D scattering pattern in Figure 4.4.2c emerges at γ_{max} = 19.4% with only two scattering spots of maximum intensity on the primary ring along the velocity direction. This anisotropic pattern becomes more evident at γ_{max} = 23.6% and Pe_r = 0.24.

As described in section 3.3.2, the scattering pattern is the Fourier transform of the underlying real space structure.[139] The primary orientation of the scattering patterns is rotated 90 degree relative to that of the underlying real space structure. The anisotropic scattering pattern with two peaks along the velocity direction (Figure 4.4.2d) is thus indicative of the alignment of sheared hard dumbbells along the vorticity direction at γ_{max} = 23.6% and Pe_r = 0.24. Here we propose two possible vorticity alignments. First, the sheared hard dumbbells may get aligned along the vorticity direction, forming the ‘string-like’ or ‘chain-like’ structures. Recently, the group of Cohen[190] observed the vorticity-aligned strings in the sheared hard-sphere colloids by the confocal microscopy. Based on Stokesian dynamics simulations, they proposed that the formation of the string structure along the vorticity direction in the hard sphere suspension is due to the rotation motion of a pair of spheres. This motion includes both radial motions along the line connecting their centres and rotational motions around the centre of mass of the pair. In concentrated suspensions, the rotational motion induces strong particle migration along the gradient direction and leads to random collisions between particles of different shear

velocities. These collisions enhance diffusion to a greater degree along the flow direction than along the vorticity direction, which eventually leads to the formation of vorticity-aligned strings.[190] The motion of a pair of spheres is analogous to the translation motion and rotation motion of the hard dumbbells used in this study (see Chapter 3). Thus, we propose that hard dumbbells under oscillatory shear may form the vorticity-aligned string structure similar to that in sphere systems as discussed above.

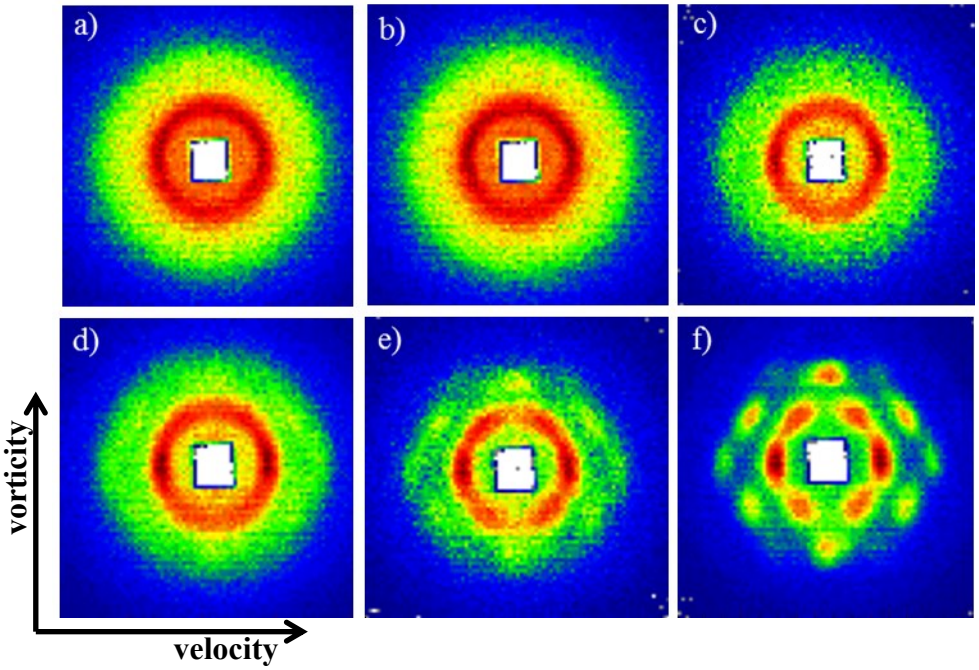

Figure 4.4.2 2D scattering patterns of the hard dumbbell suspension in the plastic crystalline phase (ϕ_{eff} = 0.60) at rest (a) and in the oscillatory shear field with f = 1Hz and various strains (b) γ_{max} = 10%, Pe_r = 0.10 (c) γ_{max} = 19.4%, Pe_r = 0.20 (d) γ_{max} = 23.6%, Pe_r = 0.24 (e) γ_{max} = 42.3%, Pe_r = 0.44 over the first 600 oscillations and (f) the following 900 oscillations. (b), (c) and (d) correspond to the scattering averaging over the last 900 oscillation cycles at the respective shear strain. The experiment scatterings displayed here are recorded in the velocity-vorticity scattering plane.

Second, the anisotropic scattering with two spots of maximum intensity along the velocity direction may be explained by the shear-induced alignment of hard dumbbells with their major axis along the vorticity direction. Shear[191]- or flow[192]-induced orientations have been commonly investigated in micellar solutions by rheo-SANS. It was shown that aligned anisotropic micelles yield anisotropic scattering patterns. The orientation perpendicular to the velocity enhances the scattering intensity along the velocity direction, while the orientation parallel to the velocity enhances the scattering intensity along the vorticity direction.[140, 148, 193] The two scattering spots of maximum intensity along the velocity direction may be

correlated with the shear-induced orientation of the hard dumbbells with the major axis perpendicular to the velocity direction.

The light area outside the first ring is probably indicative of the onset of the formation of the single crystal oriented from the polycrystallites. With a further increase in the shear strain, the Debye-Scherrer rings transform into Bragg peaks after the first 600 oscillations with γ_{max} = 42.3% and Pe_r = 0.44 (see Figure 4.4.2e). The hexagonal pattern becomes more pronounced after more oscillations (see Figure 4.4.2f). The two equatorial spots of maximum scattering intensity that are indicative of a vorticity-aligned structure remain in the developed six-fold scattering pattern. It thus can be summarized that at the end of the linear viscoelastic region, the oscillatory shear up to γ_{max} = 23.6% induces the formation of the vorticity-aligned structures. The vorticity-alignment is maintained until the formation of the first periodic structure.

4.4.1.3 Twinned FCC at low strain

The first periodic structure indicated by the six-fold plane in Figure 4.4.2e emerges at an oscillatory shear of γ_{max} = 42.3%, f = 1Hz, Pe_r = 0.44 and remains stable until γ_{max} = 50% and Pe_r = 0.52 (see Figure 4.4.1c), where G' reaches its plateau. The six-fold hexagonal SANS pattern at γ_{max} = 50% is comparable to the typical Bragg spot pattern from a shear ordered dispersion.[194] In order to evaluate the structure of the shear-induced crystal, the anisotropic 2D scattering pattern shown in Figure 4.4.1c is integrated by dividing the scattering patterns into six equal sectors through the LAMP-SANS software (provided by ILL). More details related to the radial integration are given in Chapter 7. The radial integration indicates that the crystalline peaks appear at the following magnitudes of the scattering vector (q, defined by Eq.(3.2.1)) (nm^{-1}): 0.0132, 0.0225, 0.0263, 0.0346. The peak positions can be indexed as $1:\sqrt{3}:2:\sqrt{7}$, which agrees well with the theoretical prediction for the 2d hexagonal planes by the model calculation (see section 3.4.2). Since the first peak is located at 0.0132 nm^{-1}, the lattice parameter d is determined to be 472 ± 5nm.

To analyse the underlying dynamics, the Brownian dynamic computer (BD) simulations have been performed by Nils Heptner[132] on the hard dumbbells in the plastic crystalline phase with ϕ = 0.55 and L^* = 0.24. Figure 4.4.3a shows the experimental scattering pattern of the sheared hard dumbbells at ϕ_{eff} = 0.60 and L^* = 0.24, which present the average over 900 oscillations at γ_{max} = 50%, f = 1 Hz and Pe_r = 0.52. The six-fold pattern indicates that the hard

dumbbells form hexagonal layers in the velocity-vorticity plane, which is the experimental scattering plane as defined in Figure 3.3.3. In Figure 4.4.3b, the simulated structure factor averaging 250 oscillatory shear cycles with f = 15.30 Hz and γ_{max} = 15% (and Pe_r = 2.28 is shown for the hard dumbbells with ϕ = 0.55 and L^* = 0.24. The positions of scattering spots for the simulated structure factor (Figure 4.4.3b) virtually coincide with the experiment results (Figure 4.4.3a), indicating that the hard dumbbells form a twinned fcc structure under low strain. Since the form factor of hard dumbbells is not included in the simulated structure factor, we cannot make a quantitative comparison between the scattering intensities of the experimental and simulation results.

The corresponding simulation snapshots in the velocity-gradient plane at a maximum displacement, the unstrained state and the other maximum displacement within one oscillatory shear cycle are displayed in Figure 4.4.3c from left to right. It is necessary to mention that the hard dumbbells in Figure 4.4.3c are reduced in diameter to 0.5 D (D is the diameter of the dumbbell-shaped microgels see Figure 1.3.1) for a better visibility of the structure. It indicates that the hexagonal layers are stacked in ABC sequence when the oscillatory shear is at one maximum position (left in Figure 4.4.3c), while in ACB sequence for the other maximum position (right in Figure 4.4.3c). At the equilibrium position of the oscillation (middle in Figure 4.4.3c), the layers are bridge-site stacked and a body-centered-tetragonal (bct) phase is temporarily formed. This finding is comparable to the formation of two oscillating fcc twins from hard spheres under low strain.[152, 156] Based on the simple geometric packing mode proposed by Ackerson *et al.*[152, 161] (see section 3.4), the hard dumbbells particles are most densely packed along the vorticity direction in the hexagonal layers. The oscillation shear induces hard dumbbell particles to oscillate between two neighbouring triangular voids to minimize the stress caused by the collisions with other particles during the applied shear.[156]

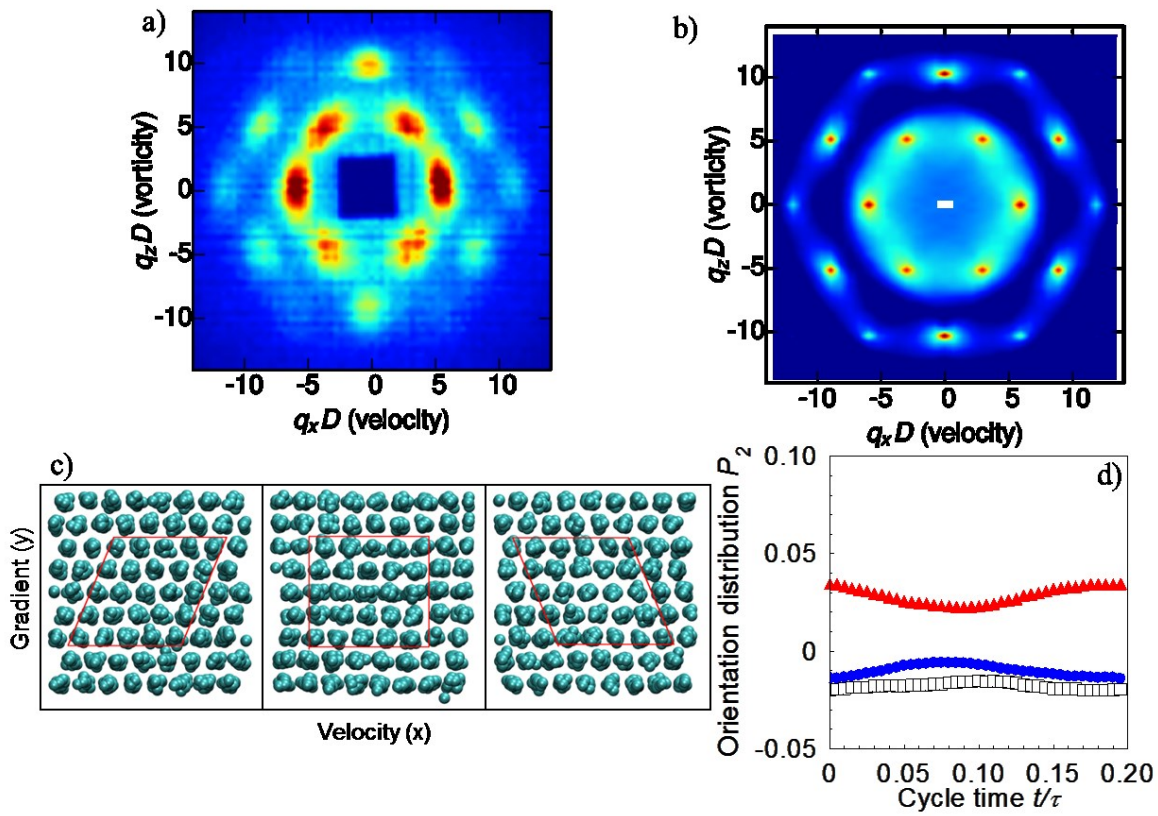

Figure 4.4.3 (a) 2D experimental scattering pattern of hard dumbbells (ϕ_{eff} = 0.60) in an oscillatory shear field (f = 1 Hz, γ_{max} = 50%, Pe_r = 0.52). This pattern is rescaled by $q_x D$ to facilitate the comparison with the results of BD simulations. (b) The calculated 2D structure factors in the velocity-vorticity plane by BD simulations, averaging 75 oscillatory shear cycles with f = 15.30 Hz and γ_{max} = 15% and Pe_r = 2.28. (c) Simulation snapshots of sheared dumbbells with ϕ = 0.55 and L^* = 0.24 in the velocity-gradient plane after the application of 75 oscillatory shear cycles with f = 15.30 Hz and γ_{max} = 15% and Pe_r = 2.28. The three figures (from left to right) show that the oscillation is at a maximum displacement, at the equilibrium position and at the other maximum displacement, respectively. The layers are stacked in ABC sequence at one extreme position, while in ACB sequence at the other one. (d) The structure analysis is done to display averaged orientations distribution of shear dumbbells over time by $\langle P_2 \rangle_i$ (t), where i denotes the orientation axis, which refers to velocity direction x, gradient direction y and vorticity direction z, respectively. $\langle P_2 \rangle_{vorticity}$ (filled circles), $\langle P_2 \rangle_{velocity}$ (filled triangles) and $\langle P_2 \rangle_{gradient}$ (open squares) are defined as the order parameters to describe the orientations along the vorticity, velocity and gradient direction, respectively. The BD simulations have been performed by Nils Heptner.[132]

Figure 4.4.3d displays the structure analysis on the orientations of hard dumbbells that are averaged over the 250 oscillatory shear cycles. The orientations of hard dumbbells along the vorticity, velocity and gradient directions are denoted by $\langle P_2 \rangle_{vorticity}$, $\langle P_2 \rangle_{velocity}$ and $\langle P_2 \rangle_{gradient}$, respectively, which are calculated according to Eq. (3.4.5) in Chapter 3. Figure 4.4.3d demonstrates that $\langle P_2 \rangle_{vorticity}$ and $\langle P_2 \rangle_{velocity}$ swings above and below zero but is not sinusoidal within the sinusoidal period of applied oscillatory shears. The time dependent,

sinusoidal shear strain is displayed in Figure 3.3.2. $\langle P_2 \rangle_{velocity}$ and $\langle P_2 \rangle_{vorticity}$ vary with the sinusoidal strain in opposite way and the variation amplitudes are larger than their average values. However, $\langle P_2 \rangle_{gradient}$ is relatively stable with the applied sinusoidal strain, which remains below zero for the whole averaged time. It is thus indicated that the orientations along the vorticity and velocity direction are preferred for the hard dumbbells at low strain, while the orientation along the gradient direction is nearly negligible.

Figure 4.4.3a shows that the intensities of the two equatorial spots on the innermost ring are stronger than the other four, and that of the two scattering spots on the second ring along the vortictiy direction are higher than the others. Based on the discussion in Figure 4.4.2, the intensity variation may be due to the shear-induced vorticity alignment of the hard dumbbell particles. There are two possibilities for the shear-induced vorticity alignment: one is the closing packing structure along the vorticity direction and the other is the alignment of hard dumbbells with the major axis parallel to the vorticity direction. According to the geometrical model, the hard dumbbells in the oscillating twin structure are expected to be most densely packed along the vorticity direction in the hexagonal plane. However, the model calculation[161] (see section 3.4.2 and Figure 3.4.3) indicates that the most dense packing in the twinned fcc structure may not affect the intensity of scattering spots on the same ring given that the hexagonal layers are perfectly stacked. Therefore, it is likely that the shear alignment of the hard dumbbells with the major axis parallel to the vorticity direction is the reason for the intensity variation observed in Figure 4.4.2a.

Additionally, the simulation results in Figure 4.4.3b shows an intensity variation with two stronger scattering spots along the velocity directions. However, the intensity distribution is not quantitatively comparable to that observed in the experiment results (Figure 4.4.3a). The intensity variation from the simulation results may be explained by the stacking faults[195] or the bridge-site stacked layers at the equilibrium position of the oscillation (middle in Figure 4.4.3c). Moreover, the BD simulations performed by Nils Heptner[132] does not show the vorticity alignment structure at low strain. This may because that the BD-simulations neglect the hydrodynamic interactions of the sheared hard dumbbells.

In conclusion, the experimental and theoretical studies demonstrate that the hard dumbbell particles form the oscillating twinned fcc structure at the oscillatory shear of $f = 1$ Hz, $\gamma_{max} = 50\%$, $Pe_r = 0.52$, where the particles are closest packed along the vorticity direction. As

indicated by the experiment results, the hard dumbbells at low strain may be slightly oriented with their major axis parallel to the velocity direction.

4.4.2 Partially oriented sliding layers at high strain

In the following, we discuss the experimental and simulated results obtained at high strain. When the strain amplitudes are increased up to approximately 100%, a second six-fold scattering pattern appears at γ_{max} = 90%, Pe_r = 0.94, indicating the formation of hexagonal layers in the velocity-vorticity scattering plane. As shown in Figure 4.4.1e, the pattern keeps stable until Pe_r = 1.20 and shows a 30° shift with respect to the pattern of the twinned fcc formed at Pe_r = 0.52. The crystalline peaks are determined via the radial integration by sectors (see Chapter 7) at the following q (nm^{-1}) positions: 0.0133, 0.0225, 0.0263, 0.0346, which are identical with that of the twinned fcc.

To facilitate the comparison with the simulated results, the experimental results (Figure 4.4.4a) at large strain (γ_{max} = 116%, Pe_r = 1.20) are rescaled by the diameter D (see Figure 1.3.1a).The simulated structure factor is shown in Figure 4.4.4b from the BD simulations on the hard dumbbells with L^* = 0.24 and ϕ_{eff} = 0.55 after the shear melting of the fcc crystal by 250 oscillations of high strain (f = 15.30 Hz and γ_{max} = 30%, Pe_r = 4.56). A comparison between the experimental and simulated results indicates that the hard dumbbells form hexagonal layers under high strain. The corresponding simulation snapshots in the velocity-gradient plane are shown in Figure 4.4.4c, indicating the random stacking of the layers. This theoretical finding is similar to the sliding layers of hard spheres investigated by van Blaaderen *et al.* via BD simulations and confocal microscopy.[156] As discussed in section 3.4, the hard sphere suspensions are observed to form a hexagonally ordered structure under large strain by Ackerson with light scattering.[152] The six-fold experimental and simulated patterns (see Figure 4.4.4) are comparable to the calculated pattern of sheared hard spheres (Figure 3.4.3b), which corresponds to the registered random stacked layers as discussed in section 3.4. It indicates that the hexagonal layers of hard dumbbells slip past one another along zig-zag paths due to the registrations between layers.

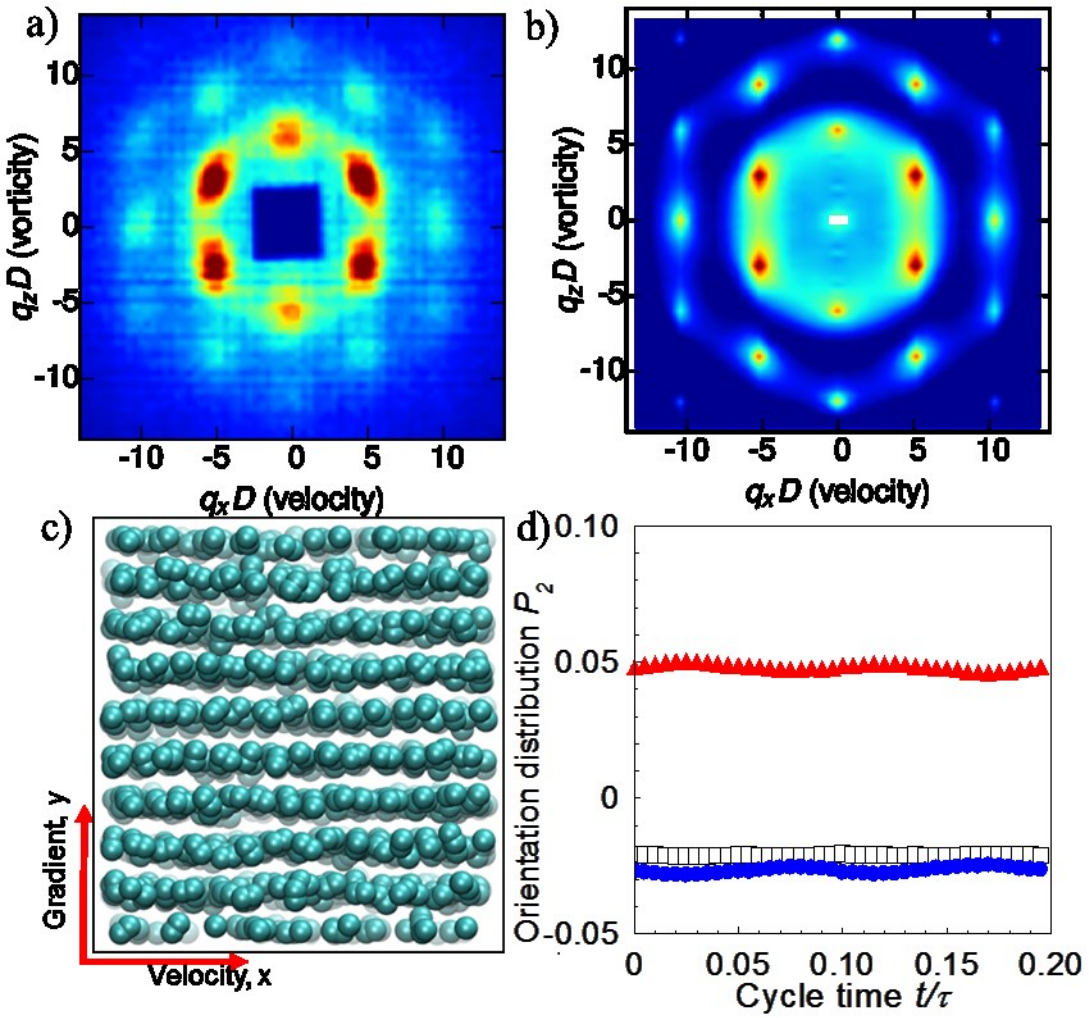

Figure 4.4.4 (a) Experimental scattering 2D pattern of hard dumbbells in the plastic crystalline phase (ϕ_{eff} = 0.60) under oscillatory shears (γ_{max} = 116%, Pe_r = 1.20, f = 1Hz) (b) The calculated 2D structure factor based on the Brownian dynamics simulation[132] on the shear melting of the fcc crystal under oscillatory shear of f = 15.30 Hz and γ_{max} = 30%, Pe_r = 4.56. The calculation is built for the model system of hard dumbbells in the plastic crystalline phase with L^* = 0.24 and ϕ_{eff} = 0.55. The corresponding simulation snapshots (c) of sheared dumbbells with ϕ = 0.55 and L^* = 0.24 in the velocity-gradient plane after the application of 250 oscillatory shear cycles with f = 15.30 Hz and γ_{max} = 30%, Pe_r = 4.56. (d) The corresponding orientation distribution of $\langle P_2 \rangle_i$ (t) denotes the averaged orientation distribution over time, and i denotes the orientation axis, which refers to velocity direction x (filled triangles), gradient direction y (open squares) and vorticity direction z (filled circles), respectively.

Based on the geometric packing model as discussed in section 3.4.1,[152, 160] the shear-induced hexagonal planes here are oriented with a close-packed direction parallel to the velocity axis for the sliding layers at $Pe_r \sim 1$. However, the hexagonally ordering planes are oriented with a close-packed direction perpendicular to the velocity axis for the case of the twinned fcc

structure (see Figure 4.4.3) at $Pe_r \sim 0.5$. A structural reorganization is thus realized by increasing the applied oscillatory shear, which is indicated by the 30° shift between the two respective scattering patterns. The work reported on hard spheres[160, 189] indicates that this structure reorganization has to take place at high strain to facilitate the easiest motion of the hexagonal planes along the velocity direction.

In the following, we discuss about the orientations of the hard dumbbells based on the structural analysis that has been performed by Heptner[132] for the sliding layers. $<P2>_{velocity}$, $<P2>_{gradient}$ and $<P2>_{vorticity}$ are shown in Figure 4.4.4d to characterize the orientations of the hard dumbbells under high strain along the velocity, gradient, and vorticity directions, respectively. It demonstrates that within the whole average time, $<P2>_{gradient}$ is almost constant below zero. $<P2>_{velocity}$ and $<P2>_{vorticity}$ are observed to be independent on the applied sinusoidal strain. In opposite to the case for the twinned fcc structure (see Figure 4.4.3d), the variation amplitudes for both $<P2>_{velocity}$ and $<P2>_{vorticity}$ are much smaller than their respective average values. Moreover, $<P2>_{velocity}$ is above zero and $<P2>_{vorticity}$ is below zero for the whole range of time and strain. This indicates that the hard dumbbells in the sliding layers are favourably oriented along the velocity direction. Thus, we name this microstructure of hard dumbbells at high strain as the partially oriented sliding layers.

From the experiment and theory study, we conclude that the hard dumbbells in the plastic crystalline phase form the partially oriented sliding layers at high strain. Unlike the twinned fcc at low strain, the shear-induced hexagonal planes at high strain are oriented with the closed packed direction parallel to the velocity direction. Moreover, the hard dumbbells particles in the hexagonal plane are favourably aligned with the major axis parallel to the velocity direction.

4.4.2.1 Intermediate stage (γ_{max}: 60%-90%)

As discussed above, the hard dumbbell suspensions in the plastic crystalline phase undergo a structural reorganization from the twinned fcc structure to the partially oriented sliding layers. Simultaneously, the orientations of hard dumbbells are changed from the strain-related alignment to the strain-independent alignment with the major axis parallel to the velocity direction. In the following we focus on the intermediate phase in between the structural and orientation reorganization that corresponds to the second yielding event at $60\% < \gamma_{max} < 90\%$ (see Figure 4.4.1). The corresponding experimental scattering patterns are displayed in Figure

4.4.5, which indicates that the sheared dumbbells undergo the successive structural reorganization from the twinned fcc structure to the partially oriented sliding layers with an increase in the applied strain amplitudes within the range from 60% to 90%.

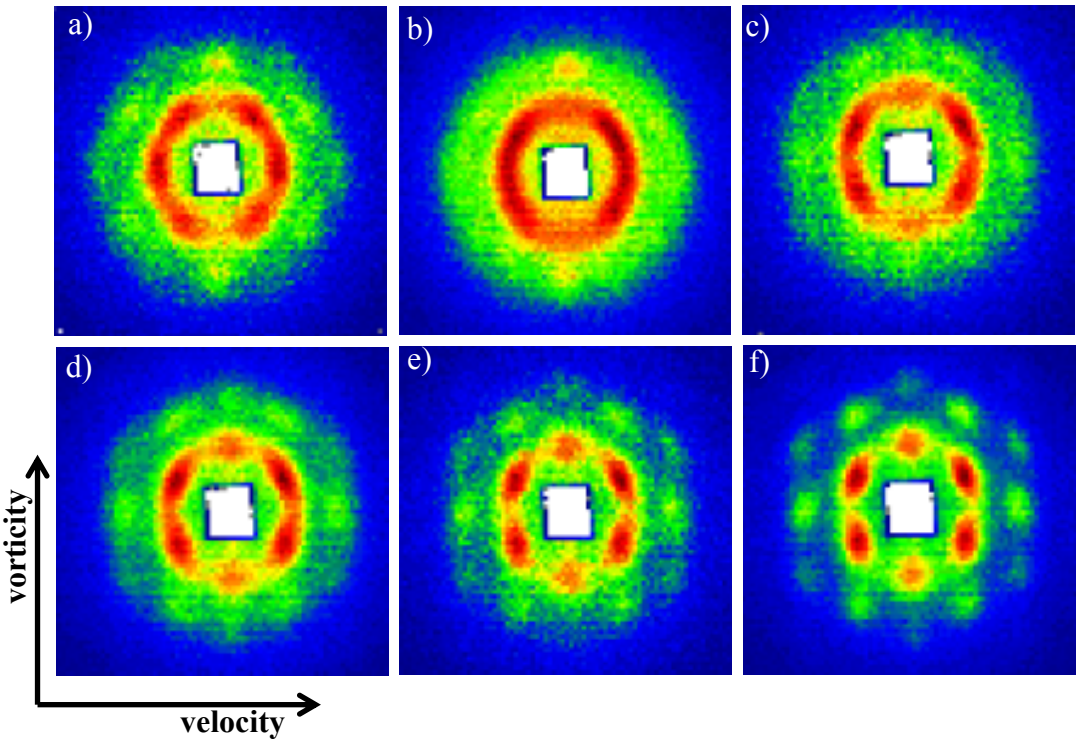

Figure 4.4.5 Experimental scattering 2D patterns of the hard dumbbells with ϕ_{eff} = 0.60 averaging (a) the first 600 oscillations and (b) the following 900 oscillations at γ_{max} = 60%, Pe_r = 0.62. Experimental scattering 2D patterns of hard dumbbells over (c) the first 600 oscillations and (d) the following 900 oscillations at γ_{max} = 70%, Pe_r = 0.76. (e) and (f) are the experimental scattering patterns under oscillatory shear with γ_{max} = 90% and Pe_r = 0.97 for the first 600 and the following 900 oscillations, respectively. Experimental scattering results shown here are recorded in the velocity-vorticity scattering plane.

Applying an oscillatory shear of γ_{max} = 60%, the six-fold plane referring to the twinned fcc structure disappears within the first 600 oscillations (see Figure 4.4.5a). With increasing time, most of these scattering spots vanish yielding the anisotropic scattered pattern with two scattering spots along the vorticity direction as shown in Figure 4.4.5b. However, the scattering spots of the second hexagonal pattern become visible for the first 600 oscillations at γ_{max} = 70%, Pe_r = 0.76 (see Figure 4.4.5c) and become more pronounced after another 900 oscillations as shown in Figure 4.4.5d. When the applied strain is increased up to γ_{max} = 90%

and Pe_r = 0.97, the second hexagonal pattern with sharp Bragg spots is developed gradually (see Figure 4.4.5e and f).

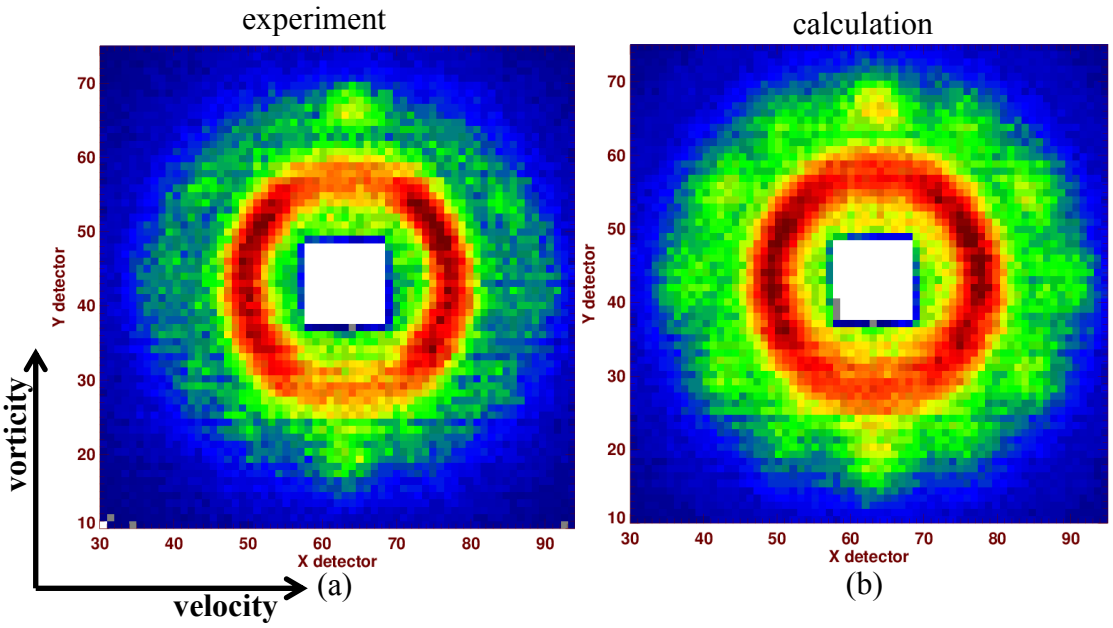

Figure 4.4.6 (a) Experimental scattering 2D patterns of the hard dumbbell suspensions with ϕ_{eff} = 0.60 over 900 oscillations at f = 1 Hz, γ_{max} = 60%, and Pe_r = 0.62 and (b) corresponding calculated scattering pattern by the LAMP-SANS software. The calculation result is a superposition result of 0.3 times pattern at 50%, 0.25 times pattern at 116%and 0.45 times of polycrystalline pattern. Both experimental and calculated results are shown in the velocity-vorticity scattering plane.

Figure 4.4.6 displays the scattering of the sheared hard dumbbells at γ_{max} = 60%, Pe_r = 0.65, which corresponds to the second maximum of G'' (see Figure 4.4.1). The data interpretation has been done based on the calculation by the LAMP-SANS software. The experimental scattering (Figure 4.4.6a, the enlarged version of Figure 4.4.5b) is comparable to the calculated pattern (Figure 4.4.6b), which is the superposition of 0.3 times the pattern measured at γ_{max} = 50% (Figure 4.4.1c), 0.25 times the pattern at γ_{max} = 116% (Figure 4.4.1e) and 0.45 times the polycrystalline pattern (Figure 4.4.1a). This means that the twinned fcc structure is shear molten forming a polycrystalline phase in the intermediate phase. Since the scattering pattern in Figure 4.4.6a averages over 900 oscillations during this structural reorganization, it is reasonable to assume that the scattering pattern is the superposition of the polycrystalline, the twinned fcc and the partial oriented sliding layers.

To elucidate the dynamics of hard dumbbells under various strains, BD simulations have been performed by Heptner[132] on the hard dumbbells in the plastic crystalline phase with L^* =

0.24 and ϕ_{eff} = 0.55. They are subjected to the oscillatory shear at f = 15.30 Hz and various strain amplitudes with Pe_r ranging from 0.25 to 17.5. The twinned fcc is observed at low strain of γ_{max} = 5% and Pe_r = 0.75, and the partially oriented sliding layers is at γ_{max} = 30% *and* Pe_r = 4.56, which agrees with the experimental results as discussed above. The simulation results in the intermediate phase are shown in Figure 4.4.7a for the hard dumbbells with L^* = 0.24 and ϕ_{eff} = 0.55 after the application of oscillatory shear with f = 15.30 Hz and γ_{max} = 20%, Pe_r = 3.04. In the simulated scattering pattern, no sharp Bragg peaks but only bright rings are observed, indicating a shear-distorted disordered structure. The slight spots on the innermost ring may indicate that a small portion of sheared hard dumbbells is partially ordered. The corresponding structural analysis of the sheared hard dumbbells at different amplitudes is shown in Figure 4.4.7b by the order and orientation parameters (Q_4, W_4 and $\langle P_2 \rangle_{velocity}$ as defined in section 3.4.3). At γ_{max} = 20% and Pe_r = 3.04, Q_4 and $\langle P_2 \rangle_{velocity}$ are nearly zero which indicates that there is neither hexagonal order nor favourable orientation of the hard dumbbells in the intermediate phase. This finding is in accord with the experimental results shown in Figure 4.4.6.

Moreover, Figure 4.4.7 displays that the bond order parameter Q_4 decreases from 0.15 with the increasing strain amplitudes from 5% to 20% until its minimum (nearly zero), while W_4 increases correspondingly from 0.1 and reaches its plateau at γ_{max} = 20% ~25%. As discussed above, the twinned fcc structures is observed at γ_{max} = 5% and the intermediate phase of the sheared dumbbells is at γ_{max} = 20% ~ 25%. The corresponding orientation parameter $\langle P_2 \rangle_{velocity}$ decreases until zero when γ_{max} is increased from 5% (the twinned fcc structure) to 20% ~25% (the intermediate phase). It means that both shear-induced hexagonal orders and orientations are lost in the intermediate phase.

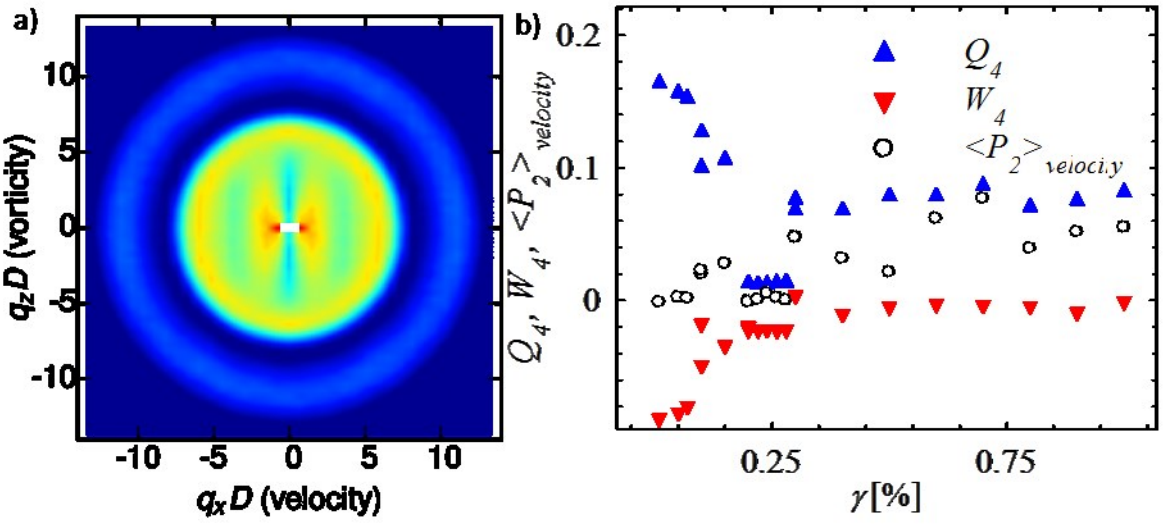

Figure 4.4.7 (a) 2D structure factors calculated by BD simulations on the hard dumbbells of $L^* = 0.24$ and $\phi_{eff} = 0.55$ after the application of $f = 15.30$ Hz and $\gamma_{max} = 20\%$, $Pe_r = 3.04$. (b) The structure analysis at various strain amplitudes and fixed frequency, $f = 15.30$ Hz , where the twinned fcc emerges at $\gamma_{max} = 5\%$ and $Pe_r = 0.75$, the intermediate phase is at $\gamma_{max} = 20\%$, and $Pe_r = 3.04$ and the sliding layers structure is at $\gamma_{max} = 30\%$, *and* $Pe_r = 4.56$. $<P_2>_{velocity}$ presents the orientation distribution with major axis along the velocity direction, Q_4 and W_4 are the bond order parameter to describe the crystal structure. The specified definitions are described in Chapter 3.

Both the order parameters (Q_4 and W_4) and the orientational parameter $<P_2>_{velocity}$ are enhanced when the shear strain is increased up to $\gamma_{max} = 30\%$ and $Pe_r = 4.56$. It means that the partially oriented sliding layers are formed with the hard dumbbells particles being aligned parallel to the velocity direction. The discussion above indicates that the shear-induced hexagonal order and orientations of the sheared hard dumbbells vary with different strain amplitudes. An intermediate phase is formed during the structural evolution from the twinned fcc to the partially oriented sliding layers, where the sheared dumbbells are free of hexagonal orders and favorable orientations. As shown in Figure 4.4.1, the intermediate state corresponds to the second yielding event, where *G"* is at its maximum. The dissipation of energy during the structural reorganization as discussed above should be the reason for the maximum of *G"* at $\gamma_{max} \sim 60\%$, which corresponds to the double yielding behaviour as discussed in section 4.3.

In conclusion, the phase behaviour of the concentrated hard dumbbell suspensions has been investigated by rheo-SANS experiments and BD computer simulations. By rheo-SANS it is observed that the plastic crystal in equilibrium is polycrystalline structure. Applying an oscillatory shear to the suspensions in this phase one can induce five non-equilibrium structures with increasing strain amplitudes. Compared with the BD simulation results, they are identified as

- the vorticity-alignment structure at $\gamma_{max} \sim 23.6\%$, $Pe_r \sim 0.24$,
- the twinned fcc structure at $\gamma_{max} = 50\%$ and $Pe_r = 0.52$,
- the intermediate structure at $\gamma_{max} = 60\%$, $Pe_r = 0.62$,
- the partially oriented sliding layers at $\gamma_{max} = 116\%$ and $Pe_r = 1.20$,
- the string structure at $\gamma_{max} = 500\%$ and $Pe_r = 5.20$.

Presumably, the vorticity alignment results from the shear-induced alignment of the hard dumbbells perpendicular to the velocity direction which is probably kept until the formation of the twinned fcc structure. The comparable experiment and simulation results indicate that the hard dumbbells under increasing shear strains undergo a shear-induced structural reorganization from the twinned fcc to the partially oriented sliding layers of hard dumbbells. The twinned fcc structure is shear-melted in the intermediate phase, where a polycrystalline phase is observed to be formed during the structure reorganization. The twinned fcc structure are formed at low strain, where hard dumbbells are slightly oriented along the velocity direction. At high strain, the partially oriented sliding layers are formed, where the hard dumbbells are preferably oriented along the velocity direction. To the best of our knowledge, we report here the first time the shear-induced partially oriented sliding layers formed from the hard dumbbells with $L^* < 0.4$.

During the shear-induced structural reorganization, the twinned fcc structure is shear melted prior to the formation of the partially oriented sliding layers, yielding an intermediate structure that are free of hexagonal order and favourable orientations of hard dumbbells. The corresponding energy dissipation should be the reason for the second yielding event observed along the dependence of G' and G'' on γ. The structural evolution under increasing shear strains is the underlying mechanism for the double yielding behaviour of hard dumbbells as discussed in section 4.3.

4.4.3 Biphasic region of hard dumbbells with $L^* \sim 0.24$

The phase diagram in Figure 4.2.1b reveals that hard dumbbells with $L^* \sim 0.24$ are in the biphasic gap with ϕ_{eff} ranging from 0.50 to 0.56. The rheological study in section 4.3 demonstrates that the hard dumbbells suspensions in the biphasic gap only show one yielding event along the dependence of G' and G'' on γ. To clarify the corresponding structural evolution, rheo-SANS experiments have been performed on the hard dumbbell suspensions in the biphasic gap under oscillatory shear with $f = 1$ Hz and various strains as listed in Table 7.3.1. The DPM_a suspensions (see Table 4.1.1) at $\phi_{eff} = 0.51$ are used as the model system, where the plastic crystal with a fraction of ca. 20% coexists with the fluid (see Figure 4.2.1). Figure 4.4.8 presents the 2D experimental patterns

a. at rest
b. $\gamma_{max} = 19.4\%$ and $Pe_r = 0.16$ at the end of linear viscoelastic region
c. $\gamma_{max} = 50\%$ and $Pe_r = 0.42$,
d. $\gamma_{max} = 60\%$ and $Pe_r = 0.50$,
e. $\gamma_{max} = 116\%$ and $Pe_r = 0.97$,
f. $\gamma_{max} = 1000\%$ and $Pe_r = 8.38$,

A hexagonal pattern of weak Bragg spots is observed at $\gamma_{max} = 50\%$ (Figure 4.4.8b), while a second hexagonal pattern turns up at $\gamma_{max} = 116\%$ (Figure 4.4.8e), showing a 30° shift with respect to the former one. The 30° shift indicates that that the hard dumbbells in the biphasic gap undergo the similar structural evolution to that for the plastic crystalline phase. The shear-induced twinned fcc structure is formed at low strain ($\gamma_{max} = 50\%$), which is reorganized to the partially oriented sliding layers at high strain ($\gamma_{max} = 116\%$).

The isotropic scattering pattern in Figure 4.4.8a reveals the fluid state of the hard dumbbell suspensions in the biphasic gap at rest. Figure 4.4.8b displays the scattering pattern with two sharp equatorial scattering spots along the velocity direction after the application of the oscillatory shear of $\gamma_{max} = 19.4\%$ and $Pe_r = 0.20$. The anisotropic scattering is similar to that observed for the hard dumbbells in the fully crystalline phase under shear at $\gamma_{max} = 23.6\%$ and $Pe_r = 0.24$ (see Figure 4.4.8d). According to the discussion in section 4.4.1.2, the two sharp equatorial scattering spots probably correspond to a vorticity alignment structure, where the sheared hard dumbbells are aligned favourably in the vorticity direction. Therefore, it is concluded that the hard dumbbells in the biphasic gap form the shear-induced vorticity-alignment structure at the end of the linear viscoelastic regime.

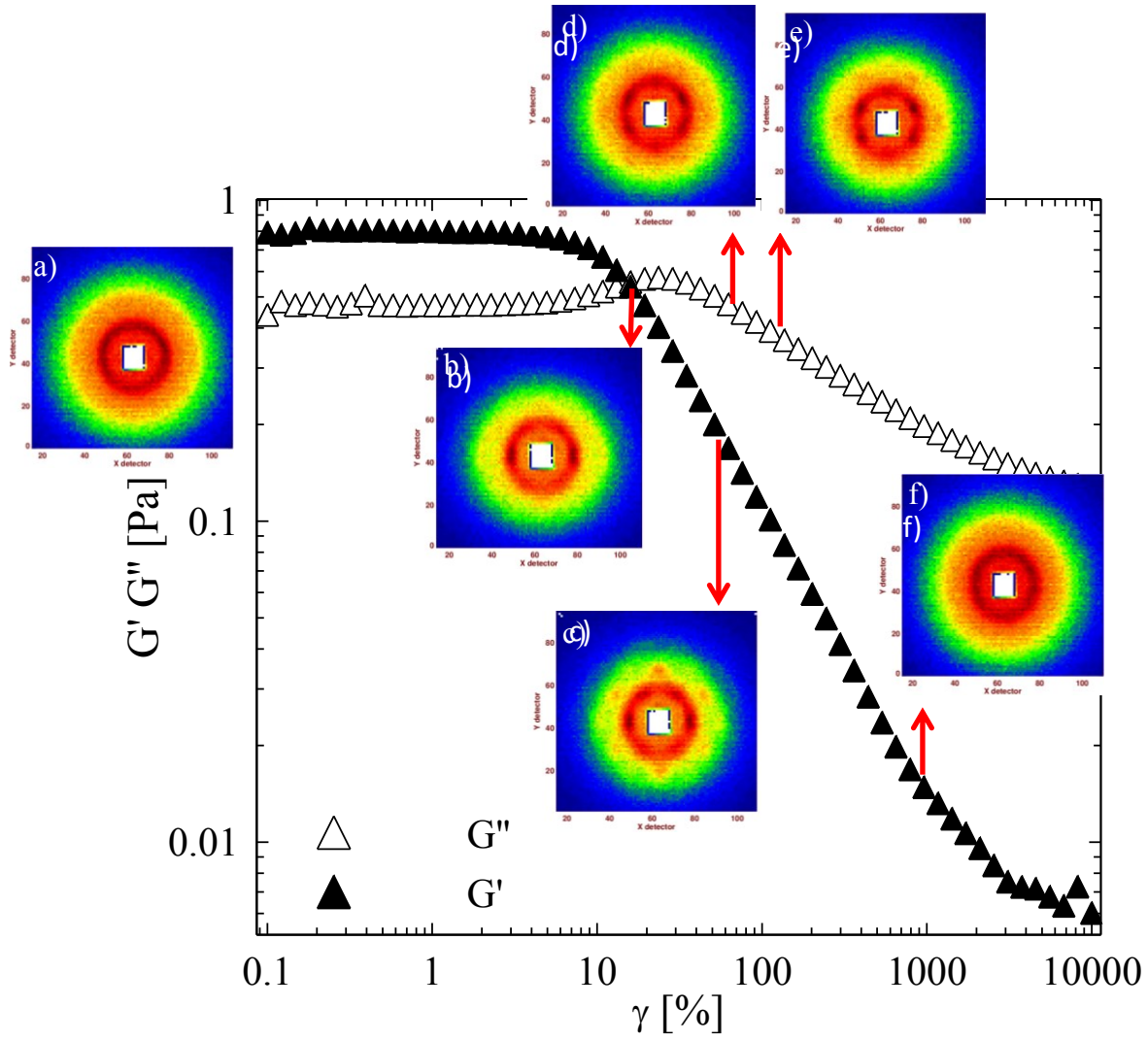

Figure 4.4.8 2D SANS plots for the hard dumbbell suspensions in the biphasic gap with ϕ_{eff} = 0.51 at rest (a) and under oscillatory shears with the fixed frequency, f = 1 Hz and various strains with amplitude: 19.4% and Pe_r = 0.16 (b), 50% and Pe_r = 0.42 (c), 60% and Pe_r = 0.50 (d), 116% and Pe_r = 0.97 (e) and 1000%, Pe_r = 8.38 (f).

When the strain amplitude is increased up to γ_{max} = 50%, a hexagonal plane with weak Bragg scattering spots is formed as shown in Figure 4.4.8c. The peak positions are determined by the radial integration at 0.0132 nm^{-1}, 0.0225 nm^{-1} and 0.0263 nm^{-1}, which are comparable to that for the plastic crystalline phase at γ_{max} = 50% and Pe_r = 0.52 (see Figure 4.4.1c). However, the Bragg spots are faint for the biphasic gap and the Debye-Scherrer ring is still visible. It is indicated that the hard dumbbells in the biphasic gap can form hexagonally orders under low strain, which coexist with the fluid of disorders. The two strong equatorial scattering spots along the velocity directions implies that the shear-induced velocity alignment formed at γ_{max} = 19.4% and Pe_r = 0.16 (see Figure 4.4.8b), which is maintained until γ_{max} = 50% in the formation of the twinned fcc structure.

Moreover, the formed hexagonal layers can be easily shear melted, and a four-fold hexagonal pattern as shown in Figure 4.4.8d is formed when the strain amplitude is increased up to 60% and Pe_r = 0.50. The four-fold pattern remains stable until γ_{max} = 116% and Pe_r = 0.97 as shown in Figure 4.4.8e, which shows a 30° shift with respect to the pattern induced by low strain (see Figure 4.4.8c). This indicates that the structure of the hard dumbbells is reorganized from the twinned fcc to the sliding layers. Based on the radial integration by sectors (see Chapter 7), the peak positions are found to be the same as that for the twinned fcc structure as shown in Figure 4.4.8c. This four-fold scattering differs from the six-fold pattern (Figure 4.4.1e) observed for the shear-induced sliding layers of the hard dumbbells in the plastic crystalline phase. Based on the discussion in section 0, the four-fold pattern in Figure 4.4.8e indicates the shear-induced hexagonal planes of hard dumbbells are expected to slip freely over another along straight lines at large strain (γ_{max} = 116% and Pe_r = 0.97). It is similar to the pattern observed for the hard spheres at $\phi_{eff} < 0.58$ in the freely slipping layers by Ackerson *et al.* (see section 3.4) [152, 196].

In conclusion, the shear-induced structural evolution of the hard dumbbells in the biphasic gap is similar to that for the plastic crystalline phase in two main points. First, the hard dumbbells form the comparable vorticity-alignment structure at low strain of γ_{max} = 19.4% and Pe_r = 0.16 before the formation of the twinned fcc structure. Second, the hard dumbbells in the biphasic gap undergo the same transition from the twinned fcc to the sliding layers with the increasing strain amplitudes. However, no perfect periodic structure is formed from the hard dumbbells in the biphasic gap due to the existence of a fluid phase. As for the sliding layers, the shear-induced hexagonal plane of the hard dumbbells at ϕ_{eff} = 0.51 move along straight lines which is different from the zig-zag path for the hard dumbbells in the plastic crystal at ϕ_{eff} = 0.60. This finding agrees with that observed for the sheared hard spheres at various volume fractions.[152]

4.4.4 Effect of L^*

The Monte Carlo simulations in Figure 1.2.2[52] (see Chapter 1) predict that the phase behaviour of the hard dumbbells is determined by L^* and ϕ. The width of the biphasic gap decreases with an increase in L^* ($L^* < 0.4$). This is verified by the crystallization experiment in section 4.2 using the dumbbell-shaped microgels with a higher L^*. Moreover, the time-

dependent rheological measurements in section 4.2 indicate that the crystallization of the hard dumbbell suspensions with $L^* = 0.30$ is slower than that of the dumbbells with the smaller $L^* = 0.24$. The fully crystallized hard dumbbells with $L^* \sim 0.24$ exhibits double yielding events in oscillatory shear field of 1 Hz (see section 4.3), which are related to the shear-induced structural evolution. The hard dumbbells with $L^* \sim 0.30$ exhibit only one yielding event under the same shear. However, this system shows two yielding events as shown in Figure 4.3.3 when the shear frequency is increased to 5 Hz or when the shear cycles are increased by five times at $f = 1$Hz (see section 4.3). To clarify the underlying structural evaluation for the hard dumbbell with $L^* \sim 0.30$, rheo-SANS measurements have been performed for the DPM_b microgels ($L^* \sim 0.30$ see Table 4.1.1) in the fully crystalline phase ($\phi_{eff} = 0.60$, 12.87 wt.-%, at 15°C) under various oscillatory shear strains with $f = 5$ Hz. The measured strain amplitudes as displayed in Table 7.3.1 are chosen to elucidate the dependence of G' and G'' on γ. Figure 4.4.9 displays a series of representative 2D experimental scattering patterns that are measured

a. at rest
b. $\gamma_{max} = 16\%$ and $Pe_r = 0.29$ (the end of the linear viscoelastic region),
c. $\gamma_{max} = 42.3\%$ and $Pe_r = 0.75$(the plateau for G'),
d. $\gamma_{max} = 51.5\%$ and $Pe_r = 0.89$ (the maximum of G''),
e. $\gamma_{max} = 92.6\%$ and $Pe_r = 1.62$
f. $\gamma_{max} = 300\%$ and $Pe_r = 5.37$
g. $\gamma_{max} = 1000\%$ and $Pe_r = 17.84$

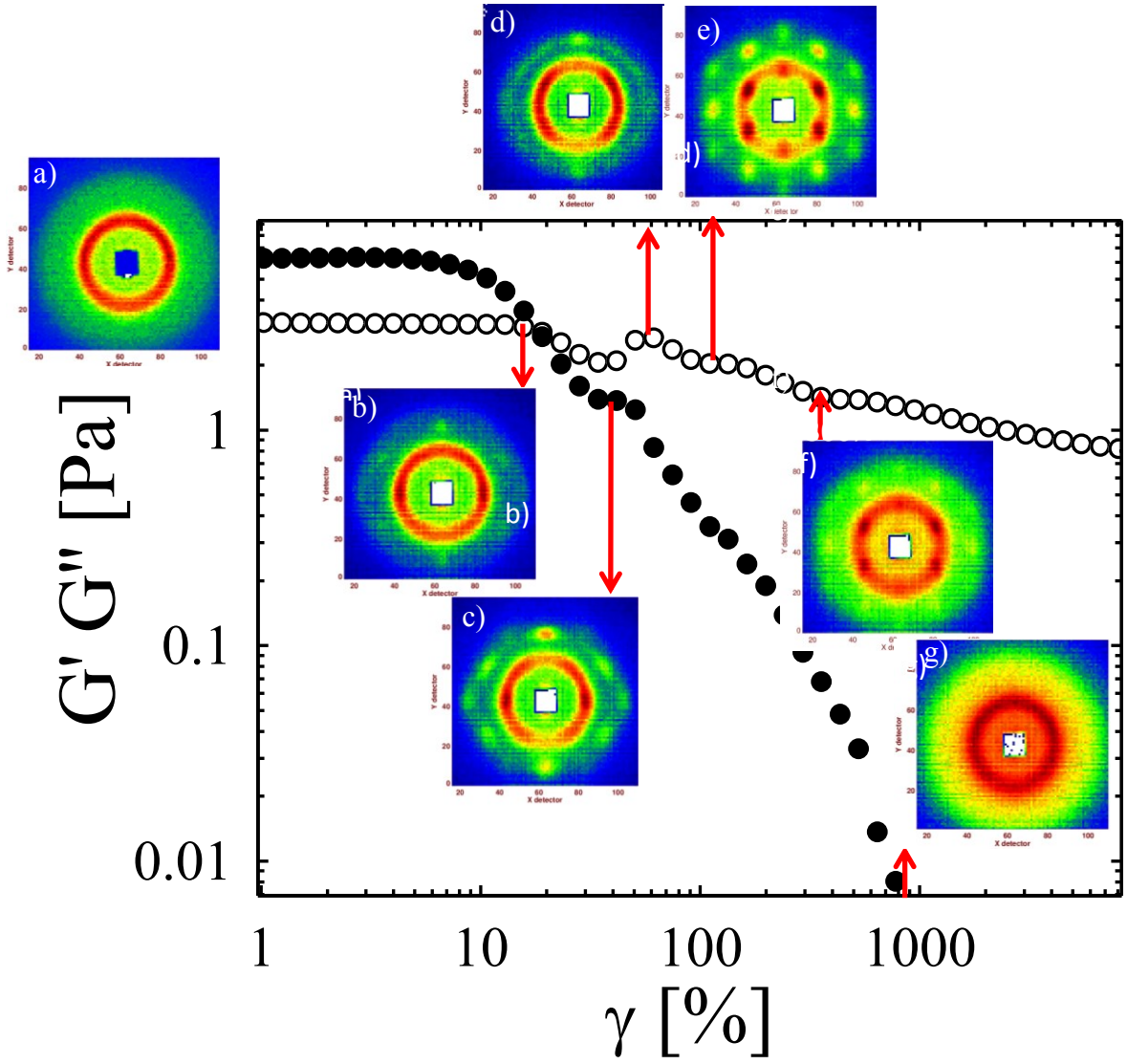

Figure 4.4.9 Yielding behaviour of the hard dumbbells with $L^* \sim 0.30$ (the DPM b microgels) in the fully crystalline phase ($\phi_{eff} = 0.60$) in the oscillatory shear of 5 Hz, and the corresponding 2D scattering patterns are measured by SANS. Along the dependence of *G'* and *G''* on various strains: (a) at rest (b) 16% ($Pe_r = 0.29$, the end of the linear regime), (c) 42.3% ($Pe_r = 0.75$ the plateau of G', the minimum for G''), (d) 51.5% ($Pe_r = 0.90$, the maximum for G''), (e) 92.6% ($Pe_r = 1.62$), (f) 300% ($Pe_r = 5.37$), (g) 1000% ($Pe_r = 17.84$).

The DPM_b microgels at $\phi_{eff} = 0.60$ showing Bragg reflections are determined to be in the plastic crystalline phase according to the experimental phase diagram in Figure 4.2.1. The corresponding 2D scattering pattern in Figure 4.4.9a indicates that the plastic crystals in equilibrium has a polycrystalline structure. The isotropic scattering pattern of the hard dumbbells with $L^* \sim 0.30$ does not show visible changes with increasing strains in the linear viscoelastic region until Pe_r is increased up to 0.18 ($\gamma_{max} = 10\%$). The scattering with the two equatorial scattering (see Figure 4.4.9b) indicating a vorticity alignment structure is observed

at γ_{max} = 24% and Pe_r = 0.42. When the shear strain is increased up to γ_{max} = 52% and Pe_r = 0.75, the first six-fold pattern emerges as shown in Figure 4.4.9c, which is indexed as the twinned fcc structure. The intensity variation on the same ring may be explained by the shear alignment of the hard dumbbells parallel to the vorticity direction with a certain preference. A scattering pattern without indications of preferred orientations or periodic structures are shown in Figure 4.4.9d at γ_{max} = 51.5% and Pe_r = 0.91, which is referred to the intermediate phase. A further increase in shear strain induces the formation of the second six-fold scattering pattern (see Figure 4.4.9e) with a 30° shift with respect to the first one. The six-fold scattering corresponds to the partially oriented sliding layers, where the hexagonal layers move along zig-zag paths due to the registration of neighbouring layers. Afterwards, a four-fold scattering pattern as shown in Figure 4.4.9e is observed, indicating the formation of the string-like structure before shear melting.

The radial integration based on different sectors by the LAMP-SANS software (see section 7.3.4) indicates that the Bragg peaks of the two hexagonal experimental patterns emerge at q positions (nm^{-1}) of 0.019, 0.033 and 0.038, which can be indexed as $1:\sqrt{3}:2$. The shear-induced periodic structure formed from the DPM_b suspensions ($L^* \sim 0.30$) is indexed to be identical with that from the DPM_a suspensions ($L^* \sim 0.24$). The lattice parameter d calculated based on the first peak position at 0.019 nm^{-1} is 330.5 ± 10 nm. It is worth noting that d from the periodic structure of the DPM_a microgels is 472 ± 5 nm, which is 1.4 times of d for the DPM_b suspensions (330.5 ± 10 nm). The variation between the lattice parameters is ascribed to different sizes of the two model systems. As listed in Table 4.1.1, the radius of the DPM_a microgels ($L^* \sim 0.24$) at 10 °C is 220.5 nm, which is ca. 1.5 times of the radius of the DPM_b microgels ($L^* \sim 0.30$, R_H = 147.9 nm).

In general, the plastic crystal of hard dumbbells with $L^* \sim 0.30$ has a polycrystalline structure in equilibrium, which develops into five different non-equilibrium structures with increasing shear strains. They are the vorticity alignment structure, the twinned fcc, the intermediate structure, the partially oriented sliding layers and the string structure. Therefore, the hard dumbbells with $L^* \sim 0.30$ in the plastic crystalline phase undergo the same shear-induced structural evolution under shear with f = 5 Hz as that of the hard dumbbells with $L^* \sim 0.24$ under oscillatory shear with f = 1 Hz (see Figure 4.4.1). However, the oscillatory shear denoted by Pe_r (the calculation of Pe_r is done according to Eq. (3.3.5)) that is required to induce the corresponding structure varies with L^*. Table 4.4.1 lists the shear strain that is

necessary to induce the non-equilibrium structures in both DPM_a suspensions with $L^* \sim 0.24$ and DPM_b suspensions with $L^* \sim 0.30$ in the plastic crystalline phase. The discussed non-equilibrium structures in Table 4.4.1 include the vorticity alignment structure, the twinned fcc structure, the intermediate structure and the partially oriented sliding layers. D^R used for the calculation of Pe_r is obtained through DLS and DDLS measurements (see Chapter 3).

Table 4.4.1 Comparison of Pe_r that is need for the formation of vorticity alignment structure, the twinned fcc, the intermediate structure and the partially oriented sliding layers in the hard dumbbells with $L^* \sim 0.24$ and $L^* \sim 0.30$. D^R is obtained from DLS and DDLS measurements (the principles are described in section 3.2).

sample	D^R [s^{-1}]	Pe_r (aligned)	Pe_r (twinned fcc)	Pe_r (intermediate state)	Pe_r (sliding layer)
DPM_a (L^* : 0.24)	6.05	0.24	0.52	0.62	1.20
DPM_b (L^* : 0.30)	17.70	0.29	0.75	0.89	1.62

For hard dumbbells with $L^* \sim 0.24$ in the fully crystalline phase, the twinned fcc crystal can be formed at $Pe_r = 0.52$, while $Pe_r = 0.75$ is necessary for the hard dumbbells with $L^* \sim 0.30$. The partially oriented sliding layers are induced by shear at $Pe_r = 1.20$ in the hard dumbbell suspension with $L^* \sim 0.24$ and at $Pe_r = 1.62$ for the hard dumbbell suspension with $L^* \sim 0.30$. In conclusion, the fully crystallized hard dumbbells with $L^* = 0.30$ undergo the same structural evolution as that of $L^* = 0.24$ in the plastic crystalline phase, but need oscillation higher and longer shear (denoted by Pe_r) than the latter. It can be explained by the argument that the hard dumbbells with $L^* \sim 0.30$ is closer to the glass state than that with $L^* \sim 0.24$ for the same volume fraction. Thus, longer and stronger oscillations are required for the structural evolution due to the slowdown of the dynamics in the vicinity of the glass transition. This finding accords with that of the rheological study in section 4.2.2.2 and 4.3.2.

5. Thermosensitive hollow capsules

In Chapter 4 the dumbbell-shaped microgels were applied as the model system for the investigation of the crystallization and phase behaviour of hard dumbbells. In this chapter, the dumbbell-shaped microgels are used as templates to prepare thermosensitive hollow Janus dumbbells. Additionally, spherical core-shell microgels are applied as templates for the preparation of their corresponding hollow capsules. The work of this part aims at the synthesis and characterization of thermosensitive hollow capsules of different shapes.

Thermosensitive hollow capsules[197-198] have attracted a lot of interest in recent years. These systems have been widely used as carriers in catalysis[199] and for the controlled delivery of encapsulated materials.[89, 91] Up to now, different methods have been developed to fabricate the thermosensitive hollow capsules mainly based on poly (N-isopropylacrylamide) (PNIPA) and its copolymers.[200-201] The layer by layer (LbL) approach invented by Decher *et al.* is one of the most popular methods to fabricate hollow capsules.[202-203] Möhwald and his co-workers further extended this method for the development of thermosensitive hollow capsule systems based on copolymers containing a PNIPA block.[204] However, the thermosensitivity of the resulting hollow capsules is only partially reversible. Recently, the template strategy based on core-shell precursors has been applied to fabricate the porous structure and hollow spheres.[198, 200, 205-206] A series of spherical hollow capsules have been prepared based on this approach, which are mainly applied as carriers in drug delivery with controlled release.[89, 197, 207] For example, Wu *et al.* have demonstrated that the release rate of the loaded materials in the thermosensitive PNIPA semi-hollow spheres is related with the environmental temperature and the shell thickness.[207]

However, to date only rare examples of anisotropic hollow capsules[208] have been reported despite the fact that the anisotropic shape might be useful for the applications as carrier systems. For example, non-spherical synthetic carriers are reported to possess distinct advantages in the applications for targeted drug delivery.[92, 209-210] Thus, we present in this work the first report on the synthesis and analysis of the thermosensitive dumbbell-shaped hollow capsules.

In this chapter, monolayer and bilayer thermosensitive hollow spheres have been prepared based on the template strategy by dissolving the polystyrene cores in THF. Subsequently, we extend the template strategy to synthesize hollow Janus dumbbells using the respective

templates. A comprehensive characterization including transmission electron microscopy (TEM), cryo-TEM and dynamic light scattering (DLS), has been performed. Special emphasis is put on the morphology and thermosensitivity of hollow capsules thus obtained.

5.1 Hollow spherical capsules

5.1.1 Thermosensitive hollow spheres

Two different thermosensitive hollow spheres based on the PNIPA network crosslinked by N,N′-methylene-bis (acrylamide) (BIS) have been synthesized via the template strategy as shown in Figure 5.1.1. The route described in the upper part results in the monolayer hollow capsules, while the one in the bottom part leads to the bilayer hollow capsules. To prepare the monolayer hollow capsules, the crosslinked PNIPA shell is attached onto the surface of polystyrene (PS) seeds followed with the removal of the PS cores via the THF treatment.

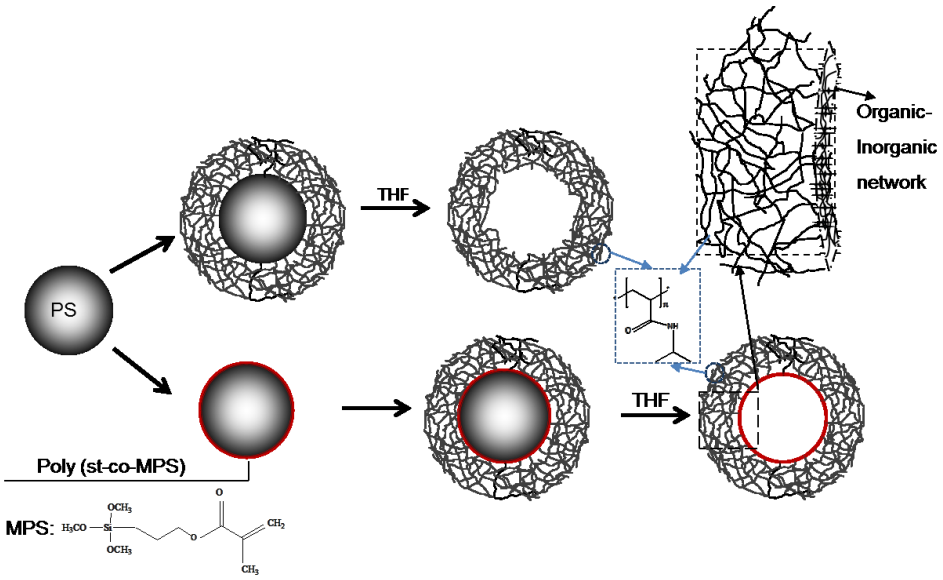

Figure 5.1.1 Schematic figure of hollow capsules produced by the template-based approach, the upper part represents the procedure for the monolayer hollow spheres, while the routine shown in the lower part leads to the bilayer hollow capsules.

In case of the bilayer hollow capsules, PS seeds are first coated with a copolymer layer of styrene and 3-(trimethoxysilyl) propyl methacrylate (MPS).[167] A hybrid copolymer structure with an organic-inorganic network is expected to be formed onto the surface of the PS spheres from the hydrolysis and condensation of the trimethoxysilyl groups of MPS monomers.[167] Then a cross-linked PNIPA shell is attached onto the surface of the modified PS seeds.

Finally, the THF treatment is applied to remove the PS cores, which results in the bilayer hollow spheres.

5.1.2 Monolayer hollow spheres

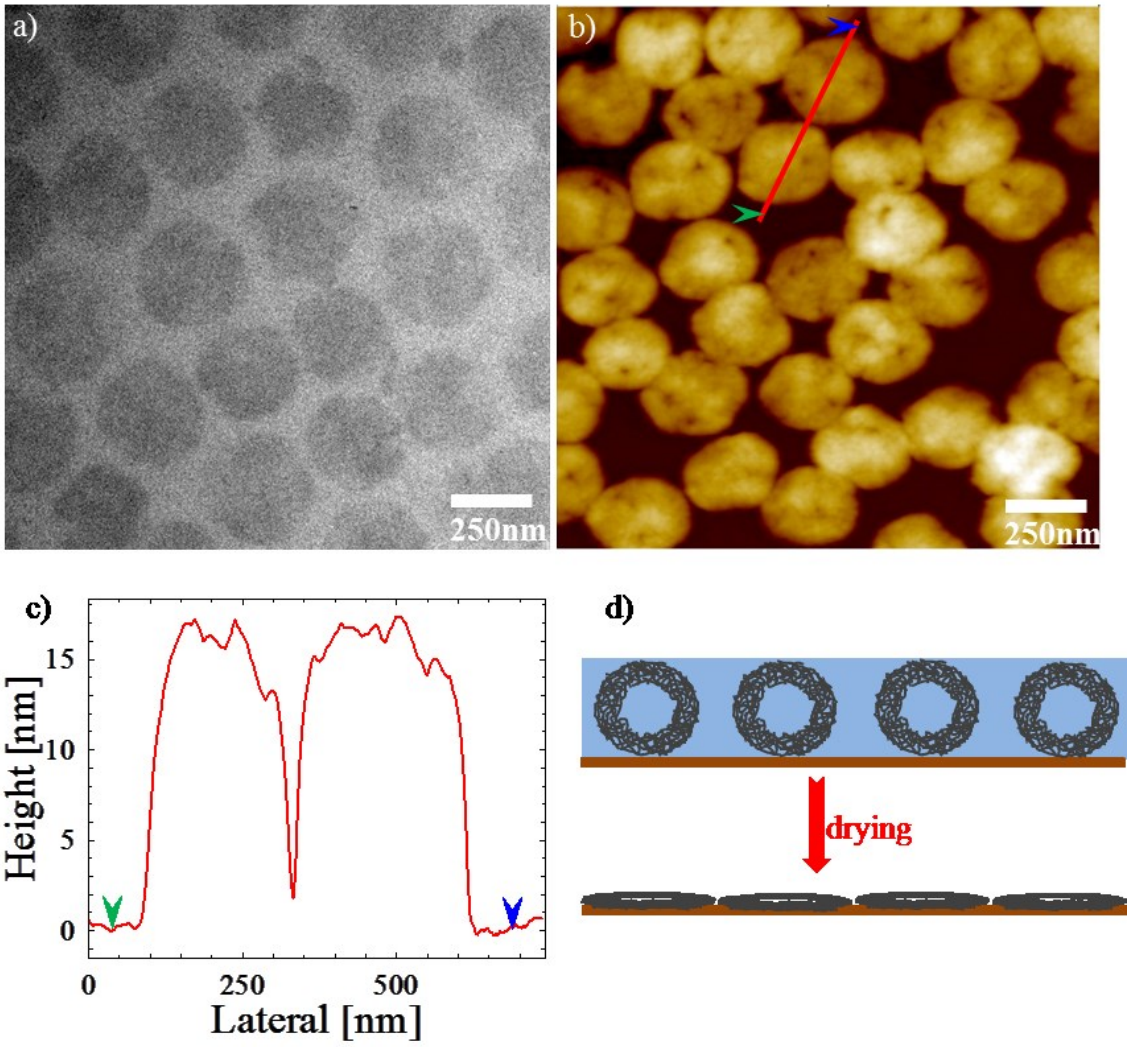

Figure 5.1.2 (a) TEM micrograph and (b) height image from SFM characterization of the monolayer hollow spheres in dry state, (c) shows the cross-section along the solid red line marked in (b), the two arrows indicate the starting and ending points along the solid line. SFM samples are prepared using Mica as substrates via spin coating at a speed of 70 rpm. Schematic figure (d) is to illustrate the deformation of hollow capsules in the drying process for the sample preparation.

The TEM micrograph in Figure 5.1.2 demonstrates that the spherical morphology of the monolayer hollow capsules is maintained after the removal of PS cores. The height image in Figure 5.1.2b shows the comparable surface morphology as that observed in the TEM image. The cross section in Figure 5.1.2c along the solid line marked in Figure 5.1.2b reveals a 'pancake' surface morphology of the capsules with a diameter of ca. 300 nm and a height of

ca. 7 nm. The hollow structure is ascribed to the formation of the 'pancake' surface morphology, which makes the capsules collapsed onto the substrate during the sample preparation. The deformation process of the monolayer hollow capsules during the sample preparation is shown schematically in Figure 5.1.1d. With the evaporation of water during the sample preparation, the monolayer hollow capsules are collapsed gradually onto the substrate and finally get deformed into the 'pancake' morphology.

To investigate the structure of the hollow capsules *in situ*, cryo-TEM measurements have been performed by vitrifying the suspension of the particles. It is worth noting that the hollow capsules are not visible in the cryo-TEM image without staining due to the low contrast of the PNIPA shell against water in the swollen state. Sodium phosphotungstate[211] is therefore used to stain the particles to enhance the contrast between the sample and the medium. Figure 5.1.3a displays that a well-defined hollow structure can be observed for the monolayer hollow capsules dispersed in 1.7 mM sodium phosphotungstate. The hollow capsules are monodisperse and no aggregation is observed. Additionally, no free residual polymer can be found in the medium, indicating the high effectiveness of the removal of PS cores by THF.

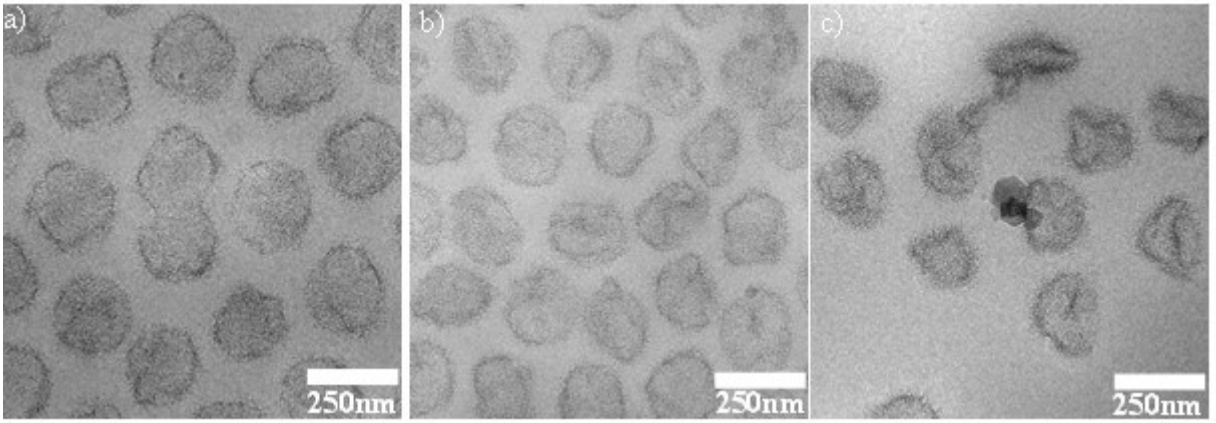

Figure 5.1.3 Cryo-TEM images of hollow spherical capsules stained by different sodium phosphotungstate concentrations (a) 1.7 mM, (b) 3.4 mM, and (c) 6.8 mM, respectively. The aim of sodium phosphotungstate is to enhance the contrast between sample and medium.

To clarify the effect of sodium phosphotungstate on the morphology of hollow capsules, a series of salt concentrations are used to stain hollow spheres as shown in Figure 5.1.3. Partially deformation can be found for some of the hollow capsules stained by 3.4 mM sodium phosphotungstate (see Figure 5.1.3b), while the monolayer hollow capsules are

completely deformed when they are dispersed in 6.8 mM sodium phosphotungstate as shown in Figure 5.1.3c.

DLS measurements have been performed to investigate the dimensional information of the stained monolayer hollow capsules which can be compared with the results of cryo-TEM measurements. The results are summarized in Table 5.1.1. More than 200 particles are counted from cryo-TEM images for each salt concentration to obtain the average radius. As shown in Table 5.1.1, the particle size of the monolayer hollow capsules determined from the DLS measurements is comparable to that from the cryo-TEM characterization within experimental error. Moreover, it is found that the staining process with sodium phosphotungastate at concentrations up to 1.7 mM has nearly no effect on the size of the hollow capsules. When the stained salt concentration is above 1.7 mM, $R_{H,}$ however, decreases markedly with the increase of the stained salt concentration. This finding also accords with the results from the cryo-TEM measurements.

Table 5.1.1 Dimensional information of the hollow capsules at 20 °C with various sodium phosphotungastate salt concentrations, determined by DLS measurements and cryo-TEM images (estimated radius).

Stained Salt [mM]	Viscosity [pa*s][1]	D^T [10^{-12} m^2*s^{-1}] [2]	R_H [nm] (DLS)	R [nm] (cryo-TEM)
0	1.01 E-3	1.40	153	---
1.7	0.99 E-3	1.36	159	146
3.4	1.00 E-3	1.60	135	135
6.8	1.01 E-3	1.89	112	119

[1] Measured by Antoparr Rheometer 301 with DG 26.7/T2007AL geometry at 20 °C.

[2] D^T is the translational diffusion resulted from the DLS measurements at 20 °C.

Thus, the cryo-TEM image of the monolayer hollow capsules stained by 1.7 mM sodium phosphotungstate represents the morphology of the monolayer hollow capsules in solution. As displayed in Figure 5.1.3a, the monolayer hollow capsules maintain the spherical morphology with a hollow structure after the removal of PS cores. The slight irregularity of morphology observed in Figure 5.1.3a maybe due to the fluctuation of the PNIPA shell.[212]

To investigate the thermosensitivity of the monolayer hollow spherical capsules, DLS measurements have been performed at different temperatures. The temperature dependence

of hydrodynamic radius of the microgels before and after the removal of PS is summarized in Figure 5.1.4.

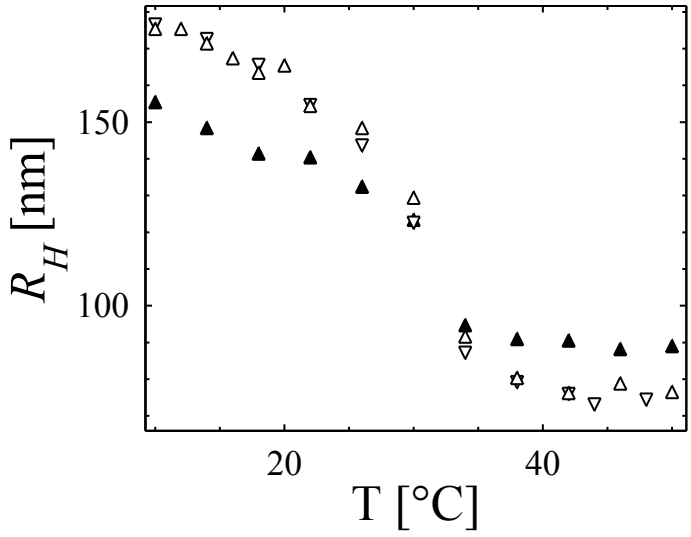

Figure 5.1.4 The dependence of R_H on temperature for the spherical microgels with PS cores (filled triangles) and the monolayer hollow spherical capsules after the removal of PS cores. Upwards triangles denote the dependence of R_H on increasing T, while downwards triangles indicate that on decreasing T.

The monolayer hollow capsules after the removal of PS show a thermosensitive property with LCST at ca. 32 °C, which is similar to that of corresponding spherical microgels before the removal of PS cores. Moreover, the swelling and de-swelling behaviour of the monolayer hollow capsules is reversible with increasing and decreasing temperatures. It is interesting to note that R_H of the hollow capsules are larger than that of the spherical microgels at T < LCST, but much smaller for T > LCST. This demonstrates that hollow capsules can swell and shrink to a larger extend than the spherical core-shell microgels before the removal of PS cores. Combined with the thermosensitivity, the hollow structure may be advantageous for applications as e.g. carriers for delivery of drugs with controlled release.[89, 213]

5.1.3 Bilayer hollow spheres

For the preparation of the bilayer hollow spheres, core-shell microgels with PS seeds coated with a thin layer of poly (styrene-co-MPS) has been prepared first. Subsequently, the core is removed as schematically described in Figure 5.1.1. E. Bourgeat-Lami *et al.* have synthesized such poly (styrene-co-MPS) layers with the organic-inorganic network to prepare Si-OH functionalized latex.[167] Because of the hydrolytically cross-linked methoxysilyl group of the MPS monomers, the poly (styrene-co-MPS) layer is expected to be insoluble in THF. Section

5.1.2 has shown that the cross-linked PNIPA is stable in THF and the dissolved PS can pass through its network. In this section, THF is also chosen to prepare the bilayer hollow capsules. TEM measurements have been carried out to investigate the morphology of the purified bilayer hollow capsules as shown in Figure 5.1.5.

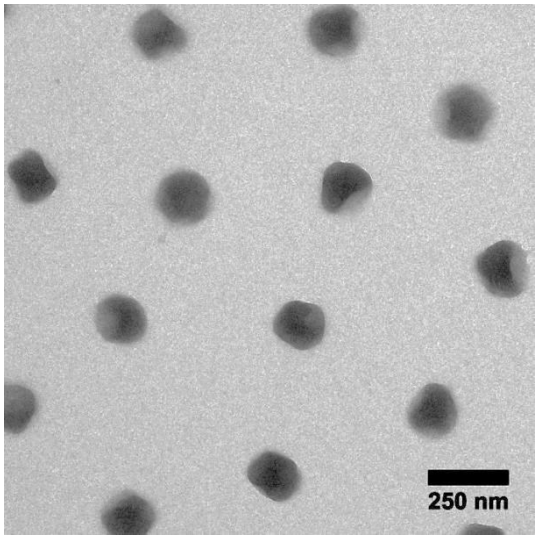

Figure 5.1.5 TEM micrograph of the purified bilayer hollow spherical capsules. The sample is prepared on the copper grids.

The TEM image in Figure 5.1.5 reveals that the bilayer hollow capsules in the dry state are partially deformed. The morphology for the bilayer capsules is very different from the 'pancake' morphology of the monolayer hollow capsules shown in Figure 5.1.2. This difference indicates a higher mechanical stability of the poly (styrene-co-MPS) hollow spheres as compared to the pure PNIPA-shells. The observed deformation of the particles, however, indicates that the poly (styrene-co-MPS) layer is not hard enough to maintain the perfect spherical morphology of the bilayer hollow capsules in a dry state. Based on the DLS measurements, the radius of PS seeds is 63.7 nm and that of the PS-MPS seeds is 73.6 nm. The thickness of the copolymer layer is determined to be ca. 10 nm. This thin copolymer layer can be thus partially deformed (see Figure 5.1.5) by the collapsed PNIPA shell during the drying process.

Cryo-TEM measurements have been performed to investigate the morphology of the bilayer hollow capsules in solution as displayed in Figure 5.1.6. Based on the cryo-TEM image in Figure 5.1.6, the bilayer spherical capsules are observed to have a well-defined core-shell structure. The cross-linked PNIPA shell is well maintained with its spherical morphology. The core inside, which can be seen clearly in the enlarged inset in Figure 5.1.6, is a hollow sphere

but with some deformation. As discussed above, it corresponds to the poly (styrene-co-MPS) layer with a thickness of ca. 10 nm, and thus is sensitive to the external force. The observed deformations are probably due to the swelling of the PNIPA shell at room temperature. As described in Chapter 7, the PNIPA shell has been fabricated at 80 °C by the seeded polymerization[29]. We assume that the PNIPA shell at that temperature is in the equilibrium state, where the hollow core is expected to show a regular spherical morphology without deformations. The cryo-TEM measurements at high temperature, however, have not been successfully performed yet due to the limitation of the temperature chamber.

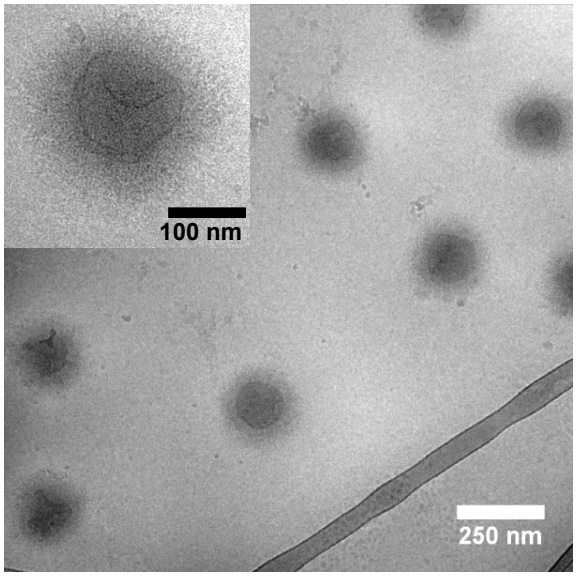

Figure 5.1.6 Cryo-TEM micrograph of the bilayer hollow capsules at room temperature (T: ca. 25 °C) in water, the inset shows one single particle of higher magnification. The image proves that the bilayer hollow capsule have a core-shell structure with the hollow sphere as core.

The DLS measurements have been performed to investigate the size of the bilayer hollow capsules at different temperatures as shown in Figure 5.1.7. It demonstrates that the removal of PS cores casts nearly no effect on the thermosensitivity of the bilayer hollow capsules. The hydrodynamic radius of the bilayer hollow capsules is comparable to that of their spherical microgels with PS-MPS cores. Moreover, the morphology of the bilayer hollow capsules is well-kept owing to the much harder copolymer layer. The copolymer hollow spheres have the silanol groups on their surfaces that can be easily modified by reactions with various silane reagents or grafting of other metal oxides (e.g. TiOx[214]).

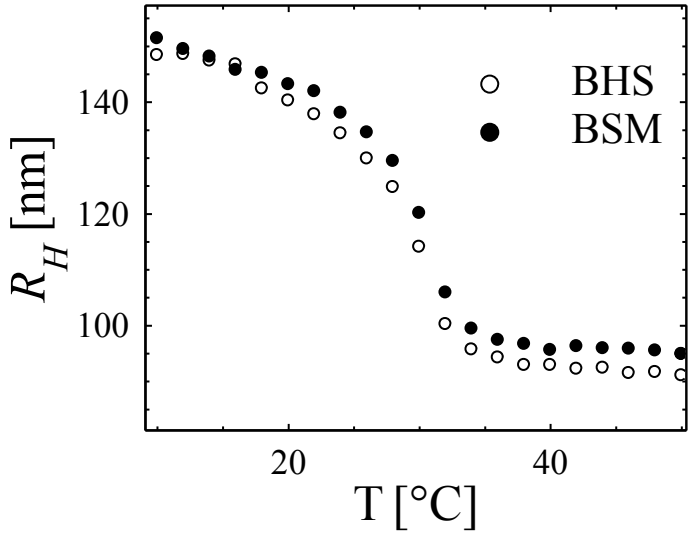

Figure 5.1.7 Temperature dependence of the bilayer hollow capsules (BHS) and the corresponding spherical microgels (BSM), the measured temperature ranges from 10 °C to 50 °C.

In conclusion, the selective removal of PS cores via THF can be used to prepare both monolayer and bilayer hollow spherical capsules. DLS measurements indicate that the thermosensitivity of the hollow capsules are well maintained with the reversible swelling-shrinking behaviour. The monolayer hollow capsules can swell and shrink over a larger volume after the removal of PS cores. However, the bilayer hollow capsules show the same dependence of the radius on temperature as that of the microgels with PS cores. Due to the well-defined morphology, the monolayer and bilayer hollow capsules can probably serve as model system to investigate the phase behaviour of capsule systems. Moreover, the thin copolymer hollow sphere of the bilayer hollow spheres with silanol groups on their surfaces may be used for possible applications, for example as nano-reactors.[214]

5.2 Hollow Janus dumbbells

5.2.1 Thermosensitive hollow Janus dumbbells

The template strategy used for the preparation of hollow spheres is applied in this section to prepare thermosensitive hollow Janus dumbbells (see Figure 5.2.1). Here the dumbbell-shaped microgels are used as the template system, which are prepared as schematically shown in Figure 4.1.1. It is demonstrated that the PS cores are selectively dissolved in THF. The work in section 5.1 indicates that the copolymer layer coated on to the surface of one sphere seeds is stable in THF due to the organic-inorganic network. Moreover, the organic-inorganic

network allows the dissolved polystyrene to diffuse through. The PS of the dumbbell-shaped cores can thus be removed by THF, resulting in well-defined and monodisperse hollow Janus dumbbells with thermosensitivity. The detailed recipe for the preparation of the hollow Janus dumbbells is described in the experimental part in Chapter 7.

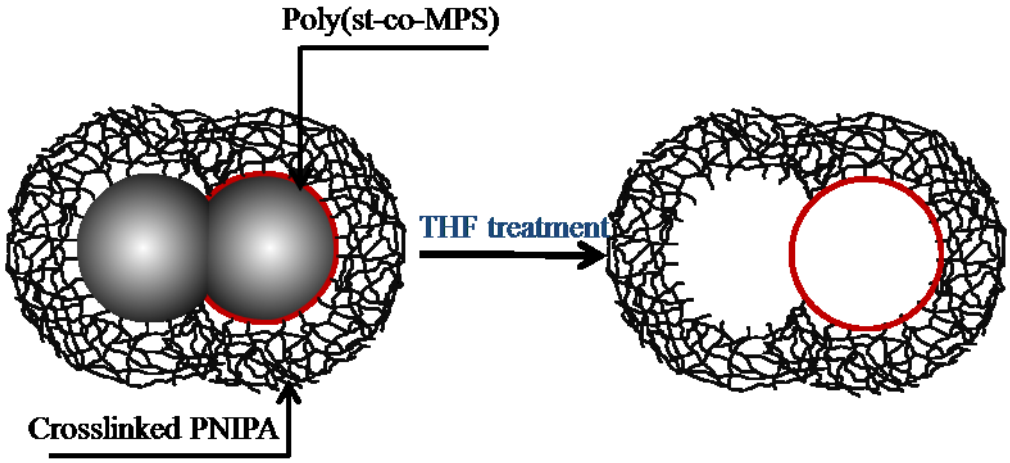

Figure 5.2.1 Preparation procedures for the thermosensitive hollow Janus dumbbells through THF treatment. The template is the dumbbell-shaped microgel system with a cross-linked PNIPA shell attached on the dumbbell-shaped core, which is prepared as schematically shown in Figure 4.1.1. The red circle displays the poly(st-co-MPS) copolymer layer that is fabricated to facilitate the growth of the second sphere for the dumbbell-shaped core.

5.2.2 Dissolution of Janus dumbbell-shaped core

The dumbbell-shaped microgels consisting of a dumbbell-shaped PS core and a cross-linked PNIPA shell are used as the template to prepare hollow Janus dumbbells. The dumbbell-shaped core particles, as displayed in Chapter 4, are synthesized by the phase separation method and have a Janus-type structure.[55] TEM images in Figure 4.1.2 display that they are homogeneous by means of the overall size and their aspect ratio. Moreover, the fused spheres in one dumbbell-shaped core particle are nearly identical in size. The cryo-TEM image in Figure 4.1.3 demonstrates that the dumbbell-shaped core particles consist of two partially fused spheres with different structures: one side is homogeneously spherical while the other side reveals a core-shell structure. The shell of the core-shell sphere corresponds to the poly (styrene-co-MPS) layer which is fabricated in the synthesis routine as schematically shown in Figure 4.1.1. In the following, the dissolution process of the Janus-type dumbbell cores using THF will be discussed in detail since this process is a crucial step for the generation of hollow PNIPA Janus microgels.

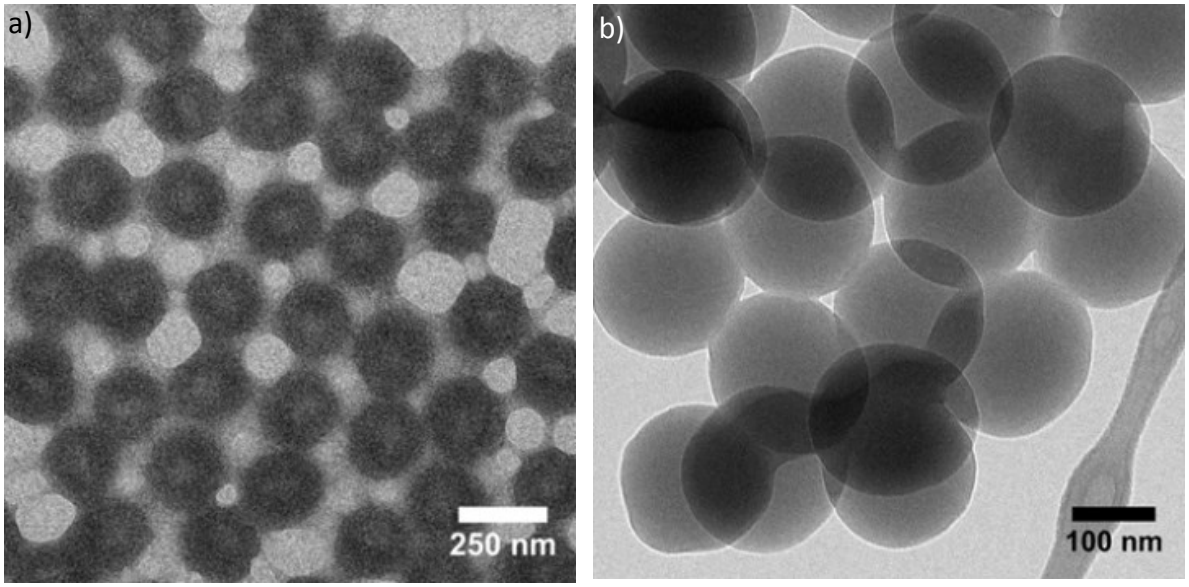

Figure 5.2.2 TEM images of the dumbbell-shaped core particles after (a) the first cycle of cleaning and (b) the final cycle of cleaning.

We first treat the dumbbell-shaped core particles with THF. This leads to the formation of hollow spheres as shown by TEM analysis (see Figure 5.2.2). These spheres indicate that the pure PS sphere can be easily dissolved in THF while the copolymer hybrid shell remains its spherical morphology. The dissolution of PS is not complete after the first cycle cleaning with THF, which can be deduced by PS leftover around the spherical particles as observed in Figure 5.2.2a. By monitoring the cleaning process after each cycle it is found that in total thirty runs of centrifugation, decantation and re-dispersion are necessary to achieve complete removal of the core material. No traceable amounts of polymer have been found around the spherical particles anymore after this procedure (see Figure 5.2.2b). The cleaning process finally leads to the formation of spherical particles showing a rather low contrast in TEM (Figure 5.2.2b). These spherical particles correspond to the thin hybrid shells of poly (styrene-co-MPS) copolymer, which are fabricated for the synthesis of dumbbell-shaped cores (see Figure 4.1.1).

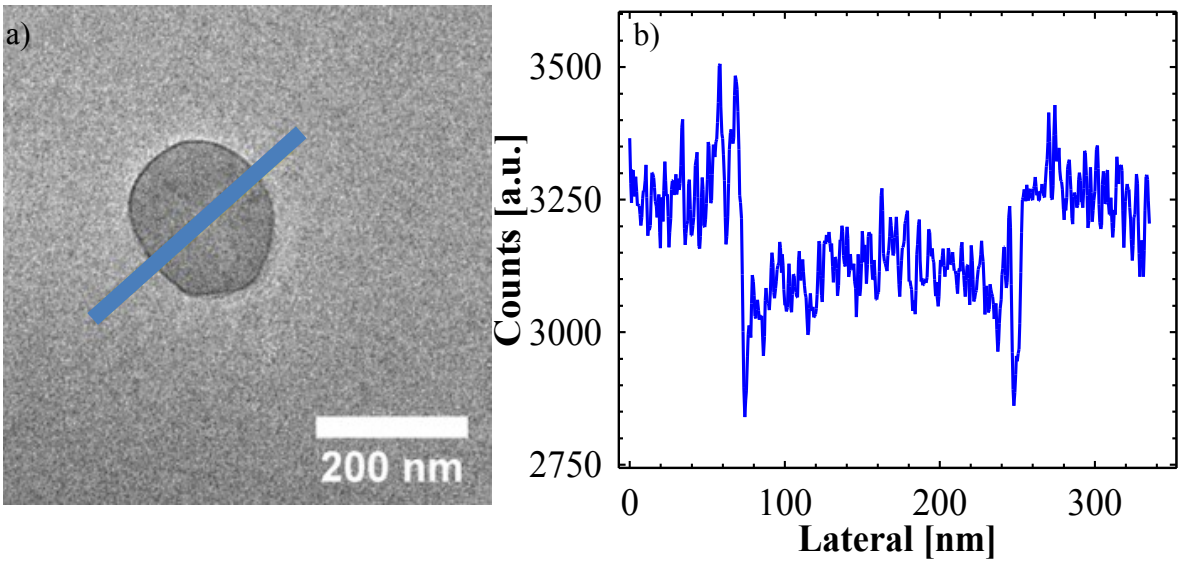

Figure 5.2.3 (a) Cryo-TEM micrograph of dumbbell-shaped core after the removal of PS via THF and the solid line marks the radial direction, and (b) corresponding gray profile along radial direction.

To address this point in further detail, the particles are vitrified after the removal of the PS core directly in THF for the cryo-TEM measurements. The obtained image and the corresponding gray profile are summarized in Figure 5.2.3. A cryo-TEM micrograph of a particle vitrified in THF (Figure 5.2.3a) indicates a spherical particle with a hollow structure after the removal of PS via THF from the dumbbell-shaped core. The hybrid shell of the resulting hollow sphere exhibits only ca. 10 nm thickness and is difficult to discern from the background. Nevertheless, the grey scale profile along the center of the particle (see Figure 5.2.3b) clearly exhibits a hollow structure of the copolymer sphere. We therefore conclude that the poly (styrene-co-MPS) copolymer layer cannot be dissolved by THF whereas pure PS from the inner part is able to diffuse through this layer, resulting in the hollow spheres. This is in accord with the findings already reported in section 5.1. The insolubility of the hybrid shell is due to the hydrolytically cross-linked methoxy silyl groups of MPS copolymer. The organic-inorganic network of the hybrid shell has already been reported in details by E. Bourgeat-Lami *et al.*[167]

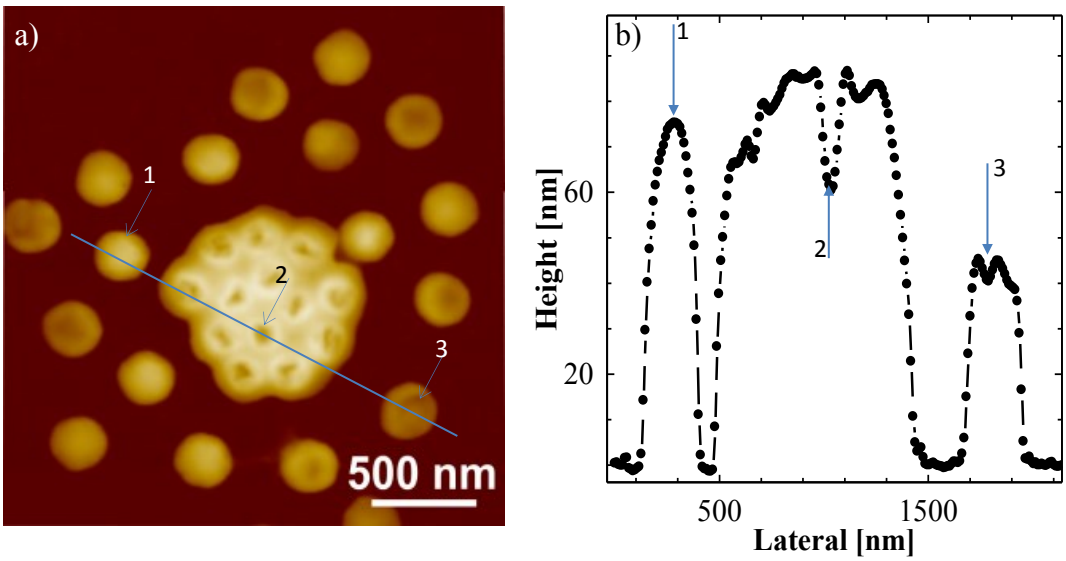

Figure 5.2.4 (a) SFM height image of the dumbbell-shaped core after the removal of PS via THF and (b) the corresponding cross section along the solid line in (a), showing different collapse state of isolated (marked by 1 and 3) and agglomerated particle (marked by 2) in the dried state.

Further details can be deduced from SFM measurements. Figure 5.2.4a displays the SFM height image of a selected area demonstrating two different morphologies of particles on the surface. The isolated particles have mostly pancake like morphology. The one exemplified in Figure 5.2.4a (marked by 1) has the height of ca. 70 nm and diameter of ca. 280 nm. The upper limit of the tip broadening by the conical tip can be estimated as $tan(\alpha)h$, where h is the height of the object and α is the cone opening, which is 50 nm for the tips we used. Substantial flattening of isolated particles on the surface indicates their hollow nature. Particles in clusters exhibit typically donut or red blood cell topography (marked by 2 in Figure 5.2.4a). Some isolated particles are slightly deformed, as the one exemplified in Figure 5.2.4a (marked by 3). SFM measurement demonstrates that single, hollow particles lying dry on the substrate collapse resulting in the pancake surface morphology because that the thin shell of hollow spheres cannot support their spherical morphology. In a more dense packing, a supporting of the wall by neighbouring hollow particles results in donut or red blood cell topography.

5.2.3 Hollow Janus dumbbells

The effective cleaning procedure via THF now facilitates the preparation of thermosensitive hollow Janus dumbbells. The PNIPA networks crosslinked by BIS is reported to be stable in

THF.[200] Thus, thermosensitive hollow Janus dumbbells are prepared using dumbbell-shaped microgels as a template using THF to remove PS, as shown in Figure 5.2.1.

Figure 5.2.5 displays the surface morphology of the thermosensitive hollow Janus dumbbells in the dried state as investigated by SFM (a) and TEM (b). The SFM height image reveals dumbbell-shaped particles with one sphere obviously having a larger height (brighter color) than the other. This is due to the hollow copolymer sphere from the dumbbell-shaped core after the removal of PS via THF as described above. This finding is verified by TEM micrographs shown in Figure 5.2.5b. The dumbbell-shaped particles are clearly visible having one side with a high contrast due to the copolymer layer and one rather light colored part that consists only of the collapsed PNIPA shell.

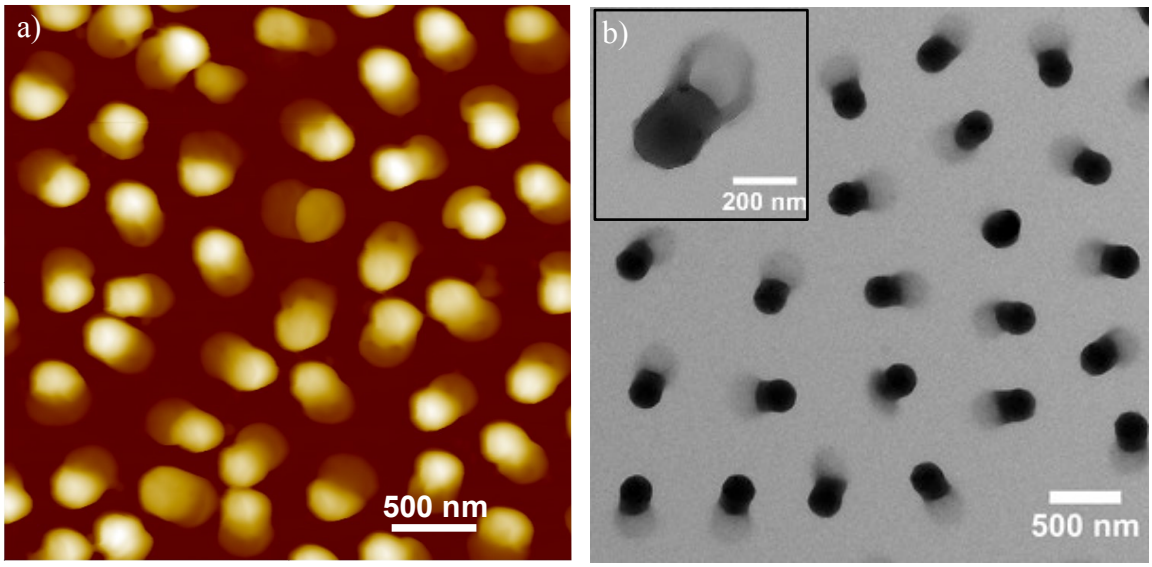

Figure 5.2.5 (a) Height image from SFM measurements and TEM (b) images of the thermosensitive hollow Janus dumbbells resulted from the removal of PS from the dumbbell-shaped microgels. The inset in (b) shows one particle of higher magnification measured by TEM. Both images clearly indicate the Janus structure of hollow dumbbells.

Cryo-TEM measurements of the dumbbell-shaped, hollow Janus capsules are shown in Figure 5.2.6 demonstrating that the dumbbell-shaped morphology of the PNIPA network is well maintained after the removal of PS. This shows that PS can be effectively removed from the dumbbell-shaped core particles through the PNIPA network without destroying the network. This is in full accord with the TEM- and SFM-measurements displayed in Figure 5.2.5.

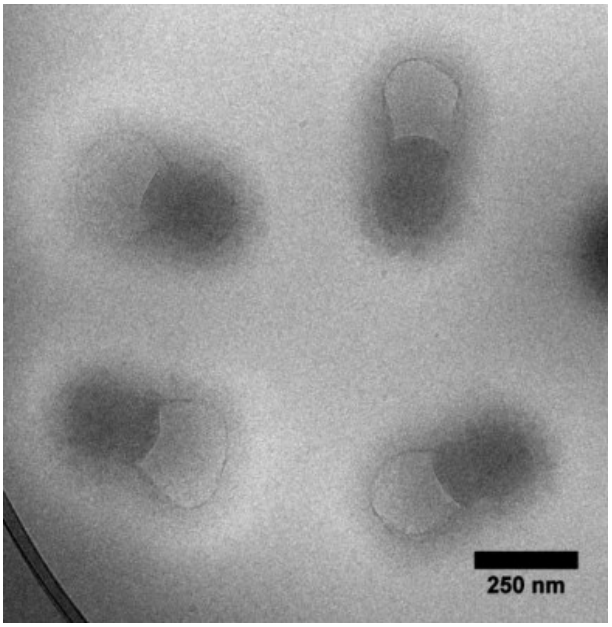

Figure 5.2.6 Cryo-TEM image of the thermosensitive hollow Janus dumbbell-shaped capsules and the sample preparation was done at 20 °C. The image proves the Janus character of the particles showing a hollow side of the microgel (light gray) and partially hollow part (dark gray) composed of PNIPA shell and poly (styrene-co-MPS) copolymer layer.

DLS and DDLS can now be used to investigate the change of the size of the thermosensitive hollow Janus dumbbells with temperature. Rotational and translational diffusion coefficients of the hollow PNIPA microgels were measured by DDLS in a temperature regime from 10 °C to 25 °C. In order to screen the electrostatic interactions from possible residual charges from the synthesis, the Janus dumbbells were dispersed in 50 mM KCl solution. As shown in Figure 5.2.7a, the autocorrelation function includes two discrete exponential decays. The slow relaxation mode characterizes the translational motion ($\Gamma_{slow} = D^T q^2$) and the fast mode is related to the rotational motion ($\Gamma_{fast} = D^T q^2 + 6D^R$).[88] A very weak third mode can be observed at some low angles which may be due to the fluctuation of the PNIPA network[212].

Figure 5.2.7b displays the corresponding relaxation process plotted as a function of the square of the scattering vector. The slow mode measured from DLS is comparable to that from DDLS within experimental error. Based on the slow mode, the translational diffusion coefficient D^T can be calculated. Our work on the dumbbell-shaped microgels in Chapter 4 showed that the resulting rotational diffusion of the dumbbell-shaped microgels has a rather large error due to the weak signal of the fast mode. However, DDLS can accurately measure D^T and D^R of dumbbell-shaped PS cores due to the reliable signal. Thus, the radius of one

sphere and center to center distance L can be calculated with accuracy. Combined with the fixed length L, D^T at various temperatures can provide reliable calculation for dimensional information. The resulting D^T of the hollow Janus dumbbells at temperatures of 10 °C, 20 °C and 25 °C and their comparison with the dumbbell-shaped microgels is listed in Table 5.2.1.

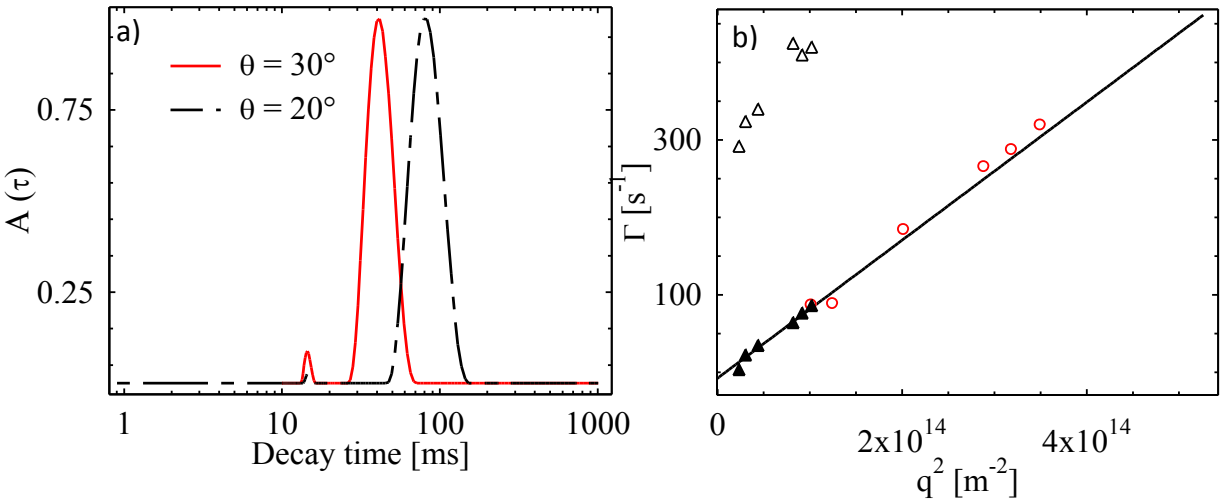

Figure 5.2.7 (a) DDLS-relaxation time distributions (CONTIN-plots) calculated from the intensity autocorrelation functions for hollow Janus dumbbells in 50 mM KCl solution at 20 °C. From scattering angle θ = 20° (solid line in panel a) to θ = 30° (dashed line in panel a). (b) The corresponding relaxation processes are plotted as a function of the square of the scattering vector (q^2) showing DLS slow mode (open circles) for hollow Janus dumbbells, DDLS slow mode (filled triangles) and DDLS fast mode (open triangles). The solid line is the linear fitted data according to the corresponding mode.

Table 5.2.1. Characterization of hollow Janus dumbbells and the comparison with that of dumbbell-shaped microgels, experimental diffusion coefficients D^T measured from both DLS and DDLS experiments.

Sample	D^T_{DLS} 10 °C [$10^{-12}m^2s^{-1}$]	D^T_{DLS} 20 °C [$10^{-12}m^2s^{-1}$]	D^T_{DDLS} 20 °C [$10^{-12}m^2s^{-1}$]	D^T_{DLS} 25 °C [$10^{-12}m^2s^{-1}$]
Dumbbell-shaped microgels	0.62±0.01	0.94±0.01	0.92±0.01	1.12±0.01
Hollow Janus dumbbells	0.64±0.02	0.95±0.01	0.90±0.01	1.17±0.01

This comparison demonstrates that D^T of the hollow Janus dumbbells differs only by 5% from that of the dumbbell-shaped microgels. This difference is within the experimental error. It indicates that dimensional information of Janus dumbbells is more or less identical with that

of the dumbbell-shaped microgels before the removal of PS core. Hence, the dumbbell shape imposed by the core is well kept for hollow Janus dumbbells. This is in agreement with the cryo-TEM image shown in Figure 5.2.6.

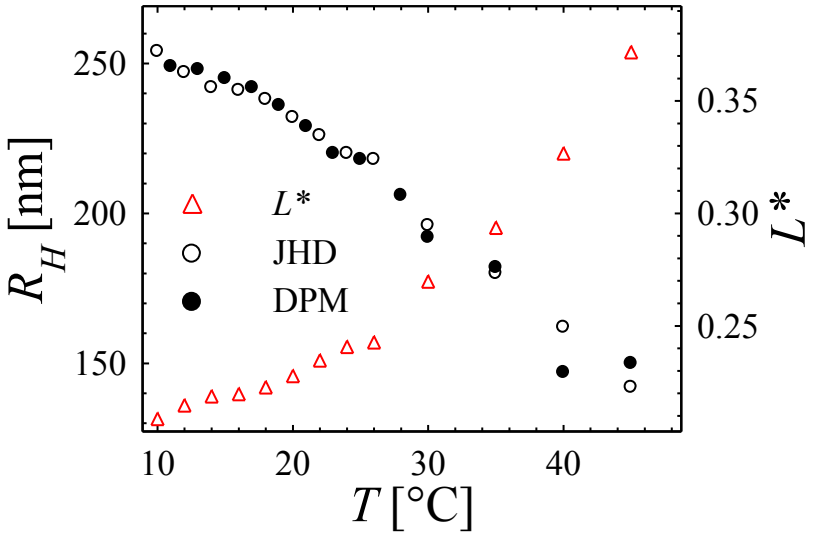

Figure 5.2.8 Temperature dependence of hydrodynamic radius of one sphere in the dumbbell-shaped microgels (filled circles) and hollow Janus dumbbells after the removal of PS core (empty circles). With R_H decreases with increasing T, and L^* increases correspondingly, marked by empty triangles. Temperature ranges from 10 to 50 °C, dumbbell-shaped microgels dispersed in salt free water before and after the removal of PS show comparable thermo-responsive property.

The analysis of D^T as the function of temperature shows that R_H of the hollow Janus dumbbells have a similar temperature dependence as the dumbbell-shaped microgels. Thus, the shell thickness decreases linearly with increasing temperature (T from 10 °C to 22.5 °C). When T is above LCST, the shell shrinks further and the thickness decreases from ca. 140 nm at 10 °C to ca. 50 nm at 45 °C, leading to the aspect ratio increased from 0.21 to 0.38 as shown in Figure 5.2.8. Hence, the DDLS measurements demonstrate that hollow dumbbells maintain the thermosensitivity after the removal of PS.

In conclusion, homogeneous thermosensitive hollow Janus dumbbells have been synthesized for the first time. They exhibit a well-defined Janus structure with two partially fused hollow PNIPA spheres. One PNIPA sphere is hollow while the other has a hollow core with a hybrid wall consisting of the copolymer of PS and PMPS with a thickness of ca. 10 nm. DLS and DDLS measurements prove that hollow Janus dumbbells exhibit a thermosensitivity comparable to the dumbbell-shaped microgels. Hence, the radius and aspect ratio of hollow Janus dumbbell is tunable within a certain range by temperature. Thus, the hollow Janus

hollow dumbbells can use a model system to study phase behaviour of anisotropic capsule systems.

Additionally, the work of this part opens the way to a wide variety of Janus structures and applications. The hollow hybrid sphere core in one PNIPA sphere has silanol groups on its surface[35, 167] and surface modifications can easily be provided by reactions with various silane reagents or grafting of other metal oxides (e.g. TiOx[214]). Moreover, the two different hollow cores can be used as nanoreactors.

6. Summary and outlook

The work of this thesis aims to investigate the phase behaviour of hard dumbbells as a function of aspect ratio, L^*, and volume fractions. Thermosensitive dumbbell-shaped microgels consisting of a dumbbell-shaped polystyrene (PS) particle as core and a thermosensitive poly(N-isopropylacrylamide) (PNIPA) network as shell have been used as a model system of hard dumbbells in this study. Using the model system with $L^* \sim 0.24$ and $L^* \sim 0.30$, the phase behaviour of the hard dumbbells have been investigated in different phases.

- First, the model system of hard dumbbells has been successfully synthesized and characterized by methods of TEM, cryo-TEM, DLS and DDLS. The model systems are highly monodisperse, which can form plastic crystals indicated by Bragg reflections. The visual evidence for the crystallization has been further supported by the rheological measurements. The experimental phase diagrams of the hard dumbbells with $L^* \sim 0.24$ and $L^* \sim 0.30$ are comparable to the prediction of the Monte Carlo (MC) simulations.[52-53] Moreover, the coexistence width for the biphasic gap decreases with an increase of L^* from 0.24 to 0.30.
- In the second part of the thesis, the yielding behaviour of hard dumbbells in different crystalline phases has been explored by the viscoelastic measurements. The hard dumbbells in the biphasic gap show one single yielding event under increasing oscillation shear. However, the fully crystallized hard dumbbells exhibit the double yielding behaviour along the dependence of storage modules (G') and loss modules (G'') on increasing shear strains, which is found to be related with crystallizations.
- In the next step, rheo-SANS experiments have been carried out to investigate the equilibrium and nonequilibrium structure of the plastic crystal that corresponds to the double yielding behaviour of the hard dumbbells. The experimental results are compared with the BD simulations performed by Nils Heptner[132] to elucidate the dynamics of sheared hard dumbbells. The experimental results reveal that the plastic crystal in equilibrium is polycrystalline, which evolves into five different non-equilibrium structures with increasing shear strains. The vorticity-alignment structure is firstly formed at the end of the linear viscoelastic region, which may correspond to the alignment of hard dumbbells perpendicular to the velocity direction. The twinned fcc structure is formed at low strain ($Pe_r \sim 0.5$) with a close packed direction perpendicular to the velocity direction. An increase in the applied shear strain can shear melt the twinned fcc,

yielding an intermediate structure prior to the formation of the partially oriented sliding layers at high strain ($Pe_r > 1$). A string-like structure is observed before complete shear melting of the shear-induced hexagonal layers. The twinned fcc structure, the intermediate structure and the partially oriented sliding layers structure have been observed by the BD simulations. Combined with the shear-induced microstructural evolution, the orientations of hard dumbbells are changed as well by the increasing shear strains. The orientations of the hard dumbbell particles along the velocity and vorticity directions are preferred for the twinned fcc structure. However, the hard dumbbells are favorably oriented parallel to the velocity direction at high strain for the partially oriented sliding layers. Moreover, an intermediate structure without favorable orientation and hexagonal order is formed during the structure reorganization from the twinned fcc to the partially oriented sliding layers. The formation of the intermediate structure corresponds to the second yielding event.

- Additionally, the comparison between the phase behaviour at $L^* \sim 0.24$ and $L^* \sim 0.30$ indicates that the hard dumbbells in the plastic crystalline phase with various L^* ($L^* < 0.4$) exhibit a comparable structural evolution under oscillation. However, more extensive and longer oscillations are needed to induce hexagonal orders for the hard dumbbells with a larger L^* since it is closer to the glassy state.
- In the last part, we extend this study to the hollow Janus dumbbells that are fabricated using the dumbbell-shaped microgels as templates. In addition, the monolayer and bilayer hollow spheres have been prepared as well from their respective microgel templates. A comprehensive characterization including TEM, SFM, cryo-TEM, DLS and DDLS has been carried out to investigate this series of hollow capsules. These hollow capsules can be used as model systems to investigate the phase behaviour of capsule systems.

In conclusion, this thesis provides a comprehensive investigation on the phase behaviour of the hard dumbbells with $L^* < 0.4$. The experiment phase diagrams verify the theoretical prediction of MC simulations at $L^* \sim 0.24$ and $L^* \sim 0.30$. The structure analysis of the plastic crystal and its structural evolution under oscillation shear offer an underlying interpretation for the yielding behaviour of hard dumbbells. This study is of great importance for the further work in creating novel crystal structures from anisotropic colloids. Moreover, the hollow capsules of different morphology provide access to the study on the phase behaviour of capsules systems.

7. Experimental

7.1 Materials

Sodium dodecyl sulfate (SDS) (Fluka), potassium persulfate (KPS) (Fluka), 3-(trimethoxysilyl) propyl methacrylate (MPS) (Sigma-Aldrich), 4-styrenesulfonic acid sodium salt hydrate (NaSS) (Sigma-Aldrich), 2,2'-azobis (2-methylpropionitrile) (AIBN) (Sigma-Aldrich), N-isopropylacrylamide (NIPA) (Sigma-Aldrich), N,N′-methylenebis (acrylamide) (BIS) (Sigma-Aldrich), deuterium oxide (> 99%) (D_2O) (Sigma-Aldrich) and tetrahydrofuran (THF) (Sigma-Aldrich) were used as received, styrene (Sigma-Aldrich) was purified by inhibitor remover (Sigma-Aldrich). Millipore water used was purified by reverse osmosis (MilliRo; Millipore) and ion exchange (MilliRo; Millipore).

7.2 Synthesis procedures

7.2.1 Synthesis of the core-shell spherical microgels

7.2.1.1 Polystyrene spherical seeds

The synthesis of PS spherical seeds was performed in a 1 L three-necked glass flask through conventional emulsion polymerization.[29] First, 0.42g SDS was firstly dissolved in 275 mL water under stirring at 200 rpm, which was controlled by a mechanical stirrer (EUROSTAR). Next, 30g styrene was charged into the reactor under stirring. After a complete mixture (stirring for 20 minutes), 0.3g KPS dissolved in 25 mL H_2O was added into the mixture. The reaction was done under nitrogen atmosphere and the temperature was controlled at 70 °C. PS cores used as seeds for the preparation of the core-shell spherical microgels were cleaned through dialysis for 3 days with Millipore water.

7.2.1.2 Core-shell polystyrene spherical seeds

Using spherical PS seeds, a copolymer layer of styrene and MPS was coated onto the surface of PS seeds via the seeded emulsion polymerization,[167] which aimed to facilitate the growth of the second sphere for the dumbbell-shaped cores.[55] The core-shell PS spheres are referred as PS-MPS spheres. During this step, 166.8 g of PS latex with (solid content: 7.94 wt.-%) was diluted with 50 mL H_2O in a 1 L three-necked glass flask that was used as the reactor. Then 1.25g MPS and 0.08 AIBN were dissolved in 12.53 g styrene, which was charged into the

reactor under stirring at 250 rpm. 20 minutes later, the reaction was started by increasing the temperature to 70 °C under nitrogen atmosphere. 8 hours later, the reaction was finished and the latex was cooled to the room temperature. The resulting PS-MPS cores were purified via dialysis for 3 days against Millipore water. The water was changed twice one day to remove the possible residual monomer and the extra stabilizer

7.2.1.3 Core-shell spherical microgels

The core-shells spherical microgels were synthesized in this step by attaching a shell of PNIPA network cross-linked by BIS onto the surface of spherical cores through the seeded emulsion polymerization.[31, 215] Here we prepared two types of core-shell spherical microgels: one has the pure PS spherical seeds (section 7.2.1.1) as core, while the other one is with the core-shell PS-MPS spherical seeds (section 7.2.1.2) as core. The two types of core-shell spherical microgels were prepared following the same procedure described as below.

First, 2 L three-necked glass flasks were used as the reactor. For the first type of spherical microgels, 98.10 g (weight content: 8.03.-wt% g) PS core latex was mixed with 231.90 mL water containing 8.36 g PNIPA and 0.57 g BIS. For the second type of spherical microgels, 162.5 g (weight content: 4.85wt.-%) PS-MPS spherical seeds core latex was charged into the reactor and then mixed with 177.50 mL water containing 8.36 g PNIPA and 0.57 g BIS. After a complete mixture (stirring for ca. 20 minutes), 0.3 g KPS dissolved in 10 mL H_2O was charged into the reactor under nitrogen atmosphere. The reaction started by increasing the temperature to 80 °C, and ran for 4.50 hours.

The core-shell microgels were purified by ultrafiltration to remove all possible traces of free polymers in the aqueous suspension of microgels. The ultrafiltration was carried out in 0.75 L serum replacement cells with membranes on their bottoms. The membranes based on cellulose nitrate (Schleicher & Schuell and Millipore) with pore sizes of 200 nm were used to remove the dissolved polymers, possible ions, and excess surfactant. The serum replacement cell was filled with ca. 500 mL microgels dispersions, and the serum replacement against Millipore water was carried out at an overpressure of nitrogen of 1.2 Par. The purification progress lasted until the conductivity of serum was equal to that of the pure Millipore water (1.0 μS/cm, measured by the conductivity meter from WTW). In general, the purification process took ca. 1 month and needed ca. 40 L Millipore water.

7.2.2 Synthesis of the dumbbell-shaped microgels

7.2.2.1 Dumbbell-shaped PS core

Table 7.2.1 Specified recipe for the synthesis of dumbbell-shaped PS core particles: The PS-MPS sphere is the PS seeds with a copolymer layer of PS and MPS attached onto its surface. The copolymer aimed to facilitate the growth of the second sphere of the dumbbell-shaped core particles.

		DPC_a	DPC_b
Step I PS spheres	m (SDS) [g]	0.42	0.45
	m (KPS) [g]	0.31	0.30
	m (styrene) [g]	30	30
	m (H_2O) [g]	300	300
Step II PS-MPS spheres	m (PS) [g]	166.8 of 7.94 wt.-%	187.6 of 7.06wt.-%
	m (styrene) [g]	12.53	12.53
	m (MPS) [g]	1.25	1.25
	m (AIBN) [g]	0.08	0.08
	m (H_2O) [g]	300	300
Step III DPC	m(PS/MPS)[g]	138.5of 7.78wt.-%	138.5of 7.06wt.-%
	m (styrene) [g]	32.91	32.91
	m (AIBN) [g]	0.18	0.18
	m (NaSS) [g]	0.45	0.45
	m (H_2O) [g]	182.8	171.28

Based on the seeded polymerization technique of Park *et al*.,[55] the homogeneous dumbbell-shaped core particles were prepared following the routine as shown in Figure 4.1.1. Two baths of different dumbbell-shaped core (the DPC_a and the DPC_b) were synthesized following the recipe in Table 7.2.1. The PS seeds and PS-MPS seeds were synthesized following the procedures described in section 7.2.1. In this step, a 500 mL three-necked glass flask as the reactor, the NaSS solution was mixed with the PS-MPS latex under stirring at 200 rpm. After

20 minutes, AIBN dissolved in styrene was charged into the reactor, which would swell into the PS-MPS spherical particles. The reaction was started by increasing the temperature to 70 °C under nitrogen atmosphere. The reaction lasted for 8 hours. In the end, the homogeneous dumbbell-shaped PS cores were obtained and purified by dialysis for 3 days with water.

7.2.2.2 Dumbbell-shaped microgels

In this part, a shell of PNIPA network cross-linked by BIS was fabricated onto the surface of aimed core particles through the seeded emulsion polymerization.[31, 215] Different core particles were used as seeds for the synthesis of different types of microgels following the recipe displayed in Table 7.2.2. The purified DPC_a and DPC_b particles were applied as the core particles for the preparation of the dumbbell-shaped microgels with L *~ 0.24 (DPM_a) and the dumbbell-shaped microgels with L* ~ 0.30 (DPM_b), respectively. In a typical run, a 2L three-necked glass flask served as the reactor, where the PS core latex was mixed with a certain amount of water containing a mixture of NIPA and BIS monomers. After a complete mixture (stirring for ca. 20 minutes), KPS dissolved in H_2O was charged into the reactor under nitrogen atmosphere. The reaction started by increasing the temperature to 80 °C, and ran for 4.50 hours. Afterwards, the dumbbell-shaped microgels were cleaned by ultrafiltration as discussed above. When the purification process was complete, 0.05 M KCl solution was used to replace the pure water to screen the possible residual charges left from the synthesis.

Table 7.2.2 Specified recipe for the synthesis of spherical and dumbbell-shaped microgels. The DPC_a core and the DPC_b core are the seeds for the preparation of the dumbbell-shaped microgels with L *~ 0.24 (DPM_a) and the dumbbell-shaped microgels with L* ~ 0.30 (DPM_b), respectively.

	m (core) [g]	m (NIPA) [g]	m (BIS) [g]	m (KPS) [g]	m (H_2O) [g]
DPM_a	150.6 of 7.13wt.-%	11.70	0.81	0.3	350
DPM_b	153.5 of 6.99wt.-%	11.70	0.80	0.3	350

7.2.3 Preparation of thermosensitive hollow capsules

A series of core-shell thermosensitive microgels were used as templates to prepare the thermosensitive hollow capsules of different morphology. As listed in Table 7.2.3, the dumbbell-shaped microgels (DPM) were used as the templates for the preparation of the thermosensitive hollow Janus dumbbells (HJD). The spherical microgels (SM) that consist of PS spheres as core and crosslinked PNIPA as shell were applied as templates for the monolayer hollow spherical capsules (MHS). The bilayer core-shell microgels (BSM) with PS-MPS spheres as core and crosslinked PNIPA as shell were applied as the template to synthesize the bilayer hollow spherical capsules (BHS).

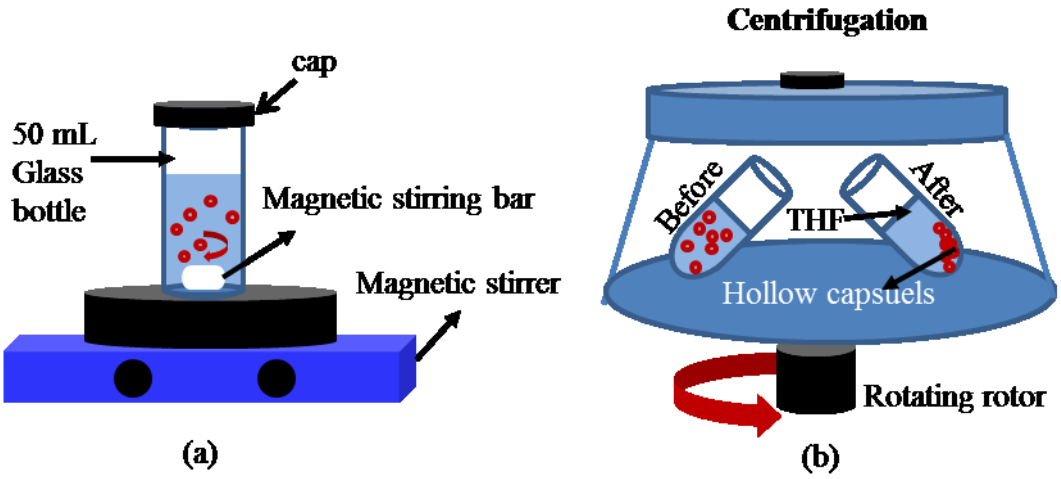

Figure 7.2.1 Sketch of the preparation of thermosensitive hollow capsules, (a) the setup for dissolution of PS cores in a 50 mL glass bottle with a cap, which will prevent the solvent evaporation and (b) the purification of dissolved PS via centrifugation.

During the preparation of the thermosensitive hollow capsules, the PS cores were selectively removed by the THF treatment. The preparation procedure for each hollow capsule was mainly divided into three steps. First, the concentrated core-shell microgel dispersions (10-15 wt.-%) were diluted with THF in a 50 mL glass bottle with a cap to the weight concentration of ca. 0.5 wt.-%. The microgels dispersed in THF were stirred overnight as schematically shown in Figure 7.2.1 a. Second, the dispersions were purified via centrifugation to remove the dissolved PS. During the centrifugation process (see Figure 7.2.1 b), the microgels were precipitated at the bottom, while the dissolved PS stayed in THF as the supernatant. The centrifugation tubes used in this part of work were made of Phenol formaldehyde resins

(Herolab), which were stable under THF at room temperature and below the speed of 10000 rpm. The microgels were re-dispersed in THF after the centrifugation and were kept under stirring overnight. Three runs of centrifugation, decantation and re-dispersion process were carried out every day until the microgels were free of PS. Due to the various structures of the thermosensitive microgels, the required cleaning cycles and the centrifugation speeds were different to prepare the three types of hollow capsules. Table 7.2.3 summarized the preparation procedures for the three types of hollow capsules, including the used template, the necessary number of cleaning cycles and the applied centrifugation speed. Finally, the purified hollow capsules were re-dispersed in Millipore water and another three cycles of centrifugation, decantation and re-dispersion process were performed to replace THF from the cleaning procedure.

Table 7.2.3 Overview of the information of the preparations for three types of hollow capsules, including their respective templates, the number of cleaning cycles (N_c); the centrifugation time per cycle (t_c) and the centrifugation speed.

Sample	Template	N_c	*tc (min)*	Centrifugation speed (rpm)
MHS	SM	10	*15*	6000
BHS	BSM	30	*15*	5000
JHD	DPM	60	*12*	8000

7.3 Characterization

7.3.1 Light scattering

The dimensional information of the microgel systems was characterized by light scattering. As discussed in Chapter 3, the Brownian motion of colloidal particles causes the light scattered from a dispersion to fluctuate with time.[13] These fluctuating intensities are detected and recorded in the light scattering experiment, and the obtained autocorrelation function provides access to the diffusion coefficients of the colloidal dispersion. In this work, dynamic light scattering (DLS) was used to analyze the translational diffusion.[13] In case of the dumbbell-shaped system, both DLS and depolarized dynamic light scattering (DDLS) experiments were necessary to measure both translational and rotational diffusions, which corresponded to the translational motion and rotational motion, respectively.

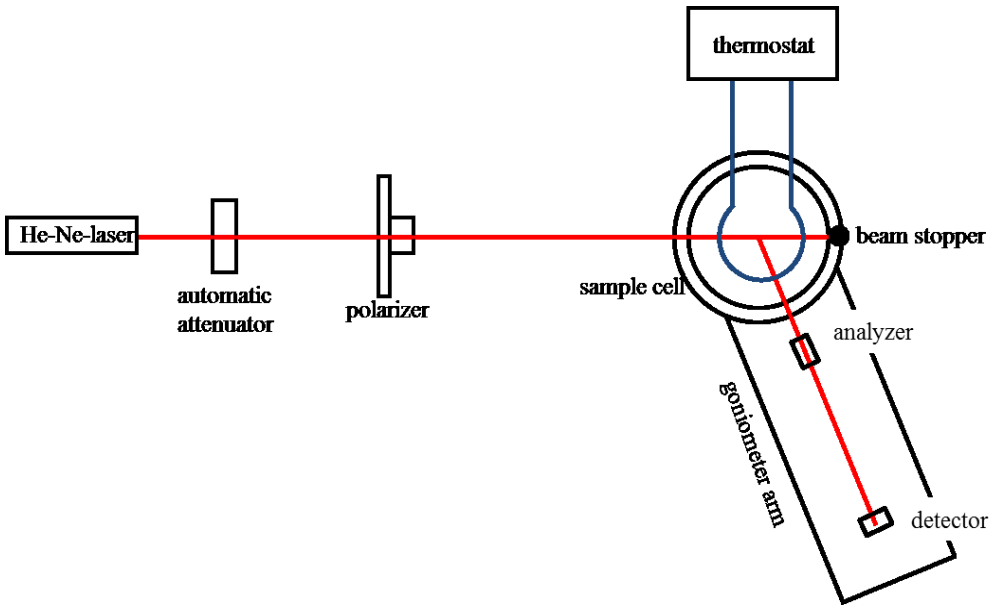

Figure 7.3.1 Schematic figure of the ALV -4000 compact goniometer system that is used for the DLS and DDLS experiments in this work. The red line denotes the beam path in a normal measurement.

The equipment that was used for the DLS and DDLS experiments is a ALV-4000 compact goniometer system equipped with a Helium-Neon-Laser (He-Ne-Laser) as schematically shown in Figure 7.3.1. The He-Ne-Laser is a class 3b laser, which emits light at a wavelength (λ) of 632.8 nm (red light) and has a power output of 35 mW. The automatic attenuator adjusts the incoming laser intensity for each sample and scattering angles to optimize the

scattering results. The polarizer mounted before the sample cell is a so-called Glan-Thompson-Prisma from the Halle company to increase the ratio of the vertically polarized light. The extinction of this polarizer (the ratio of vertical polarized light to horizontally polarized light) is 10000 : 1. The analyzer that is mounted before the detector is a Glan-Thompson-Prisma as well, which is used to filter the light according to its polarization. For the DLS experiments, the analyzer is set with an angle of 2.5°, while for the DDLS experiments, the angle is 92.5°. In the sample cell, toluene is used as the inner matching fluid and the temperature is controlled by a thermostat (Rotilabo, ±0.1 °C). The avalanche photo diode (APD) is the detector of the ALV-4000, which is mounted in the goniometer arm. The light is focused via a collecting lens (after the analyzer) into an optic fiber cable. The optic fiber cable conducts the scattered light to the APD, which transforms the light signal into an electric signal. The goniometer arm is movable in a theta range from 0° to 180°. However, the angle range measured in this work is limited from 20° to 120° to protect the detector. All electric parts of the ALV-4000 are firstly connected with LSE-5004 and then transferred to the computer via a USB connector. The ALV-4000/ LSE-5004 controls the goniometer, measures the temperature in the sample cell and correlates the incoming signal.

7.3.1.1 DLS measurements

As for the light scattering experiments, the samples were prepared in the dust-free fume hood (ADS Laminaire). To avoid aggregations or impurities in the measured sample, all the samples were filtered via syringe filters (Pall). The type of filter was chosen according to the size of samples. Dumbbell-shaped core particles were prepared with concentration of 0.001 wt.-% and then filtered through 0.45 μm nylon filters (Pall). Afterwards, the sample was charged into a dust free quartz glass cuvettes. Particles were firstly diluted to obtain a final concentration of 0.005 wt.-% and then filtered through a 1.2 μm nylon filter.All the DLS measurements were carried out with angles between 20° and 120° by a measurement step of 5°. Prior to measurements of thermosensitive microgels, one hour was set for the temperature equilibrium. Three single measurements were recorded at each angle and averaged.

7.3.1.2 DDLS measurements

As for the dumbbell-shaped systems, the DDLS measurements have been performed. Compared to the setup used for the DLS measurements, the polarization plane of the Glan Thomson analyzer was changed by 90° for the DDLS measurements. Five runs for each

scattering angle have been carried out between 20° and 50° with an angular step of 2.5° for the dumbbell-shaped cores. In case of the dumbbell-shaped microgels at 25 °C, five runs at scattering angles between 20° and 40° with an angular step of 1.5° for 20°-30° and 2.5° for 30-40° were recorded, respectively.

The intensity of autocorrelation functions were evaluated using the CONTIN software provided by the manufacturer (ALV Correlator Software 3.0). As a result, the DLS measurements provided the translational diffusion coefficient D^T, while the DDLS measurements yielded both D^T and rotational diffusion coefficient D^R. The hydrodynamic radius of the spherical systems was calculated based on the Einstein-Stokes equation.[216] The dimensional information of the dumbbell-shaped systems was calculated through the shell model and thus the center to center distance (L) and the diameter of one composed sphere (D) were obtained. More details about the calculations were explained in Chapter 3.

7.3.2 Electron microscopy

The morphology of the core systems including both spherical and dumbbell-shaped cores was investigated by the transmission electron microscopy (TEM). Carbon support film (200 mesh, Science Services, Munich, Germany) have been pretreated by the glow discharge for 10 seconds. TEM specimens were prepared by dropping approximately 5 µL of a 0.1 wt.-% solution on a TEM copper grid After 2 minutes, the excess liquid was blotted with a filter paper. The remaining liquid film on the TEM grid was dried at room temperature for at least one hour. The specimen was inserted into the sample holder (EM21010, JEOL GmbH, Eching, Germany) and transferred to a JEOL JEM-2100 with a LaB_6 cathode (JEOL GmbH, Eching, Germany). The TEM was operated at an acceleration voltage of 200 kV. All images were recorded digitally by a bottom-mounted 4k CMOS camera system (TemCam-F416, TVIPS, Gauting, Germany) and proceeded with a digital imaging processing system (EM-Menu 4.0, TVIPS, Gauting, Germany).

Cryo-TEM was used to visualize the particles *in situ*, in particular for the morphology of the microgels system. Cryo-TEM specimens were prepared by vitrification of thin liquid films supported on a TEM copper grid (600 mesh, Science Services, Munich, Germany) in liquid ethane at its freezing point. The specimen was inserted into a cryo-transfer holder (CT3500, Gatan) and transferred to a Zeiss EM922 EFTEM. Measurements were carried out at

temperatures around 90 K. The TEM was operated at an acceleration voltage of 200 kV. Micrographs were digitally recorded using a bottom-mounted, TVIPS TemCam-F416 16bit CMOS camera with a field of view of 4k*4k. Saturation effects were avoided by keeping the intensity below 15000. The histograms of the 16 bit micrographs were adjusted using the free software package ImageJ. In addition, cryo-TEM has been extended to perform a quantitative analysis of the gray scale of the micrographs in order to obtain the local electron density of the particles.

7.3.3 Scanning force microscopy (SFM)

The sample for SFM was prepared by placing 20 µL of the suspensions on a mica substrate. 10 seconds later, the sample was dried by the spin coating with a speed of 50 rpm if not specially stated. The images were recorded by operating in peak force mode (MultiMode SFM, Bruker Corporation; Nanoscope 8 SFM controller). Silicon cantilevers were used with typical resonance frequencies of 70 kHz and spring constants of 2 N/m. (Olympus Corporation). The tips exhibited an asymmetric cone shape with the maximum opening angle of 35° and a typical apex radius of 7 nm, with an upper limit of 10 nm, as provided by the manufacturer.

7.3.4 Rheology and Rheo-SANS

7.3.4.1 Rheology

The rheological measurements were performed with a stress-controlled rotational rheometer Physica MCR301 (Anton Paar). In general, there are three types of geometries that can be used on a rotational rheometer to create a viscometric or nearly viscometric flow as shown in Figure 7.3.2 in a schematic manner. They are the cone and plate geometry, the parallel disks geometry and the coaxial cylinders geometry, respectively. Each type of geometry has its own advantages and disadvantages. A cone and plate geometry can provide a uniform shear rate through the sample, which is important for the transient measurements. Moreover, only a small amount of sample is necessary when the radius of the tools is kept small. However, it can be problematic to measure suspensions of large particles by the cone and plate geometry. Owing to the adjustable gap height, the parallel disks are more suitable for large particles. In addition, the shear rate can be changed by varying the rotational speed and by changing the gap, which facilitate the characterization of wall slip. Unfortunately, the shear rate in this geometry is not uniform but varies linearly in the radial direction, which complicates the

calculation of viscosity. Both geometries, however, are unsuitable when sedimentation happens in the measured sample. Even with a minor settling, the top platen would rotate in an essentially liquid phase. In this case, the coaxial cylinders are suitable, where a settling distance only causes a local effect near the top of the cylinders. A disadvantage of the Couette cell is that the loading of viscous materials in a Couette geometry is much more difficult than the other two geometries. In this work, the cone and plate geometry is chosen for normal rheological measurement on the Physica MCR301. The Physica MCR501 with a Couette cellis applied for the combination with small angle neutron scattering experiments (D11, ILL, Grenoble).

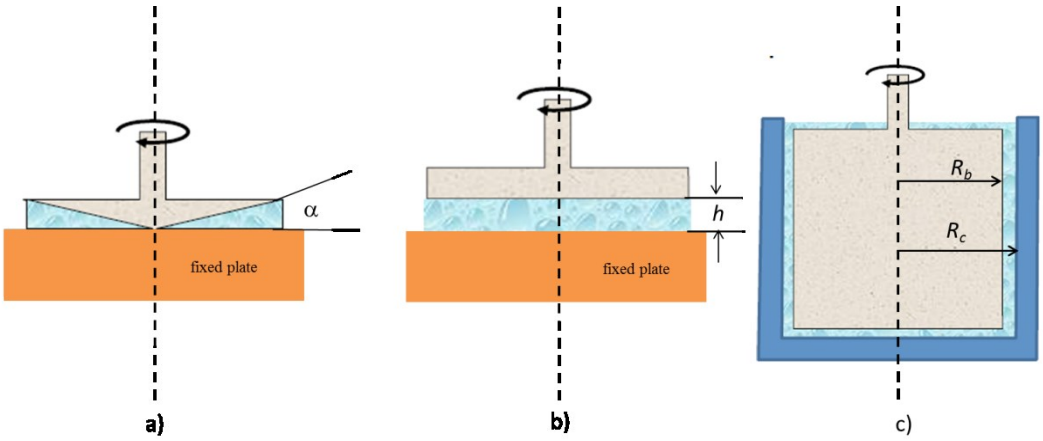

Figure 7.3.2 Geometries of the rotational rheometer: (a) cone and plate; (b) parallel disks; (c) coaxial cylinders (Couette).

The motions in these three geometries are generated by moving the walls, which drags the fluid in the geometry. Based on the drag flows, the rotational rheometer creates a simple shear flow in which the flow field is laminar and the shear rate is constant throughout the sample.[137] The kinematic of the flow is set by the rheometer, which is independent of the sample's rheology. Then measurements of the forces and torques acting on the geometry lead to the stresses (σ). The ratio of the shear stress to the shear rate ($\dot{\gamma}$) yields the viscosity. The rotational rheometer can perform measurements in two basic modes, the shear steady mode and the oscillatory shear mode. Based on the shear steady mode, the steady state flow curve, overshoot and the stress relaxation of materials can be measured. The oscillatory measurements can be performed through the oscillatory shear mode to characterize the viscoelastic properties of matter. The measurement protocols include, for example, the strain amplitudes sweep at a fixed frequency to study the linear and nonlinear regimes, the time

sweep at fixed frequency and fixed strain amplitude to test the time stability, and the frequency sweep at fixed strain amplitude.

Two main measurement protocols are discussed in Figure 7.3.3, including the flow curve and the amplitudes sweep. The steady state experiments are normally performed by increasing the shear rate. In principle, the same viscosities should be generated by decreasing the shear rate. A hysteresis as shown in Figure 7.3.3a may be caused by intrinsic time effects or a shear rate and time dependent structure. The steady state experiments based on the hysteresis are useful to probe thixotropic systems. The amplitudes sweep in the oscillatory shear flow is commonly used to investigate the viscoelastic properties of suspensions,[137, 178] which is denoted by the storage modules (G') and the loss modules (G'').

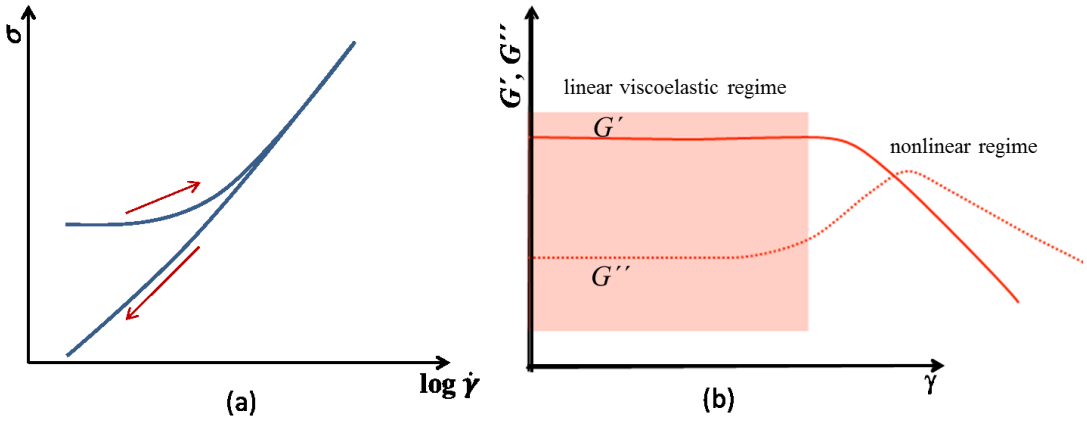

Figure 7.3.3 (a) Flow curve that is measured based on the steady shear mode, that is the dependence of σ on the increasing and decreasing $\dot{\gamma}$ (b) the dependence of G' and G'' on the increasing strain amplitudes, which is measured in the oscillatory shear field with fixed f.

In this work, four different measurements were performed to investigate the phase behaviour of the hard dumbbell suspensions in various crystalline phases. They were the measurements of flow curve, the strain amplitudes sweep at fixed frequency, the time sweep, and the frequency sweep. The flow curve experiment was performed by increasing the shear rate from 0.001 s^{-1} to 1000 s^{-1} with a logarithmic time ramp of 1000 s to 10 s and then decreasing from 1000 s^{-1} to 0.001 s^{-1} with a logarithmic time ramp of 10 s to 1000 s. Time sweep experiments were set at 1% strain and 1Hz frequency in the linear viscoelastic region to test the time stability. Yielding behaviour has been investigated at the fixed frequency (1 Hz or 5 Hz) and various strains of amplitudes ranging from 0.1% to 1000%. For each measurement, 60 points were measured with 100 s per point. The frequency sweep at a fixed strain amplitude (γ_{max} =

1%) was done in the frequency range from 10 Hz to 0.001Hz with a logarithmic time ramp of 600 s to 20 s. For all the measurements, samples were pre- sheared at a shear rate of 100 s^{-1} for 200 s and a waiting time (t_w) of 60s was followed in order to guarantee that all measured samples started with the same non-equilibrium initial state. For the flow curve experiments, t_w = 1 h is set to allow the crystallization to set in.

7.3.4.2 Rheo-SANS

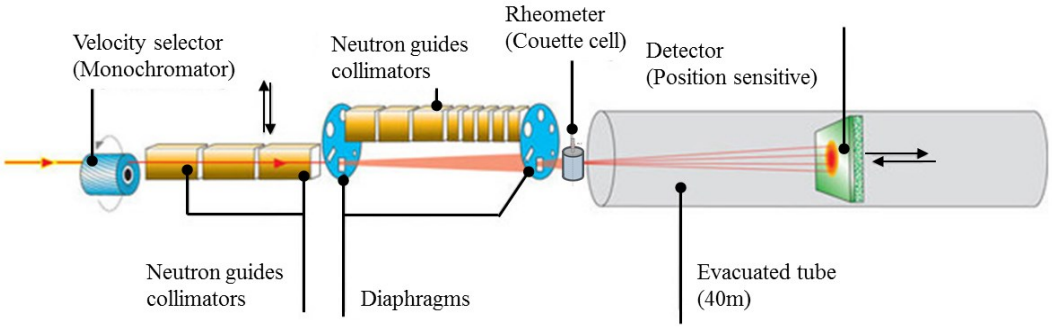

Figure 7.3.4 Instrument layout of the rheo-SANS setup (D11, Grenoble). The stress-controlled rheometer (Physica MCR501, Anton Paar) with a couette cell was used to apply oscillatory shear.

The rheo-SANS experiments were carried out at D11 in Grenoble to investigate the structural evolution of hard dumbbell suspensions under oscillatory strain. The rheo-SANS set up as shown in Figure 7.3.4 was built based on the combination of SANS and a rheometer (Physica MCR 501, Anton Paar) with a Couette cell. A polychromatic beam from the cold source was monochromated by a helical slot (ASTRIUM) velocity selector, which selected neutrons of ± 9% about a mean wavelength determined by the rotation speed of the drum. The wavelength used in this study was 13 Å. The collimators were used to filter the incident beam stream so that only those travelling parallel to a specific direction can pass through. The diaphragms used in this work had a aperture with a diameter of 5 mm, which aimed at regulating the amount of light that can pass. The instrument was equipped with a 96 * 96 cm^2 He gas detector (CERCA) with a 7.5 * 7.5 mm^2 resolution. The distance between the detector and the sample can be varied from 1.2 m to 39 m. In this study, all experiments were done with a distance of 39 m except several transmission measurements and static experiments, which were done at 8 m.

The rheometer with a Couette cell was mounted to perform rheological measurements on samples with the measuring system CTD 200/GL. The used Couette geometry was composed of a fixed quartz cup with a diameter of 50 mm and a movable cylinder with a diameter of 49 mm. The gap between the measuring cup and cylinder was determined to be 0.5 mm. However, the solved trap did not fit well with the quartz measuring cylinder due to the design problems. The Ti cylinder (ME49/Ti/SANS) of the same size was used to provide a good solvent protection. In principle, the rheo-SANS setup as shown in Figure 7.3.4 allows measurements with the incident beam along the flow direction or the center line of the shear cell. Due to the time limitation, SANS experiments in this work were only carried out with the incident radiation propagating in the radial direction as schematically shown in Figure 7.3.5. This corresponds to measurements with component of the scattering vector in the gradient direction of zero magnitude. The structure factor is thus projected in the vorticity-velocity scattering plane.

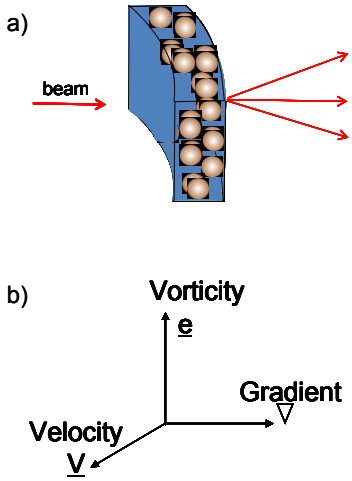

Figure 7.3.5 (a) Detailed schematic for the measured part of the Couette cell. The red lines denote the beam path (b) Orientation of the main scattering geometries: $\underline{V}$ is velocity, $\underline{\nabla}$ is gradient and $\underline{e}$ is vorticity.

As shown in Table 7.3.1, the DPM_a suspensions with L* ~ 0.24 at volume fractions of 0.51 and 0.60 and the DPM_b suspension with L* ~ 0.30 at volume fraction of 0.60 were measured at rest and under shear, respectively. After the loading of each sample, nearly one hour was set for the temperature equilibrium. SANS experiments were followed to measure the scattering of the hard dumbbell suspensions in equilibrium, which lasted 15 min to collect around one million counts.

Table 7.3.1 Pe_r of hard dumbbells in the oscillatory shear field at measured temperature (DPM_a, 10 °C and 15 °C; DPM_b 15 °C). D^R used for the calculation is achieved by the DLS and DDLS measurement and shell modelling.[132]

	DPM_a 10 °C ($\phi = 0.60, f = 1$ Hz)	DPM_a 15 °C ($\phi = 0.51, f = 1$Hz)	DPM_b 15 °C ($\phi = 0.63, f = 5$ Hz)
D_r [s^{-1}]	6.05	7.50	17.70
Pe_r (γ_{max} = 1%)	0.01	0.008	0.018
Pe_r (γ_{max} = 5%)	0.05	0.04	0.09
Pe_r (γ_{max} = 10%)	0.10	0.08	0.18
Pe_r (γ_{max} = 16%)	-	-	0.29
Pe_r (γ_{max} = 19.4%)	0.20	0.16	-
Pe_r (γ_{max} = 23.6%)	0.24	0.20	0.42
Pe_r (γ_{max} = 42.3%)	0.44	0.36	0.75
Pe_r (γ_{max} = 50%)	0.52	0.42	0.89
Pe_r (γ_{max} = 60%)	0.62	0.50	-
Pe_r (γ_{max} = 62.6%)	-	-	1.12
Pe_r (γ_{max} = 70.9%)	0.73	0.59	1.27
Pe_r (γ_{max} = 76%)	-	-	1.36
Pe_r (γ_{max} = 90%)	0.93	0.75	1.61
Pe_r (γ_{max} = 116%)	1.20	0.97	2.08
Pe_r (γ_{max} = 136%)	-	-	2.43
Pe_r (γ_{max} = 166%)	-	-	2.97
Pe_r (γ_{max} = 201%)	-	-	3.60
Pe_r (γ_{max} = 300%)	-	-	5.37
Pe_r (γ_{max} = 500%)	5.19	4.19	8.92
Pe_r (γ_{max} = 1000%)	10.38	8.38	17.84

Each sample was pre-sheared at a shear rate of 100 s^{-1} for 200 s and then followed t_w of 60 s to initialize all the samples at the same non-equilibrium state. SANS experiments were then performed under oscillatory shear with a fixed frequency (1 Hz for the DPM_a suspension or 5 Hz for the DPM_b suspensions) and various strains along the dependence of *G'* and *G''*. A list of the applied strain amplitudes and Pe_r are summarized in Table 7.3.1 for each sample, which were chosen according to the dependence of *G'* and *G''* on γ. D^R used for the calculation of Pe_r was resulted from the DDLS and DLS measurements. More details related with the calculations for D^R and Pe_r were specified in Chapter 3.

Each of these measurements lasted at least 25 min, the scattering of the first 10 min was recorded to present the structural evolution after the application of certain oscillatory shear. For the case that more oscillations were needed, another 10 min scattering run was followed. As long as the scattering became stable with time, a scattering run of 15 min was performed on the shear-induced crystals.

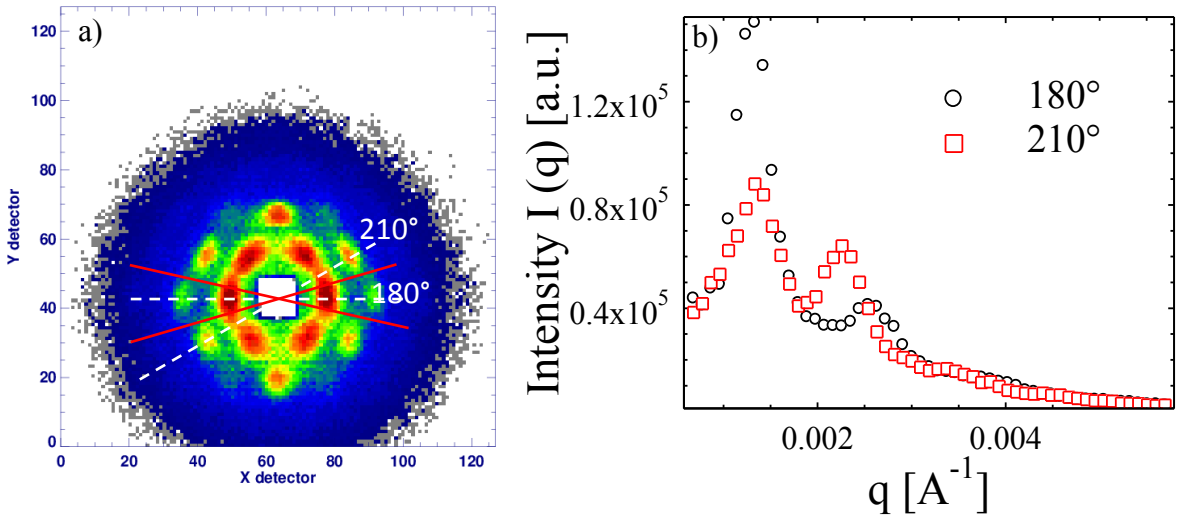

Figure 7.3.6 The radial integration by sectors through the LAMP-SANS software based on (a) 2D scattering pattern of the hard dumbbell suspension (ϕ_{eff} = *0.60*) under oscillatory shear (f = 1 Hz, γ_{max} = 50%, Pe_r = 0.52). The two dashed lines denoted by 180° and 210° are marked to show the centre line of two integrated sectors. The two solid red lines display the integrated sector with centre line of 180°. (b) the scattering intensity I(q) based on the two integrated sectors, the empty circles mark the radial integration over the sector along the centre line of 180°, and empty squares denote the radial integration along the centre line of 210°. The peak positions are determined at 0.00132, 0.00225, 0.00263, 0.00346 A^{-1}, which are indexed as $1:\sqrt{3}:2:\sqrt{7}$.

Scattering and transmission measurements were carried out on the empty sample cells and the dispersed solution (50 mM D_2O) with the distances of 8 m and 39 m, respectively. To collect one million counts, a transmission measurement lasted ca. 10 min and a scattering

measurement lasted 15 min. These measurements are necessary for the background subtraction in the data evaluation process, which was done through the LAMP-SANS software. The scattering data of samples was thus obtained according to

$$\boldsymbol{I(q)} = \boldsymbol{I_s(q)} - \boldsymbol{(1-\phi) I_{cell}(q) - \phi * I_{D2O}(q)} \ , \qquad (7.3.1)$$

where $I_s(q)$ is the original scattering data, $I_{cell}(q)$ is scattering data from empty cell, $I_{D2O}(q)$ is for empty cell filled with 50 mM D_2O, and ϕ is volume fraction of measured sample.

The data evaluation of the scattering was done by the radial integration via the LAPM-SANS software. Figure 7.3.6a presents the integration process by sectors using the anisotropic scattering pattern of the DPM_a suspension under oscillatory shear (f = 1 Hz, γ_{max} = 50%, Pe_r = 0.52) as an example. Due to the symmetry of the scattering pattern, the two integrated sectors with centre line of 180° and 210° were chosen to represent all the shown peaks. Take the sector with centre line of 180° as an example, the boundaries of integrated sector are labelled via the two solid lines (see Figure 7.3.6a). The results of radial integration in Figure 7.3.6b indicated that the crystalline peaks appear at q's (A^{-1}): 0.00132, 0.00225, 0.00263, 0.00346, respectively. Based on the peak positions, the crystal structure was indexed as 2D hcp layers.[161] As for the underlying dynamics, the Brownian dynamic simulations were performed by theoretical calculations of Nils Heptner within his Ph.D work.[132]

Bibliography

[1]. Pusey, P.; Van Megen, W., Phase behaviour of concentrated suspensions of nearly hard colloidal spheres. *Nature* **1986**, *320* (6060), 340-342.

[2]. Anderson, V. J.; Lekkerkerker, H. N., Insights into phase transition kinetics from colloid science. *Nature* **2002**, *416* (6883), 811-815.

[3]. Longuet-Higgins, H. C.; Widom, B., A rigid sphere model for the melting of argon. *Mol. Phys.* **1964**, *8* (6), 549-556.

[4]. Antl, L.; Goodwin, J. W.; Hill, R. D.; Ottewill, R. H.; Owens, S. M.; Papworth, S.; Waters, J. A., The preparation of poly(methyl methacrylate) latices in non-aqueous media. *Colloids. Surf.* **1986**, *17* (1), 67-78.

[5]. Johnson, P. M.; van Kats, C. M.; van Blaaderen, A., Synthesis of colloidal silica dumbbells. *Langmuir* **2005**, *21* (24), 11510-11517.

[6]. Deng, T. S.; Zhang, Q. F.; Zhang, J. Y.; Shen, X.; Zhu, K. T.; Wu, J. L., One-step synthesis of highly monodisperse hybrid silica spheres in aqueous solution. *J. Colloid Interface Sci.* **2009**, *329* (2), 292-299.

[7]. Senff, H.; Richtering, W., Temperature sensitive microgel suspensions: Colloidal phase behavior and rheology of soft spheres. *J. Chem. Phys.* **1999**, *111* (4), 1705-1711.

[8]. Pusey, P. N.; Poon, W. C. K.; Ilett, S. M.; Bartlett, P., Phase behaviour and structure of colloidal suspensions. *J. Phys.: Condens. Matter* **1994**, *6* (23), 29.

[9]. Hunter, G. L.; Weeks, E. R., The physics of the colloidal glass transition. *Rep. Prog. Phys.* **2012**, *75* (6), 066501.

[10]. Pelton, R., Polystyrene and polystyrene-butadiene latexes stabilized by poly (n-isopropylacrylamide). *J. Polym. Sci., Part A: Polym. Chem.* **1988**, *26* (1), 9-18.

[11]. Kuijk, A.; Byelov, D. V.; Petukhov, A. V.; van Blaaderen, A.; Imhof, A., Phase behavior of colloidal silica rods. *Faraday Discuss.* **2012**, *159*, 181.

[12]. Tripathy, M.; Schweizer, K. S., The influence of shape on the glassy dynamics of hard nonspherical particle fluids. I. Dynamic crossover and elasticity. *J. Chem. Phys.* **2009**, *130* (24), 244906.

[13]. Russel, W. B.; Saville, D. A.; Schowalter, W. R., *Colloidal dispersions*. Cambridge University Press: **1992**.

[14]. Crassous, J. J.; Siebenbürger, M.; Ballauff, M.; Drechsler, M.; Henrich, O.; Fuchs, M., Thermosensitive core-shell particles as model systems for studying the flow behavior of concentrated colloidal dispersions. *J. Chem. Phys.* **2006**, *125* (20).

[15]. Poon, W.; Pusey, P., Phase transition of spherical colloids. In *Observation, prediction and simulation of phase transitions in complex fluids*, Springer: **1995**; pp 3-51.

[16]. Van Winkle, D. H.; Murray, C., Layering transitions in colloidal crystals as observed by diffraction and direct-lattice imaging. *Phys. Rev. A* **1986**, *34* (1), 562.

[17]. Aastuen, D.; Clark, N.; Cotter, L.; Ackerson, B. J., Nucleation and growth of colloidal crystals. *Phys. Rev. Lett.* **1986**, *57* (14), 1733.

[18]. Marshall, L.; Zukoski, C. F., Experimental studies on the rheology of hard-sphere suspensions near the glass transition. *J. Phys. Chem.* **1990**, *94* (3), 1164-1171.

[19]. Siebenbürger, M.; Fuchs, M.; Ballauff, M., Core-shell microgels as model colloids for rheological studies. *Soft Matter* **2012**, *8* (15), 4014-4024.

[20]. Pusey, P., The effect of polydispersity on the crystallization of hard spherical colloids. *J. Phys.* **1987**, *48* (5), 709-712.

[21]. Pusey, P.; Van Megen, W., Observation of a glass transition in suspensions of spherical colloidal particles. *Phys. Rev. Lett.* **1987**, *59*, 2083-2086.

[22]. Poon, W. C.; Weeks, E. R.; Royall, C. P., On measuring colloidal volume fractions. *Soft Matter* **2012**, *8* (1), 21-30.

[23]. Pusey, P.; Zaccarelli, E.; Valeriani, C.; Sanz, E.; Poon, W. C.; Cates, M. E., Hard spheres: Crystallization and glass formation. *Phil. Trans. R. Soc. A* 2009, *367* (**1909**), 4993-5011.

[24]. Auer, S.; Frenkel, D., Suppression of crystal nucleation in polydisperse colloids due to increase of the surface free energy. *Nature* **2001**, *413* (6857), 711-713.

[25]. Mills, R. L.; Olinger, B.; Cromer, D. T., Structures and phase diagrams of n2 and co to 13 gpa by x-ray diffraction. *J. Chem. Phys.* **1986**, *84* (5), 2837-2845.

[26]. Torquato, S.; Truskett, T. M.; Debenedetti, P. G., Is random close packing of spheres well defined? *Phys. Rev. Lett.* **2000**, *84* (10), 2064.

[27]. Radin, C., Random close packing of granular matter. *J. Stat. Phys.* **2008**, *131* (4), 567-573.

[28]. Crassous, J.; Wittemann, A.; Siebenbürger, M.; Schrinner, M.; Drechsler, M.; Ballauff, M., Direct imaging of temperature-sensitive core-shell latexes by cryogenic transmission electron microscopy. *Colloid. Polym. Sci.* **2008**, *286* (6-7), 805-812.

[29]. Lu, Y.; Ballauff, M., Thermosensitive core–shell microgels: From colloidal model systems to nanoreactors. *Prog. Polym. Sci.* **2011**, *36* (6), 767-792.

[30]. Kim, J.; Deike, I.; Dingenouts, N.; Norhausen, C.; Ballauff, M. In *The volume transition in thermosensitive core-shell latex particles investigated by small-angle x-ray scattering and dynamic light scattering*, Macromol. Symp., Wiley Online Library: **1999**; pp 217-225.

[31]. Dingenouts, N.; Norhausen, C.; Ballauff, M., Observation of the volume transition in thermosensitive core-shell latex particles by small-angle x-ray scattering. *Macromolecules* **1998**, *31* (25), 8912-8917.

[32]. Crassous, J. J.; Ballauff, M.; Drechsler, M.; Schmidt, J.; Talmon, Y., Imaging the volume transition in thermosensitive core-shell particles by cryo-transmission electron microscopy. *Langmuir* **2006**, *22* (6), 2403-2406.

[33]. Crassous, J. J.; Siebenbürger, M.; Ballauff, M.; Drechsler, M.; Hajnal, D.; Henrich, O.; Fuchs, M., Shear stresses of colloidal dispersions at the glass transition in equilibrium and in flow. *J. Chem. Phys.* **2008**, *128* (20), 204902.

[34]. Siebenburger, M.; Fuchs, M.; Winter, H. H.; Ballauff, M., Viscoelasticity and shear flow of concentrated, noncrystallizing colloidal suspensions: Comparison with mode-coupling theory. *J. Rheol.* **2009**, *53* (3), 707-726.

[35]. Brader, J. M.; Siebenburger, M.; Ballauff, M.; Reinheimer, K.; Wilhelm, M.; Frey, S. J.; Weysser, F.; Fuchs, M., Nonlinear response of dense colloidal suspensions under oscillatory shear: Mode-coupling theory and fourier transform rheology experiments. *Phys. Rev. E* **2010**, *82* (6).

[36]. Schild, H. G., Poly(n-isopropylacrylamide): Experiment, theory and application. *Prog. Polym. Sci.* **1992**, *17* (2), 163-249.

[37]. Hoover, W. G.; Gray, S. G.; Johnson, K. W., Thermodynamic properties of the fluid and solid phases for inverse power potentials. *J. Chem. Phys.* **1971**, *55* (3), 1128-1136.

[38]. Paulin, S. E.; Ackerson, B. J., Observation of a phase transition in the sedimentation velocity of hard spheres. *Phys. Rev. Lett.* **1990**, *64* (22), 2663-2666.

[39]. Purnomo, E. H.; van den Ende, D.; Mellema, J.; Mugele, F., Rheological properties of aging thermosensitive suspensions. *Phys. Rev. E* **2007**, *76* (2), 021404.

[40]. Amann, C. P.; Siebenbürger, M.; Krüger, M.; Weysser, F.; Ballauff, M.; Fuchs, M., Overshoots in stress-strain curves: Colloid experiments and schematic mode coupling theory. *J. Rheo.* **2013**, *57* (1), 149-175.

[41]. Fuchs, M., Nonlinear rheological properties of dense colloidal dispersions close to a glass transition under steady shear. *Adv. Polym. Sci.* **2010**, *236*, 55-115.

[42]. Hajnal, D.; Fuchs, M., Flow curves of colloidal dispersions close to the glass transition asymptotic scaling laws in a schematic model of mode coupling theory. *Eur. Phys. J. E* **2009**, *28* (2), 125-138.

[43]. Stieger, M.; Pedersen, J. S.; Lindner, P.; Richtering, W., Are thermoresponsive microgels model systems for concentrated colloidal suspensions? A rheology and small-angle neutron scattering study. *Langmuir* **2004**, *20* (17), 7283-7292.

[44]. Fuchs, M.; Ballauff, M., Flow curves of dense colloidal dispersions: Schematic model analysis of the shear-dependent viscosity near the colloidal glass transition. *J. Chem. Phys.* **2005**, *122* (9).

[45]. Frenkel, D.; Mulder, B.; McTaque, J., Phase diagram of a system of hard ellipsoids. *Phys. Rev. Lett.* **1984**, *52* (4), 287-290.

[46]. Frenkel, D.; Mulder, B., The hard ellipsoid-of-revolution fluid: I. Monte carlo simulations. *Mol. Phys.* **1985**, *55* (5), 1171-1192.

[47]. Mulder, B.; Frenkel, D., The hard ellipsoid-of-revolution fluid: Ii. The y-expansion equation of state. *Mol. Phys.* **1985**, *55* (5), 1193-1215.

[48]. Singer, S. J.; Mumaugh, R., Monte carlo study of fluid–plastic crystal coexistence in hard dumbbells. *J. Chem. Phys.* **1990**, *93* (2), 1278-1286.

[49]. Vega, C.; Paras, E. P. A.; Monson, P. A., Solid-fluid equilibria for hard dumbbells via monte-carlo simulation. *Journal of Chemical Physics* **1992**, *96* (12), 9060-9072.

[50]. Vega, C.; Paras, E. P. A.; Monson, P. A., On the stability of the plastic crystal phase of hard dumbbell solids. *The Journal of Chemical Physics* **1992**, *97* (11), 8543-8548.

[51]. Wojciechowski, K. W., Monte carlo simulations of highly anisotropic two-dimensional hard dumbbell-shaped molecules: Nonperiodic phase between fluid and dense solid. *Physical Review B* **1992**, *46* (1), 26-39.

[52]. Marechal, M.; Dijkstra, M., Stability of orientationally disordered crystal structures of colloidal hard dumbbells. *Phys. Rev. E* **2008**, *77* (6), 061405.

[53]. Vega, C.; Monson, P., Plastic crystal phases of hard dumbbells and hard spherocylinders. *J. Chem. Phys.* **1997**, *107* (7), 2696-2697.

[54]. Mock, E. B.; De Bruyn, H.; Hawkett, B. S.; Gilbert, R. G.; Zukoski, C. F., Synthesis of anisotropic nanoparticles by seeded emulsion polymerization. *Langmuir* **2006**, *22* (9), 4037-4043.

[55]. Park, J. G.; Forster, J. D.; Dufresne, E. R., High-yield synthesis of monodisperse dumbbell-shaped polymer nanoparticles. *J. Am. Chem. Soc.* **2010**, *132* (17), 5960.

[56]. Glotzer, S. C.; Solomon, M. J., Anisotropy of building blocks and their assembly into complex structures. *Nat. Mater.* **2007**, *6* (7), 557-562.

[57]. Lee, S. H.; Gerbode, S. J.; John, B. S.; Wolfgang, A. K.; Escobedo, F. A.; Cohen, I.; Liddell, C. M., Synthesis and assembly of nonspherical hollow silica colloids under confinement. *J. Mater. Chem.* **2008**, *18* (41), 4912-4916.

[58]. Hosein, I. D.; Lee, S. H.; Liddell, C. M., Dimer-based three-dimensional photonic crystals. *Adv. Funct. Mater.* **2010**, *20* (18), 3085-3091.

[59]. Mock, E. B.; Zukoski, C. F., Determination of static microstructure of dilute and concentrated suspensions of anisotropic particles by ultra-small-angle x-ray scattering. *Langmuir* **2007**, *23* (17), 8760-8771.

[60]. Mock, E.; Zukoski, C., Investigating microstructure of concentrated suspensions of anisotropic particles under shear by small angle neutron scattering. *J. Rheo.* **2007**, *51* (3), 541-559.

[61]. Zerrouki, D.; Baudry, J.; Pine, D.; Chaikin, P.; Bibette, J., Chiral colloidal clusters. *Nature* **2008**, *455* (7211), 380-382.

[62]. Solomon, M. J., Directions for targeted self-assembly of anisotropic colloids from statistical thermodynamics. *Curr. Opin. Colloid Interface Sci.* **2011**, *16* (2), 158-167.

[63]. Grzelczak, M.; Vermant, J.; Furst, E. M.; Liz-Marzán, L. M., Directed self-assembly of nanoparticles. *ACS Nano* **2010**, *4* (7), 3591-3605.

[64]. Lee, S. H.; Fung, E. Y.; Riley, E. K.; Liddell, C. M., Asymmetric colloidal dimers under quasi-two-dimensional confinement. *Langmuir* **2009**, *25* (13), 7193-7195.

[65]. Forster, J. D.; Park, J.-G.; Mittal, M.; Noh, H.; Schreck, C. F.; O'Hern, C. S.; Cao, H.; Furst, E. M.; Dufresne, E. R., Assembly of optical-scale dumbbells into dense photonic crystals. *ACS Nano* **2011**, *5* (8), 6695-6700.

[66]. Panczyk, M. M.; Park, J.-G.; Wagner, N. J.; Furst, E. M., Two-dimensional directed assembly of dicolloids. *Langmuir* **2012**, *29* (1), 75-81.

[67]. Nagao, D.; Sugimoto, M.; Okada, A.; Ishii, H.; Konno, M.; Imhof, A.; van Blaaderen, A., Directed orientation of asymmetric composite dumbbells by electric field induced assembly. *Langmuir* **2012**, *28* (16), 6546-6550.

[68]. Peng, B.; Vutukuri, H. R.; van Blaaderen, A.; Imhof, A., Synthesis of fluorescent monodisperse non-spherical dumbbell-like model colloids. *J. Mater. Chem.* **2012**, *22* (41), 21893-21900.

[69]. Demirörs, A. F.; Johnson, P. M.; van Kats, C. M.; van Blaaderen, A.; Imhof, A., Directed self-assembly of colloidal dumbbells with an electric field. *Langmuir* **2010**, *26* (18), 14466-14471.

[70]. Murthy, C. S.; Singer, K.; Klein, M. L.; McDonald, I. R., Pairwise additive effective potentials for nitrogen. *Molecular Physics* **1980**, *41* (6), 1387-1399.

[71]. Velikov, K. P.; van Dillen, T.; Polman, A.; van Blaaderen, A., Photonic crystals of shape-anisotropic colloidal particles. *Applied Physics Letters* **2002**, *81* (5), 838-840.

[72]. Hosein, I. D.; John, B. S.; Lee, S. H.; Escobedo, F. A.; Liddell, C. M., Rotator and crystalline films via self-assembly of short-bond-length colloidal dimers. *Journal of Materials Chemistry* **2009**, *19* (3), 344-349.

[73]. Li, Z.-Y.; Gu, B.-Y.; Yang, G.-Z., Large absolute band gap in 2d anisotropic photonic crystals. *Phys. Rev. Lett.* **1998**, *81* (12), 2574.

[74]. Shibayama, M.; Tanaka, T., Volume phase transition and related phenomena of polymer gels. In *Responsive gels: Volume transitions i*, Springer: **1993**; pp 1-62.

[75]. Kratz, K.; Hellweg, T.; Eimer, W., Structural changes in pnipam microgel particles as seen by sans, dls, and em techniques. *Polym. J.* **2001**, *42* (15), 6631-6639.

[76]. Kratz, K.; Eimer, W., Swelling properties of colloidal poly (n-isopropylacrylamide) microgels in solution. *Berichte der Bunsengesellschaft für physikalische Chemie* **1998**, *102* (6), 848-854.

[77]. Nagao, D.; van Kats, C. M.; Hayasaka, K.; Sugimoto, M.; Konno, M.; Imhof, A.; van Blaaderen, A., Synthesis of hollow asymmetrical silica dumbbells with a movable inner core. *Langmuir* **2010**, *26* (7), 5208-5212.

[78]. Mulvaney, P.; Giersig, M.; Ung, T.; Liz-Marzán, L. M., Direct observation of chemical reactions in silica-coated gold and silver nanoparticles. *Adv. Mater.* **1997**, *9* (7), 570-575.

[79]. Gu, H.; Zheng, R.; Zhang, X.; Xu, B., Facile one-pot synthesis of bifunctional heterodimers of nanoparticles: A conjugate of quantum dot and magnetic nanoparticles. *J. Am. Chem. Soc.* **2004**, *126* (18), 5664-5665.

[80]. Liddell, C. M.; Summers, C. J., Monodispersed zns dimers, trimers, and tetramers for lower symmetry photonic crystal lattices. *Adv. Mater.* **2003**, *15* (20), 1715-1719.

[81]. Yin, Y.; Zhou, S.; You, B.; Wu, L., Facile fabrication and self-assembly of polystyrene–silica asymmetric colloid spheres. *J. Polym. Sci., Part A: Polym. Chem.* **2011**, *49* (15), 3272-3279.

[82]. Hoffmann, M.; Siebenburger, M.; Harnau, L.; Hund, M.; Hanske, C.; Lu, Y.; Wagner, C. S.; Drechsler, M.; Ballauff, M., Thermoresponsive colloidal molecules. *Soft Matter* **2010**, *6* (6), 1125-1128.

[83]. Kim, J.-W.; Larsen, R. J.; Weitz, D. A., Synthesis of nonspherical colloidal particles with anisotropic properties. *J. Am. Chem. Soc.* **2006**, *128* (44), 14374-14377.

[84]. Sheu, H. R.; El-Aasser, M. S.; Vanderhoff, J. W., Phase separation in polystyrene latex interpenetrating polymer networks. *J. Polym. Sci., Part A: Polym. Chem.* **1990**, *28* (3), 629-651.

[85]. Chen, Y. C.; Dimonie, V.; El-Aasser, M. S., Effect of interfacial phenomena on the development of particle morphology in a polymer latex system. *Macromolecules* **1991**, *24* (13), 3779-3787.

[86]. Mock, E. B.; Zukoski, C. F., Emulsion polymerization routes to chemically anisotropic particles. *Langmuir* **2010**, *26* (17), 13747-13750.

[87]. Crassous, J. J.; Dietsch, H.; Pfleiderer, P.; Malik, V.; Diaz, A.; Hirshi, L. A.; Drechsler, M.; Schurtenberger, P., Preparation and characterization of ellipsoidal-shaped thermosensitive microgel colloids with tailored aspect ratios. *Soft Matter* **2012**, *8* (13), 3538-3548.

[88]. Hoffmann, M.; Lu, Y.; Schrinner, M.; Ballauff, M.; Harnau, L., Dumbbell-shaped polyelectrolyte brushes studied by depolarized dynamic light scattering. *J. Phys. Chem. B* **2008**, *112* (47), 14843-14850.

[89]. Wei, H.; Cheng, S. X.; Zhang, X. Z.; Zhuo, R. X., Thermo-sensitive polymeric micelles based on poly(n-isopropylacrylamide) as drug carriers. *Prog. Polym. Sci.* **2009**, *34* (9), 893-910.

[90]. Hu, J.; Zhou, S.; Sun, Y.; Fang, X.; Wu, L., Fabrication, properties and applications of janus particles. *Chem. Soc. Rev.* **2012**, *41* (11), 4356-4378.

[91]. Walther, A.; Müller, A. H. E., Janus particles: Synthesis, self-assembly, physical properties, and applications. *Chem. Rev.* **2013**, *113* (7), 5194-5261.

[92]. Mitragotri, S., In drug delivery, shape does matter. *Pharm. Res.* **2009**, *26* (1), 232-234.

[93]. Mitragotri, S.; Lahann, J., Physical approaches to biomaterial design. *Nat Mater* **2009**, *8* (1), 15-23.

[94]. Skotheim, J.; Secomb, T., Red blood cells and other nonspherical capsules in shear flow: Oscillatory dynamics and the tank-treading-to-tumbling transition. *Phys. Rev. Lett.* **2007**, *98* (7), 078301.

[95]. Hellweg, T.; Dewhurst, C. D.; Brückner, E.; Kratz, K.; Eimer, W., Colloidal crystals made of poly(n -isopropylacrylamide) microgel particles. *Colloid & Polymer Science* **2000**, *278* (10), 972-978.

[96]. Pelton, R., Temperature-sensitive aqueous microgels. *Adv. Colloid Interface Sci.* **2000**, *85* (1), 1-33.

[97]. Okubo, T.; Suzuki, D.; Yamagata, T.; Katsuno, A.; Sakurai, M.; Kimura, H.; Tsuchida, A., Colloidal crystallization of thermo-sensitive gel spheres of poly (n-isopropyl acrylamide). *Colloid. Polym. Sci.* **2011**, *289* (3), 291-299.

[98]. Suzuki, D.; Horigome, K.; Yamagata, T.; Shibata, K.; Tsuchida, A.; Okubo, T., Colloidal crystallization of thermo-sensitive gel spheres of poly (n-isopropyl acrylamide). Influence of degree of cross-linking of the gels. *Colloid. Polym. Sci.* **2011**, *289* (17-18), 1799-1808.

[99]. Senff, H.; Richtering, W.; Norhausen, C.; Weiss, A.; Ballauff, M., Rheology of a temperature sensitive core−shell latex. *Langmuir* **1998**, *15* (1), 102-106.

[100]. Crassous, J. J.; Régisser, R.; Ballauff, M.; Willenbacher, N., Characterization of the viscoelastic behavior of complex fluids using the piezoelastic axial vibrator. *J. Rheo.* **2005**, *49* (4), 851-863.

[101]. Dingenouts, N.; Seelenmeyer, S.; Deike, I.; Rosenfeldt, S.; Ballauff, M.; Lindner, P.; Narayanan, T., Analysis of thermosensitive core-shell colloids by small-angle neutron scattering including contrast variation. *PCCP* **2001**, *3* (7), 1169-1174.

[102]. Heskins, M.; Guillet, J. E., Solution properties of poly (n-isopropylacrylamide). *Journal of Macromolecular Science—Chemistry* **1968**, *2* (8), 1441-1455.

[103]. Neely, W. B., Solution properties of polysaccharides. Iv. Molecular weight and aggregate formation in methylcellulose solutions. *Journal of Polymer Science Part A: General Papers* **1963**, *1* (1), 311-320.

[104]. Kujawa, P.; Winnik, F. M., Volumetric studies of aqueous polymer solutions using pressure perturbation calorimetry: A new look at the temperature-induced phase transition of poly(n-isopropylacrylamide) in water and d2o. *Macromolecules* **2001**, *34* (12), 4130-4135.

[105]. Hooper, H. H.; Yu, J.; Sassi, A. P.; Soane, D. S., Viscosity transitions in aqueous suspensions of hydrogel microspheres. *J. Appl. Polym. Sci.* **1997**, *63* (10), 1369-1372.

[106]. Öle Kiminta, D.; Luckham, P.; Lenon, S., The rheology of deformable and thermoresponsive microgel particles. *Poly* **1995**, *36* (25), 4827-4831.

[107]. Senff, H.; Richtering, W., Influence of cross-link density on rheological properties of temperature-sensitive microgel suspensions. *Colloid. Polym. Sci.* **2000**, *278* (9), 830-840.

[108]. Crassous, J. J.; Rochette, C. N.; Wittemann, A.; Schrinner, M.; Ballauff, M.; Drechsler, M., Quantitative analysis of polymer colloids by cryo-transmission electron microscopy. *Langmuir* **2009**, *25* (14), 7862-7871.

[109]. Seelenmeyer, S.; Deike, I.; Rosenfeldt, S.; Norhausen, C.; Dingenouts, N.; Ballauff, M.; Narayanan, T.; Lindner, P., Small-angle x-ray and neutron scattering studies of the volume phase transition in thermosensitive core-shell colloids. *J. Chem. Phys.* **2001**, *114* (23), 10471-10478.

[110]. Karg, M.; Hellweg, T., New "smart" poly(nipam) microgels and nanoparticle microgel hybrids: Properties and advances in characterisation. *Curr. Opin. Colloid Interface Sci.* **2009**, *14* (6), 438-450.

[111]. Ballauff, M., Saxs and sans studies of polymer colloids. *Curr. Opin. Colloid Interface Sci.* **2001**, *6* (2), 132-139.

[112]. Wu, S.; Dzubiella, J.; Kaiser, J.; Drechsler, M.; Guo, X.; Ballauff, M.; Lu, Y., Thermosensitive au-pnipa-nanopartikel mit "dotter-schale"-architektur: Katalysatoren mit einstellbarer selektivität. *Angew. Chem.* **2012**, *124* (9), 2272-2276.

[113]. Lu, Y.; Wittemann, A.; Ballauff, M.; Drechsler, M., Preparation of polystyrene-poly (n-isopropylacrylamide)(ps-pnipa) core-shell particles by photoemulsion polymerization. *Macromol. Rapid Commun.* **2006**, *27* (14), 1137-1141.

[114]. Berne, B. J.; Pecora, R., *Dynamic light scattering: With applications to chemistry, biology, and physics*. Courier Dover Publications: **2000**.

[115]. Russel, W. B.; Saville, D. A.; Schowalter, W. R., Brownian motion. *Colloidal Dispersions* **1989**, *3*.

[116]. Einstein, A., *Investigations on the theory of the brownian movement*. DoverPublications. com: **1956**.

[117]. Löwen, H., Brownian dynamics of hard spherocylinders. *Phys. Rev. E* **1994**, *50* (2), 1232.

[118]. Perrin, F., Mouvement brownien d'un ellipsoide-i. Dispersion diélectrique pour des molécules ellipsoidales. *J. phys. radium* **1934**, *5* (10), 497-511.

[119]. Perrin, F., Mouvement brownien d'un ellipsoide (ii). Rotation libre et dépolarisation des fluorescences. Translation et diffusion de molécules ellipsoidales. *J. phys. radium* **1936**, *7* (1), 1-11.

[120]. Debye, P. *Polar molecules*; Dover: **1929**.

[121]. Favro, L. D., Theory of the rotational brownian motion of a free rigid body. *Phys. Rev.* **1960**, *119* (1), 53-62.

[122]. Pecora, R., *Dynamic light scattering: Applications of photon correlation spectroscopy*. Springer: **1985**.

[123]. Tirado, M. M.; Martínez, C. L.; de la Torre, J. G., Comparison of theories for the translational and rotational diffusion coefficients of rod-like macromolecules. Application to short DNA fragments. *J. Chem. Phys.* **1984**, *81* (4), 2047-2052.

[124]. García de la Torre, J.; del Rio Echenique, G.; Ortega, A., Improved calculation of rotational diffusion and intrinsic viscosity of bead models for macromolecules and nanoparticles. *J. Phys. Chem. B* **2007**, *111* (5), 955-961.

[125]. Kirkwood, J. G., The general theory of irreversible processes in solutions of macromolecules. *J. Polym. Sci.* **1954**, *12*, 1-14.

[126]. Riseman, J.; Kirkwood, J., The statistical mechanical theory of irreversible processes in solutions of macromolecules. *Rheology: theory and applications* **1956**, *1*.

[127]. Bloomfield, V.; Dalton, W.; Van Holde, K., Frictional coefficients of multisubunit structures. I. Theory. *Biopolymers* **1967**, *5* (2), 135-148.

[128]. Filson, D. P.; Bloomfield, V. A., Shell model calculations of rotational diffusion coefficients. *Biochemistry (Mosc).* **1967**, *6* (6), 1650-1658.

[129]. Bloomfield, V.; Van Holde, K.; Dalton, W., Frictional coefficients of multisubunit structures. Ii. Application to proteins and viruses. *Biopolymers* **1967**, *5* (2), 149-159.

[130]. Bloomfield, V. A.; Filson, D. P. *Shell model calculations of translational and rotational frictional coefficients*, J. Polym. Sci. Pol. Sym., Wiley Online Library: **1968**; pp 73-83.

[131]. Carrasco, B.; García de la Torre, J., Hydrodynamic properties of rigid particles: Comparison of different modeling and computational procedures. *J. Biophys.* **1999**, *76* (6), 3044-3057.

[132]. Heptner, N. Ph.D thesis. Ph.D thesis Humboldt University Berlin **2014**.

[133]. Brenner, H., Coupling between the translational and rotational brownian motions of rigid particles of arbitrary shape: Ii. General theory. *J. Colloid Interface Sci.* **1967**, *23* (3), 407-436.

[134]. Rotne, J.; Prager, S., Variational treatment of hydrodynamic interaction in polymers. *J. Chem. Phys.* **1969**, *50* (11), 4831-4837.

[135]. Garcia de la Torre, J.; Carrasco, B., Hydrodynamic properties of rigid macromolecules composed of ellipsoidal and cylindrical subunits. *Biopolymers* **2002**, *63* (3), 163-167.

[136]. Barnes, H. A.; Hutton, J. F.; Walters, K., *An introduction to rheology*. Elsevier: **1989**; Vol. 3.

[137]. Wagner, N. J.; Mewis J., *Colloidal suspension rheology* Cambridge University Press: **2012**.

[138]. Formaggia, L.; Gerbeau, J. F.; Nobile, F.; Quarteroni, A., On the coupling of 3d and 1d navier–stokes equations for flow problems in compliant vessels. *Comput. Methods Appl. Mech. Eng.* **2001**, *191* (6–7), 561-582.

[139]. Feigin, L.; Svergun, D. I.; Taylor, G. W., *Structure analysis by small-angle x-ray and neutron scattering*. Springer: **1987**.

[140]. Hayter, J. B.; Penfold, J., Determination of micelle structure and charge by neutron small-angle scattering. *Colloid. Polym. Sci.* **1983**, *261* (12), 1022-1030.

[141]. Hayter, J. B.; Penfold, J., Use of viscous shear alignment to study anisotropic micellar structure by small-angle neutron scattering. *J. Phys. Chem.* **1984**, *88* (20), 4589-4593.

[142]. Kirchhoff, T.; Löwen, H.; Klein, R., Dynamical correlations in suspensions of charged rodlike macromolecules. *Phys. Rev. E* **1996**, *53* (5), 5011.

[143]. Eberle, A. P. R.; Porcar, L., Flow-sans and rheo-sans applied to soft matter. *Curr. Opin. Colloid Interface Sci.* **2012**, *17* (1), 33-43.

[144]. Weigandt, K. M.; Pozzo, D. C.; Porcar, L., Structure of high density fibrin networks probed with neutron scattering and rheology. *Soft Matter* **2009**, *5* (21), 4321-4330.

[145]. Weigandt, K. M.; Porcar, L.; Pozzo, D. C., In situ neutron scattering study of structural transitions in fibrin networks under shear deformation. *Soft Matter* **2011**, *7* (21), 9992-10000.

[146]. Schmidt, G.; Nakatani, A. I.; Butler, P. D.; Karim, A.; Han, C. C., Shear orientation of viscoelastic polymer-clay solutions probed by flow birefringence and sans. *Macromolecules* **2000**, *33* (20), 7219-7222.

[147]. Laun, H. M.; Bung, R.; Hess, S.; Loose, W.; Hess, O.; Hahn, K.; Hadicke, E.; Hingmann, R.; Schmidt, F.; Lindner, P., Rheological and small angle neutron scattering investigation of shear-induced particle structures of concentrated polymer dispersions submitted to plane poiseuille and couette flow. *J. Rheol.* **1992**, *36* (4), 743-787.

[148]. Butler, P., Shear induced structures and transformations in complex fluids. *Curr. Opin. Colloid Interface Sci.* **1999**, *4* (3), 214-221.

[149]. Pieranski, P., Colloidal crystals. *Contemp. Phys.* **1983**, *24* (1), 25-73.

[150]. Xia, Y.; Gates, B.; Yin, Y.; Lu, Y., Monodispersed colloidal spheres: Old materials with new applications. *Adv. Mater.* **2000**, *12* (10), 693-713.

[151]. Pusey, P. N.; Vanmegen, W.; Bartlett, P.; Ackerson, B. J.; Rarity, J. G.; Underwood, S. M., Structure of crystals of hard colloidal spheres. *Phys. Rev. Lett.* **1989**, *63* (25), 2753-2756.

[152]. Ackerson, B. J., Shear induced order and shear processing of model hard sphere suspensions. *J. Rheol.* **1990**, *34* (4), 553-590.

[153]. Hoffman, R. L., Discontinuous and dilatant viscosity behavior in concentrated suspensions. Ii. Theory and experimental tests. *J. Colloid Interface Sci.* **1974**, *46* (3), 491-506.

[154]. Ackerson, B. J.; Clark, N. A., Shear-induced partial translational ordering of a colloidal solid. *Phys. Rev. A* **1984**, *30* (2), 906-918.

[155]. Ackerson, B. J.; Pusey, P. N., Shear-induced order in suspensions of hard-spheres. *Phys. Rev. Lett.* **1988**, *61* (8), 1033-1036.

[156]. Besseling, T.; Hermes, M.; Fortini, A.; Dijkstra, M.; Imhof, A.; van Blaaderen, A., Oscillatory shear-induced 3d crystalline order in colloidal hard-sphere fluids. *Soft Matter* **2012**, *8* (26), 6931-6939.

[157]. Erpenbeck, J. J., Shear viscosity of the hard-sphere fluid via nonequilibrium molecular dynamics. *Phys. Rev. Lett.* **1984**, *52* (15), 1333.

[158]. Woodcock, L. V., Origins of thixotropy. *Phys. Rev. Lett.* **1985**, *54* (14), 1513-1516.

[159]. Heyes, D. M., Shear thinning and thickening of the lennard-jones liquid. A molecular dynamics study. *J. Chem. Soc., Faraday Trans.* **1986**, *82* (9), 1365-1383.

[160]. Yan, Y.; Dhont, J.; Smits, C.; Lekkerkerker, H., Oscillatory-shear-induced order in nonaqueous dispersions of charged colloidal spheres. *Phys. Stat. Mech. Appl.* **1994**, *202* (1), 68-80.

[161]. Loose, W.; Ackerson, B. J., Model calculations for the analysis of scattering data from layered structures. *J. Chem. Phys.* **1994**, *101* (9), 7211-7220.

[162]. Clark, N. A.; Ackerson, B. J., Observation of the coupling of concentration fluctuations to steady-state shear flow. *Phys. Rev. Lett.* **1980**, *44* (15), 1005-1008.

[163]. Dhont, J. K., *An introduction to dynamics of colloids*. Elsevier: **1996**.

[164]. Allen, M. P.; Evans, G. T.; Frenkel, D.; Mulder, B., Hard convex body fluids. *AdChP* **1993**, *86*, 1-166.

[165]. Steinhardt, P. J.; Nelson, D. R.; Ronchetti, M., Bond-orientational order in liquids and glasses. *Phys. Rev. B* **1983**, *28* (2), 784-805.

[166]. Wang, Y.; Teitel, S.; Dellago, C., Melting of icosahedral gold nanoclusters from molecular dynamics simulations. *J. Chem. Phys.* **2005**, *122* (21), -.

[167]. Bourgeat-Lami, E.; Tissot, I.; Lefebvre, F., Synthesis and characterization of sioh-functionalized polymer latexes using methacryloxy propyl trimethoxysilane in emulsion polymerization. *Macromolecules* **2002**, *35* (16), 6185-6191.

[168]. King, R. J.; P.Talim, S., *J. Phys. E: Instrum* **1971**, *4*.

[169]. Degiorgio, V.; Piazza, R.; Corti, M.; Stavans, J., Dynamic light scattering study of concentrated dispersions of anisotropic spherical colloids. *J. Chem. Soc., Faraday Trans.* **1991**, *87* (3), 431-434.

[170]. Bolhuis, P.; Frenkel, D., Tracing the phase boundaries of hard spherocylinders. *Journal of Chemical Physics* **1997**, *106* (2), 666-687.

[171]. Imhof, A.; van Blaaderen, A.; Dhont, J. K. G., Shear melting of colloidal crystals of charged spheres studied with rheology and polarizing microscopy. *Langmuir* **1994**, *10* (10), 3477-3484.

[172]. Chen, L. B.; Zukoski, C. F.; Ackerson, B. J.; Hanley, H. J. M.; Straty, G. C.; Barker, J.; Glinka, C. J., Structural-changes and orientational order in a sheared colloidal suspension. *Phys. Rev. Lett.* **1992**, *69* (4), 688-691.

[173]. Vermant, J.; Solomon, M. J., Flow-induced structure in colloidal suspensions. *J. Phys.: Condens. Matter* **2005**, *17* (4), R187-R216.

[174]. Zhang, R.; Schweizer, K. S., Theory of coupled translational-rotational glassy dynamics in dense fluids of uniaxial particles. *Phys. Rev. E* **2009**, *80* (1).

[175]. Falk, M. L.; Langer, J. S.; Pechenik, L., Thermal effects in the shear-transformation-zone theory of amorphous plasticity:Comparisons to metallic glass data. *Phys. Rev. E* **2004**, *70* (1), 011507.

[176]. Fuchs, M.; Cates, M. E., Theory of nonlinear rheology and yielding of dense colloidal suspensions. *Phys. Rev. Lett.* **2002**, *89* (89), 248304.

[177]. Fuchs, M.; Cates, M. E., Schematic models for dynamic yielding of sheared colloidal glasses. *Faraday Discuss.* **2003**, *123*, 267-286.

[178]. Haw, M. D.; Poon, W. C. K.; Pusey, P. N.; Hebraud, P.; Lequeux, F., Colloidal glasses under shear strain. *Phys. Rev. E* **1998**, *58* (4), 4673-4682.

[179]. Petekidis, G.; Moussaid, A.; Pusey, P. N., Rearrangements in hard-sphere glasses under oscillatory shear strain. *Phys. Rev. E* **2002**, *66* (5).

[180]. Pham, K. N.; Petekidis, G.; Vlassopoulos, D.; Egelhaaf, S. U.; Poon, W. C. K.; Pusey, P. N., Yielding behavior of repulsion- and attraction-dominated colloidal glasses. *J. Rheo.* **2008**, *52* (2), 649-676.

[181]. Le Grand, A.; Petekidis, G., Effects of particle softness on the rheology and yielding of colloidal glasses. *Rheol. Acta* **2008**, *47* (5), 579-590.

[182]. Kramb, R. C.; Zukoski, C. F., Nonlinear rheology and yielding in dense suspensions of hard anisotropic colloids. *J. Rheol.* **2011**, *55* (5), 1069-1084.

[183]. Zhang, R.; Schweizer, K. S., Dynamic free energies, cage escape trajectories, and glassy relaxation in dense fluids of uniaxial hard particles. *J. Chem. Phys.* **2010**, *133* (10).

[184]. Kramb, R. C.; Zukoski, C. F., Exploration of the volume fraction above which suspensions of spherical and weakly anisotropic colloid particles cannot flow. *J. Rheol.* **2011**, *55* (5), 1085-1101.

[185]. Kramb, R. C.; Zukoski, C. F., Yielding in dense suspensions: Cage, bond, and rotational confinements. *J. Phys.: Condens. Matter* **2011**, *23* (3).

[186]. Chen, K.; Schweizer, K. S., Theory of yielding, strain softening, and steady plastic flow in polymer glasses under constant strain rate deformation. *Macromolecules* **2011**, *44* (10), 3988-4000.

[187]. Kramb, R. C.; Zhang, R.; Schweizer, K. S.; Zukoski, C. F., Glass formation and shear elasticity in dense suspensions of repulsive anisotropic particles. *Phys. Rev. Lett.* **2010**, *105* (5), 055702.

[188]. Koumakis, N.; Petekidis, G., Two step yielding in attractive colloids: Transition from gels to attractive glasses. *Soft Matter* **2011**, *7* (6), 2456-2470.

[189]. Haw, M. D.; Poon, W. C. K.; Pusey, P. N., Direct observation of oscillatory-shear-induced order in colloidal suspensions. *Phys. Rev. E* **1998**, *57* (6), 6859-6864.

[190]. Cheng, X.; Xu, X.; Rice, S. A.; Dinner, A. R.; Cohen, I., Assembly of vorticity-aligned hard-sphere colloidal strings in a simple shear flow. *Proc. Natl. Acad. Sci.* **2012**, *109* (1), 63-67.

[191]. Förster, S.; Konrad, M.; Lindner, P., Shear thinning and orientational ordering of wormlike micelles. *Phys. Rev. Lett.* **2005**, *94* (1), 017803.

[192]. Trebbin, M.; Steinhauser, D.; Perlich, J.; Buffet, A.; Roth, S. V.; Zimmermann, W.; Thiele, J.; Förster, S., Anisotropic particles align perpendicular to the flow direction in narrow microchannels. *Proc. Natl. Acad. Sci.* **2013**, *110* (17), 6706-6711.

[193]. Kalus, J.; Hoffman, H., Nearest neighbor order in an aligned solution of interacting rod-like micelles. *J. Chem. Phys.* **1987**, *87* (1), 714-722.

[194]. Dux, C.; Versmold, H., Light diffraction from shear ordered colloidal dispersions. *Phys. Rev. Lett.* **1997**, *78* (9), 1811-1814.

[195]. Solomon, T.; Solomon, M. J., Stacking fault structure in shear-induced colloidal crystallization. *J. Chem. Phys.* **2006**, *124*, 134905.

[196]. Paulin, S. E.; Ackerson, B. J.; Wolfe, M. S., Equilibrium and shear induced nonequilibrium phase behavior of pmma microgel spheres. *J. Colloid Interface Sci.* **1996**, *178* (1), 251-262.

[197]. Shi, J.; Du, C.; Shi, J.; Wang, Y.; Cao, S., Hollow multilayer microcapsules for ph-/thermally responsive drug delivery using aliphatic poly (urethane-amine) as smart component. *Macromol. Biosci.* **2013**, *13* (4), 494-502.

[198]. Nayak, S.; Gan, D.; Serpe, M. J.; Lyon, L. A., Hollow thermoresponsive microgels. *Small* **2005**, *1* (4), 416-421.

[199]. Wu, S.; Dzubiella, J.; Kaiser, J.; Drechsler, M.; Guo, X.; Ballauff, M.; Lu, Y., Thermosensitive au-pnipa yolk–shell nanoparticles with tunable selectivity for catalysis. *Angew. Chem. Int. Ed.* **2012**, *51* (9), 2229-2233.

[200]. Zhang, F.; Wang, C. C., Preparation of thermoresponsive core-shell polymeric microspheres and hollow pnipam microgels. *Colloid. Polym. Sci.* **2008**, *286* (8-9), 889-895.

[201]. Zhu, D.; Wang, F.; Gao, C.; Xu, Z., Construction of ps/pnipam core-shell particles and hollow spheres by using hydrophobic interaction and thermosensitive phase separation. *Front. Chem. Sci. Eng.* **2008**, *2* (3), 253-256.

[202]. Wu, D.; Xu, F.; Sun, B.; Fu, R.; He, H.; Matyjaszewski, K., Design and preparation of porous polymers. *Chem. Rev.* **2012**, *112* (7), 3959-4015.

[203]. Decher, G.; Hong, J. D., Buildup of ultrathin multilayer films by a self-assembly process .2. Consecutive adsorption of anionic and cationic bipolar amphiphiles and polyelectrolytes on charged surfaces. *PCCP* **1991**, *95* (11), 1430-1434.

[204]. Glinel, K.; Sukhorukov, G. B.; Möhwald, H.; Khrenov, V.; Tauer, K., Thermosensitive hollow capsules based on thermoresponsive polyelectrolytes. *Macromol. Chem. Phys.* **2003**, *204* (14), 1784-1790.

[205]. Caruso, F., Hollow capsule processing through colloidal templating and self-assembly. *Chem. Eur. J.* **2000**, *6* (3), 413-419.

[206]. Zha, L.; Zhang, Y.; Yang, W.; Fu, S., Monodisperse temperature-sensitive microcontainers. *Adv. Mater.* **2002**, *14* (15), 1090-1092.

[207]. Qian, J.; Wu, F., Thermosensitive pnipam semi-hollow spheres for controlled drug release. *J. Mater. Chem. B* **2013**, *1* (28), 3464-3469.

[208]. Shchepelina, O.; Kozlovskaya, V.; Kharlampieva, E.; Mao, W.; Alexeev, A.; Tsukruk, V. V., Anisotropic micro- and nano-capsules. *Macromol. Rapid Commun.* **2010**, *31* (23), 2041-2046.

[209]. Decuzzi, P.; Godin, B.; Tanaka, T.; Lee, S. Y.; Chiappini, C.; Liu, X.; Ferrari, M., Size and shape effects in the biodistribution of intravascularly injected particles. *J. Controlled Release* **2010**, *141* (3), 320-327.

[210]. Best, J. P.; Yan, Y.; Caruso, F., The role of particle geometry and mechanics in the biological domain. *Adv. Healthc. Mater.* **2012**, *1* (1), 35-47.

[211]. Hall, C. E., Electron densitometry of stained virus particles. *J. Biophys. Biochem. Cytol.* **1955**, *1* (1), 1-12.

[212]. Bolisetty, S.; Hoffmann, M.; Lekkala, S.; Hellweg, T.; Ballauff, M.; Harnau, L., Coupling of rotational motion with shape fluctuations of core-shell microgels having tunable softness. *Macromolecules* **2009**, *42* (4), 1264-1269.

[213]. Tanner, P.; Baumann, P.; Enea, R.; Onaca, O.; Palivan, C.; Meier, W., Polymeric vesicles: From drug carriers to nanoreactors and artificial organelles. *Acc. Chem. Res.* **2011**, *44* (10), 1039-1049.

[214]. Mul, G.; Zwijnenburg, A.; van der Linden, B.; Makkee, M.; Moulijn, J. A., Stability and selectivity of au/tio$_2$ and au/tio$_2$/sio$_2$ catalysts in propene epoxidation: An *in situ* ft-ir study. *J. Catal.* **2001**, *201* (1), 128-137.

[215]. Ballauff, M.; Lu, Y., "Smart" nanoparticles: Preparation, characterization and applications. *Polym. J.* **2007**, *48* (7), 1815-1823.

[216]. Kholodenko, A. L.; Douglas, J. F., Generalized stokes-einstein equation for spherical particle suspensions. *Phys. Rev. E* **1995**, *51* (2), 1081-1090.

List of Figures

Figure 1.1.1 Phase diagram of hard spheres .[9] As shown in the top part, monodisperse hard spheres with $\phi > \phi_{freeze}$ crystallize,[23] and the glass transition (in the bottom part) is at ϕ_g~0.58.[2, 24–25] Random-close packing of the spheres is reached at ϕ_{rcp} = 0.64 and a dense packing of spheres is at ϕ_{cp} = 0.74..... 1

Figure 1.1.2 Scheme of the thermosensitive core-shell microgels. The PNIPA shell is attached onto the surface to the PS cores. At room temperature of ca. 25 °C, the PNIPA network takes up the dispersion medium water, which will be mostly expelled when the temperature is raised above 32 °C.[36] 2

Figure 1.2.1 Schematic figure of a hard dumbbell that consists of two interpenetrating identical spheres. *L* denotes the center to center distance and *D* represents the diameter of one composed sphere. The particle's anisotropy is defined by aspect ratio, $L^* = L/D$..... 3

Figure 1.2.2 The phase diagram of hard dumbbells in the number density ρ^* (and the packing fraction ϕ) versus $L^* = L/D$ representation.[52] *F* denotes the fluid phase and CP1 means the periodic crystal. The aperiodic phase (aper) is stable only in a narrow region of the phase diagram. The stable fcc type plastic crystal is denoted by filled squares, the hcp plastic crystal phase is denoted by empty squares. The coexistence densities for $L^* < 0.9$ are taken from Refs. [49-50]..... 4

Figure 1.2.3 Unit cells for various structures of dumbbells crystals. They were obtained by sedimentation of charged dumbbells in a refractive index matching solvent within the presence of an electric field. (a) Tetragonal unit cell of dumbbell crystals formed from dumbbells with $L^* = 0.9$ in an electric field of 28 V_{rms}/mm. The crystal has a *P4/nmm* symmetry with space group number 129. (b) Based-centered monoclinic phase observed for dumbbells with $L^* = 0.7$ in a field of 23 V_{rms}/mm and for dumbbells with $L^* = 0.44$ in a field of 78 V_{rms}/mm. (c) Based-centered monoclinic phase observed less frequently for charged dumbbells of $L^* = 0.44$. (d) Body-centered-tetragonal (bct) phase observed for dumbbells with $L^* = 0.7$ and $L^* = 0.44$ at higher electric fields. 'E' stands for the electric field and 'g' for the direction of gravity.[69] 6

Figure 1.2.4 Schematic representation for the reversible transition of thermosensitive dumbbell-shaped microgels from fluid-to-solid via adjusting temperature from 40°C to 10°C. The dumbbell-shaped microgels have a thermosensitive PNIPA shell attached onto the surface of dumbbell-shaped cores, which is swollen by water at low temperature e.g. 10 °C. However, water will be expelled when the temperature is increased to 40°C.[36, 75-76] In this way, the volume fraction of the particles can be adjusted by temperature. 7

Figure 1.3.1 (a) Scheme of dumbbell-shaped microgels that can serve as the hard dumbbell model system. The residual charges from the synthesis is screened by the addition of salt (potassium chloride, KCl), resulting in sterically stabilized hard dumbbells. The diameter of one sphere is marked as D, center to center distance is L, the thickness of PNIPA shell is L_H. For the dumbbell-shaped core, the radius of one composed sphere is denoted as R_C. (b) schematic illustration of thermosensitive Janus dumbbells that are prepared via the selective removal of THF using the dumbbell-shaped microgels as templates. The thermosensitive Janus dumbbells with well-defined morphology can also be used as the model system of hard dumbbells, which may have different phase behaviour from hard dumbbells with solid cores. 9

Figure 3.1.1 Illustration of the thermosensitivity of the dumbbell-shaped core-shell microgel, which consists of a dumbbell-shaped PS core and a thermosensitive PNIPA shell. The morphology of the core is proved not to change the temperature dependence of the PNIPA shell.[82] 13

Figure 3.1.2 Orientation of one single dumbbell particle with respect to Cartesian coordinate system with its origin at the center of the particle. The solid red line is along the major axis of the particle and u is defined as the unit vector along the major axis. The dashed line represents the projection of the hard dumbbells on the x-y plane. ϕ tracks the position of the projected end point on the x-y plane. 15

Figure 3.2.1 The light scattering setup with two pairs of commonly used polarization directions. Scattering geometry I: *VV* configuration with a polarizer of the vertical direction and an analyzer of the vertical direction. Scattering geometry II: *VH* configuration with a polarizer of the vertical direction and an analyzer of the horizontal direction. *V* and *H* refer to directions that are vertical and horizontal with respect to the scattering plane, respectively... 16

Figure 3.2.2 Two-dimensional analogy of the shell model for a hard dumbbell, which is seen as a shell of small identical beads (denoted by the small empty cycles). There are three possibilities to arrange the small beads: tangent to the inner face of the surface, centered on the surface or tangent to the outer surface (our choice). Owing to the limit of very small bead size, the small difference between these possibilities can vanish. 19

Figure 3.3.1 Shear flow between sliding (upper) and fixed (bottom) plates with a distance of h in between, and the upper plate moves with a velocity in V direction. A liquid is contained between the two parallel plates. 20

Figure 3.3.2 Oscillatory shear flow: a time dependent, sinusoidal deformation, $\gamma_t = \gamma_0 sin\omega t$ (the solid line) and the corresponding strain rate $\gamma_t = \gamma_0 \omega cos\omega t$ (denoted by the dashed line). δ is the phase angle that defined by the phase shift between stress and strain. .. 22

Figure 3.3.3 (a) Schematic illustration of the rheo-SANS setup with the commonly used Couette flow cell. ω and γ denote the angular frequency and the strain of the oscillatory shear applied by the rheometer, respectively. The coordinate frame with velocity(v), velocity gradient ($\bigtriangledown$v)and vorticity (e) directions is defined to describe the scattering planes for available geometries.[143] They are: (b) radial, (c) tangential and (d) e- $\bigtriangledown$v plane flow cell geometries that allow for scattering in e-v, e-$\bigtriangledown$v, $\bigtriangledown$v -v planes, respectively..... 25

Figure 3.4.1 Observed scattered intensity distributions of hard spheres undergoing oscillatory shear flow. The incident laser beam is parallel to the velocity gradient direction. (a) Threefold pattern produced by a fcc structure, (b) and its fcc twin structure, (c) sixfold pattern produced by a registered random stacking of layers, (d) fourfold pattern produced by a centering of slipping layers over the other, (e) scattering pattern by the string-like ordering, (f)scattering pattern with a diffuse Debye-Scherrer ring by the amorphous or liquid-like ordering.[152] 27

Figure 3.4.2 Geometric packing of hard spheres at low and high strains, corresponding to the shear-induced twinned fcc structure and the sliding layer phase. (a) and (b) refer to the twin structures having the characteristic …ABCA…stacking sequence. Registered randomly stacked layers having no characteristic…ACAB…stacking order. The layers may slip over one another along the zig-zag path as indicated in (c) or along the straight lines as marked in (d). (e) String-like ordering where the layers become disordered but regular spacing of particles along the velocity direction persists. (f) Amorphous or liquid-like equilibrium

ordering indicating the distortion of the isotropic equilibrium order when a shear flow is not present.[152] 29

Figure 3.4.3 Juxtaposition of the main predictions of the stacking model calculations. The relative intensity of the spots of the three innermost rings in the ***kv-ke***plane is indicated analogously to contour plots of real scattering data: (a) corresponds to random registered scattering (highly twinned fcc crystal); The sliding layers performing motion along zig-zag paths (b) for $0.58 < \phi < 0.64$ or straight lines(c) at $\phi < 0.58$.[132] 30

Figure 4.1.1 Illustration of the preparation routine for the thermosensitive dumbbell-shaped microgels that can serve as the hard dumbbell model system in this study. 34

Figure 4.1.2 TEM micrograph of the dumbbell-shaped PS cores (a) DPC_a (b) DPC_b. They are used as seeds for the preparation of the DPM_a microgels and the DPM_b microgels, respectively. 36

Figure 4.1.3 Cryo-TEM micrograph of a dumbbell-shaped PS core particle, a red line is drawn to indicate the major axis direction (a), and the corresponding normalized gray scale profile along the major axis (b), a black arrow is used to guide eyes to one shoulder on the right side of the gray profile. A homogeneous shell is observed on the core-shell structured part on the right side, which corresponds to the random copolymer of styrene and MPS. 37

Figure 4.1.4 Cryo-TEM images of the dumbbell-shaped microgels: (a) the DPM_a microgels and (b) the DPM_b microgels. The circles of dash line mark the particles with different orientations. The measurements are done at room temperature with T ~ 25 °C. 38

Figure 4.1.5 DDLS-relaxation time distributions (CONTIN-plots) of the DPC_a core (a) dispersed in water at 20 °C and the DPM_a microgel (c) dispersed in 50mM KCl solution at 25 °C calculated from the intensity autocorrelation functions. The corresponding relaxation processes are plotted as a function of the square of the scattering vector ($q2$) for the DPC_a core (b) and the DPM_a microgels (d). The symbols indicate that: DLS slow mode (open circle), DDLS slow mode (open triangle) and DDLS fast mode (open square) and the solid lines in (b) and (d) are the fitted data according to corresponding modes. 39

Figure 4.1.6 Temperature dependence of L_H for the dumbbell-shaped microgels dispersed in salt-free solutions (filled triangle) and 50 mM KCl solution (empty triangle) by DLS. The

filled square marks L_H measured by cryo-TEM at room temperature (T ~ 25 °C). In the temperature regime from 10 to 22.5 °C, L_H was found to decrease linearly with temperature (L_H = -1.57*T (°C) + 137.39; r^2 = 0.99). The corresponding L^* are denoted by filled circles.41

Figure 4.2.1 a) Crystallization of the DPM_a suspensions with various effective volume fractions (ϕ_{eff} = 0.50, 0.54, 0.59 from left to right) at 7 ± 1 °C and formed crystals are indicated by Bragg reflections (b) the corresponding phase diagram based on the visual observation. (c) Direct observation on crystallization of the DPM_b suspensions with ϕ_{eff} = 0.50, 0.55, 0.57 from left to right, and (d) its corresponding phase diagram. Dashed lines in (a) and (c) are used to mark the phase boundaries. The phase diagram achieved based on the linear extrapolation is denoted by solid line for the DPM_a suspension with L^* ~ 0.24 (b) and the DPM_b suspension with L^* ~ 0.30 (d).The filled triangles in (b) and (d) indicate the freezing and melting volume fractions predicted by the MC simulations[52] for hard dumbbells with L^* = 0.24 and 0.30, respectively. 44

Figure 4.2.2 The experimental phase diagram (denoted by the red squares) is compared with the prediction of MC simulations (solid black line[52]) for L^* = 0.24 and L^* = 0.30. The blue line is used to mark the corresponding L^*..... 45

Figure 4.2.3 Rheological behaviour of the DPM_a suspensions in different phases with various volume fractions: the time dependence of storage modulus *G'* (filled circles) and loss modulus *G"* (empty circles) were measured under oscillatory shear strain with γ_{max} = 1% and f = 1 Hz. Panels a), c), e) display the dependence of *G'* and *G"* on time for the DPM_a suspensions with ϕ of 0.40, 0.51, 0.63, respectively. The shear stress versus both increasing (upwards triangles) and decreasing (down wards triangles) shear rate of the DPM_a suspensions with ϕ_{eff} of 0.40, 0.51, 0.63 are shown in b), d), f), respectively. 47

Figure 4.2.4 Rheological behaviour of the DPM_b suspensions in different phases with various volume fractions: Shear stress versus both increasing (upwards triangles) and decreasing (down wards triangles) shear rate at ϕ of 0.36, 0.52, 0.64 are shown in a), c), e) respectively. The dependence of *G'* (filled sqaures) and G" (empty squares) on time are measured in oscillatory shear field with γ_{max} = 1% and f = 1 Hz. b), d), f) on the right side display the time dependent *G'* and *G"* of the DPM_b suspensions with ϕ of 0.36, 0.52, 0.64, respectively. 50

Figure 4.3.1 Time dependence of G' and G'' in the oscillatory shear field of f = 1 Hz and γ_{max} = 1% (a). The dependence of G' and G'' on frequency under oscillatory shear with γ = 1% after various t_w (b) and strain sweep with f = 1Hz after various t_w (c) of the hard dumbbell suspensions at ϕ_{eff} = 0.55. As for the frequency and strain sweep, the different waiting times are set according to time window (a). The upwards triangles mean G curve after t_w = 60 s, downwards triangles represent G curve after t_w = 3000 s and circles stand for G curve after t_w =10000 s. For all three sets of symbols, the filled ones refer to G' and the empty ones are for G''. 53

Figure 4.3.2 The yielding behaviour of the DPM_a suspension with $L^* \sim 0.24$ in the fully crystalline phase ϕ_{eff} = 0.60. It is measured in the oscillatory shear field with $f = 1$ *Hz* as a function of increasing γ (upwards triangles) and decreasing γ (downwards triangles). Filled triangles indicate storage modules, G' and empty triangles indicate loss modules, G''. 55

Figure 4.3.3 (a) Dependence of G' and G'' on increasing γ for the hard dumbbells with $L^* \sim$ 0.30 in the plastic crystalline phase under oscillatory shear of f = 1Hz (circles) and f = 5Hz (squares). This measurement is performed with default setting (100s/point). (b) The dependence of G' and G'' on γ of the hard dumbbells with $L^* \sim$ 0.30 in the plastic crystalline phase that is measured under oscillatory shear of f = 1Hz with 500 s/point. The filled symbols denote G', while open symbols represent G''. 56

Figure 4.4.1 Evolution of the plastic crystal (a) formed from the hard dumbbells with $L^* \sim$ 0.24 and ϕ_{eff} = 0.60 under oscillatory shears at fixed frequency (f = 1 Hz) increasing strain amplitudes. The applied strain amplitudes are chosen based on the dependence of G' and G'' on γ at: γ_{max} = 23.6% and Pe_r = 0.24 (b), γ_{max} = 50% and Pe_r = 0.52 (c), γ_{max} = 60% and Pe_r = 0.62 (d), γ_{max} = 116% and Pe_r = 1.20 (e) and γ_{max} = 500% and Pe_r = 5.2 (f), respectively. 59

Figure 4.4.2 2D scattering patterns of the hard dumbbell suspension in the plastic crystalline phase (ϕ_{eff} = 0.60) at rest (a) and in the oscillatory shear field with f = 1Hz and various strains (b) γ_{max} = 10%, Pe_r = 0.10 (c) γ_{max} = 19.4%, Pe_r = 0.20 (d) γ_{max} = 23.6%, Pe_r = 0.24 (e) γ_{max} = 42.3%, Pe_r = 0.44 over the first 600 oscillations and (f) the following 900 oscillations. (b), (c) and (d) correspond to the scattering averaging over the last 900 oscillation cycles at the respective shear strain. The experiment scatterings displayed here are recorded in the velocity-vorticity scattering plane. 62

Figure 4.4.3 (a) 2D experimental scattering pattern of hard dumbbells (ϕ_{eff} = 0.60) in an oscillatory shear field (f = 1 Hz, γ_{max} = 50%, Pe_r = 0.52). This pattern is rescaled by $q_x D$ to facilitate the comparison with the results of BD simulations. (b) The calculated 2D structure factors in the velocity-vorticity plane by BD simulations, averaging 75 oscillatory shear cycles with f = 15.3 Hz and γ_{max} = 15% and Pe_r = 2.28. (c) Simulation snapshots of sheared dumbbells with ϕ = 0.55 and L^* = 0.24 in the velocity-gradient plane after the application of 75 oscillatory shear cycles with f = 15.3 Hz and γ_{max} = 15% and Pe_r = 2.28. The three figures (from left to right) show that the oscillation is at a maximum displacement, at the equilibrium position and at the other maximum displacement, respectively. The layers are stacked in ABC sequence at one extreme position, while in ACB sequence at the other one. (d) The structure analysis is done to display averaged orientations distribution of shear dumbbells over time by $\langle P_2 \rangle_i$ (t), where i denotes the orientation axis, which refers to velocity direction x, gradient direction y and vorticity direction z, respectively. $\langle P_2 \rangle_{vorticity}$ (filled circles), $\langle P_2 \rangle_{velocity}$ (filled triangles) and $\langle P_2 \rangle_{gradient}$ (open squares) are defined as the order parameters to describe the orientations along the vorticity, velocity and gradient direction, respectively. The BD simulations have been performed by Nils Heptner.[132] 65

Figure 4.4.4 (a) Experimental scattering 2D pattern of hard dumbbells in the plastic crystalline phase (ϕ_{eff} = 0.60) under oscillatory shears (γ_{max} = 116%, Pe_r = 1.20, f = 1Hz) (b) The calculated 2D structure factor based on the Brownian dynamics simulation[132] on the shear melting of the fcc crystal under oscillatory shear of f = 5τ and γ_{max} = 70%, Pe_r = 10.63. The calculation is built for the model system of hard dumbbells in the plastic crystalline phase with L^* = 0.24 and ϕ_{eff} = 0.55. The corresponding simulation snapshots (c) of sheared dumbbells with ϕ = 0.55 and L^* = 0.24 in the velocity-gradient plane after the application of 250 oscillatory shear cycles with f = 15 Hz and γ_{max} = 30%, Pe_r = 4.56. (d) The corresponding orientation distribution of $\langle P_2 \rangle_i$ (t) denotes the averaged orientation distribution over time, and i denotes the orientation axis, which refers to velocity direction x (filled triangles), gradient direction y (open squares) and vorticity direction z (filled circles), respectively. 68

Figure 4.4.5 Experimental scattering 2D patterns of the hard dumbbells with ϕ_{eff} = 0.60 averaging (a) the first 600 oscillations and (b) the following 900 oscillations at γ_{max} = 60%, Pe_r = 0.62. Experimental scattering 2D patterns of hard dumbbells over (c) the first 600 oscillations and (d) the following 900 oscillations at γ_{max} = 70%, Pe_r = 0.76. (e) and (f) are the

experimental scattering patterns under oscillatory shear with γ_{max} = 90% and Pe_r = 0.97 for the first 600 and the following 900 oscillations, respectively. Experimental scattering results shown here are recorded in the velocity-vorticity scattering plane. 70

Figure 4.4.6 (a) Experimental scattering 2D patterns of the hard dumbbell suspensions with ϕ_{eff} = 0.60 over 900 oscillations at f = 1 Hz, γ_{max} = 60%, and Pe_r = 0.62 and (b) corresponding calculated scattering pattern by the LAMP-SANS software. The calculation result is a superposition result of 0.3 times pattern at 50%, 0.25 times pattern at 116% and 0.45 times of polycrystalline pattern. Both experimental and calculated results are shown in the velocity-vorticity scattering plane. 71

Figure 4.4.7 (a) 2D structure factors calculated by BD simulations on the hard dumbbells of L^* = 0.24 and ϕ_{eff} = 0.55 after the application of f = 15 Hz and γ_{max} = 20%, Pe_r = 3.04. (b) The structure analysis at various strain amplitudes and fixed frequency, f = 15 Hz , where the twinned fcc emerges at γ_{max} = 5% and Pe_r = 0.75, the intermediate phase is at γ_{max} = 20%, and Pe_r = 3.04 and the sliding layers structure is at γ_{max} = 30%, *and* Pe_r = 4.56. $<P_2>_{velocity}$ presents the orientation distribution with major axis along the velocity direction, Q_4 and W_4 are the bond order parameter to describe the crystal structure. The specified definitions are described in Chapter 3. 73

Figure 4.4.8 2D SANS plots for the hard dumbbell suspensions in the biphasic gap with ϕ_{eff} = 0.51 at rest (a) and under oscillatory shears with the fixed frequency, f = 1 Hz and various strains with amplitude: 19.4% and Per = 0.16 (b), 50% and Per = 0.42 (c), 60% and Per = 0.50 (d), 116% and Per = 0.97 (e) and 1000%, Per = 8.38 (f). 76

Figure 4.4.9 Yielding behaviour of the hard dumbbells with $L^* \sim 0.30$ (the DPM b microgels) in the fully crystalline phase (ϕ_{eff} = 0.60) in the oscillatory shear of 5 Hz, and the corresponding 2D scattering patterns are measured by SANS. Along the dependence of *G'* and *G"* on various strains: (a) at rest (b) 16% (Pe_r = 0.29, the end of the linear regime), (c) 42.3% (Pe_r = 0.75 the plateau of G', the minimum for G"), (d) 51.5% (Pe_r = 0.90, the maximum for G"), (e) 92.6% (Pe_r = 1.62), (f) 300% (Pe_r = 5.37), (g) 1000% (Pe_r = 17.84). 79

Figure 5.1.1 Schematic figure of hollow capsules produced by the template-based approach, the upper part represents the procedure for the monolayer hollow spheres, while the routine shown in the lower part leads to the bilayer hollow capsules. 83

Figure 5.1.2 (a) TEM micrograph and (b) height image from SFM characterization of the monolayer hollow spheres in dry state, (c) shows the cross-section along the solid red line marked in (b), the two arrows indicate the starting and ending points along the solid line. SFM samples are prepared using Mica as substrates via spin coating at a speed of 70 rpm. Schematic figure (d) is to illustrate the deformation of hollow capsules in the drying process for the sample preparation. 84

Figure 5.1.3 Cryo-TEM images of hollow spherical capsules stained by different sodium phosphotungstate concentrations (a) 1.7 mM, (b) 3.4 mM, and (c) 6.8 mM, respectively. The aim of sodium phosphotungstate is to enhance the contrast between sample and medium. 85

Figure 5.1.4 The dependence of R_H on temperature for the spherical microgels with PS cores (filled triangles) and the monolayer hollow spherical capsules after the removal of PS cores. Upwards triangles denote the dependence of R_H on increasing T, while downwards triangles indicate that on decreasing T. 87

Figure 5.1.5 TEM micrograph of the purified bilayer hollow spherical capsules. The sample is prepared on the copper grids. 88

Figure 5.1.6 Cryo-TEM micrograph of the bilayer hollow capsules at room temperature (T: ca. 25 °C) in water, the inset shows one single particle of higher magnification. The image proves that the bilayer hollow capsule have a core-shell structure with the hollow sphere as core. 89

Figure 5.1.7 Temperature dependence of the bilayer hollow capsules (BHS) and the corresponding spherical microgels (BSM), the measured temperature ranges from 10 °C to 50 °C. 90

Figure 5.2.1 Preparation procedures for the thermosensitive hollow Janus dumbbells through THF treatment. The template is the dumbbell-shaped microgel system with a cross-linked PNIPA shell attached on the dumbbell-shaped core, which is prepared as schematically shown in Figure 4.1.1. The red circle displays the poly(st-co-MPS) copolymer layer that is fabricated to facilitate the growth of the second sphere for the dumbbell-shaped core. 91

Figure 5.2.2 TEM images of the dumbbell-shaped core particles after (a) the first cycle of cleaning and (b) the final cycle of cleaning. 92

Figure 5.2.3 (a) Cryo-TEM micrograph of dumbbell-shaped core after the removal of PS via THF and the solid line marks the radial direction, and (b) corresponding gray profile along radial direction. 93

Figure 5.2.4 (a) SFM height image of the dumbbell-shaped core after the removal of PS via THF and (b) the corresponding cross section along the solid line in (a), showing different collapse state of isolated (marked by 1 and 3) and agglomerated particle (marked by 2) in the dried state. 94

Figure 5.2.5 (a) Height image from SFM measurements and TEM (b) images of the thermosensitive hollow Janus dumbbells resulted from the removal of PS from the dumbbell-shaped microgels. The inset in (b) shows one particle of higher magnification measured by TEM. Both images clearly indicate the Janus structure of hollow dumbbells. 95

Figure 5.2.6 Cryo-TEM image of the thermosensitive hollow Janus dumbbell-shaped capsules and the sample preparation was done at 20 °C. The image proves the Janus character of the particles showing a hollow side of the microgel (light gray) and partially hollow part (dark gray) composed of PNIPA shell and poly (styrene-co-MPS) copolymer layer. 96

Figure 5.2.7 (a) DDLS-relaxation time distributions (CONTIN-plots) calculated from the intensity autocorrelation functions for hollow Janus dumbbells in 50 mM KCl solution at 20 °C. From scattering angle θ = 20° (solid line in panel a) to θ = 30° (dashed line in panel a). (b) The corresponding relaxation processes are plotted as a function of the square of the scattering vector (q^2) showing DLS slow mode (open circles) for hollow Janus dumbbells, DDLS slow mode (filled triangles) and DDLS fast mode (open triangles). The solid line is the linear fitted data according to the corresponding mode. 97

Figure 5.2.8 Temperature dependence of hydrodynamic radius of one sphere in the dumbbell-shaped microgels (filled circles) and hollow Janus dumbbells after the removal of PS core (empty circles). With R_H decreases with increasing T, and L^* increases correspondingly, marked by empty triangles. Temperature ranges from 10 to 50 °C, dumbbell-shaped microgels dispersed in salt free water before and after the removal of PS show comparable thermo-responsive property. 98

Figure 7.2.1 Sketch of the preparation of thermosensitive hollow capsules, (a) the setup for dissolution of PS cores in a 50 mL glass bottle with a cap, which will prevent the solvent evaporation and (b) the purification of dissolved PS via centrifugation. 107

Figure 7.3.1 Schematic figure of the ALV -4000 compact goniometer system that is used for the DLS and DDLS experiments in this work. The red line denotes the beam path in a normal measurement. 109

Figure 7.3.2 Geometries of the rotational rheometer: (a) cone and plate; (b) parallel disks; (c) coaxial cylinders (Couette). 113

Figure 7.3.3 (a) Flow curve that is measured based on the steady shear mode, that is the dependence of σ on the increasing and decreasing $\boldsymbol{\gamma}$ (b) the dependence of *G'* and *G"* on the increasing strain amplitudes, which is measured in the oscillatory shear field with fixed *f*. . 114

Figure 7.3.4 Instrument layout of the rheo-SANS setup (D11, Grenoble). The stress-controlled rheometer (Physica MCR501, Anton Paar) with a couette cell was used to apply oscillatory shear. 115

Figure 7.3.5 (a) Detailed schematic for the measured part of the Couette cell. The red lines denote the beam path (b) Orientation of the main scattering geometries: V is velocity, ∇ is gradient and e is vorticity. 116

Figure 7.3.6 The radial integration by sectors through the LAMP-SANS software based on (a) 2D scattering pattern of the hard dumbbell suspension ($\phi_{eff} = 0.60$) under oscillatory shear (f = 1 Hz, γ_{max} = 50%, Pe_r = 0.52). The two dashed lines denoted by 180° and 210° are marked to show the centre line of two integrated sectors. The two solid red lines display the integrated sector with centre line of 180°. (b) the scattering intensity I(q) based on the two integrated sectors, the empty circles mark the radial integration over the sector along the centre line of 180°, and empty squares denote the radial integration along the centre line of 210°. The peak positions are determined at 0.00132, 0.00225, 0.00263, 0.00346 A^{-1} , which are indexed as 1: 3: 2: 7. 118

List of Tables

Table 4.1.1 Dimensional information of the dumbbell-shaped particles used in this study: the DPM_a microgels with $L^* \sim 0.24$ and the DPM_b microgels with $L^* \sim 0.30$, and their corresponding dumbbell-shaped cores (DPC). The dimensional information displayed here is achieved via DLS and DDLS measurements.....35

Table 4.1.2 Characterization of experimental diffusion coefficients D^T, measured from both DLS and DDLS experiments. D^R for the DPC_a and DPC_b cores is measured from DDLS measurements at 20 °C. D^R of the DPM_a and DPM_b microgles is calculated by the shell model based on D^T and L. The calculated dimensional information R_H and L for DPC cores at 20 °C and DPM microgels at 10 °C, 15 °C and 20 °C are included as well.....40

Table 4.4.1 Comparison of Pe_r that is need for the formation of vorticity alignment structure, the twinned fcc, the intermediate structure and the partially oriented sliding layers in the hard dumbbells with $L^* \sim 0.24$ and $L^* \sim 0.30$. D^R is obtained from DLS and DDLS measurements (the principles are described in section 3.2).....81

Table 5.1.1 Dimensional information of the hollow capsules at 20 °C with various sodium phosphotungastate salt concentrations, determined by DLS measurements and cryo-TEM images (estimated radius).....86

Table 5.2.1. Characterization of hollow Janus dumbbells and the comparison with that of dumbbell-shaped microgels, experimental diffusion coefficients D^T measured from both DLS and DDLS experiments.....97

Table 7.2.1 Specified recipe for the synthesis of dumbbell-shaped PS core particles: The PS-MPS sphere is the PS seeds with a copolymer layer of PS and MPS attached onto its surface. The copolymer aimed to facilitate the growth of the second sphere of the dumbbell-shaped core particles.....105

Table 7.2.2 Specified recipe for the synthesis of spherical and dumbbell-shaped microgels. The DPC_a core and the DPC_b core are the seeds for the preparation of the dumbbell-shaped microgels with L *~ 0.24 (DPM_a) and the dumbbell-shaped microgels with L* ~ 0.30 (DPM_b), respectively.....106

Table 7.2.3 Overview of the information of the preparations for three types of hollow capsules, including their respective templates, the number of cleaning cycles (N_c); the centrifugation time per cycle (t_c) and the centrifugation speed.....108

Table 7.3.1 Pe_r of hard dumbbells in the oscillatory shear field at measured temperature (DPM_a, 10 °C and 15 °C; DPM_b 15 °C). D^R used for the calculation is achieved by the DLS and DDLS measurement and shell modelling.[132].....117

List of Abbreviations

σ	shear stress
λ	wavelength
γ_{max}	amplitude of shear strain
γ	shear strain
ϕ_{rcp}	random close packing volume fraction
ϕ_g	volume fraction at the glass transition
ϕ_{freeze}	volume fraction below the freezing point
ϕ_{eff}	effective volume fraction
Γ_{slow}	slow relaxation rates
Γ_{fast}	fast relaxation rates
$\boldsymbol{u}$	the unite vector along the major axis
t_w	waiting time
THF	tetrahydrofuran
TEM	Transmission electron microscopy
T	temperature
t	time
SFM	Scanning force microscopy
SDS	sodium dodecyl sulfate
SAXS	small angle X-ray scattering
rheo-SANS	combination of rheology and small angle neutron scattering
R_c	radius of one composed sphere

R_C	the radius of one sphere in the dumbbell-shaped core
$\boldsymbol{q}$	scattering vector
q	magnitude of scattering vector
PS	polystyrene
PHSA	poly-(12 hydroxystearic acid)
PNIPA	poly (N-isopropylacrylamide)
PMMA	poly(methyl methacryalate)
Pe	Péclet number
MPS	3-(trimethoxysilyl) propyl methacrylate
MCT	mode-coupling theory
MC	Monte Carlo
L_H	the thickness of PNIPA shell
LCST	lower critical solution temperature
L_C*	aspect ratio of the corresponding DPC particles
L	center to center distance
l	long axis length
KPS	peroxodisulfate
KCl	potassium chloride
k	Boltzmann constant
JHD	Janus hollow dumbbells
hcp	hexagonal closed packed
G''	storage modeules
G'	elastic modules

fcc	face-centered cubic
f	frequency
D^T	translational diffusion
D^R	rotational diffusion
DPM	dumbbell-shaped microgels
DPC	dumbbell-shaped cores
DLS	dynamic light scattering
DDLS	depolarized dynamic light scattering
D	diameter of one sphere in dumbbells
BIS	N, N'-methylenebis (acrylamide)
BD simulation	Brownian dynamics simulation
bct	body-centered tetragonal
$\dot{\gamma}$	shear rate
Q_4	the second order invariant four bond order parameters
Pe_r	rotational Péclet number
$\widehat{W}_4$	the third order invariant the bond order parameters
USAXS	Ultra-small-angle X-ray scattering

List of Publications

- Chu, F.; Siebenbürger, M.; Polzer, F.; Stolze, C.; Kaiser, J.; Hoffmann, M.; Heptner, N.; Dzubiella, J.; Drechsler, M.; Lu, Y., Synthesis and characterization of monodisperse thermosensitive dumbbell-shaped microgels. *Macromol. Rapid Commun.* **2012,** *33* (12), 1042-1048.

- Chu, F., Polzer, F., Severin, N., Lu, Y., Ott, A., Rabe,J. P., Ballauff, M., Thermosensitive hollow janus dumbbells. *Colloid and Polymer Science* **2014**, 1-9.

- Chu, F., Polzer, F., Lu, Y., Ott, A., Ballauff, M., Monolayer and bilayer structured thermosensitive hollow spheres. (*In preparation)* **2014**.

- Chu, F., Heptner, N.; Lu, Y., Dzubiella, J.; Ballauff, M., Equilibrium and non-equilibrium phase behaviour of hard dumbbells. (Submitted) **2014**.

Presentations at Conferences and Meetings

- Jülich soft matter days 2011, 15.11.2011-18.11.2011, Jülich, Germany, poster presentation: Dynamics of anisotropic shaped colloidal suspensions

- DPG-Frühjahrstagung 25-30.03.2012, berlin, Germany, poster presentation: Dynamics of thermosensitive core-shell dumbbell- shaped microgels

- PNI in-house research "2nd Soft Matter & Life Science Workshop"20.03.2012, Potsdam, Germany, oral presentation: Thermosensitive dumbbell-shaped microgels: one ideal model to investigate dynamics of anisotropic particles

- 19th ostwald kolloquium 20-21.9.2012, Berlin, Germany, poster presentation: Phase Behaviour of Anisotropic Shaped Colloidal Suspensions

- The XVIth International Congress on Rheology 5-10.08.2012, Lisbon, Portugal, oral presentation: Yielding in dense suspensions of dumbbell-shaped colloids

- 46th Biennial Meeting of the German Colloid Society, Paderborn, Germany, poster presentation: Anisotropic shaped colloidal model system

- 27^{th} Conference of the European Colloid and Interface Society, Sofia, Bulgaria, poster presentation: Thermosensitive dumbbell-shaped microgels: one ideal model to investigate dynamics of anisotropic particles

- The European society of Rheology 2014, Karlsuhe, Germany, oral presentation: Dynamics of thermosensitive core-shell dumbbell-shaped microgels

Acknowledgement

First and foremost, I wish to thank my supervisor, Prof. Dr. Matthias Ballauff, who has supported me throughout the past three years. Mr. Ballauff has supported me not only by providing me the opportunity to work in his group, but also through academic discussions and emotional encouragement through the whole work to finish this thesis. Much thanks to him for introducing me to the interesting hard dumbbell system and helping me come up with the thesis topic. Moreover, I appreciate his patience and precious comments to improve my writing and presentation skills.

Furthermore, I would like to thank my group leader, Dr. Yan Lu. During the whole work, she always supported me with useful discussions about all problems in experiments. Especially for the first year, she gave me full support for the synthesis and characterization of the model system.

Moreover, I thank Nils Heptner and Prof. Dr. Joachim Dzubiella for the cooperation with all the theoretical simulations and useful discussions. The simulations performed by Nils Heptner play an important role in the data evaluations for both light scattering and rheo-SANS experiments.

Much thanks to Dr. Frank Polzer for his efforts on all cryo-TEM measurements, to Andreas Ott, Cao Jie and Julian Kaiser for all TEM measurements. I thank Prof. Dr. Jürgen P. Rabe for offering the opportunity to perform SFM measurements in his lab and all the assistance and efforts from Dr. Nikolai Severin during measurements. For the DLS and DDLS measurements, I appreciate all the useful guidance and help from Dr. Christian Schneider, Martin Hoffman and Christian Rabe. Especially to Dr. Christian Schneider, who offered helpful introductions and comments.

For the rheo-SANS part, I would like to thank all the people who supported me during the measurements at ILL (D11, Grenoble) and data evaluations, especially to my local contact Peter Lindner and his colleges who offered the precious beam time and technically supporting. Much thanks to my colleges Andreas Ott, Dr. Miriam Siebenbürger, Michael Oberle, Weihua Wang who attended the rheo-SANS experiments at ILL.

In the following, I would like to thank all the colleges in HZB for the friendly work environment with nice breaks. In particular, I would like to thank Dr. Nikoline Hansen for her kindness and great help. Prior to my arrival, she helped me rent a nice flat, which is really helpful and great. Additionally, I would like to thank all the help from my colleges from Andreas Ott, Nils Heptner and Karol Palczynski for all the kindness during the normal life and all the great time after work. Next, I would like to thank my best friend in Berlin, Carmen Stolze, who introduced me to her friends and family and brought me the feeling of home in Berlin. Of course, all my friends from the HZB Badminton group and all my Chinese friends in Berlin are highly appreciated.

Last but not the least, I express my sincerely thanks to my parents, who give me the best view to the world and the simple but most precious love, to my brothers and sister for all the beautiful moments. Moreover, I would like to thank another two special people: Dr. Fenghua Zhang (my best friend) and Yang Liu (my husband), who are as important as my family. In China, there is one old saying: having a bosom friend is one of the niceties of life. I am lucky that I have them two who are always the one that can share the happy and unhappy times for the last eight years. Moreover, I thank Yang Liu for all his patience and care as a family member, understanding and encouragement as a close friend.

Selbstständigkeitserklärung

Hiermit erkläre ich die vorliegende Arbeit selbst verfasst und nur unter Zuhilfenahme der angegebenen Hilfsmittel angefertigt zu haben.

Ferner erkläre ich, dass ich nicht anderweitig mit oder ohne Erfolg versucht habe, eine Dissertation einzureichen oder mich einer Doktorprüfung zu unterziehen.